Towards predicting cavitation noise using scale-resolving simulations
The importance of inflow turbulence

Klapwijk, M.D.

DOI
10.4233/uuid:db85b819-cf0b-4909-8e02-9d75ca52b130

Publication date
2021

Document Version
Final published version

Citation (APA)
Klapwijk, M. D. (2021). *Towards predicting cavitation noise using scale-resolving simulations: The importance of inflow turbulence*. [Dissertation (TU Delft), Delft University of Technology]. https://doi.org/10.4233/uuid:db85b819-cf0b-4909-8e02-9d75ca52b130

TOWARDS PREDICTING CAVITATION NOISE USING SCALE-RESOLVING SIMULATIONS

THE IMPORTANCE OF INFLOW TURBULENCE

TOWARDS PREDICTING CAVITATION NOISE USING SCALE-RESOLVING SIMULATIONS

THE IMPORTANCE OF INFLOW TURBULENCE

Proefschrift

ter verkrijging van de graad van doctor
aan de Technische Universiteit Delft,
op gezag van de Rector Magnificus prof. dr. ir. T.H.J.J. van der Hagen,
voorzitter van het College voor Promoties,
in het openbaar te verdedigen op woensdag 3 november 2021 om 12:30

door

Maarten Derk KLAPWIJK

Master of Science in Marine Technology,
Nederland,
geboren te Capelle aan den IJssel, Nederland.

Dit proefschrift is goedgekeurd door de

promotor: Prof.dr. ir. T.J.C. van Terwisga
promotor: Prof.dr. ir. J. Westerweel

Samenstelling promotiecommissie:

Rector Magnificus,	voorzitter
Prof.dr.ir. T.J.C. van Terwisga,	Technische Universiteit Delft, promotor
Prof.dr.ir. J. Westerweel,	Technische Universiteit Delft, promotor
Onafhankelijke leden:	
Prof.dr.ir. G.J.F. van Heijst,	Technische Universiteit Eindhoven
Prof.dr. S. Hickel,	Technische Universiteit Delft
Prof.dr. R. Bensow,	Chalmers University of Technology
Dr. F.S. Pereira,	Los Alamos National Laboratory
Overige leden:	
Dr. G.N.V.B. Vaz,	blueOasis
Reserve lid:	
Prof.dr.ir. B.J. Boersma,	Technische Universiteit Delft

Dr. T. Lloyd en dr. G. Vaz hebben in belangrijke mate aan de totstandkoming van het proefschrift bijgedragen.

Dit onderzoek is gefinancieerd door de Nederlandse Organisatie voor Wetenschappelijk Onderzoek (NWO) als onderdeel van het NOISOURCE project (ALWTW.2016.008).

Keywords: turbulence, scale-resolving simulations, cavitation, acoustics

Printed by: Gildeprint

Front & Back: Turbulent wake of an elliptic wing, visualised using the Q-criterion ($Q = 0.1$) and a cavitating tip vortex.

Typeset in LaTeX.

ISBN 978-94-6384-259-4

An electronic version of this dissertation is available at
http://repository.tudelft.nl/.

Capital letters were always the best way of dealing with things you didn't have a good answer to.

Douglas Adams, "Dirk Gently's Holistic Detective Agency"

SUMMARY

There is increasing attention for the effects of anthropogenic underwater radiated noise (URN) on marine fauna. This is expected to lead to regulations with respect to the maximum permitted sound emissions of ships. It is known that cavitating tip vortices, generated by ship propellers, are some of the key contributors to URN. Consequently, there is a need to evaluate propeller designs with respect to noise generation in a design stage. Computational fluid dynamics (CFD) has the potential to offer detailed insights into cavitating vortex dynamics and noise sources, at a reasonable cost. URN can be efficiently estimated using CFD in combination with an acoustic analogy. In order to use such predictions in a design process, it is essential to understand and quantify the errors associated with the numerical predictions of noise sources. This thesis investigates the reliability of such evaluations and aims to reduce occurring modelling errors.

To compute noise sources, it is necessary to simulate cavitation dynamics using scale-resolving simulations (SRS). Here, part of the turbulence kinetic energy spectrum is resolved in space and time, as opposed to being modelled using Reynolds averaged Navier-Stokes (RANS). The SRS method of choice in this work is the partially averaged Navier-Stokes (PANS) method. Bridging models, such as PANS, exhibit a smooth transition and absence of commutation errors between RANS and large eddy simulation (LES) zones, in contrast to hybrid models such as detached eddy simulation (DES). The formulation allows for a theoretical decoupling of the discretisation and modelling errors, thereby enabling verification and validation processes.

PANS allows the user to select the ratios of resolved-to-total turbulence kinetic energy and dissipation (rate). Appropriate settings and methods to estimate these settings *a priori* are investigated. Furthermore, a new PANS closure is developed, which offers improved convergence behaviour compared to more commonly used models, and is better suited to application for multiphase flows.

It has been shown repeatedly in literature that SRS should be accompanied by physical inflow boundary conditions, where time-varying fluctuations, resembling turbulence, should be inserted upstream of the object of interest, to prevent laminar solutions. However, from literature it is clear that for maritime applications this is often neglected. To the knowledge of the author, there is no previous application of such an inflow in combination with cavitation. In this PhD thesis, a synthetic inflow turbulence generator (ITG) is implemented, and tested for several test cases in wetted and cavitating conditions. For these cases, the numerical errors, consisting of discretisation, iterative and statistical errors are evaluated.

Firstly, the results when using the ITG are compared against recycling flow results for a turbulent channel flow, using different SRS methods. It was shown that the ITG can deliver a resolved turbulent inflow at lower computational cost. Secondly, the effect of neglecting such an inflow was tested for the Delft Twist 11 hydrofoil, where it was shown that simulating such a flow with a low ratio of resolved-to-total turbulence kinetic energy can lead to flow separation at the wing leading edge. This is in contrast to experimentally observed behaviour. The inclusion of the ITG can reduce this modelling error, although the sheet cavity dynamics remain largely unaffected. Finally, an elliptical wing with a cavitating tip vortex is simulated. The observed vortex dynamics are compared against a semi-analytical model from literature. To obtain vortex dynamics, the ITG was shown to be necessary. The far-field noise generated by the vortex is quantified and related to the cavity dynamics.

Some of the main contributions of this research are improved insight in the use of SRS in cavitating conditions, in simulating cavity dynamics and in using an ITG to obtain flow fields representative of experimental conditions. In this way it has enhanced our understanding of the ability and limitations in the prediction of acoustic sources due to cavitation. To improve predictions of cavitation dynamics it is recommended to address the cavitation model and the method which describes the cavity interface, to reduce the discrepancy in average cavity size between simulations and experimental observations.

SAMENVATTING

Er is steeds meer aandacht voor de effecten van antropogeen onderwater uitgestraald geluid (URN) op mariene fauna. De verwachting is dat dit leidt tot regelgeving met betrekking tot de maximaal toegestane geluidsuitstoot van schepen. Het is bekend dat caviterende tipwervels gegenereerd door scheepsschroeven enkele van de belangrijkste oorzaken van URN zijn. Dit leidt tot de noodzaak om schroefontwerpen in een ontwerpfase te evalueren met betrekking tot de geluidsproductie. Numerieke stromingsleer (CFD) biedt de kans om, tegen een redelijke prijs, gedetailleerde inzichten te bieden in caviterende vortexdynamica en geluidsbronnen. URN kan efficient worden ingeschat met gebruik van CFD in combinatie met een akoestische analogie. Om dergelijke voorspellingen in een ontwerpprocess te gebruiken is het noodzakelijk om de fouten geassocieerd met numerieke voorspellingen van geluidsbronnen te begrijpen en te kwantificeren. Dit proefschrift onderzoekt de betrouwbaarheid van dergelijke voorspellingen en heeft als doel om hierbij optredende modelleringsfouten te verminderen.

Om geluidsbronnen te berekenen is het noodzakelijk om cavitatiedynamica te simuleren met behulp van schaaloplossende simulaties (SRS). Hierbij wordt een deel van het turbulente kinetische energiespectrum wordt opgelost in de tijd en ruimte, dit in tegenstelling tot gemodelleerd middels *Reynolds averaged Navier-Stokes* (RANS). De SRS methode die de voorkeur heeft in dit onderzoek is *partially averaged Navier-Stokes* (PANS). Eigenschappen van *bridging* modellen, zoals PANS, zijn een soepele overgang and afwezigheid van commutatiefouten tussen RANS en *large eddy simulation* (LES) zones, in tegenstelling to hybride modellen zoals *detached eddy simulation* (DES). De formulering zorgt voor een theoretische ontkoppeling van discretizatiefouten en modelleringsfouten, wat verificatie en validatie mogelijk maakt.

Bij PANS kan de gebruiker de ratio van opgeloste-tot-totale turbulente kinetische energie en turbulentiedissipatie kiezen. Geschikte instellingen, en methodes on deze instellingen *a priori* in te schatten zijn onderzocht. Tot slot is er een nieuw PANS-KSKL model ontwikkeld. Dit model vertoont verbeterd convergentiegedrag vergeleken met andere veelgebruikte modellen, en is meer geschikt voor meer-phase stromingen.

In de literatuur is herhaaldelijk aangetoond dat SRS gepaard moet gaan met fysieke instroomrandvoorwaarden, waarbij stroomopwaarts in de tijd variërende fluctuaties, die lijken op turbulentie, moeten worden toegevoegd om laminaire oplossingen te voorkomen. Echter, het is duidelijk uit literatuur dat dit voor maritieme toepassingen meestal niet gedaan wordt. Voor zover bekend bij de auteur is er geen eerdere toepassing van een dergelijk instroming in combinatie met cavitatie. In dit proefschrift is een synthetische instroomturbulentiegenerator (ITG) geïmplementeerd en getest voor verschillende casussen in stromingen met en zonder cavitatie. Voor deze casussen zijn de numerieke fouten, bestaande uit discretizatie, iterative en statistische fouten geëvalueerd.

Ten eerste worden de resultaten, verkregen met ITG, vergeleken met de resultaten verkregen via het recirculeren van de stroming voor een turbulente kanaalstroom, waar-

bij verschillende SRS methoden gebruikt worden. Er is aangetoond dat de ITG een turbulente instroming kan leveren tegen lagere rekenkosten. Ten tweede is het effect van het verwaarlozen van een turbulente instroming getest voor de Delft Twist 11 vleugel, waarbij is aangetoond dat het simuleren van een dergelijke stroming met een lage opgeloste-tot-totale turbulente kinetische energie ratio kan leiden tot loslating van de stroming bij de voorrand van de vleugel. Dit in tegenstelling tot het experimenteel geobserveerde gedrag. Het gebruik van de ITG kan deze modelleringsfout verminderen, hoewel de vliescaviteitdynamiek grotendeels onbeïnvloed blijft. Tot slot is een elliptische vleugel met een caviterende tipwervel gesimuleerd. De hierbij geobserveerde vortexdynamica is vergeleken met een semi-analytisch model uit de literatuur. Om de vortexdynamica te verkrijgen is de ITG noodzakelijk gebleken. Het verre-veldgeluid, gegenereerd door de vortex, is gekwantificeerd en gerelateerd aan de caviteitsdynamiek.

Enkele van de belangrijkste bijdragen van dit onderzoek zijn een verbeterd inzicht in het gebruik van SRS in caviterende condities, in het simuleren van caviteitsdynamiek en in het gebruik van een ITG om stromingen te simuleren die representatief zijn voor experimentele condities. Hierdoor is ons begrip van de mogelijkheden en beperkingen van het voorspellen van akoestische bronnen door cavitatie, vergroot. Om voorspellingen van cavitateitsdynamiek te verbeteren wordt het aanbevolen om cavitatiemodellen en de methodes die de het caviteitsoppervlak beschrijven te modificeren, om de discrepantie in formaat van de gemiddelde cavitateit tussen simulaties and en experimentele observaties te verkleinen.

CONTENTS

6 Delft Twist 11 Hydrofoil **101**

7 Elliptical wing **133**

8 Conclusions **165**

LIST OF TABLES

LIST OF FIGURES

NOMENCLATURE

Symbol	Description	Unit
Roman letters		
a_{ij}	anisotropic part of the Reynolds stress tensor	$\mathrm{m^2/s^2}$
a_{ij}	Lund transformation matrix	s
b	filtering coefficient	
c	chord	m
c_0	speed of sound	m/s
D	destruction term	
D	diameter	m
d	nearest wall distance	m
E	energy	
E	error	
e	eccentricity	
e	sampling error	
F_b	body-force	N
f	flux	$\mathrm{m^3/s}$
f	frequency	Hz
G	grid	
G_{pp}	pressure cross-spectral density	
g	gravitational acceleration	$\mathrm{m/s^2}$
H	‘high’ Reynolds number approach	$f_\varepsilon = 1.0$
$\mathscr{I}$	turbulence intensity	%
K	resolved turbulence kinetic energy	$\mathrm{m^2/s^2}$
K_σ	stiffness term	
k_x	axial wavenumber ($k_x = 2\pi/\lambda$)	rad/m
k	modelled turbulence kinetic energy	$\mathrm{m^2/s^2}$
L	‘low’ Reynolds number approach	$f_\varepsilon = f_k$
L	turbulent length scale	m
$\mathscr{L}$	integral length scale	m
L_{vK}	von Kármán length scale	m
L_2	Euclidean norm	
L_∞	maximum norm	
l_t	turbulent length scale	m
M	‘moderate’ Reynolds number approach	$f_k < f_\varepsilon < 1.0$
$\dot{m}$	cavitation source term	$\mathrm{kg/(m^3 s)}$
N	number	

Symbol	Description	Unit
N_c	number of cells	
n	concentration	1/m^3
$\boldsymbol{n}$	normal vector	m
n	wavenumber in azimuthal direction	
P	pressure	Pa
P	production term	
q	observed order of convergence	
q	source term	
q_∞	dynamic pressure ($1/2\rho U_\infty^2$)	Pa
R	radius	m
Re_{ij}	resolved Reynolds stresses	m^2/s^2
R_{pp}	normalised pressure two-point spanwise correlation	
$\boldsymbol{r}$	radial vector	
r	radius	m
r	random numbers	
r_c	cavity radius	m
r_{eff}	effective radius	m
r_{pp}	pressure two-point spanwise correlation	Pa^2
$\boldsymbol{res}$	residuals	
S	magnitude of strain-rate tensor	1/s
S	source term	
S	surface	m^2
S_{ij}	strain rate tensor	1/s
s	span	m
T	Lagrangian time scale	s
T_{ij}	Lighthill stress tensor	kg/(m s^2)
T_{ij}	sub-test filter stress tensor	m^2/s^2
T_ω	contribution of surface tension	
t	time	s
t_η	Kolmogorov time scale	s
U	uncertainty	
U	velocity	m/s
u_τ	wall friction velocity	m/s
u_η	Kolmogorov velocity scale	m/s
V	volume	m^3
$\boldsymbol{x}$	position	m
$\boldsymbol{x}$	receiver location	m
x_c	cell size in chordwise direction	m
x_s	cell size in spanwise direction	m
x_t	cell size in tangential direction	m
$\boldsymbol{y}$	noise source location	m
Greek letters		
α	angle of attack	°

Symbol	Description	Unit
α	volume fraction	
Γ	diffusion constant	m^2/s
γ^2	spanwise coherence	
γ	intermittency	
Δ	interval or change	
δ	boundary layer thickness	m
Δ	cell size	m
δ_{ij}	Kronecker delta	
Δ_{avg}	volumetric average cell size	m/s
E	resolved dissipation	m^2/s^2
ε	modelled dissipation	m^2/s^2
η	Kolmogorov length scale	m
θ	angle	°
κ	von Kármán constant	
κ	wavenumber	$1/m$
κ_x	wavenumber	$1/m$
Λ	spanwise correlation length	m
λ	wavelength	m
λ_e	linear interpolation factor	
λ_g	transverse Taylor micro-scale	m
μ	dynamic viscosity	$kg/(ms)$
ν	kinematic viscosity	m^2/s
ν_t	kinematic eddy-viscosity	m^2/s
ψ	spatially correlated numbers	
ρ	density	kg/m^3
τ	retarded time	s
τ	sub-filter, or Reynolds, stress tensor	m^2/s^2
τ_w	skin friction	N/m^2
ϕ	arbitrary scalar quantity	
ϕ_{pp}	acoustic pressure power spectral density	
Ψ	temporally and spatially correlated numbers	
ω	modelled dissipation rate	$1/s$
Ω	resolved dissipation rate	$1/s$
Ω_{ij}	vorticity rate tensor	$1/s^2$
Mathematical operators		
$\langle\phi\rangle$	spatial averaged value	
$\langle\phi\rangle$	filtered value	
$\overline{\phi}$	temporal averaged value	
$\nabla\times$	curl	
$\nabla\cdot$	divergence	
$\dot{\phi}$	flux	
∇	gradient	
$\hat{\phi}$	spatial average vector	

Symbol	Description	Unit
$\hat{\phi}$	unit vector	
$H(f)$	Heaviside function	
K_n	modified Bessel function of the second kind (also known as a MacDonald function)	
K_n'	first derivative of modified Bessel function of the second kind	
∇^2	Laplacian	
$\lvert\phi\rvert$	magnitude	
$\mathrm{D}\phi/\mathrm{D}t$	material derivative	$\frac{\partial\phi}{\partial t} + U_i \cdot \frac{\partial\phi}{\partial x_i}$
$\partial/\partial x$	partial derivative with respect to x	
ϕ_{rms}	root mean square	
σ_ϕ	standard deviation	
$\tilde{\phi}$	normalised value	
$\tilde{\phi}$	composite value	
$\widehat{\phi}$	filtered value on larger test filter	
Sub- and superscripts		
ϕ_0	undisturbed/mean value	
ϕ_{95}	95% confindence interval	
ϕ_x	axial direction	
ϕ_b	bulk value	
ϕ_b	bubble	
ϕ_c	comparison	
ϕ^c	convective	
ϕ_{corr}	corrected value	
ϕ_D	drag	
ϕ_d	discretisation	
ϕ^d	diffusive	
ϕ_{exp}	experimental	
ϕ_f	skin friction	
ϕ_θ	azimuthal direction	
ϕ_i	input	
ϕ_{it}	iterative	
ϕ_∞	value in the far-field	
ϕ_L	lift	
ϕ_{le}	value at leading edge	
ϕ_l	liquid	
$\phi_{\max}$	maximum value	
$\phi_{\min}$	minimum value	
ϕ_n	normal direction	
ϕ_n	numerical value	
ϕ_*	non-dimensionalised value	
ϕ_p	points	
ϕ_p	pressure	

Symbol	**Description**	**Unit**
ϕ_{ref}	reference value	
ϕ_r	radial direction	
ϕ_s	statistical	
ϕ_{TG}	value at turbulence generator	
ϕ_τ	based on wall friction velocity	
ϕ_t	turbulent	
ϕ_{tip}	value at wing tip	
ϕ_v	vapour	
ϕ^+	normalized wall unit	
ϕ'	fluctuation	
Non-dimensional groups		
C_ϕ	force coefficient	$\phi/(Sq_\infty)$
C_f	skin friction coefficient	τ_w/q_∞
Co	Courant number	$\lvert U\rvert\Delta t/\Delta x$
C_p	pressure coefficient	p/q_∞
f_ε	modelled-to-total ratio of turbulence dissipation	ε/E
f_k	modelled-to-total ratio of turbulence kinetic energy	k/K
$f_{k,c}$	input value of modelled-to-total ratio of turbulence kinetic energy	k/K
$\tilde{f}_k$	*a posteriori* computed modelled-to-total ratio of turbulence kinetic energy	k/K
f_l	modelled-to-total ratio of turbulence length scale	l/L
f_ω	modelled-to-total ratio of turbulence dissipation rate	ω/Ω
h_i/h_1	spatial refinement level	$\Delta x_i/\Delta x_1$
Ma	Mach number	U/c_0
Pe	Péclet number	$\rho U\Delta x/\Gamma$
Re_c	critical Reynolds number	
Re_e	effective computational Reynolds number	
Re	Reynolds number	UL/ν
R_λ	Taylor-scale Reynolds number	$u_{rms}\lambda_g/\nu$
σ	cavitation number	$\left(p-p_v\right)/q_\infty$
St	Strouhal number	fL/U_∞
t_i/t_1	temporal refinement level	$\Delta t_i/\Delta t_1$
U^+	shear normalised velocity	u/u_τ
y^+	normalised wall distance	yu_τ/ν
Acronyms		
BC	boundary condition	
CDS	central differencing scheme	
CFD	computational fluid dynamics	

Symbol	Description	Unit
CG	conjugate gradient	
CV	control volume	
DDES	delayed detached eddy simulation	
DES	detached eddy simulation	
DNS	direct numerical simulation	
EARSM	explicit algebraic Reynolds stress model	
ETV	empirical (cavitating) tip vortex	
FOU	first-order upwind	
FWH	Ffowcs Williams-Hawkings	
GMRES	generalized minimal residual method	
HPC	high performance computing	
IDDES	improved delayed detached eddy simulation	
ILES	implicit large eddy simulation	
(I)TG	(inflow) turbulence generator	
ITTC	international towing tank conference	
KSGS	k sub-grid stress	
KSKL	$k-\sqrt{k}L$ turbulence model	
LES	large eddy simulation	
MARIN	maritime research institute Netherlands	
MPI	message passing interface	
NACA	National Advisory Committee for Aeronautics (nowadays NASA)	
NASA	National Aeronautics and Space Agency (former NACA)	
NWO	Nederlandse organisatie voor wetenschappelijk onderzoek (Dutch research council)	
OASL	overall sound level	
OASPL	overall sound pressure level	
OTO	one-third octave	
PANS	partially averaged Navier-Stokes	
PDS	porous data surface	
PISO	pressure-implicit splitting of operators	
PSD	power spectral density	
QUICK	quadratic upstream interpolation for convective kinematics	
RANS	Reynolds averaged Navier-Stokes	
ReFRESCO	reliable and fast RANS equation code for ships and constructions offshore	
RMS	root mean squared	
RSM	Reynolds stress model	
SAS	scale-adaptive simulation	

Symbol	Description	Unit
SIMPLE	semi-implicit method for pressure linked equations	
SL	sound level	
SPL	sound pressure level	
SRS	scale resolving simulations	
SST	shear stress transport	
TI	turbulence intensity	
TNT	turbulent/non turbulent	
TST	transient scanning technique	
TVD	total variation diminishing	
URANS	unsteady Reynolds averaged Navier-Stokes	
URN	underwater radiated noise	
VOF	volume of fluid	
WALE	wall adaptive local eddy-viscosity	
WMLES	wall modelled large eddy simulation	
XLES	extra large eddy simulation	

1

INTRODUCTION

This chapter provides the motivation, objectives and structure of the research study.

1.1. MOTIVATION

There is an increasing awareness of the harmful environmental impact of anthropogenic underwater radiated noise (URN) generated by marine traffic [1–5], as well as more stringent requirements for comfort on board ships [6]. It is estimated that, in the last fifty years, the power level of background noise increased by a factor 30 [5], and it is predicted that shipping noise, when unaddressed, will almost double by 2030 [7], highlighting the need for action. Currently, there are few regulations relating to URN, but these are expected to arrive in the near future (see e.g. [8–10]). Cavitating tip vortices are known to be one of the main contributors to ship noise, due to their dynamic behaviour and distinct broadband sound spectrum [11]. It is known that full scale ships produce sound in the range $5 - 100,000$ Hz, and that shipping contributes significantly to the total ambient sound level in the $10 - 1000$ Hz frequency range [4, 12]. These pressure fluctuations, at frequencies higher than the blade passage frequency, occur when the cavity pattern on the propeller blade is dominated by tip-vortex cavitation [13]. To minimise URN, it is therefore desirable to predict – during the design process – the occurrence and dynamics of tip vortex cavitation, and its noise generation [13, 14].

Presently, URN is commonly evaluated by performing full scale measurements, where a ship passes an array of hydrophones and the generated noise is recorded [15]. This method suffers from a limited accuracy [16–18], while also being too expensive and impractical to apply to each new ship design. Semi-empirical prediction methods, such as the empirical (cavitating) tip vortex (ETV) method by [13], have the advantages of being easy to use and cheap, but are not necessarily accurate in all cases, e.g. cases with both vortex and sheet cavitation [13]. Alternatively, model scale tests are performed in cavitation tunnels or specialized towing tanks [19]. Model scale testing is cheaper than full scale, but is still associated with significant costs and also suffers from limited availability, when compared to the total number of new ship designs per year. Additional difficulties arise when the near-field measured noise must be scaled to full scale, far-field, radiated noise [20]. Next to the cost and difficulties in measuring URN, there is also the issue of the limited understanding of noise generating mechanisms which can be extracted from experimental measurements, making it difficult to improve propeller designs. Numerical analysis, such as computational fluid dynamics (CFD), offers the potential to gain additional insight into the details of the flow at reasonable cost. When using CFD, acoustic methods, such as acoustic analogies, can be used to estimate the far-field URN. Acoustic analogies were traditionally designed with aerospace applications in mind, but they are being used more and more in the context of predicting URN, such as in [21, 22]. However, knowledge regarding the prediction of the dynamics of tip vortex cavitation is still insufficient to obtain reliable numerical results for vortex dynamics, leading to unreliable noise predictions [23–25]. Therefore, this thesis focusses on the prediction of tip vortex dynamics, to estimate the URN. Underwater radiated noise modelling using CFD depends on turbulence, cavitation, acoustic modelling. and their interaction. The emphasis of this thesis is on resolving and/or modelling of turbulence using scale-resolving simulations (SRS).

In SRS the larger scales of turbulence are resolved, with the smaller scales modelled (until the limit of direct numerical simulation (DNS), where the full turbulence spectrum is resolved). This is in contrast to the current workhorse of maritime CFD, Reynolds averaged Navier-Stokes (RANS), where the full turbulence spectrum is modelled. The increase in available computational power during the last decades makes the use of SRS possible for high Reynolds number flows. The added physical resolution should lead to a more accurate description of the flow and a reduction of the modelling error at a reasonable cost. However, the increased physical resolution necessitates higher spatial and temporal resolutions, and leads to an increase in importance of other numerical errors sources, such as statistical and iterative errors. These errors need to be evaluated to assess the reliability of such numerical predictions.

Linked to the increased physics in SRS, is the requirement of increased physics in the inflow boundary conditions, compared to RANS. In a typical RANS simulation the inflow prescribes the velocity, and an eddy-viscosity or time-averaged turbulence kinetic energy. For SRS of attached turbulent flows, it is necessary that the inflow contains time-varying stochastic velocity fluctuations that resemble turbulence. It has been repeatedly shown that the results of large eddy simulations (LES) or DNS can be dependent on inflow conditions, e.g. [26–28]. If this is not addressed, laminar solutions can be obtained, and consequently integral quantities, such as mean forces, can be underpredicted [29]. Nevertheless, a review of the literature studying cavitation for maritime applications reveals a lack of attention for this aspect, potentially leading to large modelling errors.

1.2. BACKGROUND

1.2.1. CAVITATION IN MARITIME APPLICATIONS

Cavitation is the phase change of liquid to vapour due to low pressure [30, 31]. Inception of cavitation occurs at the location of a nucleus, such as a bubble, a particle or imperfection at a wall. In liquids such as seawater, plenty of nuclei are available, leading to the simplified inception criterion that cavitation starts when local pressure drops below the vapour pressure. For an extensive description of cavitation the reader is referred to textbooks such as [30–33].

Cavitation can be divided into three categories: bubble, sheet, and vortex cavitation [13]. These types of cavitation are illustrated for a ship propellers in Fig. 1.1, the occurrence of each type depends on the propeller geometry and loading, see e.g. [34].

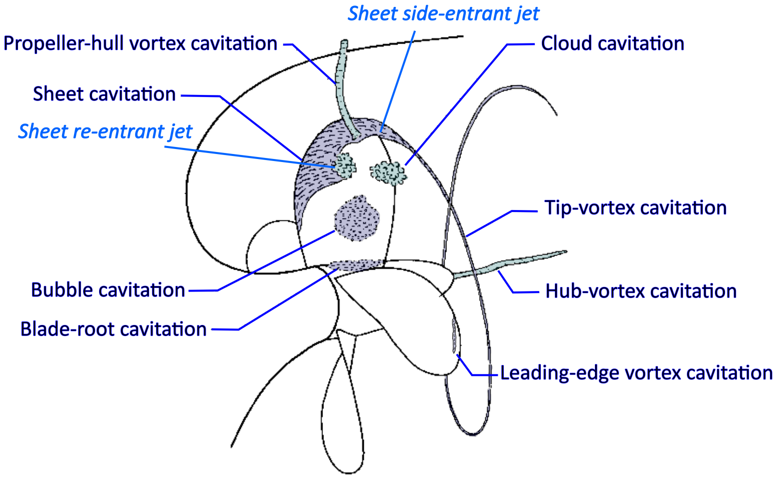

Figure 1.1: Illustration of possible cavitation patterns on ship propellers. Reproduced from Bosschers [13], adapted from [35].

Cavitation is associated with a reduction in delivered thrust, erosion damage to the propeller blades, and noise and vibration hindrance. While cavitation was observed as long ago as the 1850s, the main focus for a long time was on predicting or reducing cavitation erosion. Consequently, vortex cavitation has received less attention than bubble and shedding sheet cavitation, since those lead to the largest erosion damage. Tip vortex cavitation is almost unavoidable for propellers, since thrust is generated by the pressure difference over the blades of a propeller. Due to the finite span of a blade, this pressure difference inherently forms a tip vortex when flow moves from the high pressure side to the low pressure side at the tip of the blade. Fig. 1.2 shows model scale observations of a cavitating tip vortex. Usually the lowest pressure in the flow field is located in this tip vortex due to the high azimuthal velocity. Therefore, tip vortex cavitation is one of the first cavitation patterns to occur, especially for highly loaded propellers. It is expected to be a major source of broadband pressure fluctuations [11, 13, 36].

1.2.2. CAVITATION UNDERWATER RADIATED NOISE

Traditionally, noise and vibration hindrance were of interest from the point of view of passenger comfort. An early example is Cunard's Lusitania (1907), where during the sea trials at high speeds the stern vibrated to such an extent as to render the accommodation above the stern uninhabitable, necessitating extensive structural reinforcements and modifications [37]. URN was traditionally mainly of interest for military applica-

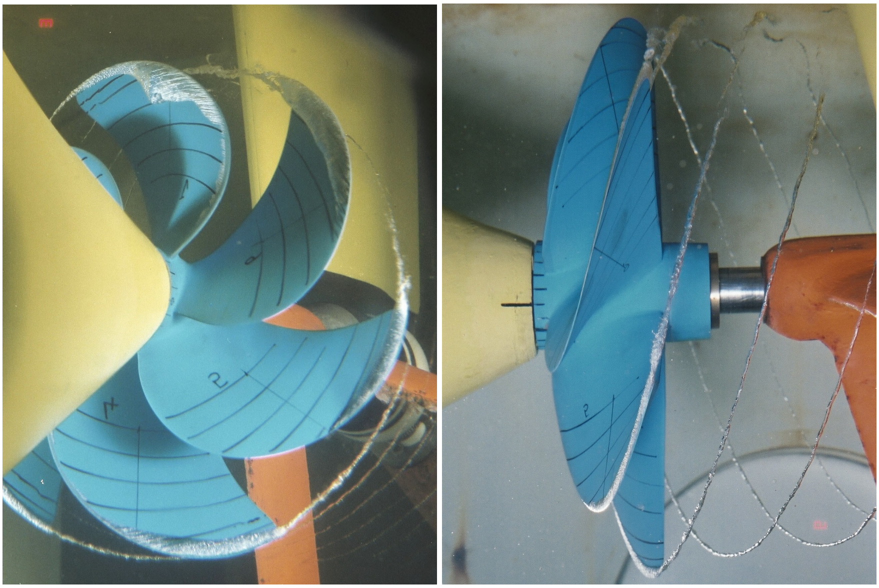

Figure 1.2: Model scale propeller exhibiting sheet and tip vortex cavitation operating in the wake of a ship hull mounted in the cavitation tunnel of MARIN. Flow from left to right. Note the additional vortex dynamics in the top position, as the blade passes through the hull wake field. Reproduced from Bosschers [13].

tions, where maintaining a low signature is important, as well as for research vessels operating acoustic sensors [38]. A newer concern is the negative effects of URN on underwater wildlife. It affects the behaviour of marine mammals and fish, and masks the sound the marine fauna produces and relies on for navigation, finding prey, mating and reproducing and resting [38, 39]. URN by anthropogenic sources has increased significantly over the last 50 years, due to the increase in number of ships as well as their size and installed power [1]. An extensive overview of research into this field is given by Duarte et al. [5].

Fig. 1.3 shows a typical sound spectrum generated by a ship. Traditionally, cavitation hindrance investigations focussed on low-frequency hull pressure fluctuations at the blade passage frequency and its harmonics, mostly caused by sheet cavitation to ensure acceptable vibration levels on board. URN however, is usually characterised by a broadband ‘hump’ at higher frequencies (between B3 and B6 in Fig. 1.3), which occurs when the cavity pattern on the propeller blade exhibits tip vortex cavitation [13]. A literature review shows that vortex cavitation research often focusses on inception, but to predict URN sound levels, it is necessary to predict dynamics of developed vortex cavitation.

Vortex cavitation dynamics have been investigated experimentally (e.g. [13, 36, 40, 41]), although obtained results suffer from scale effects, such as lower Reynolds numbers and inception problems. Also high costs are involved, making experiments less suitable for design purposes. CFD offers the potential to gain additional insight into the details of the flow, and far-field URN at reasonable cost. To predict URN, it is necessary to predict higher frequency dynamics. Such dynamics are governed by the natural vibration frequencies of the vortex, which is excited by the wake field in which the propeller operates. A purely periodic excitation would result in tonal noise at the blade passage frequency, and its harmonics. However, due to variations in the wake field by e.g. turbulence, the spectrum shows a so-called broadband hump, of which the centre frequency is hypothesised to be due to tip vortex cavity resonance [13, 42, 43]. To simulate correctly the turbulence scales ruling this phenomenon, industrial standard Reynolds averaged Navier-Stokes (RANS) CFD methods might not be sufficient. Instead, we must resort to scale resolving simulations with a resolved turbulent inflow.

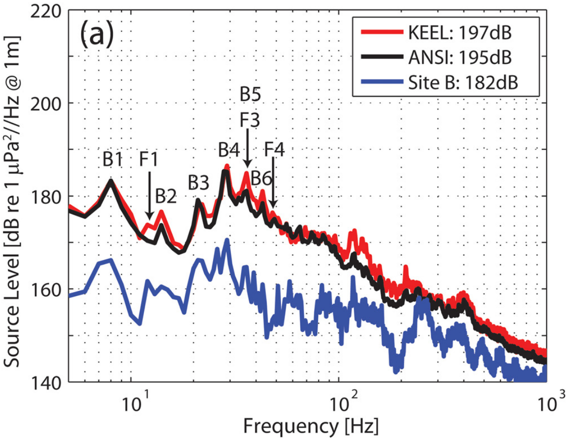

Figure 1.3: Source level spectra of a typical containership at 20.4 knots with developed cavitation on the propeller. Reproduced from Gassmann et al. [44]. The different colours correspond to different measurement locations. The harmonics of the propeller blade rate and main engine cylinder firing rate are indicated in by letters B and F, respectively. The fundamental blade rate (B1) is at 8 Hz.

1.2.3. SCALE-RESOLVING SIMULATIONS

The application of CFD in the maritime sector is moving towards more complex problems, such as massively separated flows, blunt bodies, off-design conditions, cavitation and noise predictions (see e.g. [45]). For such cases, the assumptions in traditional (unsteady) RANS approaches are too limiting, leading to an underprediction or absence of unsteady flow phenomena due to excessive levels of eddy-viscosity. Resolving the full spectrum of turbulence by means of direct numerical simulation (DNS) remains out of reach due to excessive computational cost. In DNS fluid motion must be resolved from the largest integral length scale up to the length scales at which the motion dissipates into heat (the Kolmogorov length scales). This property requires for fine computational grids and small timesteps, thereby massively increasing the computational cost. Since this cost is unaffordable for high Reynolds number flows, CFD for industrial flows has focussed on scale-resolving simulations (SRS). Here the larger scales are resolved, with the smaller scales modelled, as shown schematically in Fig. 1.4. The decrease in modelling error, due to resolving a large part of the turbulence spectrum instead of modelling it, leads to an increase in importance of numerical errors, thereby making error analysis even more relevant. In literature it is often seen that these errors are entangled and not quantified, thereby affecting the reliability of such numerical predictions.

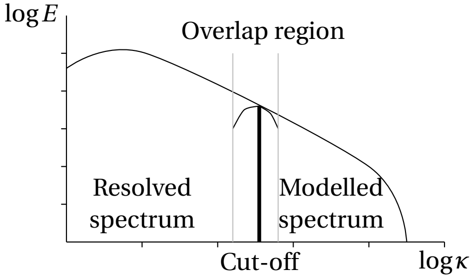

Figure 1.4: Schematic SRS wavenumber energy spectrum, showing the overlap between resolved and modelled velocity scales. E indicates the energy, and κ the wavenumber. Based on Reyes et al. [46].

SRS can be divided into three main categories: (i) Large Eddy Simulation (LES) [47], for which a filter is applied throughout the computational domain, resulting in scales larger than the filter being resolved and smaller scales being modelled using a 'sub-filter' model. The need to resolve a substantial part of the turbulence spectrum leads to stringent grid requirements in near wall regions. This implies often excessive computational cost for industrial flow problems, which typically involve complex geometries and Reynolds numbers often exceeding 10^6 in hydrodynamic applications [48]. The cost can be reduced through the use of wall modelled LES (WMLES) [49], although the definition of the interface between wall model and resolved flow is difficult for complex geometries. This has led to the rise of two alternative approaches: (ii) 'hybrid' methods, such as detached eddy simulation (DES) [50], where LES is zonally combined with RANS, which is applied in regions where the grid cannot support LES resolution; and (iii) 'bridging' methods, such as partially averaged Navier-Stokes (PANS) [51]. Bridging methods consist of a blending of RANS and DNS, but, in contrast to hybrid methods, the blending is not location dependent. Instead, it depends on user defined settings, such as the ratio of modelled-to-total turbulence kinetic energy and dissipation.

In all these approaches the ratio between resolved and modelled turbulence depends on a filter length. For LES and hybrid models, this filter length is implicitly defined by the grid, i.e. refining the grid reduces the influence of the sub-filter model [52]. Non-zonal hybrid models have the additional property that the blending function between LES and RANS depends on the local grid density [50, 53, 54]. Consequently, with grid refinement, not only the effect of the LES sub-filter model reduces in the LES region, but also a larger region of the flow is solved using LES. The modelling error is therefore entangled with – and for implicit LES (ILES) dependent on – the discretisation error, leading to a large grid sensitivity [55]. These properties make estimating the discretisation error impossible, and grid refinement studies to verify the results difficult [56, 57]. Both of these are essential to enable verification and validation processes, which are needed to assess the credibility of industrial CFD calculations [56]. An advantage of bridging models is that the filter length is set explicitly, thereby theoretically decoupling the discretisation and modelling errors [57]. Secondly, since the blend between RANS and DNS is not location dependent, there is a smoother transition between the turbulence modelling approaches. Thirdly, bridging methods with a constant ratio of modelled-to-total turbulence kinetic energy do not suffer from commutation errors, which affect hybrid methods due to the flow switching from RANS to LES regions [50, 58–60]. It was also recently shown by Pereira et al. [61] that PANS with a low ratio of modelled-to-total turbulence kinetic energy can obtain comparable results to DNS at lower computational cost. Due to these properties, bridging models are becoming attractive for industrial CFD, where extensive grid refinement studies are often unaffordable while an estimate of the numerical error is still required [62, 63]. In the current thesis, and within the user community of the CFD solver used in this work, ReFRESCO [64], there is a preference for using bridging models, i.e. PANS, over LES.

1.2.4. MULTI-PHASE MODELLING

In this work, multiphase flows are handled with the current standard method in CFD for the maritime world: volume of fluid (VOF) [65]. In VOF a single set of mass and momentum equations is solved, which a convected scalar field describing the fraction of a cell filled with one of the fluids. The fluid properties are interpolated based on this fraction. This method is known for, while satisfying mass conservation, not being able to keep a sharp interface, making the identification of the exact location of the interface difficult (see e.g. [66–73]). General consensus is that cavitation the best comparison with experimental visualizations can be observed for a vapour volume fraction of 10% vapour [74, 75], but the absence of a clear interface can potentially affect the observed vortex cavitation dynamics.

To close the set of equations a cavitation model is needed to prescribe the source term defining the phase change. A range of models, often named mass transfer models, have arisen over the years. In this thesis, one of the widely used cavitation models is employed (see e.g. [72, 74–79]), the Schnerr-Sauer model [80].

1.2.5. ACOUSTIC MODELLING

Sound can be defined as a fluctuating pressure wave moving through a compressible fluid [81]. To numerically predict acoustic pressures, compressible solvers can be used to either predict URN directly. Alternatively, incompressible solvers can be used in connection with an acoustic analogy. For an extensive overview into different methods, the reader is referred to [21, 22]. Due to the associated cost of compressible solvers, incompressible solvers are used almost exclusively in the maritime field, necessitating the use of an acoustic analogy. Following the literature on acoustics for marine noise, such as [21, 22, 82, 83], the Ffowcs Williams-Hawkings (FWH) analogy [84] is used to extract URN from the simulations. The FWH allows for a separation between sound generation and propagation. In this thesis, the porous formulation, derived by Di Francescantonio [85], is employed. In this formulation, the FWH equations are reformulated to solve the integrals on a fictitious permeable surface surrounding the noise sources. Sound propagation is assumed to be linear outside this surface, allowing this methodology to obtain the radiated sound at any arbitrary location [86].

1.3. RESEARCH OBJECTIVES

The main objective of the thesis is to develop an accurate, verified and validated numerical method for the prediction of cavitation noise sources using CFD. The CFD solver in this work is ReFRESCO [64]. The work focuses on resolving, rather than modelling, the influence of turbulence on cavitation dynamics using SRS, due to the considerable uncertainties and limitations associated with traditional modelling strategies, such as RANS. For verification and validation, both cavitating and non-cavitating conditions are considered, which allows assessment of turbulence modelling separately from cavitation modelling. The thesis aims to deliver a numerical framework that will:

1. resolve tip vortex cavitation dynamics to deliver insight in the noise generating mechanisms;
2. give insight into the numerical (iterative, discretisation, and statistical) errors and modelling errors associated with the results, by means of verifying and validating the numerical simulations;
3. reduce the modelling error of SRS by using synthetic inflow turbulence;
4. indicate the limitations of ‘standard’ mixture-based cavitation models within a VOF method for predicting cavitation dynamics and URN.

Next to that, the thesis aims to give guidelines for simulating turbulence and cavitation. While it is known that turbulence and cavitation models interact, this thesis focusses on the influence of different approaches for simulating turbulence. Different cavitation modelling approaches are beyond the scope of this work.

To reach the proposed research aims, several steps were necessary:

1. implement and verify a synthetic inflow turbulence generator (ITG) to enable a realistic, resolved turbulent, inflow to reduce modelling errors when using SRS, and to trigger cavitation dynamics;
2. evaluate, verify and validate various turbulence simulation approaches for cavitating flows, such as RANS, LES, RANS-LES hybrid and PANS;
3. apply an acoustic analogy to extract acoustic sources from the simulation and evaluate far-field pressure fluctuations;
4. develop an post-processing method to extract cavitation dynamics from a simulation, compare these with experimentally observed and theoretically predicted dynamics, and correlate these with far-field radiated noise;
5. combine the application of inflow turbulence, SRS, cavitation and FWH in a single simulation, to simulate vortex cavitation dynamics and predict the URN.

Objectives 1 and 2 are addressed in Chapters 5 and 6, while objectives 3,4 and 5 are addressed in Chapter 7. Objective 5 is relevant for industrial use of the employed in this thesis.

1.4. STRUCTURE OF THE THESIS

In this thesis, Chapter 2 describes all the mathematical models employed to simulate physical phenomena. The chapter starts from the general Navier-Stokes equations describing fluid flow, followed by a description of the numerical methods employed and giving a detailed overview of the different approaches for solving and/or modelling turbulence. Methods to generate a resolved turbulent inflow, which are essential to the current work, are described next. The approach to solve multi-phase flows is described in conjunction with cavitation modelling, followed by the acoustic analogy used to predict URN.

The methods employed for verifying and validating the numerical results are described in Chapter 3. Chapter 4 investigates different approaches to specify the ratio of modelled-to-total turbulence kinetic energy and dissipation, and derives a new PANS closure based on the KSKL model.

The remaining chapters apply the aforementioned methodologies to different test cases, namely a turbulent channel flow at $Re_\tau = 395$, the Delft Twist 11 Hydrofoil, a circular cylinder at $Re = 3900$, and an elliptical wing. Each of these chapters addresses different aspects of the applied methodologies. Chapter 5 focusses on the differences between several SRS methodologies, both with and without synthetic inflow turbulence. Chapter 6 applies the ITG, developed and tested in the previous chapter to a test case including cavitation. The errors occurring when a laminar inflow is applied are investigated for wetted flow conditions, and the effect the resolved turbulent inflow has on the cavitation behaviour is quantified. Finally Chapter 7 combines cavitation, inflow turbulence, and acoustics for a case representative of a simplified propeller. The deformations of a cavitating tip vortex are investigated and compared to experiments and a semi-analytical dispersion relation.

The thesis is concluded by Chapter 8, where the main findings and recommendations are summarised.

2

METHODOLOGY

An overview is given of the mathematical models employed in this work. Starting from the governing equations, some details concerning the CFD solver and implementation are given. The chapter focuses on the physical models relevant in this thesis, namely methods to simulate turbulence, to generate synthetic turbulence, multiphase flows including phase change, acoustic models. This overview is largely based on literature, and it is included for completeness.

2.1. GOVERNING EQUATIONS

Fluid motion is governed by conservation of mass and conservation of momentum. Conservation of mass, also known as the continuity equation [87],

$$\frac{\partial \rho}{\partial t}+\frac{\partial\left(\rho U_i\right)}{\partial x_i}=0, \tag{2.1}$$

implies that mass can neither be destroyed, nor created. In this equation U_i denotes the velocity components and ρ the density. The conservation of momentum, also known as the Navier-Stokes equation, reads for a Newtonian fluid [87]

$$\frac{\partial\left(\rho U_i\right)}{\partial t}+\frac{\partial}{\partial x_j}\cdot\left(\rho U_i U_j\right)=-\frac{\partial P}{\partial x_i}+\frac{\partial}{\partial x_j}\left[\mu\left(\frac{\partial U_i}{\partial x_j}+\frac{\partial U_j}{\partial x_i}-\frac{2}{3}\frac{\partial U_m}{\partial x_m}\delta_{ij}\right)\right]+\rho g_i. \tag{2.2}$$

with P the pressure, μ the dynamic viscosity (with $\mu=\rho\nu$, where ν is the kinematic viscosity), δ_{ij} the Kronecker delta and g_i external sources, such as gravity. Since no general analytical solution exists for these equations, we resort to numerical methods.

2.2. CFD SOLVER

The CFD code used in this thesis is ReFRESCO [64], developed at the Maritime Research Institute Netherlands (MARIN) in collaboration with organizations and universities around the world. ReFRESCO solves (unsteady) viscous flows based on the Navier-Stokes equations, together with turbulence models, cavitation models and volume-fraction transport equations for multiple phases [64, 88].

The equations are discretised in conservative form using a finite-volume method [89, 90] with all variables co-located in the cell centres. To obtain the variables at the surface of the control volume, i.e. the cell faces, interpolation is used. The integrals are approximated by using the values at the cell faces. Time integration is performed implicitly using first- or second-order schemes that support variable step sizes. In this thesis all simulations are performed with a second-order accurate time-integration.

The system of mass and momentum equations is linearised with Picard's method and solved either with a segregated or a coupled method, based on the Semi-Implicit Method for Pressure Linked Equations (SIMPLE) [91, 92] correction algorithm. In this thesis the pressure-velocity coupling is solved in a segregated manner. The use of SIMPLE allows the usage of larger time-steps (Courant numbers $U\Delta t/\Delta x$ [93] larger than one are permitted, this in contrast to the Pressure-Implicit Splitting of Operators (PISO) [94] algorithm). Nevertheless, timesteps for most of the considered SRS and cavitating flow simulations are limited by the physics which is attempted to be resolved. Fig. 2.1 shows schematically how the SIMPLE algorithm works, for more details the reader is referred to [89, 90]. All remaining equations are solved with a segregated method. The implementation is face-based permitting the use of structured and unstructured meshes with arbitrary elements. For a more extensive CFD background, the reader is referred to [89, 90], while more details concerning the implementation in ReFRESCO can be found in e.g. [88, 95–99].

2.3. APPROACHES FOR SIMULATING TURBULENCE

In this work several approaches for simulating turbulence are applied. These methods include Reynolds averaged Navier-Stokes (RANS), large eddy simulation (LES), hybrid methods, such as detached eddy simulation (DES), and bridging methods, such as partially averaged Navier-Stokes (PANS). This section provides a summary of these approaches, using a consistent notation. This section is based on the overview given by Pereira [100] which concerns single-phase flows without phase transition; the present section is a generalisation for two-phase flows with a variable density, including cavitation source terms. The main equations are described in this section, with full model details given in Appendix B.

For all approaches considered, the instantaneous quantities, Φ, are decomposed into a resolved, $\langle\Phi\rangle$, and a modelled (unresolved) component, ϕ, according to $\Phi = \langle\Phi\rangle + \phi$ [101]. Applying this decomposition to the unsteady mass conservation and incompressible, Newtonian, Navier-Stokes equations including phase change, while neglecting external forces, leads to

$$\frac{\partial\langle U_i\rangle}{\partial x_i} = \frac{\dot{m}}{\rho_v}, \tag{2.3}$$

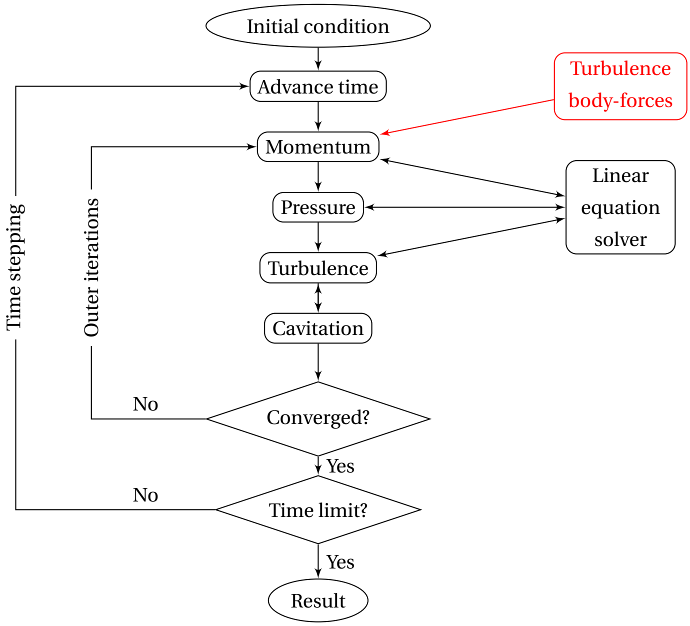

Figure 2.1: SIMPLE algorithm flow chart. The inflow turbulence generator (ITG) (see Sec. 2.4) is indicated in red. Figure based on Ferziger et al. [90].

and

$$\frac{\partial\left(\rho\langle U_i\rangle\right)}{\partial t}+\frac{\partial}{\partial x_j}\cdot\left(\rho\langle U_i\rangle\langle U_j\rangle\right)=-\frac{\partial P}{\partial x_i}+\frac{\partial}{\partial x_j}\left[\mu\left(\frac{\partial\langle U_i\rangle}{\partial x_j}+\frac{\partial\langle U_j\rangle}{\partial x_i}-\frac{2}{3}\frac{\partial\langle U_m\rangle}{\partial x_m}\delta_{ij}\right)\right] + \frac{\partial\tau_{ij}}{\partial x_j}. \tag{2.4}$$

See Appendix A for the derivation of the Navier-Stokes equations including the cavitation source term.

In these equations the subscripts l and v indicate liquid and vapour respectively, while symbols without subscript refer to the mixture. $\dot{m}$ is the source term due to the cavitation model (see Sec. 2.5.2), and τ_{ij} the sub-filter stress tensor which is computed according to [90]

$$\frac{\tau_{ij}}{\rho}=\langle U_iU_j\rangle-\langle U_i\rangle\langle U_j\rangle=2\nu_t\langle S_{ij}\rangle-\frac{2}{3}k\delta_{ij}-a_{ij}k, \tag{2.5}$$

with ν_t the eddy-viscosity, k the modelled turbulence kinetic energy and $\langle S_{ij}\rangle$ the resolved strain-rate tensor, defined as

$$\langle S_{ij}\rangle=\frac{1}{2}\left(\frac{\partial\langle U_i\rangle}{\partial x_j}+\frac{\partial\langle U_j\rangle}{\partial x_i}\right). \tag{2.6}$$

a_{ij} is the anisotropic part of the Reynolds stress tensor. For isotropic models, $a_{ij}=0$, such that Eq. 2.5 reduces to the Boussinesq hypothesis.

The difference between the respective approaches lies in the definition of the filtering operator $\langle\cdot\rangle$, which is temporal in the case of RANS and spatial for LES and PANS. Consequently, the sub-filter stress tensor is modelled differently by employing different expressions for ν_t and k.

2.3.1. REYNOLDS AVERAGED NAVIER-STOKES

In unsteady RANS, all turbulent time scales and motions are modelled, and a scale separation between deterministic and stochastic scales is assumed. In this work several commonly used two-equation RANS approaches are employed (SST and KSKL).

$k-\omega$ SST

The $k-\omega$ Shear Stress Transport (SST) model (2003 version) is a blend of a $k-\omega$ model in the wall region and a $k-\varepsilon$ model in the far-field [102]. The transport equations are

$$\frac{\partial\left(\rho k\right)}{\partial t}+\frac{\partial}{\partial x_j}\cdot\left(\rho k\langle U_j\rangle\right)=P_k-\rho\beta^*\omega k+\frac{\partial}{\partial x_j}\left(\left(\mu+\mu_t\sigma_k\right)\frac{\partial k}{\partial x_j}\right), \tag{2.7}$$

$$\frac{\partial\left(\rho\omega\right)}{\partial t}+\frac{\partial}{\partial x_j}\cdot\left(\rho\omega\langle U_j\rangle\right)=\frac{\alpha}{\nu_t}P_k-\beta\rho\omega^2+\frac{\partial}{\partial x_j}\left[\left(\mu+\mu_t\sigma_\omega\right)\frac{\partial\omega}{\partial x_j}\right]+2\rho\left(1-F_1\right)\frac{\sigma_{\omega_2}}{\omega}\frac{\partial k}{\partial x_j}\frac{\partial\omega}{\partial x_j}. \tag{2.8}$$

The other relevant expressions are

$$P_k=\min\left(\rho\nu_t\langle S\rangle,10\rho\beta^*k\omega\right)\qquad\text{and}\qquad\nu_t=\frac{a_1k}{\max\left(a_1\omega,\langle S\rangle F_2\right)}. \tag{2.9}$$

Here $\langle S\rangle$ is the magnitude of the resolved strain-rate tensor. The transport equations make use of two blending functions, F_1 and F_2, and two limiters. For details of these functions and the model constants see Sec. B.1.1.

KSKL

The $k-\sqrt{k}L$ (KSKL) model [103] introduces an additional length scale, the von Kármán length scale (L_{vK}), and exhibits a reduced eddy-viscosity. The model is also accompanied by improved iterative convergence compared to the SST model. The transport equations are defined as:

$$\frac{\partial\left(\rho k\right)}{\partial t}+\frac{\partial}{\partial x_i}\cdot\left(\rho k\langle U_i\rangle\right)=P_k-D_k+\frac{\partial}{\partial x_j}\left[\left(\mu+\frac{\mu_t}{\sigma_k}\right)\frac{\partial k}{\partial x_j}\right], \tag{2.10}$$

$$\begin{aligned}\frac{\partial\left(\rho\sqrt{k}L\right)}{\partial t}+\frac{\partial}{\partial x_i}\cdot\left(\rho\sqrt{k}L\langle U_i\rangle\right)=&\frac{\sqrt{k}L}{k}\nu_t\langle S\rangle^2\left(\zeta_1-\zeta_2\left(\frac{L}{L_{vk}}\right)^2\right)\\&-\zeta_3\rho k+\frac{\partial}{\partial x_j}\left[\left(\mu+\frac{\mu_t}{\sigma_{\sqrt{k}L}}\right)\frac{\partial\left(\sqrt{k}L\right)}{\partial x_j}\right]-6\nu\frac{\sqrt{k}L}{d^2}f_{\sqrt{k}L},\end{aligned} \tag{2.11}$$

with d denoting the distance to the closest wall, and $f_{\sqrt{k}L}$ acting as a viscous sublayer model [103]. In these equations, the eddy-viscosity and von Kármán length scale are defined as,

$$\nu_t = C_\mu^{1/4} \frac{kL}{\sqrt{k}} \qquad \text{and} \qquad L_{vK} = \kappa \frac{|U'|}{|U''|}, \tag{2.12}$$

with κ being the von Kármán constant and

$$|U'| = \sqrt{\frac{\partial \langle U_i \rangle}{\partial x_j} \frac{\partial \langle U_i \rangle}{\partial x_j}} \qquad \text{and} \qquad |U''| = \sqrt{\frac{\partial^2 \langle U_i \rangle}{\partial x_j \partial x_j} \frac{\partial^2 \langle U_i \rangle}{\partial x_k \partial x_k}}. \tag{2.13}$$

The production and destruction terms are

$$P_k = \rho \nu_t \langle S \rangle^2, \tag{2.14}$$

$$D_k = C_\mu^{3/4} \rho \frac{k^{3/2}}{L}. \tag{2.15}$$

For the model constants see Sec. B.1.2.

2.3.2. HYBRID MODELS

Hybrid models combine LES and RANS in a zonal manner. The aim is to employ LES away from the wall, but using RANS closer to the wall, to obtain a methodology which combines both accuracy and cost for high Reynolds number flows.

DDES

Delayed detached eddy simulation (DDES) [53] is an adaptation of the detached eddy simulation (DES) [50] model. In the current work, in the RANS region the SST model is used, while a sub-filter model is employed in the LES region. The switch between RANS and LES is based on the turbulent length scale l_t and a shielding function f_d. The k transport equation becomes

$$\frac{\partial (\rho k)}{\partial t} + \frac{\partial}{\partial x_j} \cdot \left(\rho k \langle U_j \rangle\right) = P_k - \frac{k^{3/2}}{l_t} + \frac{\partial}{\partial x_j} \left((\mu + \mu_t \sigma_k) \frac{\partial k}{\partial x_j} \right), \tag{2.16}$$

including the turbulent length scale

$$l_t = l_t^{RANS} - f_d \max\left(l_t^{RANS} - l_t^{SRS}, 0\right). \tag{2.17}$$

The RANS and SRS length scales are defined as

$$l_t^{RANS} = \frac{\sqrt{k}}{\beta^* \omega} \qquad \text{and} \qquad l_t^{SRS} = C_{DDES} \Delta, \tag{2.18}$$

in which Δ is the maximum cell length. The inclusion of the turbulent length scale reduces the eddy-viscosity in LES regions, allowing instabilities to develop. The coefficients and additional shielding function are given in Sec. B.2.1.

IDDES

In DDES the transition from RANS to LES inside a wall boundary layer is prohibited, which leads to a lack of resolved velocity fluctuations close to the wall. This can suppress dynamics in flow phenomena close to the wall, such as sheet cavitation. A different hybrid model is improved delayed detached eddy simulation (IDDES) [54], which aims to use DES as a Wall-Modelled LES (WMLES), while employing RANS in the near wall region instead of an analytical expression. Consequently IDDES is better able to handle separating flows, since LES is also allowed inside the boundary layer. A wall-normal resolution $y^+ = u_\tau y/\nu < 1$ at the wall is still required. In IDDES the blending is achieved by a different shielding function f_{dt}. Note that due to the different formulation, the model is prohibited to switch to RANS in the boundary layer and far-field. This can therefore deteriorate the results on a coarse grid or in the far-field. The coefficients and auxiliary functions are given in Sec. B.2.2.

XLES

The final hybrid model considered in this thesis is extra-large eddy simulation (XLES) [104]. It is similar to DDES and IDDES, but with a switching function which is not dependent on the wall distance. Furthermore, in LES mode a different sub-filter stress model to DES is used (the KSGS model, see Sec. 2.3.4). The difference between RANS and LES modes lies in the definition of the eddy-viscosity and dissipation. For RANS these are given as

$$\nu_t = l\sqrt{k} \qquad \text{and} \qquad \varepsilon = \beta_k \frac{k^{\frac{3}{2}}}{l}, \tag{2.19}$$

with $l = \sqrt{k}/\omega$, while for the LES sub-filter model

$$\nu_t = C_1 \Delta \sqrt{k} \qquad \text{and} \qquad \varepsilon = C_2 \frac{k^{\frac{3}{2}}}{\Delta}, \tag{2.20}$$

with Δ defined as the maximum cell length. The RANS model is closed with a modified equation for ω, based on the $k-\omega$ TNT model [105],

$$\frac{\partial\left(\rho\omega\right)}{\partial t} + \frac{\partial}{\partial x_j} \cdot \left(\rho\omega\langle U_j\rangle\right) = P_\omega - \beta_\omega \rho\omega^2 + \frac{\sigma_d}{\omega}\rho \max\left(\frac{\partial k}{\partial x_i}\frac{\partial \omega}{\partial x_i}, 0\right) + \frac{\partial}{\partial x_j}\left(\left(\mu + \sigma_\omega \mu_t\right)\frac{\partial \omega}{\partial x_j}\right), \tag{2.21}$$

with a production term

$$P_\omega = \rho\alpha_\omega \langle S\rangle^2. \tag{2.22}$$

The switch between RANS and LES modes is made using a composite length scale $\tilde{l}$ defined as

$$\tilde{l} = \min\left(l, C_1\Delta\right). \tag{2.23}$$

The coefficients and auxiliary functions are given in Sec. B.2.3.

2.3.3. BRIDGING MODEL

The combination of RANS with LES in hybrid models improves accuracy but may lead to commutation errors in the transition between the RANS and LES zones. An approach without commutation errors is the bridging family of models, such as the Partially Averaged Navier-Stokes (PANS) model [51, 106]. The PANS model is based on spatially filtering the Navier-Stokes equations, where the sub-filter stress tensor is modelled using a set of reformulated RANS equations including the modelled-to-total ratio of turbulence kinetic energy and dissipation,

$$f_k = \frac{k}{K} \qquad \text{and} \qquad f_\varepsilon = \frac{\varepsilon}{E}. \tag{2.24}$$

In PANS, the closure is viscosity-based (the sub-filter viscosity is a function of the modelled flow field (k,ω)), whereas in LES the closure is grid-based (sub-filter viscosity is a function of the cut-off length scale (Δ)) [46]. Consequently, in contrast to LES, the cut-off length scale of the resolved flow is not predetermined in PANS. The physical resolution is only determined by the settings, which leads to an overlap between the PANS resolved and modelled spectra [46]. Since the grid remains fixed, computations with an f_k smaller than what the grid allows are comparable to an explicitly filtered LES (although based on a different modelling framework). Computations with a very low f_k value are effectively an implicit LES (under-resolved DNS).

Two PANS models are used in this thesis, one based on the $k-\omega$ SST model and a newly derived model based on the KSKL model.

PANS-SST

The $k-\omega$ SST PANS model [57, 102] utilizes the modelled-to-total ratio of turbulence kinetic energy and dissipation rate,

$$f_\omega = \frac{\omega}{\Omega} = \frac{f_\varepsilon}{f_k}. \tag{2.25}$$

The transport equations are formulated as

$$\frac{\partial(\rho k)}{\partial t} + \frac{\partial}{\partial x_j}\cdot\left(\rho k \langle U_j\rangle\right) = P_k - \beta^* \rho\omega k + \frac{\partial}{\partial x_j}\left[\left(\mu + \mu_t \sigma_k \frac{f_\omega}{f_k}\right)\frac{\partial k}{\partial x_j}\right], \tag{2.26}$$

$$\begin{aligned}\frac{\partial(\rho\omega)}{\partial t} + \frac{\partial}{\partial x_j}\cdot\left(\rho\omega\langle U_j\rangle\right) = &\frac{\alpha}{\nu_t}P_k - \left(P' - \frac{P'}{f_\omega} + \frac{\beta\rho\omega}{f_\omega}\right)\omega + \frac{\partial}{\partial x_j}\left[\left(\mu + \mu_t\sigma_\omega \frac{f_\omega}{f_k}\right)\frac{\partial\omega}{\partial x_j}\right] \\ &+ 2\rho\frac{\sigma_{\omega 2}}{\omega}\frac{f_\omega}{f_k}(1-F_1)\frac{\partial k}{\partial x_j}\frac{\partial\omega}{\partial x_j}.\end{aligned} \tag{2.27}$$

with

$$P' = \frac{\alpha\beta^*\rho k}{\nu_t} \qquad \text{and} \qquad \nu_t = \frac{a_1 k}{\max\left(a_1\omega, \langle S\rangle F_2\right)}. \tag{2.28}$$

For the auxiliary functions and constants see Sec. B.3.1.

PANS-KSKL

The $k-\sqrt{k}L$ (KSKL) PANS model (see Chapter 4) utilizes the modelled-to-total ratio of turbulence kinetic energy and turbulent length scale,

$$f_l = \frac{l}{L} = \frac{f_k^{3/2}}{f_\varepsilon}. \tag{2.29}$$

It is known from RANS modelling that $k-\omega$ models suffer from a lack of iterative convergence, especially for multiphase flows, such as cavitation and free-surface flows. The KSKL model exhibits improved iterative convergence, lower eddy-viscosity levels, better defined boundary conditions and a lower dependency on the size of the first near-wall cell (y^+) [107]. When combining PANS with KSKL, the desirable features of PANS-SST are maintained, but with the improved iterative convergence of the KSKL model. The transport equations of the KSKL model are

$$\frac{\partial(\rho k)}{\partial t} + \frac{\partial}{\partial x_j}\cdot(\rho k\langle U_j\rangle) = P_k - D_k + \frac{\partial}{\partial x_j}\left[\left(\mu + \frac{\mu_t}{\sigma_k\sqrt{f_k}f_l}\right)\frac{\partial k}{\partial x_j}\right] \tag{2.30}$$

$$\begin{aligned}\frac{\partial\left(\rho\sqrt{k}l\right)}{\partial t} + \frac{\partial}{\partial x_j}\cdot\left(\rho\sqrt{k}l\langle U_j\rangle\right) =& \rho\frac{\sqrt{f_k}\sqrt{k}l}{f_l k}\nu_t\langle S\rangle^2\left(\zeta_1-\zeta_2\left(\frac{l}{f_l L_{vk}}\right)^2\right) - \zeta_3\rho k\frac{f_l}{\sqrt{f_k}} \\ &+ \frac{\partial}{\partial x_j}\left[\left(\mu+\frac{\mu_t}{\sigma_{\sqrt{k}l}\sqrt{f_k}f_l}\right)\frac{\partial\sqrt{k}l}{\partial x_j}\right] - 6\nu\rho\frac{\sqrt{k}l}{d^2}f_{\sqrt{k}l}.\end{aligned} \tag{2.31}$$

with

$$P_k = \rho\nu_t\langle S\rangle^2 \qquad \text{and} \qquad \nu_t = \min\left(C_\mu^{1/4}\sqrt{k}l; \frac{a_1 k}{\langle S\rangle}\right). \tag{2.32}$$

For the auxiliary functions and constants see Sec. B.3.2, for the full derivation see the Appendix C. The properties of the model are investigated in detail in Sec. 4.3.

2.3.4. LARGE EDDY SIMULATION

Large Eddy Simulation (LES) is founded on the principle that the larger scales of turbulence are resolved, while the smaller scales are modelled since they are more independent of geometry and boundary conditions. In order to enable this, the filtering operation is performed spatially; either explicitly or implicitly (on the grid). To relate the subfilter stress to the filtered strain rate, a number of models can be employed. In this work, a selection is made based on the most common models found in the open literature.

SMAGORINSKY

The Smagorinsky model [47] models the eddy-viscosity as

$$\nu_t = (C_s\Delta)^2\langle S\rangle, \tag{2.33}$$

with $\langle S\rangle = \sqrt{2\langle S_{ij}\rangle\langle S_{ij}\rangle}$ and a model constant C_s. The model constant depends on the flow and in literature values in the range $0.065 - 0.23$ are found. In this work a value of 0.10 is applied. The filtering is done implicitly, using the filter as defined by Smagorinsky:

$$\Delta = \left(\Delta_x\cdot\Delta_y\cdot\Delta_z\right)^{1/3}. \tag{2.34}$$

In the case of highly anisotropic cells, which occur often near walls, this filter is too optimistic leading to an underpredicted eddy-viscosity.

LILLY

To circumvent difficulties in obtaining a general constant for the Smagorinsky model and to improve behaviour near walls, Germano et al. [108] suggested using a constant which varies in time and space, thereby adapting to the resolved scales. Lilly [109] applied a least-squares estimate to obtain the constant, known as the Lilly or dynamic Smagorinsky model. In this approach, next to the spatial filter, a second, coarser, filter is applied. This filter, known as the 'test' filter, indicated by $\widehat{\cdot}$, is usually defined as $\widehat{\Delta} = 2\Delta$. The sub-test filter stress, T_{ij}, is defined analogously to the sub-filter stress, that is

$$T_{ij} - \frac{1}{3}\delta_{ij}T_{kk} = 2\left(C_s\widehat{\Delta}\right)^2 \widehat{\langle|S|\rangle}\widehat{\langle S_{ij}\rangle}. \tag{2.35}$$

The model constant is obtained using

$$C_s = \frac{1}{2}\frac{L_{ij}M_{ij}}{M_{ij}M_{ij}}, \tag{2.36}$$

in which the error between the resolved scales of motion L_{ij} and the local closure M_{ij} is minimized. L_{ij} is defined as the difference between the sub-filter stress on the normal filter (τ_{ij}) and on the test-filter level, T_{ij},

$$L_{ij} = T_{ij} - \widehat{\tau_{ij}} = -\widehat{u_i u_j} + \widehat{\langle u_i\rangle}\widehat{\langle u_j\rangle}, \tag{2.37}$$

and M_{ij} is defined as

$$M_{ij} = \widehat{\Delta}^2\widehat{\langle|S|\rangle}\widehat{\langle S_{ij}\rangle} - \Delta^2\widehat{\langle|S|\rangle\langle S_{ij}\rangle}. \tag{2.38}$$

A downside of this model is that the model requires spatial averaging of the constant to reduce the variability in space and time, else the value of C_s can become either negative or unphysically large [110]. Since this is often not possible for industrial flow cases due to the absence of flow homogeneity, the constant is bounded between 0 and 10 times the upper limit of the Smagorinsky constant as found in literature, so $C_s \in [0, 2.3]$.

WALE

The wall adaptive local eddy-viscosity (WALE) model by Nicoud and Ducros [111] was proposed for LES in complex geometries to account for the effects of the strain and rotation rate of the smallest resolved velocity fluctuations. It should also recover proper near-wall scaling for the eddy-viscosity without dynamic procedures. The sub-filter viscosity is determined as

$$\nu_t = L_s^2 \frac{\left(S_{ij}^d S_{ij}^d\right)^{3/2}}{\left(\langle S_{ij}\rangle\langle S_{ij}\rangle\right)^{5/2} + \left(S_{ij}^d S_{ij}^d\right)^{5/4}}, \tag{2.39}$$

based on the square of the velocity gradient tensor

$$S_{ij}^d = \frac{1}{2}\left(\langle g_{ij}\rangle^2 + \langle g_{ji}\rangle^2\right) - \frac{1}{3}\delta_{ij}\langle g_{kk}\rangle^2 \tag{2.40}$$

with

$$\langle g_{ij}\rangle = \frac{\partial \langle U_i\rangle}{\partial x_j}. \tag{2.41}$$

The length scale is given as

$$L_s = \min\left(\kappa d, C_s \Delta\right) \tag{2.42}$$

in which d indicates the wall distance and κ the von Kármán constant ($\kappa = 0.41$).

KSGS

The final sub-filter model is the k sub-grid stress (KSGS) model [112], for which a transport equation for the sub-filter turbulence kinetic energy (Eq. 2.7) is solved, with the production term and eddy-viscosity defined as

$$P_k = \mu_t \langle S\rangle^2 \qquad \text{and} \qquad \nu_t = C_1 \Delta \sqrt{k}, \tag{2.43}$$

with $C_1 = 0.05$.

ILES

An alternative approach is known as implicit LES (ILES) [113]. Instead of explicitly applying a sub-filter model, it is assumed that the added numerical diffusion due to the use of coarse(r) grids and specialised (often low order) convection schemes acts as a sub-filter model. Whilst an attractive approach due to low computational cost (no sub-filter model is required), caution is needed in employing this approach, especially in resolving structures near the presumed cut-off scale [55]. Due to the absence of a sub-filter model, the only contributing factor in the ratio of modelled-to-total kinetic energy is the grid. As a consequence making a proper grid becomes even more important than usual; the reliability of ILES for industrial flow cases on highly non-uniform, anisotropic grids can lead to large errors. The filter length varies significantly in the domain, and due to the anisotropic cells, the numerical dissipation due to the convection scheme varies in different directions. Secondly, the application of low order (upwinding) methods using coarse grids can lead to too much added dissipation, thereby not capturing finer structures [55]. Finally, the results are even more grid dependent than for normal LES, which makes proper solution verification impossible. Nevertheless, it is a widely employed approach.

In this thesis, simulations without a turbulence model are considered to be ILES.

2.3.5. REMARKS

In all approaches, the ratio between resolved and modelled turbulence depends on a filter length. In LES and hybrid models this filter length is implicitly defined by the grid, i.e. refining the grid reduces the influence of the sub-filter model. Non-zonal hybrid models have the additional issue that the blending function between LES and RANS depends on the local grid density. Consequently, with grid refinement not only the effect of the LES sub-filter model reduces in the LES region, but also a larger region of the flow is solved using LES. The modelling error is therefore entangled with, and for ILES even dependent on, the discretisation error, leading to a large grid sensitivity. These properties make estimating the discretisation error impossible, and grid refinement studies to verify the results difficult. Both of these are essential to enable verification and validation processes which are needed to assess the credibility of industrial CFD calculations. This is especially relevant for SRS methods, which are still seen as immature for industrial use. In bridging models the filter length is set explicitly, thereby theoretically decoupling the discretisation and modelling errors. Of course, when performing a computation with a high physical resolution on a coarse grid, the discretisation error will become dominant. Also the blend between RANS and DNS is not location dependent but depends on user defined settings, allowing for a smooth transition between the turbulence modelling approaches. Bridging methods with a constant physical resolution, also do not suffer from commutation errors, which affect hybrid methods due to the flow switching from RANS to LES regions [50, 58, 60]. Due to these properties, in the current thesis and within the ReFRESCO user community there is a preference for using bridging models, i.e. PANS.

Several questions remains concerning the usage of PANS. One concerns selecting a proper value for f_ε, in literature $f_\varepsilon = 1.0$ (known as the 'high Reynolds number' approach) is used almost exclusively. It is however not clear where the threshold of a high Reynolds number lies, nor what are the effects when reducing f_ε when f_k is below unity. Secondly, there is the discussion on how to select f_k. It can vary both in time or space to optimally use the computational grid, but thereby losing the error separation; or be kept constant. For all approaches, it is necessary to have a *a priori* estimate of f_k based on the grid and flow case, however no consensus exists how to do this. Chapter 4 investigates these questions in detail.

2.4. SYNTHETIC TURBULENCE GENERATOR

Traditional turbulence inflow quantities in RANS are either constant in time, or vary on a time-scale significantly larger than the timestep. For scale-resolving simulations (SRS) such as PANS or LES, the solved variables contain a time-varying component with a time scale in the order of the turbulent time scales. Therefore, for cases without flow separation or large vortical structures, the inflow must also be time-dependent; it must contain fluctuations which resemble realistic turbulence [28]. If this is not done, LES or DNS results can become unreliable due to their tendency to predict natural laminar flow over a significant portion of the object of interest, due to the lack of external flow instabilities that would encourage transition of the boundary layer [26, 27, 29]. This behaviour is also investigated in this thesis, see Chapter 6.

In hybrid methods, such as DDES and IDDES, it can also be necessary to generate these fluctuations in the region where the solver transitions from RANS to LES. In this case, turbulence in the flow needs to be transferred from a modelled to a resolved region (this is sometimes referred to as 'the grey area' issue [114]). The modelled averaged quantities need to be used in order to introduce artificial fluctuations in the LES region.

For both of these problems, methods to generate turbulence are necessary. Requirements for such methods were formulated by Tabor and Baba-Ahmadi [28], who stated that the boundary condition should: (i) be stochastically varying, (ii) be varying on scales down to the filter scale (spatially and temporally), (iii) be compatible with the Navier-Stokes equations, in the sense that the introduced fluctuations are not instantly dissipated by the solver, (iv) 'look' like turbulence, so it must possess a similar structure with coherent eddies across a range of spatial scales down to the Kolmogorov scale which interact with each other in a physical manner, (v) allow easy specification of turbulent properties (turbulence intensities, length scales, etc.), (vi) be easy to implement and to adjust to new inlet conditions. An important demand with respect to acoustic predictions is that the turbulence generation methods should be divergence-free to eliminate spurious pressure fluctuations in the numerical domain (see e.g. [114, 115]).

Turbulence generation methods discussed in the literature can generally be divided into precursor methods or synthetic turbulence methods [28], conceptually visualised in Fig. 2.2. Each of the methods spanning the two categories offers potential advantages and disadvantages, which may be judged against the overall inflow turbulence generator (ITG) requirements within this thesis:

- it should be applicable for a range of SRS turbulence models (DES, LES, PANS, DNS);
- it should allow anisotropic Reynolds stresses and length scales;
- it should allow inhomogeneous turbulence;
- developed structures should look like real turbulence in terms of length scales and time scales;
- the method ought to be usable in an industrial, parallelised, unstructured CFD code, for a range of test cases;
- the approach should be robust and ‘cheap’ to use;
- the developed fluctuations should be divergence free.

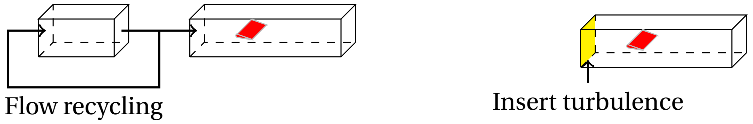

Figure 2.2: Schematic representation of precursor (left) and synthetic (right) turbulence generation methods.

2.4.1. SYNTHETIC METHODS

The generation of synthetic inflow turbulence can be done in several manners; see Tabor and Baba-Ahmadi [28] for a full overview.

The simplest method to introduce fluctuations is to apply random white noise to the velocity field. However, random noise does not contain any spatial or temporal correlations and is therefore almost immediately dissipated by the Navier-Stokes solver [116–118]. In addition, due to its lack of compatibility with the governing flow equations, it is expected that the white noise method might lead to numerical issues and lack of convergence.

Fourier methods make use of an inverse Fourier decomposition of turbulence to generate turbulence [119]. It is easily applicable to simple (rectangular) inlet domains, but can be more complex for difficult geometries. Secondly, it is difficult to apply the Fourier method systematically for general flows due to the requirement of a previous realisation of the flow that is needed for the Fourier decomposition [26, 120]. If this is not available, the amplitude and phase coefficients for a specific flow are unknown.

A similar approach, applicable for arbitrary domains, is Principal Orthogonal Decomposition method, where turbulence is decomposed into basis functions. Often only a limited number of basis functions are necessary in order to achieve a satisfactory fit to real data [121, 122]. Again, it is difficult to apply for general flows since detailed spatial and temporal data is needed in order to obtain the coefficients [21, 26].

Digital filters make use of random noise which is then filtered to obtain the desired statistical properties [28]. As for the two previous methods, the information concerning the correlation method can be a limiting factor. The filter coefficients are derived from a relationship between desired first and second-order statistics [21]. On a plane near the inlet where random turbulence is inserted the flow solver is used to correct the velocity field to be divergence free.

Synthetic Eddy Methods [123] create 2D vortices with a certain vorticity distribution on a plane near the inlet and advect them into the flow. To generate the velocity components the vorticity equation is used. An advantage compared to other synthetic methods is a reduced development length to achieve realistic turbulence [28].

2.4.2. PRECURSOR METHODS

Other general approaches are precursor methods [28], where the turbulence is obtained from a separate (precursor) calculation of an equilibrium flow. The turbulence is then introduced at the inlet of the main computation. In this method the turbulence is obtained from a full simulation, and therefore contains the appropriate characteristics and correlations. The precursor simulation does not have to be at the same turbulent Reynolds number, since the main goal of the precursor simulation is to develop realistic small turbulent scales, which are in general problem independent. When these are introduced into the main simulation, they develop into the eddies related to the main flow. The precursor simulation can be run beforehand, or concurrently with the main simulation. The precursor simulation can consist for instance of a periodic box of turbulence or a cyclic channel flow [28]. Care must be taken when designing the numerical grid for precursor methods in order to prevent interpolation errors which can potentially destroy the divergence-free flow properties. It is therefore preferable, if not necessary, to have the same grid in the plane perpendicular to the flow in the precursor and in the main domain. This can lead to practical difficulties. For instance, in the case of a channel flow as precursor for the flow around a wing in a wind tunnel; the precursor grid requires wall-refinement towards the wind tunnel walls, which is not necessary for the wing. So either interpolation occurs, or the flow near the walls of the test section for the wing must also be resolved, which adds computational cost.

2.4.3. SYNTHETIC VERSUS PRECURSOR METHODS

In light of the foreseen cases utilized in this thesis, precursor methods suffer too much from the lack of general applicability and from increased computational costs and difficulties in tuning the turbulence quantities. A synthetic method is preferable, also due to the ability to introduce it at any arbitrary location and likely reduced computational costs. The divergence-free condition in combination with the preference for a method without the need for accurate flow data beforehand leads to two possible candidates: the digital filter approach by Y. Kim et al. [124], and the synthetic eddy method by Kröger and Kornev [125]. Lloyd [21] presented a comparison between these methods for a planar jet and a channel flow. The conclusion of that study was that the method by Kröger and Kornev [125] provided better turbulence statistics in the case of homogeneous isotropic turbulence. In the case of anisotropic inhomogeneous boundary layers, the method of Y. Kim et al. [124] performed better in matching DNS data, while still requiring a long development length. It must be remarked that the outcome of such a comparison as done by Lloyd [21] could be case or flow specific. The method by Kröger and Kornev [125] may include inhomogeneous profiles in order to achieve accelerated turbulence development but at the cost of losing the divergence-free property and therefore leading to spurious pressure fluctuations. With the aim of acoustic simulations in mind, while desiring a method both applicable in free-stream and in wall-bounded flows, the method by Y. Kim et al. [124] is here considered the most appropriate choice to implement in ReFRESCO. Within the project, the original method was modified in several aspects. The results of a precursor and this synthetic method are compared in Chapter 5.

2.4.4. IMPLEMENTED DIGITAL FILTERING METHOD

In this thesis, synthetic turbulence is generated using a modified version of the digital filter method by Z.-T. Xie and Castro [126]. First proposed by Klein et al. [27], the method is easily adaptable to experimental data in order to obtain the proper length scales and statistics. However, the velocity field is not divergence free. A more efficient method was proposed by Z.-T. Xie and Castro [126] who changed the Gaussian temporal correlation function to an exponential function. It filters two-, rather than three-, dimensional data, and therefore may also yield results that are not divergence free. The length scales, spectra, mean velocity, and Reynolds stresses are reported to yield satisfactory agreement with measurements. Y. Kim et al. [124] extended this method to be divergence free. At the inlet a velocity profile for the bulk velocity is introduced in the domain. On a plane near the inlet random turbulence is inserted, where the flow solver is used to correct the velocity field to be divergence free. The random fluctuations are therefore used as an intermediate velocity. The corrected velocities are advected into the domain. Negligible additional CPU time is said to be required for this correction step [126]. It is shown that the variances and power spectra of the pressure fluctuations are only accurately predicted with the divergence-free inlet condition [126]. However, the formulation used Z.-T. Xie and Castro [126] modifies the velocity in the first non-linear PISO loop, necessitating modifications when implementing the method in ReFRESCO. This section describes the formulation of Z.-T. Xie and Castro [126], the modifications are addressed in Sec. 2.4.5.

In the current implementation the method is able to generate anisotropic, inhomogeneous turbulence, which is sufficient for most industrial applications, such as the flow around wings, propellers, ship hulls, etc. In the method random numbers, $r_{m,l,i}$, with zero mean and unit variance, are generated on a Cartesian grid at each time step. Here m, l indicate the position indices and i the velocity component. These numbers are spatially correlated using [126]

$$\psi_{m,l,i} = \sum_{j=-N}^{N} \sum_{k=-N}^{N} b_j b_k r_{m+j,l+k,i}, \tag{2.44}$$

after which they are temporally correlated with the numbers generated at the previous time step using [126]

$$\Psi_i(t) = \Psi_i(t-\Delta t)\exp\left(-\frac{\pi\Delta t}{2T}\right) + \psi_i(t)\left[1-\exp\left(-\frac{\pi\Delta t}{2T}\right)\right]. \tag{2.45}$$

Here $T = I_i/\overline{U_i}$ is the Lagrangian time scale and b_j and b_k are filter coefficients used to generate spatial correlations, and are defined as [126]

$$b_j = \frac{b'_j}{\sum\limits_{l=-N_j}^{N_j} b'^2_l} \qquad \text{and} \qquad b_k = \frac{b'_k}{\sum\limits_{m=-N_k}^{N_k} b'^2_m}, \tag{2.46}$$

with [126]

$$b'_j = \exp\left(-\frac{\pi|j|}{2n}\right) \qquad \text{and} \qquad b'_k = \exp\left(-\frac{\pi|k|}{2n}\right). \tag{2.47}$$

The spatially and temporally correlated numbers are transformed to velocity fluctuations using

$$U'_i = a_{ij}\cdot\Psi_i \tag{2.48}$$

in which a_{ij} indicates the Lund transformation matrix, which is based on a Cholesky decomposition of the Reynolds stress tensor R_{ij} [29],

$$a_{ij} = \begin{bmatrix} \sqrt{R_{11}} & 0 & 0 \\ R_{11}/a_{11} & \sqrt{R_{22}-a_{21}^2} & 0 \\ R_{31}/a_{11} & (R_{32}-a_{21}a_{31})/a_{22} & \sqrt{R_{33}-a_{31}^2-a_{32}^2} \end{bmatrix}. \tag{2.49}$$

For more details the reader is referred to Z.-T. Xie and Castro [126] and Y. Kim et al. [124].

2.4.5. MODIFICATIONS TO THE ORIGINAL DIGITAL FILTERING METHOD

In the formulation in literature the velocity is modified directly inside the first non-linear PISO loop, either at the inflow, or in the domain. In the current work, the method is used together with the SIMPLE algorithm (see Fig. 2.1), which necessitates changes in the method. The increased number of outer iterations (which can be up to $\mathcal{O} = 10^2 - 10^3$) introduces the risk of dissipating the introduced velocity fluctuations. Also, modifying the velocity field directly can introduce numerical error and spurious pressure oscillations which can affect noise predictions. To address these issues, the velocity fluctuations are transformed to a body-force term in the momentum equations, explicitly added on the right hand side of the equations. The use of body-force terms is less intrusive than modifying the velocity directly, thereby improving iterative convergence and mass conservation.

The transformation of velocity fluctuations to body-forces is achieved using

$$F_{b,i} = \frac{\left(U_{i,inflow} + U_i' - U_i\right)\rho\overline{U_i}}{L_{tg}} b \tag{2.50}$$

where $U_{i,inflow}$ is the mean velocity as defined at the ITG plane, U_i' comes from Eq. 2.48 and U_i is the instantaneous velocity in a cell, obtained from the solver at the current non-linear loop. L_{tg} indicates the distance in the flow direction over which the body-force term is applied, and b is an arbitrary multiplication factor to increase the convergence of the velocity towards the desired fluctuations. Notice that this body-force term goes to zero when the local velocity equals the desired mean (inflow) velocity plus fluctuation.

Even with the use of Eq. 2.50, the residuals still stagnate in the cells affected by the ITG (see Sec. 5.5). Therefore, from Chapter 6 onwards, a divergence-free velocity field is enforced by adding a source term, S_{tg}, to the mass and momentum equations every non-linear loop. This source term is computed by integrating the flux, f_i, through each face i for every cell of the ITG,

$$f_i = \int_S \left(\langle U_i \rangle \cdot n_i\right) \mathrm{d}S. \tag{2.51}$$

and adding this over the N_f faces of the $i-th$ cell to obtain the source term

$$S_{tg}(i) = -\sum_{i=1}^{N_f} f_i. \tag{2.52}$$

The benefits of these modifications are shown in Fig. 2.3, which presents the residuals during a single timestep. The residuals depict almost identical trends irrespective of the prescribed inflow turbulence levels, indicating that the body-force approach for introducing inflow turbulence has no adverse effects on convergence. Additionally, the number of outer loops per time step remains approximately the same, highlighting the low computational overhead of the ITG. In comparison to the approach without this source term (see Sec. 5.5), it is clear that this is a significant improvement.

2.5. MULTI-PHASE MODELLING

Multiphase flows are widespread phenomenon with a range of applications such a free-surface flows, bubbles in a fluid or cavitation. To solve such flows numerically, several methods are available in literature. Within this work there is a focus on the properties relevant for cavitation. A distinction can be made between approaches formulated in a Lagrangian framework, where the individual particles or vapour bubbles are tracked explicitly, or in an Eulerian framework, where the grid describes both the fluid flow and the cavitation [22]. Lagrangian methods are often limited to cases where the mass of dispersed phase and the particles or bubbles are small [22]. For larger mass loadings, due to the required computational effort, Eulerian methods (two-fluid models) are necessary [90]. Alternatively, the two approaches can be combined, the so-called Eulerian-Lagrangian methods, where the fluid flow and large vapour regions are solved on the grid, but bubbles smaller than the cell size are tracked explicitly [22, 128].

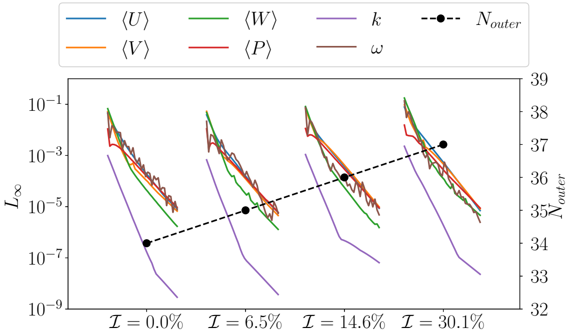

Figure 2.3: Effect of ITG on the L_∞ norm of the residuals of the momentum ($\langle U\rangle$, $\langle V\rangle$ and $\langle W\rangle$), pressure ($\langle P\rangle$) and turbulence equations (k and ω), for a single timestep. The number of outer loops N_{outer} is also indicated. Results from three simulations with increasing inflow turbulence levels and a reference simulation without resolved inflow turbulence. The residuals are normalised using the diagonal of the matrix on the left-hand side of the linearised system of equations. Figure adapted from Lidtke et al. [127].

There are several types of Eulerian methods, such as level-set, marked particles, inhomogenous and volume of fluid (VOF). Within the maritime world, including ReFRESCO, Eulerian methods with VOF are currently the most common approach, consequently the current description will focus on this method. In VOF a single set of mass and momentum equations is solved. A scalar field is convected, which describes the fraction of a cell filled with one of the fluids. The fluid properties are interpolated based on this fraction. While this method shows reliable mass conservation, it is known for not being able to keep a sharp interface, making the identification of the exact location of the interface difficult (see e.g. [66–73]).

2.5.1. VOLUME OF FLUID

The volume of fluid (VOF) [65] approach solves a single set of mass and momentum equations for the homogeneous mixture, with the fluid properties defined by the vapour volume fraction. For two phases, with cavitation, and when neglecting non-condensible gas, the vapour volume fraction is defined as

$$\alpha_v = \frac{V_v}{V_v + V_l} \tag{2.53}$$

with V indicating the phase volume. Subscripts l and v refer to the liquid and vapour respectively. From α_v the mixture properties can be calculated using

$$\rho = \alpha_v \rho_v + (1 - \alpha_v)\,\rho_l \tag{2.54}$$

$$\mu = \alpha_v \mu_v + (1 - \alpha_v)\,\mu_l \tag{2.55}$$

under the condition that

$$\alpha_l + \alpha_v = 1. \tag{2.56}$$

From this definition it follows that $\alpha_v = 1.0$ indicates a cell completely filled with vapour, while $\alpha_v = 0.0$ indicates pure liquid. Commonly a cavity interface of $\alpha_v = 0.1$ is used for comparison with experimental visualizations [74, 75]. The vapour volume fraction is a scalar field, and is described by an additional transport equation, formulated as [129]

$$\frac{\partial\left(\rho\alpha_v\right)}{\partial t} + \frac{\partial}{\partial x_i}\cdot\left(\rho\alpha_v\langle U_i\rangle\right) = \frac{\dot{m}}{\rho_v}. \tag{2.57}$$

The source term on the right hand side defines the phase change, and also affects the mass equation (Eq. 2.3). To model this source term a closure model is needed, i.e. the cavitation model.

2.5.2. CAVITATION MODELS

The function of the cavitation model is to prescribe the source term defining the phase change in Eq. 2.57 and Eq. 2.3. A range of models, often named mass transfer models, have arisen over the years. Models include those by Kubota et al. [66], Kunz et al. [67], Singhal et al. [69], Schnerr and Sauer [80], Merkle et al. [130], Iben [131], Frobenius et al. [132], Saito et al. [133], Zwart et al. [134], Senocak and Shyy [135], J. Wu et al. [136], Merkle et al. [137], Huang and G. Wang [138], and Goncalvès [139] and Konstantinov et al. [140]. Most of these formulations are based on the Rayleigh-Plesset equation for bubble dynamics, while differences concern which physics are included, the dependence on empirical parameters, and which higher-order terms are included. Niedźwiedzka et al. [141] gives a detailed overview and compares different formulations.

In this thesis, the cavitation model of choice is the Schnerr-Sauer model [80], due to its widespread usage and reasonable results obtained in literature [72, 74–79].

2.5.3. SCHNERR-SAUER MODEL

The Schnerr-Sauer cavitation model [80] is based on the Rayleigh-Plesset equation for bubble dynamics. It is based on the physical assumptions that: (i) cavitation is modelled as growth and collapse process of vapour bubbles, (ii) bubbles originate from nuclei in the flow that can grow or collapse based on the local pressure and temperature, and (iv) slip between vapour and liquid is negligible. For details on the current implementation the reader is referred to [129].

The source term is defined as

$$\frac{\dot{m}}{\rho_v} = \begin{cases} 4\pi R_b^2 n_b(1-\alpha_v)\sqrt{\frac{2}{3}\frac{|p_v-p|}{\rho_l}}, & \text{if } p < p_v; \\ -\frac{3\alpha_v}{R_b}\sqrt{\frac{2}{3}\frac{|p_v-p|}{\rho_l}}, & \text{if } p > p_v. \end{cases} \tag{2.58}$$

Here n_b is the bubble concentration per unit volume of pure liquid; this couples the number of nuclei to the water volume in a cell. This satisfies the conservation of the number of bubbles: if the bubbles grow the water volume in a cell decreases and therefore the number of bubbles in a cell decreases. A volume of water contains a number $N_b = n_b \cdot V_l$ of bubbles, with a radius R_b. For the bubble growth the Rayleigh-Plesset equation is used, which is valid under the assumption that bubbles remain spherical and no bubble-bubble interactions and bubble coalescence are taken into account.

2.6. ACOUSTIC MODELLING

Sound can be defined as a fluctuating pressure wave moving through a compressible fluid [81]. The fluctuating components of density and pressure are responsible for sound generation. In a similar way as for the turbulence models (see Sec. 2.3) density and pressure can be decomposed into a fluctuating, and mean, or undisturbed, value ρ_0 and p_0, according to

$$p = p_0 + p' \tag{2.59}$$

$$\rho = \rho_0 + \rho'. \tag{2.60}$$

Here both p_0 and ρ_0 are a function of time and space, although temporal variations are on a time-scale significantly larger than variations due to sound. The propagation of sound due to an arbitrary source $F\left(\boldsymbol{y}, t\right)$ (which can be a monopole, dipole or quadrupole) can be described by an inhomogeneous wave equation [142]

$$\frac{\partial\left(\rho u_i\right)}{\partial t} + c_0^2 \nabla \rho = F\left(\boldsymbol{y}, t\right) \tag{2.61}$$

and

$$\frac{\partial^2 \rho'}{\partial t^2} - c_0^2 \nabla^2 \rho' = F\left(\boldsymbol{y}, t\right) \tag{2.62}$$

which is derived from a linearised form (by assuming $p = c_0^2 \rho$) of the compressible momentum equation, with c_0 as the speed of sound in the considered medium. When comparing the linearised momentum equation with the compressible Navier-Stokes equations, the acoustic analogy can be obtained [21, 143]. This gives a more accurate description of the sound generated by an arbitrary source [143]. When the sound generated by viscosity is neglected, Lighthills analogy is formulated as

$$\frac{\partial\left(\rho u_i\right)}{\partial t} + c_0^2 \nabla^2 \rho = -\frac{\partial T_{ij}}{\partial x_i} \tag{2.63}$$

and

$$\frac{\partial^2 \rho'}{\partial t^2} - c_0^2 \nabla^2 \rho' = \frac{\partial^2 T_{ij}}{\partial x_i \partial x_j} \tag{2.64}$$

with T_{ij} the Lighthill stress tensor, which describes the volumetric distribution of noise sources through turbulent stresses in the fluid,

$$T_{ij} = \rho u_i u_j + \left(p - c_0^2 \rho'\right) \delta_{ij}. \tag{2.65}$$

To take the presence of stationary solid boundaries into account (where $\boldsymbol{U} \cdot \hat{\boldsymbol{n}} = 0$), Curle and Lighthill [142] modified Eq. 2.64 to obtain

$$\frac{\partial^2 \rho'}{\partial t^2} - c_0^2 \nabla^2 \rho' = \frac{\partial^2 T_{ij}}{\partial x_i \partial x_j} + \frac{\partial\left(p \cdot \boldsymbol{n}\right)}{\partial x_i}. \tag{2.66}$$

Finally Ffowcs Williams and Hawkings [84] derived a generalised inhomogeneous wave equation to obtain the sound generated by a surface S moving with a velocity v_i. A function f is defined such that $f < 0$ inside S, and $f > 0$ outside S. Assuming that S is impermeable and rigid, and neglecting sound generated due to viscosity, the analogy can be formulated as:

$$\frac{\partial^2 \rho'}{\partial t^2}H(f) - c_0^2\nabla^2\rho' H(f) = \frac{\partial^2 T_{ij}}{\partial x_i \partial x_j}H(f) + \frac{\partial\left(\rho_0 v_i\right)}{\partial t}\delta(f)\frac{\partial f}{\partial x_i}. \tag{2.67}$$

$H(f)$ is the Heaviside function equal to 1 outside of the surface S, and 0 within the surface. $\delta(f)$ is the Dirac delta, equal to ∞ for $f = 0$ and 0 for $f \neq 0$.

Following the literature on acoustics for marine noise, such as [21, 22, 82, 83], the FWH acoustic analogy is used. Advantages of this methodology include its possible application to rotating geometries [82, 144, 145], and its validity when the integration surface is placed in a non-linear flow region, such as the wake [146]. Consequently smaller domains are permitted, leading to reduced computational cost. The FWH analogy has been used for the purpose of cavitation sound predictions within an incompressible code (e.g. [22]).

In this work, the porous formulation, derived by Di Francescantonio [85], is employed. Here, the FWH equations are reformulated to solve the integrals on a fictitious surface surrounding the noise sources, thereby removing the need for solving expensive volume integrals, while mitigating the risks of solving volume integrals in cavitating regions. It also circumvents the need to know the precise location of acoustic sources, which for the foreseen test cases are located both in the flow and on the boundaries. The contributions of all these sources can be included within the porous FWH. The formulation is explained in more detail in the following section.

2.6.1. FWH IN POROUS FORMULATION

In the porous formulation, a fictitious permeable surface, also known as the porous data surface (PDS), is defined around the object of interest, inside of which the noise sources are located. During the simulation the data is interpolated to the surface, representing acoustic sources. Sound propagation is assumed to be linear outside the surface, allowing this methodology to obtain the radiated sound at any arbitrary location [86]. Fig. 2.4 gives a schematic overview of the procedure. In this section the formulation is given, for the full derivation the reader is referred to Brentner and Farassat [147].

The flow quantities required on the PDS are pressure, velocity, and density disturbances. When assuming a free-field propagation, negligible density fluctuations and a stationary porous data surface, the solution can be written as a summation of five terms, which yields the total pressure at the receiver, [148]

$$\begin{aligned} 4\pi p'(\mathrm{x},t)H(f) = {} & \underbrace{\int_S \left.\frac{\rho_0 \dot{U}_n}{|\boldsymbol{r}|}\right|_\tau \mathrm{d}S(\boldsymbol{y})}_{\text{monopole, } p'_0} + \underbrace{\int_S \left.\frac{p\hat{\boldsymbol{n}}\cdot\dot{\boldsymbol{r}}}{|\boldsymbol{r}|^2}\right|_\tau \mathrm{d}S(\boldsymbol{y})}_{\text{nearfield dipole, } p'_1} + \underbrace{\int_S \left.\frac{\rho_0 U_n U_r}{|\boldsymbol{r}|^2}\right|_\tau \mathrm{d}S(\boldsymbol{y})}_{\text{nearfield non-linear, } p'_2} \\ & + \underbrace{\int_S \left.\frac{\dot{p}\hat{\boldsymbol{n}}\cdot\hat{\boldsymbol{r}}}{c_0|\boldsymbol{r}|}\right|_\tau \mathrm{d}S(\boldsymbol{y})}_{\text{far-field dipole, } p'_3} + \underbrace{\int_S \left.\frac{\rho_0 \dot{(U_n U_r)}}{c_0|\boldsymbol{r}|}\right|_\tau \mathrm{d}S(\boldsymbol{y})}_{\text{far-field non-linear, } p'_4} \\ & + \underbrace{p'_Q(\boldsymbol{x},\boldsymbol{t})}_{\text{quadrupole volume integral outside of PDS}} . \end{aligned} \tag{2.68}$$

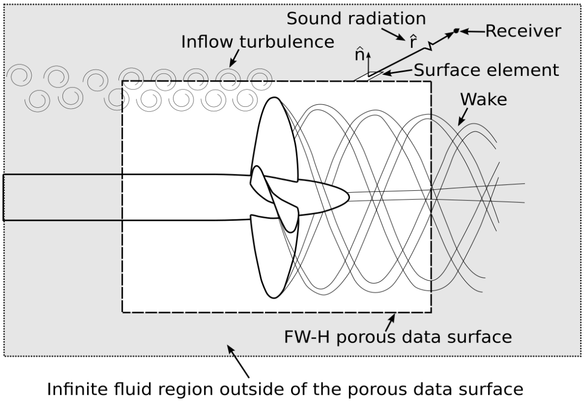

Figure 2.4: FWH concept illustrated for a marine propeller. Figure adapted from Lidtke et al. [148].

In this equation, c_0 is the speed of sound, **r** is the vector between the source **y** and receiver **x**, and **n** the surface-normal vector. The ˆ denotes a unit vector. $\boldsymbol{r}$ is the distance between source and receiver, the dot notation refers to a source time derivative. $\int_S [\ldots]\mathrm{d}S$ indicates integration over the PDS, subscripts r and n refer to the dot product with the normal unit vector along either radial ($\hat{r}$) or surface normal ($\hat{n}$) directions, respectively. Each term is evaluated at the retarded time, denoted by $[\ldots]_\tau$. This accounts for the time needed for the sound to propagate from the different sources on the surface to the receiver. The contribution of a source located at $\boldsymbol{y}(\tau)$ at the emission (retarded) time τ will reach the receiver at $\boldsymbol{x}(t)$ at time [148]

$$t = \tau + \frac{|\boldsymbol{x}(t) - \boldsymbol{y}(\tau)|}{c_0}. \tag{2.69}$$

The inclusion of retarded time ensures the appropriate phase differences between pressure waves of different sources, and thereby prevents artificial amplification or cancellation of pressure waves [148].

Due to the associated computational overhead, the quadrupole volume term $p'_Q(\boldsymbol{x}, \boldsymbol{t})$ is ignored [82, 148]. This assumption is valid if the PDS encompasses all noise sources. For more information on the implementation the reader is referred to Lidtke et al. [148].

2.7. CONCLUSIONS

The main numerical methods and models that are used in this thesis have been summarised. A number of the assumptions made in the use of these methods will be addressed in subsequent chapters, together with the approach taken to verify and validate the outcomes of computations based on these methods.

3

VERIFICATION AND VALIDATION

Errors and uncertainties are inherently associated with numerical predictions. To assess the errors, their causes and effects must be understood. A decomposition of errors is given, and several methods to assess the magnitude of these errors are discussed. It will be discussed which errors are dominating in the current context.

3.1. INTRODUCTION

The process of solving differential equations numerically gives rise to numerical errors. To be able to reliable use CFD in for practical problems, it is necessary to understand the source, and know the magnitude of, the associated errors. The difference between the exact solution and the numerical solution defines the error, however for most flows of practical interest no exact solutions are available. For such cases, it is necessary to obtain an uncertainty interval $U(\phi)$, which contains the exact solution with a certain degree of confidence. $U(\phi)$ defines an interval, and does not possess a sign, while the error $E(\phi)$ does.

In this context, verification relates to whether the equations are solved correctly, while validation indicates whether the correct equations are solved. Verification is therefore a purely numerical exercise, while validation requires some external, more trustworthy, solution to compare against. Such solutions can include experimental measurements, theory or higher fidelity computations.

This chapter gives an overview of the error sources in numerical predictions, and describes methods to compute the numerical uncertainty associated with predicted results.

3.2. NUMERICAL ERROR

The difference between the exact numerical solution ϕ_0 and the observed numerical solution ϕ equals the total numerical error [149]

$$E_n(\phi) = \phi - \phi_0. \tag{3.1}$$

It is generally accepted that numerical errors can be divided into input, round-off, iterative, discretisation, and, in the case of unsteady computations, statistical errors [149], according to

$$E_n(\phi) = E_i(\phi) + E_r(\phi) + E_{it}(\phi) + E_d(\phi) + E_s(\phi), \tag{3.2}$$

where $E_i(\phi)$ is the input error, $E_r(\phi)$ the round-off error, $E_{it}(\phi)$ the iterative error, $E_d(\phi)$ the discretisation error and $E_s(\phi)$ the statistical error. By definition, the numerical uncertainty $U_n(\phi)$ consists of the same components given in Eq. 3.2.

3.2.1. INPUT ERROR

Input errors result from differences between the simulated setup and it's real life counterpart [150]. Usually these relate to the boundary conditions, and can be either caused by insufficient or incorrect experimental information, or by the need to reduce the computational cost. In the current thesis, an attempt was made to match the numerical setup to the desired flow. Nevertheless, several sources of input error remain. For the channel flow computations, an error arises due to the finite domain dimensions; while for all computations resembling the test section in a cavitation tunnel, errors occur due to unavailable information about turbulence statistics in the inflow, potential errors the calibration of the velocity sensor in the experiments, only simulating the test section instead of the full cavitation tunnel, and not resolving the boundary layer flow on the tunnel walls. The effect of these error sources will be elaborated upon, together with the results, in Chapters 5, 6, and 7.

Methods exist to estimate the input error, often based on systematically varying input quantities, either by converging towards the experimental value (when available), or by making a control surface as function of the input variables (for instance in the work by Katsuno et al. [151]). However, such exercises are currently still unaffordable for SRS, and consequently in this thesis input errors are not quantified.

3.2.2. ROUND-OFF ERROR

All computations are performed using double-precision arithmetic, it commonly assumed that this leads to a negligible round-off error compared to the other error sources [56]. Consequently, it is not addressed in the current work. Nevertheless, it should be noted that with an increasing shift towards resolving smaller and smaller turbulent fluctuations, on finer grids with reduced timesteps, the effects of round-off error increase, especially since such errors propagate throughout the computation. In time, this might mean that double-precision arithmetic will no longer suffice, and CFD software will need to resort to quadruple arithmetic to further reduce round-off errors (see e.g. [152, 153]).

3.2.3. ITERATIVE ERROR

The system of non-linear discretised equations ($\boldsymbol{F}(\boldsymbol{x}) = \boldsymbol{b}$) describing the fluid motion is solved iteratively each timestep. When all equations are converged until machine precision ($L_\infty \approx 10^{-17}$ for double precision) this equation holds and there is a negligible iterative error. Problems arise when the solution to this equation is not fully converged, leading to an associated iterative error which is proportional to the residuals $\boldsymbol{res} = \boldsymbol{b} - \boldsymbol{F}(\boldsymbol{x})$.

Residuals are often reported using the L_2 and L_∞ norms

$$L_2\left(\Delta\phi\right) = \frac{1}{N_c}\sqrt{\sum_{i=1}^{N_c}\left(|\Delta\phi_i|\right)^2} \qquad \text{and} \qquad L_\infty\left(\Delta\phi\right) = \max\left(|\Delta\phi_i|\right) \tag{3.3}$$

with $1 \leq i \leq N_c$ where N_c is the number of cells. In this work, all residuals are normalised by the diagonal element of the left-hand-side matrix of the linearised system of equations. In the case of transient (unsteady) problems, the residuals are determined for each timestep. In practice, for flows of engineering interest it is usually not affordable, or even not possible, to reach machine precision, leading to a need to quantify the iterative error. A method to do this is to run several computations with varying convergence criteria, and check whether the results converge [154]. However, as with the input error, this is often prohibited by excessive computational cost. Also, it is sometimes not possible to converge the equations. A common example is lack of iterative convergence of the ω equation, especially in conjunction with multi-phase flows.

In the current work, where possible the iterative error is assessed. The reached convergence levels are always reported based on the L_2 and L_∞ norms typically obtained during each timestep, or the decay of the residuals is averaged over the different timesteps (designated as the time-averaged iterative convergence).

3.2.4. DISCRETISATION ERROR

The transformation of the continuous partial differential equations describing fluid motion into a system of algebraic equations using a finite grid, timestep (in the case of unsteady calculations), and discretisation schemes introduces discretisation errors. Discretisation error due to the grid is related to the grid quality, number of cells and grid arrangement; temporal discretisation error depends on the timestep size; while discretisation error caused by the schemes is related to their order in space and/or in time.

In practise, the discretisation error is usually one of the largest error sources, implying that its evaluation is essential. However this also means that often this is the only error source evaluated, thereby losing sight of the other errors. In the context of SRS, it is often assumed that the application of grids with LES/DNS guidelines in terms of wall resolution, in conjunction with second-order schemes, leads to negligible discretisation errors; and that therefore the errors do not have to be assessed. However, such LES/DNS guidelines are often obtained from codes with higher-order schemes. Since discretisation errors depend on both the number of cells and the accuracy of the schemes employed, an assessment of these errors is always necessary.

One method to quantify this error source is to perform a systematic spatial and temporal grid refinement study [56, 150, 155–158] to estimate the exact solution, order of grid convergence, and discretisation error. One method is the procedure by Eça and Hoekstra [56], which relies on a (truncated) power series expansion,

$$E_d(\phi) \approx \beta_s\left(\frac{h_i}{h_1}\right)^{q_s} + \beta_t\left(\frac{t_i}{t_1}\right)^{q_t}, \tag{3.4}$$

where h_i/h_1 and t_i/t_1 are the spatial (grid) and temporal (timestep) refinement levels, the indices s and t the spatial and temporal components, β the constants to be determined, and q the observed orders of grid convergence. To increase robustness, q

and β are determined using a least-square fitting requiring at least four grids and four timesteps for time-resolved simulations, and four grids for steady simulations. This error is translated to a discretisation uncertainty $U_d(\phi)$ as reported by [56]. Often to simplify the procedure and reduce costs, temporal and spatial resolution is coupled, assuming that $q_s = q_t$. From the discretisation error $E_d(\phi)$, the associated uncertainty $U_d(\phi)$ can be computed, which then defines an interval containing the exact solution ϕ_0 with 95% coverage, according to

$$\phi - U_d(\phi) \leq \phi_0 \leq \phi + U_d(\phi). \tag{3.5}$$

For full details on how to compute β_s, β_t, q_s, q_t, $E_d(\phi)$ and $U_d(\phi)$ the reader is referred to Eça and Hoekstra [56].

For this approach at least four grids and timesteps are required to estimate the error. Ideally, these grids and timesteps should be of sufficient resolution to resolve the flow dynamics. Under such conditions, the grids are in the so-called asymptotic range, i.e. the solutions obtained when refining the grids, converge to a single result. In this case q_s and q_t can be accurately estimated. This does imply that the coarsest grid should already be sufficiently fine, which due to computational cost is not always achievable, leading to an overpredicted $U_d(\phi)$ [100]. In those cases the approach of Pereira, Vaz, Eça, and Girimaji [57] is followed, where the discretisation error, $E_d(\phi)$, is estimated using a power series expansion

$$E_d(\phi) = \phi_1 - \phi_0 = \frac{\phi_{i+1} - \phi_1}{h_{i+1}^q - 1}. \tag{3.6}$$

where ϕ_0 indicates the estimated solution for zero discretisation error. Since it is not possible to obtain an accurate estimation of based on the data q, both a value of 1.0 and 2.0 are used. $q = 1.0$ leads to a conservative estimate, $E_{d,max}$ whereas $q = 2.0$ yields a lower value, $E_{d,min}$, which may not fulfil the 95% confidence interval condition. Both procedures are illustrated for a set of steady simulations in in Fig. 3.1.

To investigate the effect of the discretisation scheme in the equations, several convection schemes are compared. Due to the usage of a unstructured finite volume CFD code, the simulations are limited to second-order accurate schemes. The outcomes of this investigation are detailed in Sec. 5.3.3.

3.2.5. STATISTICAL ERROR

The statistical error results from the finite simulated physical time, and the dependency of the result on the initial conditions. In unsteady and especially turbulence resolving simulations, the statistical error can be one of the dominating error sources. A simple procedure to estimate the start-up time and statistical errors is compute the statistics with increasingly larger sampling periods, as applied by Pereira [100].

In the current work, a more extensive method is used: the Transient Scanning Technique (TST) by Brouwer et al. [159]. In the TST the standard deviation of the time signal is compared to the theoretically expected trend for a stochastic stationary process in order to determine how many timesteps can be used for calculating flow statistics and the associated statistical uncertainty [160]. The uncertainty is expanded to obtain a 95% confidence interval.

The procedure is illustrated in Fig. 3.2. The input can be any time-dependent input variable, the output is the TST graph. The region where the TST graph is parallel to the

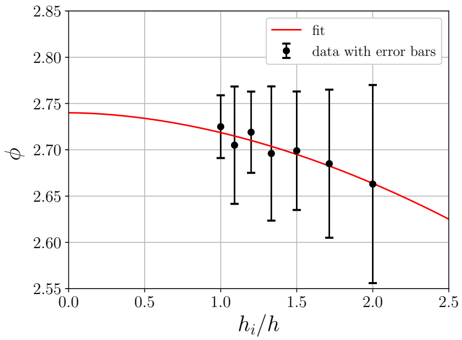

Figure 3.1: Visualisation of the discretisation error assessment. Example of a steady simulation, using Eq. 3.4 (left) and Eq. 3.6 (right) with $q = 2.0$.

−1 slopes (indicated in grey), is the stationary region, which can be used to compute the average. The uncertainty of this average can be seen on the vertical axis. The sudden increase in the TST graph at the right-side of the figure is called the hockey-stick effect, and corresponds to the start-up effect. To estimate the average this part should be removed. In CFD computations, in contrast to experimental measurements, no end effects occur and only the start-up effect is of interest. For details on the procedure the reader is referred to Brouwer et al. [159].

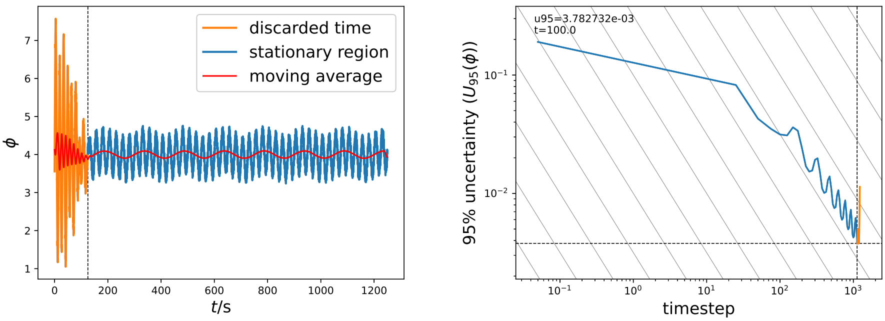

Figure 3.2: Visualisation of the TST procedure. Example signal (left) and TST result (right). Orange lines indicate the start-up effect, visible as what is known as the 'hockey-stick' in the TST graph. Graphs obtained with [161].

3.2.6. DOMINATING ERROR SOURCE

As mentioned at the beginning of this section, numerical error consists of input, round-off, iterative, discretisation and numerical error (Eq. 3.2). Traditionally (in the context of steady RANS computations), discretisation errors due to the grid and timestep are assumed to be dominating [56]. This has lead to a focus in literature on assessing the discretisation error, and by extent

$$E_n(\phi) \approx E_d(\phi). \tag{3.7}$$

However, in the context of SRS this is not necessarily true. While nobody is claiming that there are no discretisation errors (even DNS computations suffer from discretisation errors, although those are often not investigated due to the associated cost), the balance between different error sources varies. To resolve the desired turbulent flow physics, the employed spatial and temporal resolutions are such that the influence of iterative and statistical errors increases. This is especially a concern when looking at small scales and structures, which might be of an order of magnitude similar to the errors.

Investigating the statistical error is possible while running the computation, and can be computed based on a single computation, making it relatively affordable. It does often require an increase in simulated time. In contrast, properly assessing the iterative error is in most SRS cases either unaffordable or inpossible. Not only are several computations are required, each with a successively lower (i.e. more expensive) iterative convergence criterion, but also in the estimation procedure it is assumed that with an increase in outerloops, a lower convergence criterion will be reached. In practise this is often not the case, and the convergence of such computations stagnates at a certain level. Again, a well-known example of this are the ω equation in simulations including free-surface flows or cavitation. At the time of writing, it is hard to quantify the iterative error associated with such stagnated residuals.

To conclude, in the context of SRS it is crucial that all error sources are examined, even though some of these examinations are expensive or difficult. It is also important when validation against for instance experiments is attempted, that the total numerical error is used, and not only the discretisation error.

3.3. MODELLING ERROR

The modelling error $E_m(\phi)$ for a quantity ϕ, with a 95% confidence, lies in the interval defined as [150]

$$E_c(\phi) - U_v(\phi) \leq E_m(\phi) \leq E_c(\phi) + U_v(\phi) \tag{3.8}$$

with the comparison error being

$$E_c(\phi) = \phi - \phi_e, \tag{3.9}$$

i.e. the difference between the computed results ϕ and the experimentally obtained ϕ_e [162]. When it is assumed that uncertainties are uncorrelated, the validation uncertainty $U_v(\phi)$ can be computed from the input $U_i(\phi)$, numerical $U_n(\phi)$ and experimental uncertainties $U_{exp}(\phi)$ according to

$$U_v(\phi) = \sqrt{U_i(\phi)^2 + U_n(\phi)^2 + U_{exp}(\phi)^2}. \tag{3.10}$$

Here $U_n(\phi)$ is the root sum squared of the iterative, discretisation and statistical uncertainty.

3.4. CONCLUSIONS

Errors and uncertainties are inherently associated with numerical predictions. A decomposition of errors is given, and several methods to assess the magnitude of these errors were discussed.

In the context of the current work it is important to recognise that with an increase of physics in simulations, and hence a reduction of modelling errors, the estimation of numerical errors becomes more important. Also, the traditional, RANS based, assumption that discretisation errors are dominant is no longer valid in the context of SRS.

With respect to validation, an increase in physics in the computation also leads to increased demands on experimental datasets. Reduced errors in the results are a must, but also more information is needed about the experimental setup, to reduce input errors. In the following chapters these methods are applied to several flow cases, and causes of input error are identified.

4

INVESTIGATING THE USE OF PANS

Several aspects of the PANS method are investigated. First, different approaches for specifying the ratio of modelled-to-total dissipation (f_ε) are evaluated for different ratios of the modelled-to-total kinetic energy, f_k. Secondly, different approaches for specifying f_k (constant, spatially-varying or spatially- and temporally-varying) are investigated. Different f_k estimates found in literature are evaluated for two test cases: a circular cylinder at $Re = 3900$ and a turbulent channel flow at $Re_\tau = 395$. Finally, a new PANS closure is derived based on the KSKL model. The aim of this new model is to incorporate the desirable features of the KSKL model, compared to the SST model, into the PANS framework.

4.1. LOW VERSUS HIGH REYNOLDS NUMBER APPROACH

In literature, the PANS model is applied almost exclusively using $f_k \ll 1$ and $f_\varepsilon = 1.0$ (known as the 'high Reynolds number' approach), an exception being the work of [166] and [167]. This approach assumes that the PANS cut-off is located at lower wave numbers than the dissipation range and therefore that the dissipation occurs entirely at the modelled scales. This is valid if there is a clear separation between the large energy containing scales and the small dissipative scales (identifiable by the inertial subrange, which follows Kolmogorov's law) [57, 167]. Theoretically, for low Reynolds number flows, where the scales overlap, or for high Reynolds number flows with a high physical resolution (low f_k), part of the dissipation should also be resolved. This implies that f_ε should be lower than 1.0. It is expected that the resolved structures, obtained when $f_k < 1.0$, should change due to increased dissipation.

Although most maritime applications are high Reynolds number flows, it is not unlikely that some cases require high physical resolutions, i.e. low f_k. For low Reynolds numbers, an often mentioned approach is to keep $f_k = f_\varepsilon$, whereas $f_k < f_\varepsilon < 1.0$ has been recommended for moderate Reynolds numbers [106, 167]. Pereira et al. [168] state that if $f_k = f_\varepsilon$ the only change with respect to the underlying RANS model is an increase of

---

Parts of this chapter have been published in Proceedings of MARINE 2019 [163], in International Journal of Heat and Fluid Flow **80**, 108484 (2019) [164], and Journal of Fluids Engineering (2021) [165].

the effective diffusion coefficient and cross-diffusion term; these terms go infinity when f_k goes to 0. Using this approach vortex shedding for a cylinder was underpredicted, especially with lower f_k. By contrast Lakshmipathy et al. [167] obtained satisfactory results for the same test case using a finer grid, indicating a potential grid dependency. Frendi et al. [166] simulated a backward facing step, using a fixed f_k and varying f_ε. These authors state that for wall-bounded flows viscous effects and dissipation should be taken into account by lowering f_ε. Better agreement with experiments was reported with this approach, although only the parameter f_ε was varied, with f_k kept fixed as 0.2. Their results indicated a decrease in range of scales with decreasing f_ε, due to the increased dissipation.

This section evaluates the three aforementioned approaches for specifying f_ε ($f_\varepsilon = 1.0$, $f_\varepsilon = a \cdot f_k$ with $a = 2$ and $f_\varepsilon = f_k$) by applying them to a turbulent channel flow at both ‘low’ ($Re_\tau = 180$) and ‘moderate’ ($Re_\tau = 395$) Reynolds numbers. The results are compared to Direct Numerical Simulation (DNS) reference data by Moser et al. [169]. In this section, f_k values of 0.15, 0.10 and 0.05 are used, see Chapter 5. To maintain a distinction between modelling and numerical error, a strong aspect of PANS, f_k and f_ε are kept constant in time and space.

4.1.1. SPECIFYING f_ε

Kinetic energy is mostly contained in the larger scales, whereas dissipation occurs in the smallest scales; this dictates $0 \leq f_k \leq f_\varepsilon \leq 1$ [106]. For specifying f_ε, three Reynolds number regimes can be distinguished in literature, which lead to different corresponding values of f_ε: the ‘high’, ‘moderate’ and ‘low’ Reynolds number approaches. Generally speaking in the high Reynolds number case, there is a clear separation between the large energy-containing scales and the small dissipative scales (identifiable by the inertial subrange, which follows Kolmogorov’s law) [57, 167]. For a low Reynolds number flow these scales overlap. A moderate Reynolds number lies between these limits. In terms of scale separation, clearly this distinction is difficult to quantify. In generalised form, if f_ε is taken as $f_\varepsilon = a \cdot f_k$, the PANS-SST transport equations (Eq. 2.26 and 2.27) reduce to

$$\underbrace{\frac{\partial k}{\partial t} + \frac{\partial}{\partial x_j} \cdot \left(k \langle U_j \rangle\right)}_{\text{I}} = \underbrace{P_k}_{\text{II}} \underbrace{- \beta^* \omega k}_{\text{III}} + \underbrace{\frac{\partial}{\partial x_j}\left[\left(\nu + \nu_t \sigma_k \frac{a}{f_k}\right) \frac{\partial k}{\partial x_j}\right]}_{\text{IV}}, \tag{4.1}$$

$$\begin{gathered}\underbrace{\frac{\partial \omega}{\partial t} + \frac{\partial}{\partial x_j} \cdot \left(\omega \langle U_j \rangle\right)}_{\text{V}} = \underbrace{\frac{\alpha}{\nu_t} P_k}_{\text{VI}} - \underbrace{\left(\left(1 - \frac{1}{a}\right) P' + \frac{\beta \omega}{a}\right) \omega}_{\text{VII}} + \underbrace{\frac{\partial}{\partial x_j}\left[\left(\nu + \nu_t \sigma_\omega \frac{a}{f_k}\right) \frac{\partial \omega}{\partial x_j}\right]}_{\text{VIII}} \\ + \underbrace{2 \frac{\sigma_{\omega 2}}{\omega} \frac{a}{f_k} (1 - F_1) \frac{\partial k}{\partial x_j} \frac{\partial \omega}{\partial x_j}}_{\text{IX}}.\end{gathered} \tag{4.2}$$

In the k equation (4.1), term (I) indicates rate of change plus convection, (II) rate of production, (III) rate of destruction and (IV) transport by molecular and turbulent diffusion. In the ω equation (4.2) the terms are rate of change (V), rate of production (VI), rate of destruction (VII), transport by molecular and turbulent diffusion (VIII) and cross-diffusion (IX). This last term is a result of the $\varepsilon = k\omega$ transformation in the construction of the SST model [89]. The terms in red differ from the standard SST model. For these equations the effect of the three approaches for specifying f_ε will be discussed from a numerical perspective. It is clear that terms (I), (II), (III), (V) and (VI) are independent of f_k and a.

HIGH REYNOLDS NUMBER APPROACH

In this case $f_\varepsilon = 1.0$ ($a = 1.0/f_k$); here the transport by diffusion (IV and VIII) and cross-diffusion term (IX) increase proportionally to $1/f_k^2$ with decreasing f_k. The rate of destruction (VII) decreases proportionally to f_k. So for $f_k < 1.0$ the diffusion term in the k equation increases, spreading the modelled turbulent kinetic energy in space. At the same time, in the ω equation, the diffusion terms dominate over the destruction term. This implies that for low f_k values the dissipation is more spread out in space but the rate of destruction of ω is reduced.

MODERATE REYNOLDS NUMBER APPROACH

In this case $f_\varepsilon = a \cdot f_k$ with $1.0 < a < 1.0/f_k$. Consequently terms (IV), (VIII) and (IX) increase proportionally to a/f_k. Term (VII) is independent of f_k and is proportional to a. Again the diffusion terms increase, and the destruction term in the ω equation decreases. The difference between these terms is smaller than for the high Reynolds number approach, so it is expected that dissipation occurs more locally.

LOW REYNOLDS NUMBER APPROACH

In the limit of $f_\varepsilon = f_k$ ($a = 1.0$) terms (IV), (VIII) and (IX) increase proportionally to $1/f_k$. Term (VII) is now constant and reduces to $\beta\omega^2$, which is identical to the original SST model. The term containing P' disappears completely. With decreasing f_k the model remains identical to the SST model but with increased diffusion and cross-diffusion terms (IV, VIII and IX) [168].

Reyes et al. [46] derived the relationship between PANS and RANS turbulence viscosity as

$$\frac{\nu_{t,PANS}}{\nu_{t,RANS}} = \frac{f_k^2}{f_\varepsilon} \tag{4.3}$$

and related the PANS Kolmogorov scales to the physical integral scales for length (η/L), time (t_η/T) and velocity (u_η/U) as [46]

$$\frac{\eta}{L} \sim C_\mu^{3/4}\frac{f_k^{3/2}}{f_\varepsilon}, \qquad \frac{t_\eta}{T} \sim C_\mu^{1/2}\frac{f_k}{f_\varepsilon}, \qquad \frac{u_\eta}{U} \sim C_\mu^{1/2} f_k^{1/2}. \tag{4.4}$$

The effect of the different approaches on these ratios across the f_k range is shown graphically in Fig. 4.1, with $a = 2$ used throughout as example. Note that these ratios are independent of Reynolds number. The figure is corrected for the fact that f_ε cannot be not higher than f_k. The point after which the viscosity and length scales for $f_\varepsilon = 1.0$ and $f_\varepsilon = a \cdot f_k$ deviate, and where a discontinuity for the time scale is located, lies at $f_k = 1/a$. For the turbulence viscosity and the length scales, the high Reynolds number approach yields the lowest ratios across the entire f_k range, meaning that the turbulence viscosity is lowered, more unsteadiness and smaller length scales can be expected in the solution. The moderate Reynolds number approach yields the same if $f_k > 1/a$; for $f_k < 1/a$

the turbulent viscosity and length scales are larger, i.e. it is expected that the smallest structures are absent. The low Reynolds number approach yields the highest ratio for all f_k except at the limits of $f_k = 0$ or 1. The time scales however show the opposite trend, across the f_k range the lowest ratio is for the moderate Reynolds approach. The low Reynolds number approach is independent of f_k, while the high approach lies in between these limits. The velocity scales decrease with $f_k^{1/2}$ independently of f_ε.

Note that for the high Reynolds number approach there is little difference in terms of turbulence viscosity and length scales if f_k is small (in the range $f_k < 0.2$). This corresponds to the findings in Chapter 5, where only a fully developed turbulent solution was found for small f_k, but then little difference was seen between the different f_k values. In contrast, in this range the time scales are strongly affected.

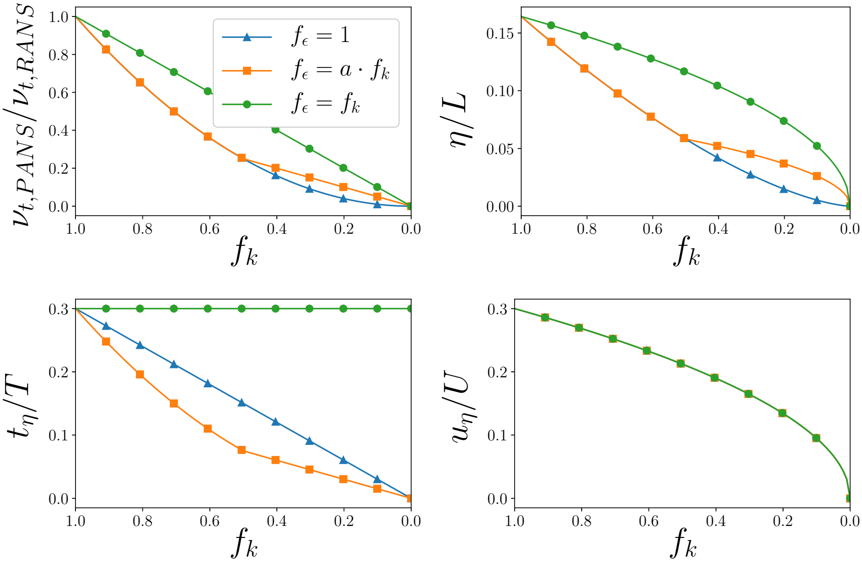

Figure 4.1: Relationship between PANS and RANS turbulence viscosity, ν_t, length, η_u/L, time, t_{η_u}/T, and velocity scales, u_{η_u}/U, versus f_k for different f_ε approaches. Here $a = 2$.

Based on these theoretical observations some questions arise concerning the use of the low Reynolds number approach. There appears to be no clear advantage; additional diffusion is added in the equations, and theoretically the the turbulent viscosity and length scales are larger than for the high Reynolds number approach, indicating that the smallest scales will be suppressed. For the moderate Reynolds number approach, small differences compared to $f_\varepsilon = 1.0$ are expected, and only for low f_k. In order to check these findings in a practical case, in the remainder of this chapter the three approaches are applied to a turbulent channel flow at two different Reynolds numbers ($Re_\tau = 395$ and 180).

4.1.2. NUMERICAL SETUP

The numerical setup will be extensively reported in chapter 5. Computations are made using a rectangular domain, with two no-slip walls oriented normal to the y-axis. The remaining boundaries are connected using periodic boundary conditions in order to approximate an infinite channel. Comparisons between different model settings are performed on a Cartesian grid, with a density of $N_x = 127$, $N_y = 95$ and $N_z = 95$ with clustering towards the walls. For $Re_\tau = 395$ this results in $x^+ \approx 12$, $y^+ \approx 0.1$ and $z^+ \approx 10$. The non-dimensional time step $\Delta t^* = u_\tau \Delta t/(2\delta) \approx 1 \times 10^{-3}$ leads to $\Delta t^+ = u_\tau^2 \Delta t/\nu \approx 0.08$ (2000 time steps per flow-through time). The grid density and time step are below LES guidelines and approach DNS resolution [55]. To maintain the proper bulk and friction Reynolds numbers, $Re_b = U_b 2\delta/\nu$ and $Re_\tau = u_\tau \delta/\nu$ respectively, a body-force is applied which is proportional to the pressure gradient $\mathrm{d}p/\mathrm{d}x = -\tau_w/\delta$, with $\tau_w = \rho u_\tau^2$ [52]. The Péclet number ($Pe = \frac{\rho u \Delta x}{\Gamma}$, with Γ the diffusion coefficient [90, 170]) has a magnitude of $\mathcal{O}(10)$. As shown in the literature, the use of scale-resolving turbulence models for a turbulent channel yields a so-called supercritical laminar solution for which many flow-through times are needed to trigger transition to the turbulent regime [171]. In order to speed up the transition, the method suggested by Schoppa and Hussain [172] is used here. The details are given in Tab. 4.1.

Table 4.1: Details of the channel flow setup.

Symbol	Case 1	Case 2
Re_τ	395	180
Re_b	13800	6300
δ [m]	0.1	0.1
U_b [m/s]	6.928×10^{-2}	3.157×10^{-2}
u_τ [m/s]	3.966×10^{-3}	1.807×10^{-3}
τ_w [N/m^2]	1.570×10^{-2}	3.259×10^{-3}
ν [m^2/s]	1.004×10^{-6}	1.004×10^{-6}
ρ [kg/m^3]	998	998

4.1.3. RESULTS FOR DIFFERENT f_ε

For all figures in this section the three approaches ('high', 'moderate' and 'low' Reynolds number) are shown from left to right, indicated as *H*, *M* and *L* respectively. For *M*, f_ε is taken as $2 \cdot f_k$, i.e. $a = 2$. For $Re_\tau = 180$, the initialisation method (Section 4.1.2) yields a laminar flow [1] for *M* and *L*. This is an indication of added dissipation (the initial perturbations are dampened). For comparison purposes, a second set of computations is performed where the computations are restarted from a fully turbulent *H* computation.

Fig. 4.2 shows the mean velocity versus the channel height. For both Re_τ values *H* matches the DNS well independently of f_k. *M* shows slight discrepancies in the profile; especially for $Re_\tau = 180$, the velocity is underpredicted near the centre. *L* at $Re_\tau = 395$ and with $f_k = 0.15$ shows a more parabolic profile, which is an indication of a laminar

---

[1] In this context laminar flow is defined as the absence of resolved velocity fluctuations, i.e. the Reynolds stresses $Re_{ij} = \overline{u_i' u_j'}/u_\tau^2 \approx 0$.

flow. Both of the lower f_k values do show a turbulent flow profile, however the boundary layer appears to be thinner than half of the channel height. The velocity is almost constant in the region $0.5 \leq y/\delta \leq 1.0$. At the lower Re_τ, both $f_k = 0.15$ and 0.10 show a laminar profile. The profile for $f_k = 0.05$ matches the DNS data reasonably well.

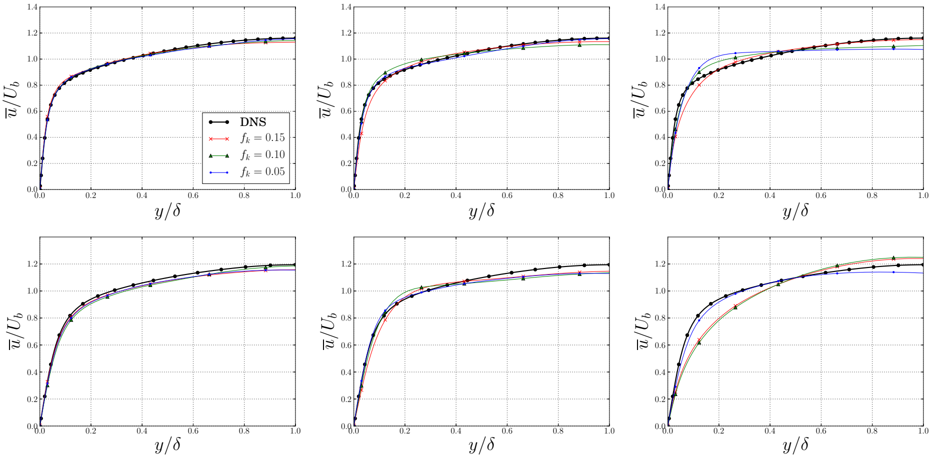

Figure 4.2: Velocity profiles ($\overline{u}/U_b$), from left to right *H*, *M* and *L* for $Re_\tau = 395$ (top) and 180 (bottom).

Fig. 4.3 shows two components of the Reynolds stress profiles. The fluctuations show that the magnitude of the Reynolds stresses are not yet fully statistically converged, however the trends between the different approaches can be compared. The statistical convergence will be investigated in detail in Sec. 5.3.2. The results for *H* and *M* are very similar. For both Re_τ, Re_{uu} and Re_{uv} both show the correct profile, the magnitude converges towards the DNS data with decreasing f_k. Re_{uv} is slightly underpredicted. Re_{uu} at $Re_\tau = 180$ is overpredicted near the wall for *H* and *M*. *L* clearly deviates from the reference data. At $Re_\tau = 395$, the Re_{uu} profiles show the correct shape, but $f_k = 0.15$ and 0.05 underpredict the magnitude. Re_{uv} is not captured by all f_k values. For $Re_\tau = 180$, the profile is correct for $f_k = 0.05$, although the magnitude is not well captured. For this Re_τ, $f_k = 0.05$ is again the only setting which captures Re_{uv} reasonably. For the other f_k settings, Re_{uv} is almost zero, indicating laminar flow, which is in agreement with the mean velocity profiles.

The turbulence kinetic energy spectra are shown in Fig. 4.4. As expected the spectra at the lower Re_τ show less scale separation, while for the higher Re_τ, a $-5/3$ slope is observed in part of the frequency range. For *H* the value of f_k has little influence on the spectra, for *M* the effect of reducing f_k is more visible. A lower f_k leads to more resolved turbulence, i.e. more energy in the spectrum and a higher cut-off frequency. This effect is the largest at $Re_\tau = 180$. The same influence of f_k is clear for *L*; only $f_k = 0.05$ at $Re_\tau = 180$ matches the reference set, but still the energy at higher frequencies is lower than for *M* and *H*. In all other computations the energy is too low, the spectrum shows again that the flow is mostly laminar. It is clear that reducing f_ε reduces the energy in the spectrum; *M* contains less energy than *H*, again especially at higher frequencies.

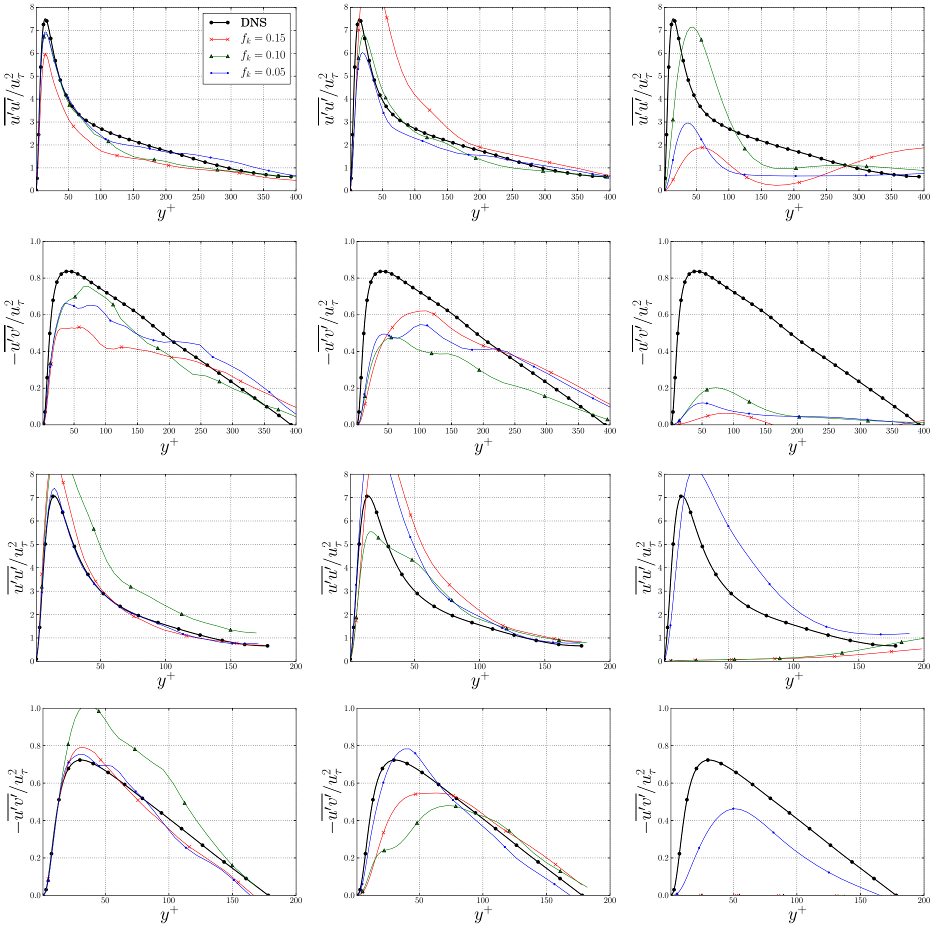

Figure 4.3: Normalised Reynolds stress profiles (Re_{ij}), from left to right H, M and L for $Re_\tau = 395$ (rows one and two) and $Re_\tau = 180$ (rows three and four).

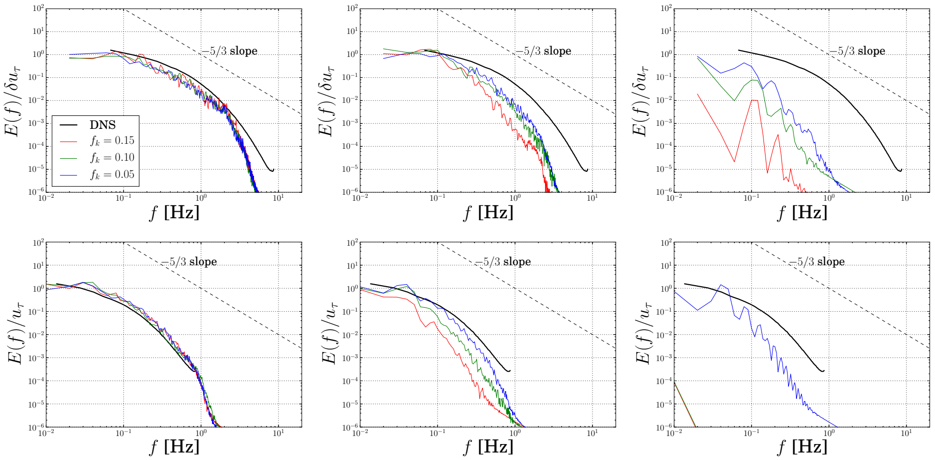

Figure 4.4: Turbulence kinetic energy spectra ($E_{u,y^+\approx 20}(f)$), from left to right *H*, *M* and *L*. $Re_\tau = 395$ (top row) and $Re_\tau = 180$ (bottom row).

Finally the effect of f_ε on the flow is visualised using structures based on the Q-criterion in Figures 4.5 and 4.6 for $Re_\tau = 395$ and 180 respectively. For both Reynolds numbers the same observations are made; for *H* the structures appear independent of f_k. *M* shows a large dependency on f_k; lowering f_k leads to more and smaller scales, for higher f_k only larger structures are observed away from the walls. This decrease in range of scales is in line with results by Frendi et al. [166]. The behaviour can be related to the definition of f_ε: for $f_\varepsilon = 1.0$, all dissipation occurs at the smallest scales, while if $f_\varepsilon < 1.0$, dissipation can also occur at larger scales. As a consequence the smaller scales are suppressed, since the turbulence is dissipated ‘earlier’. By reducing f_k and thereby also f_ε the range of scales increases again. For *L* the absence of structures for $f_k = 0.15$ for both Re_τ, and for $f_k = 0.10$ for $Re_\tau = 180$ again indicates a laminar flow. $f_k = 0.10$ at $Re_\tau = 395$ shows some large structures, but these do not resemble the turbulent structures as seen for the other approaches or for LES simulations (see Chapter 5). For $f_k = 0.05$ it is observed that the smallest structures are absent, which is in line with the turbulence kinetic spectrum.

4.1.4. CONCLUSIONS

Different approaches for specifying f_ε in the PANS model were compared based on theory and turbulent channel flow simulations. Little difference between the moderate and high Reynolds number approaches was found. The moderate Reynolds number approach does have a larger dependency on f_k, since due to the smaller value of f_ε, the turbulence dissipation is no longer confined to the smallest scales. For the low Reynolds number approach, it was demonstrated that excess diffusion is added to the equations. A laminar-like solution is obtained independent of the flow initialisation or Reynolds number. It is concluded that even at a low Reynolds number, $f_k = f_\varepsilon$ is an approach which should not be used due to the suppression of the smaller scales. Only when using

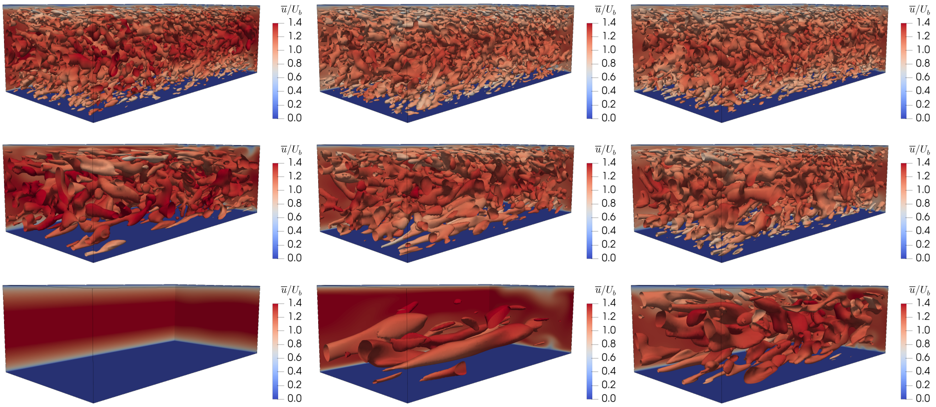

Figure 4.5: Instantaneous turbulent flow fields ($Q = 0.7$), coloured by $\overline{u}^* = \overline{u}/U_b$. From left to right $f_k = 0.15$, 0.10 and 0.05, for $f_\varepsilon = 1.0$ (first row), $f_\varepsilon = 2 \cdot f_k$ (second row) and $f_\varepsilon = f_k$ (third row). $Re_\tau = 395$.

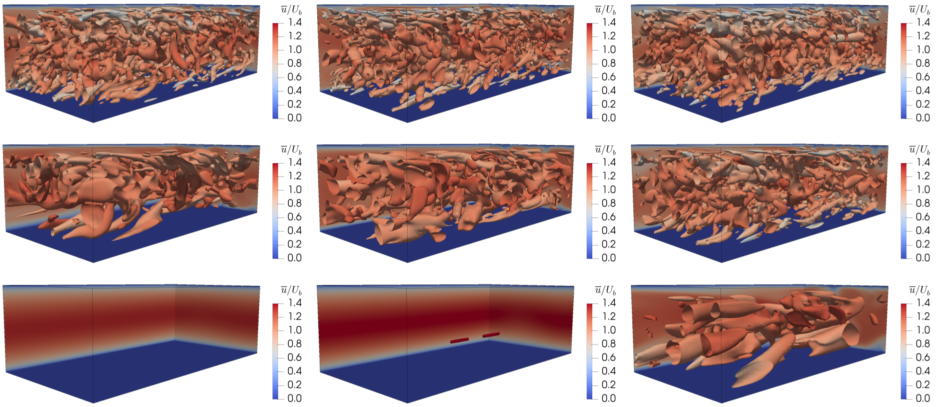

Figure 4.6: Instantaneous turbulent flow fields ($Q = 0.7$), coloured by $\overline{u}^* = \overline{u}/U_b$. From left to right $f_k = 0.15$, 0.10 and 0.05, for $f_\varepsilon = 1.0$ (first row), $f_\varepsilon = 2 \cdot f_k$ (second row) and $f_\varepsilon = f_k$ (third row). $Re_\tau = 180$.

a very low f_k (in the DNS limit) reasonable results for the mean velocity and Reynolds stress profiles can be obtained, although in that case the results obtained using $f_\varepsilon = 1.0$ also match the reference data well for the present test case, and contain more energy at the smaller scales.

For industrial flow cases at high Reynolds number, it is recommended to use $f_\varepsilon = 1.0$. That being said, if the reasoning is followed which leads to allowing f_k to vary in time and space, one can wonder whether the same should be applied to f_ε, i.e. f_ε depending on local flow quantities. There is currently no relationship to dynamically estimate f_ε found in the literature, while pursuing this method has the risk of re-introducing the problem of numerical and modelling error entanglement.

4.2. f_k ESTIMATES

For the usage of PANS two approaches can be distinguished: 1) the *Constant* f_k approach, where a constant value of f_k is used in the domain and throughout the simulation time. This approach was often used to verify the PANS model, but has mostly fallen out of favour recently since it is more computationally expensive in cases with a large range of different turbulent length scales. Theoretically, to use this approach in these cases a fine grid is required in the entire domain. In contrast, in approach 2), f_k can vary in space allowing a coarser turbulent resolution in regions where large turbulent scales are dominant. This approach can be further subdivided into *Static*, where f_k is fixed in time, or *Dynamic* for which f_k can also vary in time. Between these approaches strong disagreements exist: advocates of the *Constant* approach claim that by using a varying f_k one of the key advantages of the PANS model, the separation of modelling and discretisation error, is destroyed, and the model is reduced to a hybrid model. On the other hand, advocates of the varying f_k approach state that this way the grid, and therefore resources, can be used more optimally. It is argued that applying a constant f_k is not reasonable due to the spatial and temporal variation in turbulence length scales and grid resolution. Instead, by varying it in the domain and simulation time, the length scales which *can* be resolved, are resolved. Note however that the spatial variation in f_k reintroduces commutation error, since the PANS filtering operation does not commute with the spatial gradient [173]. Recent work such as Girimaji and Wallin [173] and Davidson [174] attempts to account for this error by adding a term in the k and momentum equations based on the gradient of f_k.

In the case of *Constant* f_k, it would be beneficial to have an *a priori* estimate of which physical parameter can be used for a particular flow on a given grid. In the case of varying f_k, the need for a reliable estimate for f_k is obvious. In the literature on the subject however, there is no consensus on which estimate to use. This section aims to give an overview of several methods found in literature and their properties. Note that all these estimates only concern f_k and all works assume $f_\varepsilon = 1.0$. The different estimates are compared for two test cases: a circular cylinder at $Re = 3900$, representative of a turbulent wake flow driven by spatially-developing coherent structures [57, 175]; and a turbulent channel flow at $Re_\tau = 395$, representative of an internal wall-bounded flow. The results of both *Static* and *Dynamic* estimates are evaluated, and compared with the *a posteriori* computed modelled-to-total ratio of turbulence kinetic energy, $\tilde{f}_k$, obtained from *Constant* f_k computations.

4.2.1. f_k ESTIMATES IN LITERATURE

The f_k estimates found in literature are divided according to category (*Static*, based on an *a priori* RANS computation, and *Dynamic*, computed during a PANS computation). Within this study the original notation is modified to maintain consistency between the different estimates and to properly compare them. Some general definitions are the grid sizes

$$\Delta_{min} = \min\left(\Delta_x, \Delta_y, \Delta_z\right), \tag{4.5}$$

$$\Delta_{max} = \max\left(\Delta_x, \Delta_y, \Delta_z\right), \tag{4.6}$$

$$\Delta_{avg} = \left(\Delta_x \cdot \Delta_y \cdot \Delta_z\right)^{\frac{1}{3}}, \tag{4.7}$$

and the characteristic turbulent length scales L_t and l_t

$$L_t = \frac{K^{\frac{3}{2}}}{E} = \frac{K^{\frac{1}{2}}}{C_\mu \Omega} \qquad \text{and} \qquad l_t = \frac{k^{\frac{3}{2}}}{\varepsilon} = \frac{k^{\frac{1}{2}}}{C_\mu \omega} \tag{4.8}$$

with a constant $C_\mu = 0.09$. For clarity, a distinction is made between L_t, based on total (modelled plus resolved) quantities and l_t, based on modelled quantities. In the case of *Static* approaches $L_t = l_t$, while in the case of *Dynamic* approaches, estimates based on both length scales can be found in literature. Note that while l_t can be obtained directly from the PANS transport equations, L_t must be obtained by computing the instantaneous velocity fluctuations, making the numerical implementation more difficult. Since $f_\varepsilon = 1.0$, dissipation occurs entirely at the smallest scales ($\varepsilon = E$ and $\omega = \Omega$). Fig. 4.7 shows a summary of the f_k estimates, sorted per approach, indicating that there is no clear relationship between estimation method and Reynolds number or number of cells. The *Static* estimates are obtained from Girimaji and Abdol-Hamid [51], Frendi et al. [166], Abdol-Hamid and Girimaji [176], Jeong and Girimaji [177], Han et al. [178], and Foroutan and Yavuzkurt [179], and the *Dynamic* estimates D. Luo et al. [62], Elmiligui et al. [180], Basu et al. [181], Song and S.-O. Park [182], Basara et al. [183], D. Luo [184], Davidson and Friess [185], and Basara et al. [186]. The formulations are given in Appendix D. In the literature, the estimates are applied to a range of test cases, including a turbulent jet, swirl in expansion, channel flow, open cavity, backward facing step, bluff bodies, square and circular cylinders, hill and hump flows. There is often little reasoning as to why a particular estimation is applied to a certain test case. This is surprising since the performance of turbulence models is in general highly case dependent. An exception is the work by D. Luo [184], in which results using *Dynamic* f_k are compared to those using a *Constant* f_k, as well as from DES, for a backward facing step. The author claims that the *Dynamic* results are 'almost comparable to the DES computation', with the *Constant* f_k underperforming in predicting skin friction and Reynolds stress profiles. However the applied grid is rather coarse in the wall-normal direction ($y^+ \approx 1$), meaning that the *Constant* f_k computation is not able to properly resolve the boundary layer, leading to poor results. The DES and *Dynamic* PANS both apply RANS in the boundary layer, leading to superior results. It is also shown in this chapter that the difference in results is smaller on a finer grid, indicating that numerical errors may play a role and therefore making it difficult to generalise this conclusion.

Note that in the literature some estimates are explicitly bounded to the interval $[0,1]$, whereas other papers do not mention this. In this study, such explicit bounds are not included to highlight the differences between estimates; of course in the implementation of these methods such bounds should be included.

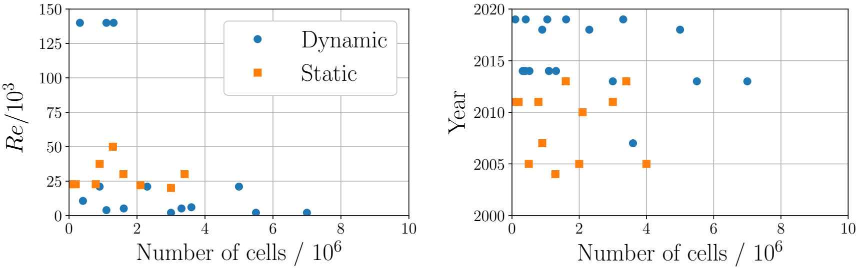

Figure 4.7: Literature overview with a selection of the available f_k estimates [51, 62, 166, 176–187]. The Reynolds numbers are based on the freestream velocity and characteristic length scale; the year indicates the year of publication. The results are shown as a function of the number of grid cells and the approach.

CONCLUSIONS BASED ON LITERATURE

An overview of the required input quantities and properties of the estimates is given in Table 4.2. A comparison of the formulation of the *Static* estimates shows that the formulations by Abdol-Hamid and Girimaji [176], Girimaji and Abdol-Hamid [51], Frendi et al. [166] and Han et al. [178] are essentially the same estimate. The magnitude can differ due to the application of different constants, but the trend is the same. This also shows that there is no consensus on how to define the grid size, which is also true for LES [52]. The grid definition could have a large effect on strongly anisotropic grids. The estimate by Jeong and Girimaji [177] appears to be incorrect due to the use of the grid size in the denominator, while that by Foroutan and Yavuzkurt [179] is the only one which by definition keeps f_k bounded between 0.0 and 1.0, which is a theoretical advantage. The other estimates are most likely explicitly bounded to a maximum value of 1.0, although this is not always clear in literature.

More variation can be found between the *Dynamic* estimates. Firstly, it is observed that the estimates by Elmiligui et al. [180], Basu et al. [181], D. Luo et al. [62], D. Luo [184] and Davidson and Friess [185] are all based on l_t, so only on modelled quantities. This is questionable since for low f_k, the RANS model has little effect on the solution. The reasoning behind this dependence on l_t instead of L_t is related to the difficulties in obtaining K for statistically unsteady flows, as recognised by Basara et al. [186] and Pereira [100]. In the case of a statistically steady flow $K = \langle K \rangle + k$, whereby $\langle K \rangle$ can be obtained from the difference between the instantaneous and mean velocity; for a statistically unsteady flow the difference between instantaneous and mean velocity leads to an overprediction of K due to the energy contained in the large scale motions. An overprediction in K results in reduced values for f_k [100].

Nevertheless, the estimates of Song and S.-O. Park [182], Basara et al. [183] and Basara et al. [186] are based on L_t, and therefore require computing K. An interesting exception to this is the method of Basara et al. [186], where the total k_t is obtained using an additional transport equation. However this estimate therefore only works in the context of a specific PANS formulation, and is thus not applicable in a general PANS formulation. Therefore it is not applied in the current work.

It is observed that due to their formulation, for all estimates (with the exception of Jeong and Girimaji [177]) $\lim_{y^+\to 0} f_k = 1$. Some arguments for this behaviour can be found in the occurrence of the smallest length scales at the wall. This implies however that the PANS model is reduced to a hybrid model with a behaviour similar to DES-like models. For some methods this is mentioned as a goal, while formulating the estimate [180, 185]. This behaviour does not happen however, with a *Constant* f_k approach.

Furthermore, it is obvious that due to the application of the different empirical constants any result can be obtained using the different estimates. The authors are therefore of the opinion that the magnitude of the estimation is less relevant than the trend of the estimation methods. All estimates are proportional to Δ^n, with often $n = 2/3$, so grid refinement only affects the magnitude. Consequently, only results for a single grid are shown in this chapter.

Table 4.2: Overview of input quantities and properties of PANS resolution estimates in literature.

Approach	Source	Input quantities				$f_k \in [0.0, 1.0]$	Calibration constant
		Grid	Length scale	Miscellaneous			
Static	Abdol-Hamid and Girimaji [176]	Δ_{max}	l_t			–	✓
	Girimaji and Abdol-Hamid [51]	Δ_{min}	l_t			–	✓
	Frendi et al. [166]	Δ_{min}	l_t	f_ε		–	✓
	Jeong and Girimaji [177]	Δ	λ_T			–	✓
	Han et al. [178]	Δ_{avg}	l_t			–	✓
	Foroutan and Yavuzkurt [179]	Δ_{avg}	l_t			✓	–
Dynamic	Elmiligui et al. [180]	Δ_{max}	l_t			✓	–
	Basu et al. [181]	Δ_{max}	l_t	Δt	$\|\|\langle \boldsymbol{U} \rangle\|\|_2$	✓	–
	Song and S.-O. Park [182]	Δ	L_t	ν	ε	–	–
	Basara et al. [183]	Δ_{avg}	L_t			–	✓
	D. Luo et al. [62]	Δ_{max}	l_t			–	✓
	D. Luo [184]	Δ_{max}	l_t			–	✓
	Davidson and Friess [185]	Δ_{max}	l_t			✓	–
	Basara et al. [186]	Δ_{avg}	$\tilde{L}_t$	k_{ssv}	ε	–	✓

4.2.2. TEST CASES

The estimates are applied to two canonical test cases: one representative of a turbulent wake flow with coherent structures, and one of an internal boundary layer flow.

The selected test case for the turbulent wake flow is the flow around a circular cylinder at $Re = 3900$. This flow was thoroughly investigated using PANS by Pereira, Vaz, Eça, and Girimaji [57] and Pereira, Eça, Vaz, and Girimaji [175]. In the current work the finest grid, and set-up, as employed by Pereira, Vaz, Eça, and Girimaji [57] and Pereira, Eça, Vaz, and Girimaji [175] are used. All terms in the equations are discretised with second-order accurate schemes. The rectangular computational domain measures $22D$ in transverse and $3D$ in span-wise direction, with an inflow located $10D$ upstream of the cylinder and the outflow $40D$ downstream, as shown in Fig. 4.8. At the inflow constant velocity, turbulence intensity ($I = 0.2\%$) and eddy-viscosity ratio ($\nu_t/\nu = 10^{-3}$) are prescribed to match the experimental conditions of Parnaudeau et al. [188]. The pressure is imposed at the top and bottom boundaries, and at the outlet the streamwise derivates are set to zero. Symmetry boundary conditions are applied in the spanwise direction. Computations are performed on a multi-block structured hexahedral grid of 4.5×10^6 cells, with dimensionless cell lengths in the tangential, normal and streamwise direction of $\overline{x}_t^+ = 1.8$, $\overline{x}_n^+ = 0.38$ and $\overline{x}_s^+ = 38.9$, and a non-dimensional time step, $\Delta t U_\infty/D = 5.209 \times 10^{-3}$ leading to a time-averaged maximum Courant number ($U\Delta t/\Delta x$ [93]) of 2.7. This was shown to be sufficient to achieve acceptable discretisation errors [57]. Round-off errors are deemed negligible due to the use of double precision arithmetic and to minimise iterative errors calculations are run until the maximum norm, L_∞, of the normalized residuals of all equations equals 10^{-5} at each time step (equivalent to $L_2 \approx 10^{-7}$). The constant f_k values employed in the current work are 0.75, 0.50 and 0.25.

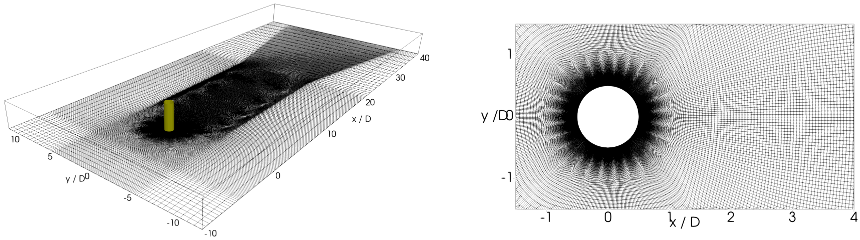

Figure 4.8: Circular cylinder computational domain and grid.

In order to investigate the effect of f_k estimates inside a boundary layer, a second test case is used: a turbulent channel flow at $Re_\tau = u_\tau\delta/\nu = 395$, see Chapter 5. Based on the results previously obtained for these test cases by Pereira, Vaz, Eça, and Girimaji [57] and in Chapter 5 the employed grids are judged to have sufficient resolution to support the applied f_k values. Consequently significantly higher estimates are dismissed as erroneous.

In order to validate the different f_k estimates, the outcomes are compared with the *a posteriori* computed ratio of modelled-to-total turbulence kinetic energy from a *Constant f_k* computation, designated $\tilde{f}_k$,

$$\tilde{f}_k = \frac{k}{\frac{1}{2}\left(\overline{u_i' u_i'}\right) + k}. \tag{4.9}$$

For a channel flow the computation of u_i' is straightforward. For a cylinder however, due to the statistically unsteady flow, it is difficult to distinguish between the time-varying mean velocity and the ensemble averaged turbulent velocity. In the results presented here this difference is neglected, leading to an overpredicted value for u_i' and consequently a reduced $\tilde{f}_k$.

4.2.3. EVALUATION OF STATIC ESTIMATES

The *Static* estimates are applied to results obtained with the $k-\omega$ SST RANS model [102]. All plots of the estimates are limited between 0.0 and 1.0, even if the estimate itself is not necessarily bounded between these limits. For the cylinder case the results are shown in a contour plot at the centre of the domain in Fig. 4.9 and the estimates, averaged in spanwise direction, are quantitatively compared on an axial line located on the domain centreline in the vertical direction in Fig. 4.10. Fig. 4.9 also shows the time-averaged axial velocity. For the channel flow case, due to the statistical stationarity, only a quantitative comparison is given. Technically, the estimates should be applied to a steady-state computation, however for the cylinder case the flow is inherently unsteady. Therefore the time-averaged quantities are used, immediately highlighting a limitation of using *Static* estimates.

The estimates of Abdol-Hamid and Girimaji [176], Girimaji and Abdol-Hamid [51] and Han et al. [178] vary in magnitude due to the different constants and/or grid sizes but overall show a similar behaviour (see Figures 4.9a, 4.9b and 4.9e). f_k is 1.0 (or larger) upstream and near the wall and decreases towards 0.0 in the wake. The lowest values can be found for Foroutan and Yavuzkurt [179], the largest for Han et al. [178]. It is clear that the estimate of Jeong and Girimaji [177] is incorrect, f_k is 1.0 in the entire domain, except in the first layer of cells near the wake (not visible in the figure). Finally the estimate of Abdol-Hamid and Girimaji [176] is similar to the estimate of Foroutan and Yavuzkurt [179], although the values in the wake are somewhat higher and the RANS region near the wall is thicker. These estimates show both a wider wake region where $f_k < 1.0$, and maintain these low values further downstream, compared to the other estimates. The plots in Fig. 4.10 show that, with the exception of the estimate of Foroutan and Yavuzkurt [179], all estimates exceed 1.0 upstream of the cylinder. The estimate of Han et al. [178] also exceeds 1.0 in the wake. Again it is clear that the estimate of Jeong and Girimaji [177] is incorrect, since it only has a proper value near the cylinder while in the rest of the domain the value is too large to be visible in the figure.

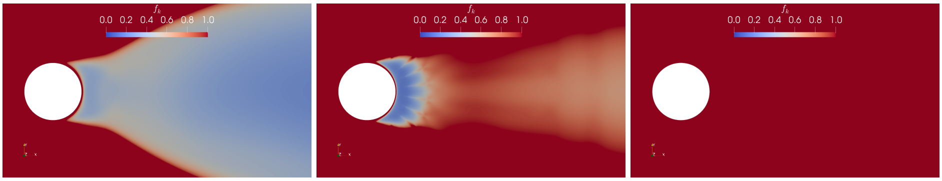

(a) Abdol-Hamid and Girimaji [176] (b) Girimaji and Abdol-Hamid [51] (c) Jeong and Girimaji [177]

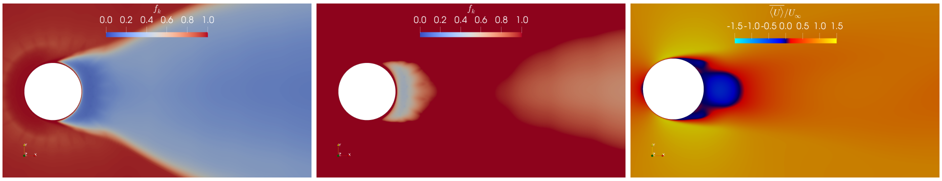

(d) Foroutan and Yavuzkurt [179] (e) Han et al. [178] (f) Mean axial velocity

Figure 4.9: *Static* f_k estimates and the time-averaged axial velocity for a circular cylinder.

For the channel flow the estimates show relatively high values. The estimate of Jeong and Girimaji [177] returns a value higher than 1.0 in the entire domain. Both Girimaji and Abdol-Hamid [51] and Han et al. [178] show a minimum value of approximately 0.5 for $y/\delta > 0.15$ and $y/\delta > 0.05$ respectively. The estimates of Abdol-Hamid and Girimaji

[176] and Foroutan and Yavuzkurt [179] have a minimum value of 0.2 in the centre, although Abdol-Hamid and Girimaji [176] increases above 1.0 at $y/\delta = 0.1$. Foroutan and Yavuzkurt [179] shows the lowest values across the channel height, and is the only one which shows a maximum of 1.0 at the wall.

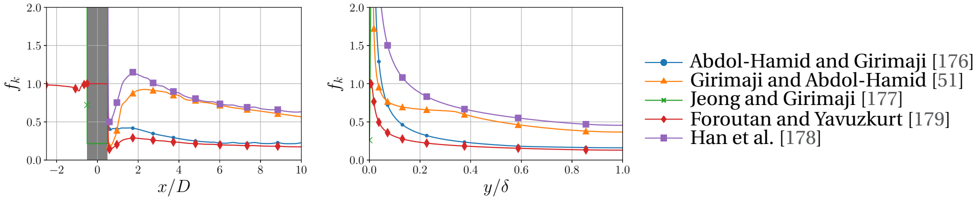

Figure 4.10: *Static* f_k estimates applied to the circular cylinder (left) and channel flow (right). The estimates for the cylinder are obtained on axial lines located on the domain centreline in the vertical direction, averaged in spanwise direction. The grey area indicates the cylinder. For the channel flow the estimates are obtained along the height of the channel.

4.2.4. EVALUATION OF DYNAMIC ESTIMATES

The *Dynamic* estimates are applied to instantaneous flow fields from PANS computations performed with f_k fixed in time and space, denoted as $f_{k,c}$. This is not how a true *Dynamic* approach should work, since this way the flow field does not depend on the estimate. The advantage of this approach is that oscillations in the estimates are suppressed. Consequently, the different estimates can be compared more objectively. In the contour plots, the results are again bounded between 0.0 and 1.0, even if the estimate itself is not. The *a posteriori* computed value $\tilde{f}_k$ is also shown for comparison. Fig. 4.11 shows the values of the estimates applied to the cylinder in a contour plot at the centre of the domain, and Fig. 4.12 shows f_k on axial lines located on the domain centreline in the vertical direction, averaged in spanwise direction.

All estimates show an increase in estimated f_k with decreasing $f_{k,c}$, indicating that in a *Dynamic* approach f_k should converge to a target value. If $f_{k,c}$ is larger than the target value, f_k is smaller than the target value, and vice versa. As observed by Davidson and Friess [185], this implies that the estimated f_k is implicitly linked to $\tilde{f}_k$. Note that due to the spatial and temporal variation of the flow field, the target f_k will also vary, leading to potentially oscillatory behaviour for f_k.

There is little difference between all the estimates whether $f_{k,c} = 0.75$ or 0.50, but the estimates increase when $f_{k,c} = 0.25$. This is an indication that the converged value, $f_{k,d}$, lies between these results. The estimates of Elmiligui et al. [180] and Basu et al. [181] show a similar behaviour, with $f_k = 1.0$ upstream, in the far-field and close to the cylinder, with lower values in the wake. The estimate of Song and S.-O. Park [182] shows a similar trend, but the values upstream and towards the far-field are significantly lower. With decreasing $f_{k,c}$, the region where $f_k \approx 1.0$ upstream and in the far-field increases. The estimate by Basara et al. [183] shows an interesting trend; because of the dependence on L_t the wake shows high f_k values in the wake centre, but lower values surrounding the wake centre. The difference is clear when comparing the estimate to the one of D. Luo et al. [62], which has an almost identical formulation but depends on l_t. The estimate of D. Luo et al. [62] is unaffected by $f_{k,c}$ in the wake, but increases in the far-field and upstream. Note that the low values in the entire domain for this estimate are mostly related to the small constant (C_{PANS}) used in the formulation. Finally the estimate of Davidson and Friess [185] shows a comparable trend, but there is less ambiguity in f_k. It is either 0.0 in the wake, or 1.0 elsewhere. The formulation therefore ensures a DES-like behaviour, as was desired in formulating the estimate.

The behaviour observed for the *a posteriori* computed ratio, $\tilde{f}_k$, differs from the estimates. Firstly, the effect of $f_{k,c}$ is clearly visible; as expected with decreasing $f_{k,c}$, $\tilde{f}_k$ decreases. Secondly, it can be seen that in general $\tilde{f}_k$ is significantly lower than $f_{k,c}$. It appears that modifying $f_{k,c}$ has little effect on $\tilde{f}_k$ in the entire domain. Instead, it mainly affects the peak values of $\tilde{f}_k$ occurring in the domain. Thirdly, due to the laminar flow upstream and in the far-field, both k and $\langle K \rangle \approx 0$, leading to $\tilde{f}_k \approx 0$, which is in strong contrast to the results of the estimated f_k values. Finally, $\tilde{f}_k$ is also low in the near-wall regions, as opposed to the estimates which all give $f_k \geq 1$ due to $\lim_{y^+ \to 0} l_t$ and $\lim_{y^+ \to 0} L_t = 0$. The peaks in the wake seem to be best predicted by the estimate of Davidson and Friess [185], most likely due to the dependence on L_t. However outside of the wake the estimate deviates from $\tilde{f}_k$.

Fig. 4.12 shows that only the estimates of Elmiligui et al. [180], Basu et al. [181] and Davidson and Friess [185] are bounded between 0.0 and 1.0 in the domain. The largest deficiencies compared to $\tilde{f}_k$ are visible upstream of the cylinder, where all the estimates return a value larger than 0.9, while it is clear that $\tilde{f}_k < f_{k,c}$. Downstream of the cylinder the estimates of Song and S.-O. Park [182], D. Luo et al. [62] and Davidson and Friess [185] have the same order of magnitude as $\tilde{f}_k$ for $f_{k,c} = 0.75$ and 0.50, but for $f_{k,c} = 0.25$ the estimates are all larger. It is important to note that only the estimates of Song and S.-O. Park [182] and D. Luo et al. [62] yield values significantly smaller than 1.0 upstream. This is relevant for cases when synthetic turbulence is added at the inflow, since the introduced fluctuations should not be dissipated before they reach the object of interest.

Fig. 4.13 shows the estimates for the channel flow case, for which $\tilde{f}_k$ is also always less than $f_{k,c}$. Note that indeed $\lim_{y^+ \to 0} \tilde{f}_k = 0$, but only in the cell closest to the wall. Again it is clear that these estimates are less suitable for an internal boundary layer flow: the estimate of Basara et al. [183] is larger than 1.0 in the entire domain, while the estimates of Elmiligui et al. [180] and Basu et al. [181] remain close to 1.0. The estimate of Song and S.-O. Park [182] is unaffected by changing $f_{k,c}$, as was also observed for the cylinder case, and is around 0.50 across the channel height. The estimate of Davidson and Friess [185] is close to 1.0 in the entire domain, again in the spirit of the desired DES-like behaviour. Only the estimate of D. Luo et al. [62] shows reasonable values ($f_k \approx 0.15$ at $y/\delta > 0.2$ for $f_{k,c} = 0.15$), which increases to 0.25 for $f_k = 0.10$ and 0.5 for $f_k = 0.05$. However close to the wall the estimate is still significantly larger than 1.0.

4.2.5. DISCUSSION AND CONCLUSIONS

The review of modelled-to-total kinetic energy f_k estimates presented in this chapter makes clear that there is no consensus on how to estimate f_k from a given flow field on a given grid, both for *Static* and *Dynamic* PANS. These approaches are both strongly dependent on this estimate, potentially leading to significant modelling errors. Due to differences in the definition of the characteristic grid dimension and the application of

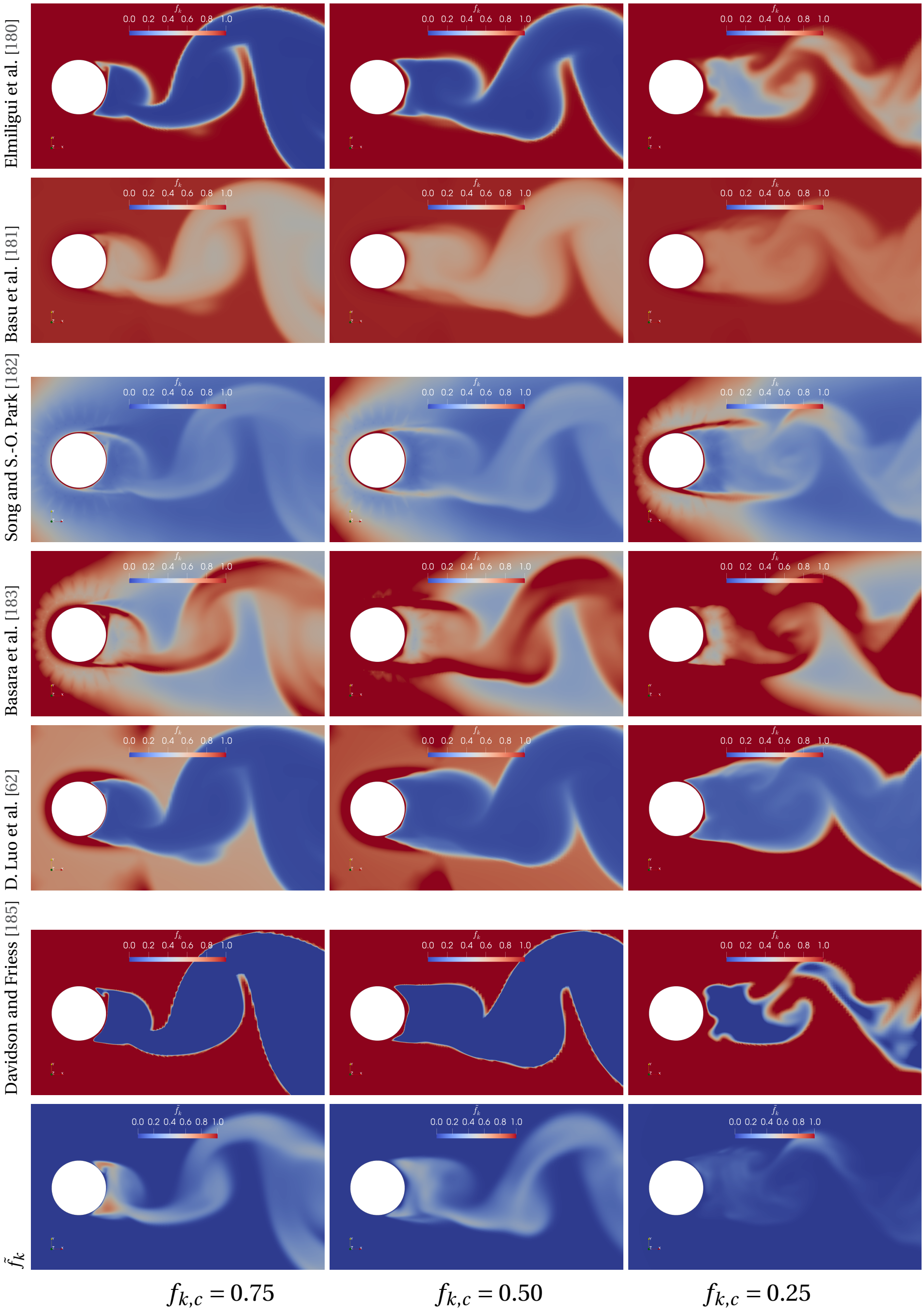

Figure 4.11: *Dynamic* f_k estimates for a circular cylinder, for different $f_{k,c}$.

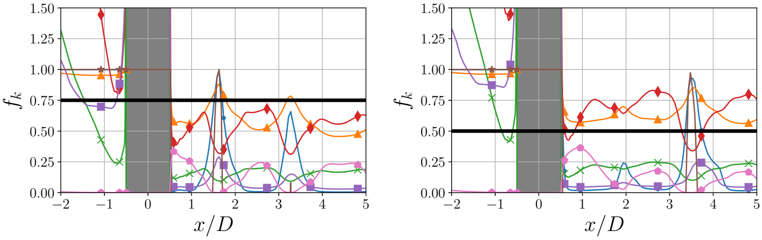

(a) $f_{k,c} = 0.75$ (b) $f_{k,c} = 0.50$

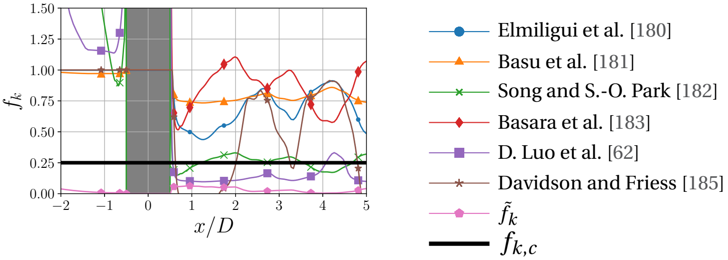

(c) $f_{k,c} = 0.25$

Figure 4.12: *Dynamic* f_k estimates and $\tilde{f}_k$, for different $f_{k,c}$. Estimates obtained on axial lines located on the domain centreline in the vertical direction, averaged in spanwise direction. The grey area indicates the cylinder.

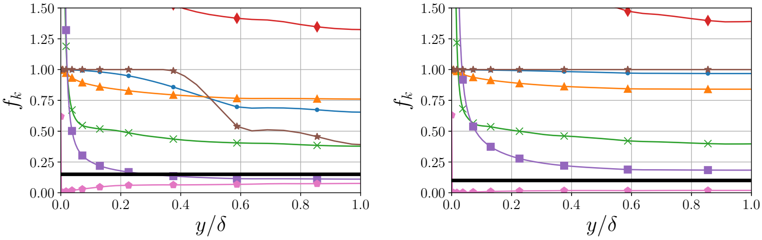

(a) $f_{k,c} = 0.15$ (b) $f_{k,c} = 0.10$

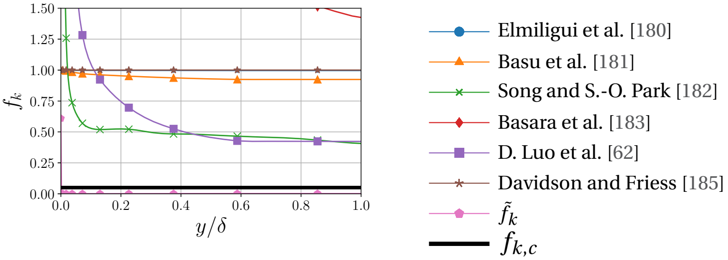

(c) $f_{k,c} = 0.05$

Figure 4.13: *Dynamic* f_k estimates and $\tilde{f}_k$, for different $f_{k,c}$. Estimates obtained along the height of the channel.

empirical constants, it is clear that the absolute values of the estimates should be treated with care. Instead more emphasis should be placed on the predicted trends. An issue unaddressed in literature is that *Static* estimates should be applied to a steady computation; however for statistically unsteady flows, such solutions are unobtainable. In this work, the mean flow field was used.

Both the *Static* and *Dynamic* estimates do not yield reasonable results for the channel flow case and significantly overpredict f_k. For the cylinder case with a *Static* computation, the estimate of Foroutan and Yavuzkurt [179] seems most appropriate, since it is the only one which is properly bounded between 0.0 and 1.0. In case of *Dynamic* PANS, only the estimates of Elmiligui et al. [180], Basu et al. [181] and Davidson and Friess [185] are bounded between these limits, although that of Basu et al. [181] generally predicts too high values. It is observed that estimates based on K instead of k generally lead to better predictions, however K is difficult to obtain in statistically unsteady flows.

It is shown that the f_k value employed in a *Constant* f_k computation, $f_{k,c}$, mostly affects the peak values of $\tilde{f}_k$ in the field, and generally $\tilde{f}_k < f_{k,c}$. This difference is sufficiently large that the author is of the opinion that even if $\tilde{f}_k$ would be corrected for the energy contained in the large scale motions, still $\tilde{f}_k \leq f_{k,c}$, which is a favourable property of the PANS model. Generally the estimates tend to give values of f_k which are significantly larger than $\tilde{f}_k$. Aside from the difference in magnitude, the trends observed for the estimates differ in key aspects from the computed $\tilde{f}_k$, indicating more fundamental issues. Most estimates are constructed such that $\lim_{y^+\to 0} f_k = 1$ in the near-wall region, since $\lim_{y^+\to 0} l_t$ and $\lim_{y^+\to 0} L_t = 0$. A comparison with $\tilde{f}_k$ shows that although this principle is correct, the region in which it is applied is not. In the *Constant* f_k computations $f_k = 1.0$ only in the first layer of cells near the wall, whereas in the estimates this occurs in the entire boundary layer. This behaviour also explains the failure of the estimates for the channel flow case, and it gives rise to the belief that the estimates should not be applied inside boundary layers. A consequence of this behaviour is that the PANS model behaves more like a DES model. This is sometimes described in literature as an advantage or a goal in the derivation of the estimate, although this does imply that the unfavourable properties of DES, such as error entanglement, are then also incorporated. A second issue with the estimates is that they all yield $f_k = 1.0$ if the resolved flow is laminar (upstream and in the far-field). This implies that in case of laminar flow, the PANS model resorts to the RANS parent model. For *Static* computations this becomes problematic if during the subsequent PANS computation synthetic turbulence is added at the inflow, since the introduced fluctuations might be dissipated before they reach the object of interest. In the opinion of the authors, it is not possible to design a general estimate (applicable in the entire domain) which does not suffer from this problem. Upstream of the object no information is available concerning the resolution which can be supported, except for the grid size. The estimates found in literature which depend on k are strongly dependent on values set at the inflow boundary condition, and the turbulence decay; whereas the estimates depending on K suffer from the fact that no information is available upstream, unless synthetic turbulence is added. To include this f_k should be below 1.0; this leads to a circular dependency. It seems that the estimates are only valid for cases which show strongly separated vortical structures; and even then only in the wake of the object. To enable the usage for other cases, it is beneficial to limit

f_k in laminar regions to a certain threshold and only apply the estimate in the wake of the object. For this threshold, no definition is available.

Finally it must be remarked that *Dynamic* PANS computations run the risk that f_k will show an oscillatory behaviour due to the strong spatial variation of the estimates. Not only is f_k temporally and spatially varying, but also the flow field upon which it is based. This combination might negatively influence the results. Although this hypothesis is not investigated in this work, it contributes to the opinion of the author that despite potential theoretical advantages to the usage of *Dynamic* PANS, the *Constant* PANS approach, with a f_k fixed in time and space, is still preferable in order to minimise errors in CFD results and increase the reliability of industrial CFD.

4.3. PANS-KSKL MODEL

From RANS modelling, it is known that there are several theoretical and practical advantages to prefer the KSKL model over $k-\omega$ based models. Firstly, the KSKL model commonly predicts lower eddy-viscosities compared to $k-\omega$ models (see e.g. F. Menter et al. [103], F. Menter and Egorov [189], and Liebrand et al. [190]). In the context of PANS, this implies that less turbulence will be modelled compared to a $k-\omega$ SST-based closure, for the same f_k value. Lower eddy-viscosities can be advantages for cases such as predicting cavitation dynamics or under water radiated noise. Secondly, the RANS KSKL model exhibits a lower dependency on the height of the first near-wall cell (y^+), thereby resulting in decreased numerical errors on the same grid [107]. Thirdly, $k-\omega$ models suffer from difficult to define boundary conditions at the outer boundary, and at the wall, where ω goes to infinity [191]. In contrast, $\sqrt{k}L$ is zero by definition at the wall, making it easier to implement in CFD codes and also improving iterative convergence. Finally, one of the shortcomings of $k-\omega$ based models is the generally poor iterative convergence of the second transport equation for the dissipation rate ω, especially in connection with multiphase problems, such as cavitation and free-surface flows (see e.g. Liebrand et al. [190] and Hoekstra and Vaz [192]). When combining this model with the PANS framework, this feature is incorporated. This leads to non-negligible iterative errors even for simulations with a high physical resolution (i.e. close to DNS), while in this case it would be reasonable to expect the discretisation error to be the dominating error source in the total numerical error. In such cases, the RANS parent model only works as a sub-filter model, of which it would be desirable to be accompanied by a small iterative error. Large iterative errors also make the estimation of discretisation errors difficult – which is one of the main attractions of PANS [57, 193] – since for such methods the iterative error should be at least two orders of magnitude lower than the discretisation error [56]. The PANS-KSKL model is expected to exhibit, like its RANS counterpart, improved iterative convergence behaviour due to the substitution of the ω equation by the $\sqrt{k}L$ equation. These properties have motivated other researchers to also favour the KSKL model, for example in the context of transition modelling [194] and the prediction of drag forces [96].

This section investigates a new PANS closure based on the $k-\sqrt{k}L$ (KSKL) model.

4.3.1. PANS-KSKL MODEL PROPERTIES

SPECIFYING f_l

The filtering of the Navier-Stokes equations depends on the values chosen for f_k and f_l. f_k determines the physical resolution of the flow, i.e. to what extent the turbulence spectrum is resolved. In the original version of PANS, the second setting $f_\varepsilon = \varepsilon / E$ determines the overlap between the energy-containing and the dissipation ranges. For ease of use it is preferable to have the same two settings for different types of PANS closures. Consequently, for $k-\omega$ based PANS models, the second parameter f_ω is related to f_ε (see e.g. Pereira, Vaz, Eça, and Girimaji [57]), using

$$f_\omega = \frac{f_\varepsilon}{f_k}. \tag{4.10}$$

Thereby the user needs to set f_k and f_ε, and the appropriate f_ω is selected in the code.

In the case of PANS-KSKL the second parameter is f_l. Following the relationship derived by Reyes et al. [46], the PANS length scales can be related to the RANS length scales using

$$\frac{l}{L}\left(= f_l\right) \sim \frac{f_k^{3/2}}{f_\varepsilon}. \tag{4.11}$$

This can also be derived when combining Eq. C.11 with the ratio of eddy-viscosities [46],

$$\frac{\nu_t}{\nu_{tT}} = \frac{f_k^2}{f_\varepsilon}. \tag{4.12}$$

IMPLICATIONS FOR SUB-FILTER QUANTITIES

The sole effect of the sub-filter model on the filtered Navier-Stokes equations is on the eddy-viscosity, the formulation of which varies between the $k-\omega$ and KSKL closures. As mentioned in the introduction, for RANS, it is commonly observed that the eddy-viscosities predicted by the KSKL model are lower than those of $k-\omega$ models. This should hold when using PANS-KSKL with $f_k < 1.0$.

A related property is that the decay in ν_t, downstream of the inlet, is affected by the closure formulation. It is known from RANS modelling that the location of transition strongly depends on the turbulence quantities, and therefore on the decay of ν_t from the inlet (see e.g. Spalart and Rumsey [195] and Lopes et al. [196]). This effect is limited for RANS simulations of high Reynolds number flows, where a 'fully turbulent' solution is assumed, but it's relative importance increases with decreasing Reynolds number. In the context of SRS, the effect of $\nu_{t,in}$ is often overlooked, since with decreasing f_k, the ν_t decreases until 0 in the limit of $f_k = 0.0$ (Chapter 6). However, for intermediate values f_k values, $\nu_{t,in}$ still has an effect on the equations being solved (i.e. Eq. 2.4), making the decay a relevant parameter. Following the derivations by Lopes [197] for the RANS SST and KSKL model, the decay of PANS-SST and PANS-KSKL can be derived. Under the assumptions of a steady, uniform flow, aligned with the x axis, sufficiently far away from walls, constant f_k in the domain, and by neglecting the diffusion terms, the decay of PANS-SST can be formulated as

$$\nu_t = \frac{\nu_{t,in}}{\left[\frac{1}{\langle U\rangle}\left(\langle U\rangle + \left(\alpha\beta^* - \alpha\beta^* f_k + \beta f_k\right)(x - x_{in})\frac{k_{in}}{\nu_{t,in}}\right)\right]^{\frac{\beta^*}{\alpha\beta^* - \alpha\beta^* f_k + \beta f_k} - 1}} \tag{4.13}$$

while the decay for PANS-KSKL is

$$\nu_t = \frac{\nu_{t,in}}{\left[\frac{1}{\langle U\rangle}\left(\langle U\rangle + \beta_{KSKL}\left(x - x_{in}\right)\frac{k_{in}}{\nu_{t,in}}\right)\right]^{\frac{\beta^*}{\beta_{KSKL}}-1}}. \tag{4.14}$$

with the subscript in indicating values at the inlet of the domain, and

$$\beta_{KSKL} = \beta^* - \zeta_3 C_\mu^{1/4} f_k. \tag{4.15}$$

See Appendix E, for the derivation of Eq. 4.13 and 4.14. The solution for the decay of ν_t for PANS-SST and PANS-KSKL model is of a similar form as the solutions for the RANS parent models, but with different constants. These constants do not only depend on the constants of the model, but are also a function of f_k. The functions are shown graphically in Fig. 4.14. Interestingly, the two closures show a different trend. For $f_k = 1.0$ (the RANS models), the KSKL model shows a larger ν_t decay, compared to the SST model. With decreasing f_k, for PANS-SST the decay increases, leading to a large decrease in ν_t downstream of the inlet. For PANS-KSKL, the decay decreases with decreasing f_k, leading to a reduced decay compared to PANS-SST. The f_k for which the decays are equal depends on the values $k_{in}/\nu_{t,in}$ and the downstream distance $x - x_{in}$. In the limit of $f_k = 0.0$, the PANS-KSKL model, theoretically, shows no decay of ν_t. This implies that with decreasing f_k, the PANS-SST model becomes less sensitive to the inlet boundary conditions, while the PANS-KSKL model becomes more sensitive to this, leading to the need to vary the modelled quantities at the inlet with varying f_k.

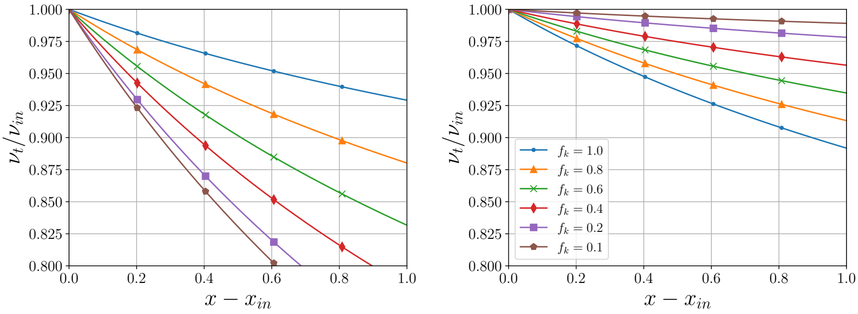

Figure 4.14: Decay of ν_t versus downstream location x as function of f_k for PANS-SST (left) and PANS-KSKL (right) according to Eq. 4.13 and 4.14, respectively. Values used for this example are $C_\mu = 0.09$, $\beta^* = 0.09$, $\alpha = 0.5$, $\zeta_3 = 0.028$, $\beta = 0.08$, $\langle U\rangle = 1.0$, $k_{in}/\nu_{t,in} = 10$.

Thirdly, there are the effects on the turbulent length scales l and L_{vk}, which appear in the second turbulence closure equation (Eq. C.17). One of the key features of the KSKL model is its inclusion of an additional length scale, the von Kármán length scale L_{vk}, given by Eq. C.14, which, without the limiters, reduces to

$$L_{vk} = \frac{\kappa\langle S\rangle}{\sqrt{\frac{\partial^2\langle U_i\rangle}{\partial {x_k}^2}\frac{\partial^2\langle U_i\rangle}{\partial {x_j}^2}}}. \tag{4.16}$$

The length scale is a function of the resolved strain rate $\langle S \rangle$ and the rate of change in the resolved acceleration $\partial^2 \langle U_i \rangle / x_j^2$. It is therefore solely based on the resolved velocity field. According to Xu et al. [198], who investigated different formulations for L_{vK} in the context of scale-adaptive simulation (SAS), the von Kármán length scale can be considered as the second length scale in a RANS model for a fully developed planar turbulent boundary layer. This would erroneously imply that L_{vK} should reduce together with f_k. Modification of f_k leads to differences in the strain rate and rate of change in acceleration, due to increased variations in the velocity field (as seen in Pereira, Vaz, Eça, and Girimaji [57] and Klapwijk et al. [193]). A consequence is that L_{vK} will increasingly vary in space and time with reducing f_k. However, the presumption in RANS is that the time-averaged velocity field – when all turbulence is modelled – is identical to the time-averaged velocity field when all turbulence is resolved. From this, it is to be expected that the time-averaged L_{vK} is also independent of f_k.

This is not the case for the second length scale in the KSKL model, l, which is part of the convected secondary quantity $\sqrt{k}l$. By definition, this depends on f_k according to the relationship derived in Eq. 4.11, and is shown in Fig. 4.15. As expected, the ratio l/L goes to zero with decreasing f_k, meaning that increasing the physical resolution leads to a RANS turbulent length scale going to zero, indicating that all turbulence should be resolved. It can also be shown that the slope of $\partial f_l / \partial f_k$ decreases when f_k approaches zero, implying an initially larger effect of reducing f_k, but less difference for lower f_k values. This is in line with results obtained with different ($k-\omega$ based) PANS closures (Chapter 5).

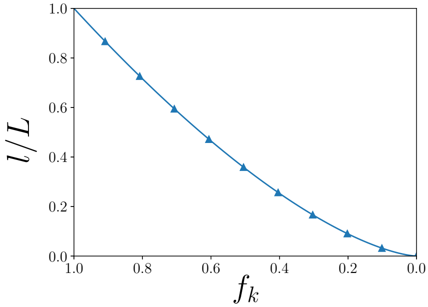

Figure 4.15: Ratio l/L versus f_k according to Eq. 4.11 with $f_\varepsilon = 1.0$. Note the inversion of the horizontal axis, $f_k = 1.0$ on the left corresponds with RANS, $f_k = 0.0$ on the right corresponds with DNS.

4.3.2. NUMERICAL EXAMPLES

The PANS-KSKL turbulence model is applied to two test cases and compared against the PANS-SST model. $f_\varepsilon = 1.0$ to avoid excessive diffusion, and constant values of f_k are employed in time and space.

TURBULENT CHANNEL FLOW AT $Re_\tau = 395$

The first test case is the canonical turbulent channel flow at $Re_\tau = u_\tau \delta / \nu = 395$, see Chapter 5.

Fig. 4.16 and Fig. 4.17 show the mean velocity, turbulence kinetic energy spectra, eddy-viscosity ratio, turbulence intensity, and Reynolds stresses, for several f_k values. Next to the PANS-KSKL, results PANS-SST results from Chapter 5 are also included. In line with the PANS-SST results, only low f_k values yield a resolved turbulent flow when using PANS-KSKL. For an explanation of this phenomenon, see Chapter 5. The magnitude of the eddy-viscosity predicted by PANS-KSKL is strongly reduced compared to PANS-SST, while the profiles are similar. For PANS-KSKL the threshold to obtain a turbulent solution is $f_k = 0.25$, while for PANS-SST the highest applicable f_k value was 0.15. This different threshold is a direct consequence of the reduced eddy-viscosity levels of the PANS-KSKL. As an example, for $f_k = 0.25$, ν_t/ν is almost 25 times higher for PANS-SST compared to PANS-KSKL, leading to dampening of the velocity fluctuations and a laminar flow solution. It is known know from literature that for SRS the effective computational Reynolds number,

$$Re_e = \frac{U\delta}{\nu + \nu_{modelled}} = \frac{U\delta}{\nu + f_k^2 \nu_t}, \tag{4.17}$$

must exceed the critical transition Reynolds number needed for the onset of instability, Re_c [175, 193]. For a turbulent channel flow, $Re_c \approx 2300$, obtained from experiments [199]. When the critical Reynolds number is equated to the effective Reynolds number for both PANS models, the relationship

$$\frac{f_{k,SST}}{f_{k,KSKL}} = \sqrt{\frac{\nu_{t,KSKL}}{\nu_{t,SST}}} \tag{4.18}$$

can be derived. From this relation, it is clear that the reduction in predicted eddy-viscosity leads to a lower threshold for PANS-SST, compared to PANS-KSKL.

Fig. 4.18 shows the modelled length scales and von Kármán length scale for several f_k values. For PANS-KSKL, the modelled length scale l is one order of magnitude smaller than for PANS-SST. In line with the explanations in Sec. 4.3.1, for the values of f_k which result in a resolved turbulent flow solution, L_{vK} is independent of f_k. $L_{vK}/\delta \approx 0.1$ in the centre, and reduces towards the wall. For higher f_k values, for this test case, theoretically L_{vK} approaches infinity, since due to the steady, laminar, flow solution the denominator goes to zero. In practice, due to the inclusion of limiters, L_{vK} will be bound to $c_{l_2}\kappa d$, which is approximately 0.05 at the channel centre, and decreases linearly to zero at the wall. This shows how the inclusion of L_{vK} allows "*the model to recognize and adjust to already resolved scales in the simulation*" [103]. This property is the foundation of SAS, as investigated in detail by Xu et al. [198]. The effect mostly occurs in unsteady calculations exhibiting separation. This feature is retained when using the model as a sub-filter model in PANS.

The different PANS closure strongly affects iterative convergence behaviour. The convergence is assessed based on the residuals, which are normalised by the diagonal element of the left-hand-side matrix of the linearised system of equations. To compare the convergence behaviour the the relaxation factors were kept constant: 0.2 for momentum, 0.2 for pressure and 0.2 for the turbulence equations. Fig. 4.19 shows the time-averaged convergence of all equations for the first 20 iterations per timestep, using

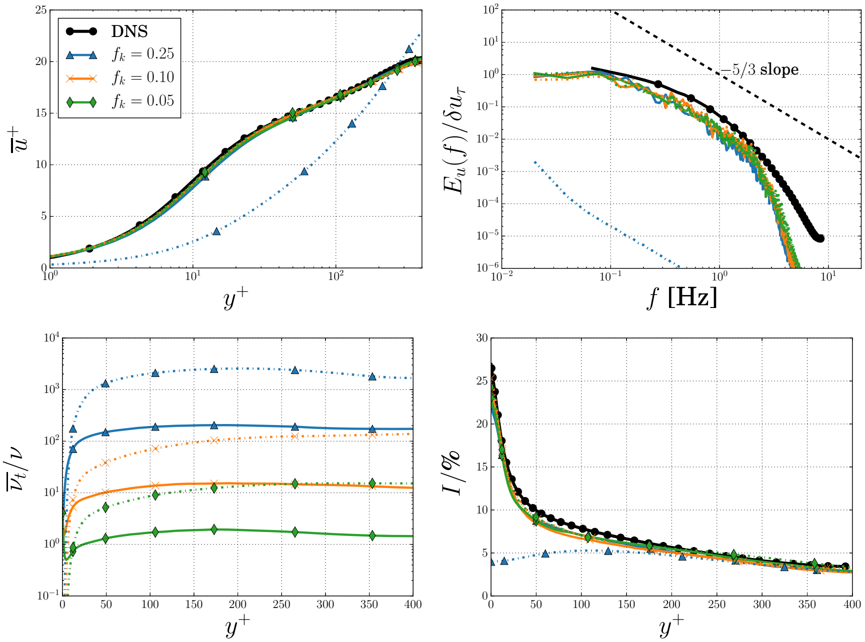

Figure 4.16: Turbulent channel flow. Normalised mean velocity ($\overline{u}^+ = \overline{u}/u_\tau$), turbulence kinetic energy spectra ($E_u(f)$ at $y^+ \approx 20$), eddy-viscosity ratio (ν_t/ν) and turbulence intensity ($\mathscr{I} = \overline{u_i'}/U_b$), using PANS-KSKL (solid lines), PANS-SST (dashed lines) and DNS [169]. From left to right, and top to bottom $\overline{u}^+$, $E_u(f)$ at $y^+ \approx 20$, ν_t/ν and $\mathscr{I}$.

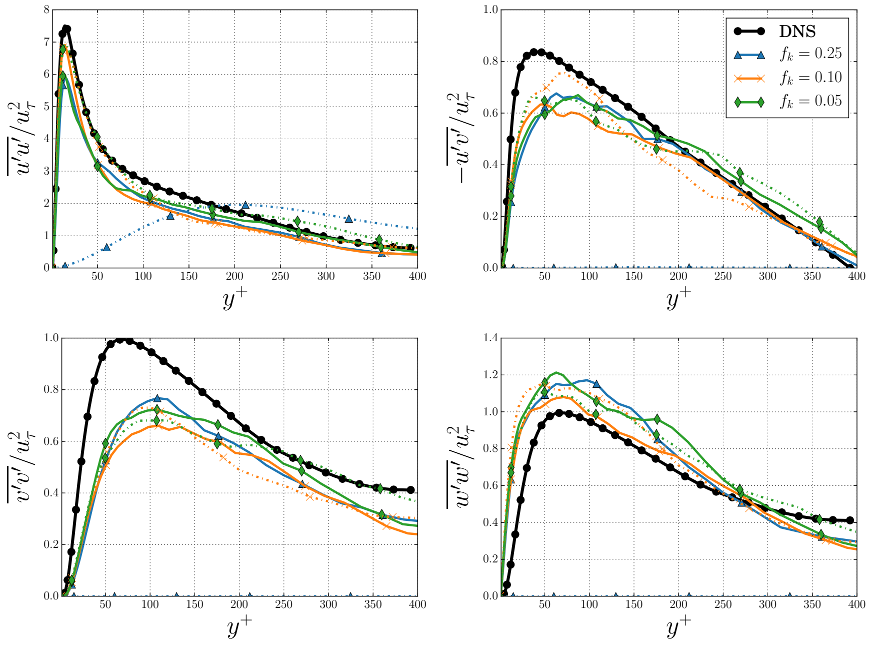

Figure 4.17: Turbulent channel flow. Normalised Reynolds stress profiles ($Re_{ij} = \overline{u'_i u'_j}/u_\tau^2$) using PANS-KSKL (solid lines), PANS-SST (dashed lines) and DNS [169]. From left to right, and top to bottom Re_{uu}, Re_{uv}, Re_{vv} and Re_{ww}.

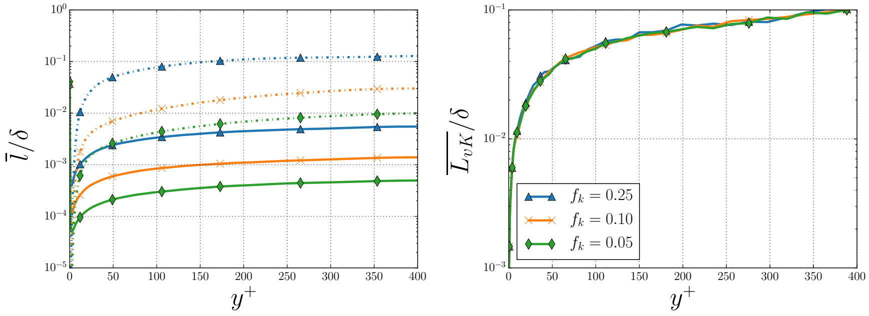

Figure 4.18: Turbulent channel flow. Turbulence integral length scale (left) and von Kármán length scale (right) using PANS-KSKL (solid lines) and PANS-SST (dashed lines).

$f_k = 0.1$, while Fig. 4.20 shows the effect of varying f_k on the convergence of the k and ω and $\sqrt{kl}$ equations. As expected, the convergence of the momentum, pressure and turbulence kinetic energy equations is hardly affected, but the residuals of the second turbulence equation vary significantly. The ω equation for PANS-SST with low f_k stagnates at $L_\infty \approx 10^{-2} - 10^{-3}$, with L_2 being two orders of magnitude lower. For PANS-KSKL, the $\sqrt{kl}$ equation both starts at a lower residual, as well as exhibiting a stronger decay. The equation reaches $L_\infty \approx 10^{-8}$, and is thereby the best converged equation. Using these settings the wall clock time of a typical run time is approximately 5 days on 50 cores (Intel Xeon E5-2660 v3 CPU (10 core) at 2.60 GHz, with InfiniBand communication), this is independent of the choice for turbulence method.

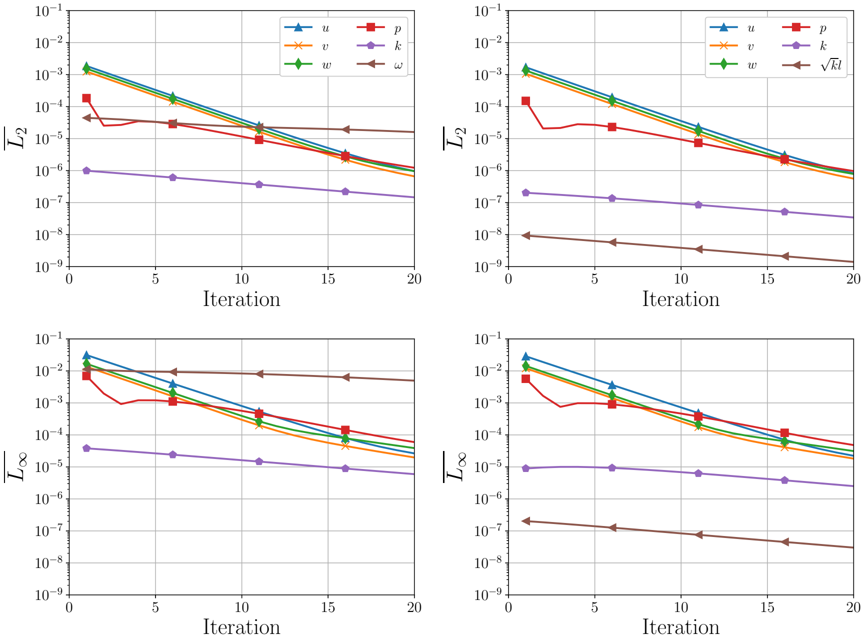

Figure 4.19: Turbulent channel flow. Time-averaged iterative convergence for the different equations, using PANS-SST (left) and PANS-KSKL (right) with $f_k = 0.1$.

Investigating the effect of f_k on the convergence of the turbulence equations (as shown in Fig. 4.20) indicates that reducing f_k (i.e. reducing the effect of the sub-filter model) leads to reduced residuals, both for the k, and the ω and $\sqrt{kl}$ equations. The one exception is the ω equation for $f_k = 0.25$, which shows residuals four orders of magnitude lower than for $f_k = 0.10$ or 0.05. However, as seen in Fig. 4.16 and Fig. 4.17, this simulation predicts an incorrect laminar flow, hence these low residuals are related to the unrepresentative flow field. As shown earlier, the residuals of the $\sqrt{kl}$ equation are on average five orders of magnitude lower than for the ω equation, and – with the exception of the $f_k = 0.05$ case – keep decreasing linearly with an increasing iteration number. These results confirm the expected behaviour that a reduction of f_k (i.e. approaching DNS), leads to a reduction in iterative errors due to the sub-filter turbulence model

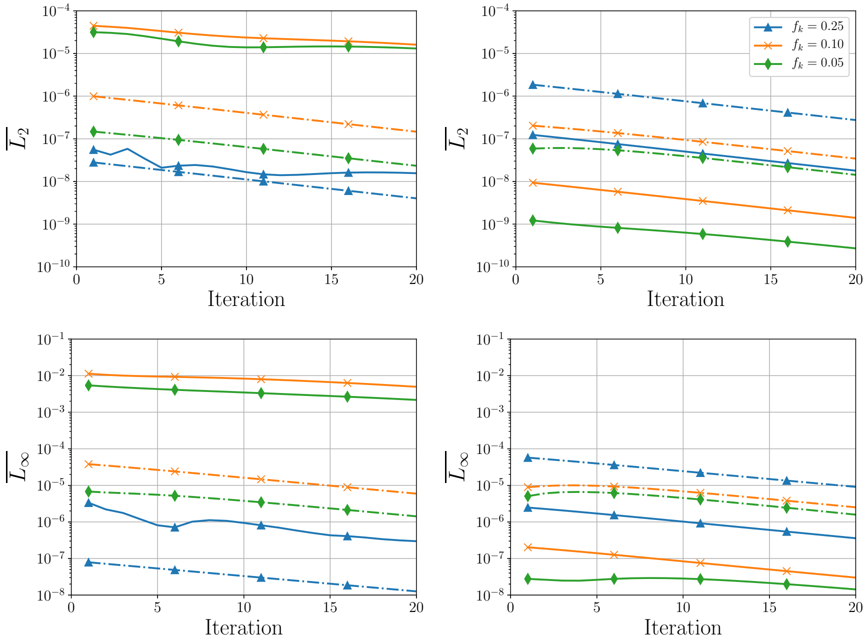

Figure 4.20: Turbulent channel flow. Time-averaged iterative convergence for k (dashed lines), and ω and $\sqrt{k}l$ (solid lines) equations, using PANS-SST (left) and PANS-KSKL (right) for varying f_k.

ELLIPTICAL WING

The second case is an elliptical wing with a NACA66_2-415 cross-section, a root-chord of $c_0 = 0.1256$ m and a wingspan of $b = 0.15$ m, at $Re = U_\infty c_0/\nu = 8.95 \times 10^5$, see Chapter 7. The wing is simulated in wetted and cavitating flow conditions (with a cavitation number $\sigma = \left(p_\infty - p_v\right)/\left(1/2\rho U_\infty^2\right) = 4.2$ and 1.7,respectively) where p_∞ is the far-field pressure and p_v the vapour pressure. The simulations use the ITG to prevent leading edge separation. Turbulent fluctuations are added at $x/c_0 = -2.4$, homogeneous isotropic turbulence is prescribed, resulting in a turbulence intensity at the location of the wing tip of $\mathscr{I}_{tip} \approx 0.4\%$, with an integral length scale of $\mathscr{L}/c_0 = 0.6$ ($\mathscr{L}/r_c \approx 80$). The wall clock time of a typical run time is approximately 7 days on 200 cores (Intel Xeon E5-2660 v3 CPU (10 core) at 2.60 GHz, with InfiniBand communication), this is again independent of the choice for turbulence method.

The time-averaged obtained residuals for PANS-KSKL and PANS-SST for the momentum (u, v, w), pressure (p), vapour volume fraction (α_v) and turbulence equations, are shown in Fig. 4.21. The relaxation factors were 0.25 for momentum, 0.10 for pressure, 0.25 for turbulence and 0.25 for the cavitation equation. The convergence for PANS-SST and PANS-KSKL is similar for momentum, pressure and vapour volume fraction. For PANS-KSKL, the convergence of the turbulence kinetic energy equation is slightly reduced compared to PANS-SST, which has been observed before in the context of RANS predictions for propellers [200], and is likely related to the reduced eddy-viscosity. A reduction in eddy-viscosity reduces diffusion (see Eq. C.12), thereby making the transport equation for k more difficult to solve. The main difference however, occurs again for the second turbulence equation. For PANS-SST, the ω equation stagnates at $\overline{L_2} = 10^{-3}$ with $\overline{L_\infty} = 10^1$. This is a common occurrence for $k-\omega$ models in conjunction with cavitation modelling (see e.g. [190, 201]). In contrast, the $\sqrt{k}l$ equation continues to converge, and within 50 iterations reaches $\overline{L_2} = 10^{-10}$, even when used in combination with the vapour volume fraction transport equation. This demonstrates that the superior convergence behaviour of the KSKL closure is maintained in multiphase flow conditions.

The predicted kinematics of the cavitating tip vortex are analysed at $x/c_0 = 0.5$ downstream of the wing tip. Fig. 4.22 shows the time- and circumferential-averaged profiles of axial ($\overline{u_x}/U_\infty$) and azimuthal velocity ($\overline{u_\theta}/U_\infty$), eddy-viscosity ratio ($\overline{\nu_t}/\nu$), normalised modelled turbulence kinetic energy ($\overline{k}/U_\infty^2$) and normalised second turbulence variable along the radius. Only the azimuthal velocity is compared to data obtained using PIV [43]. The vapour volume fraction and pressure coefficient ($\overline{C_p} = (\overline{p} - p_\infty)/\left(1/2\rho U_\infty^2\right)$) are given in Fig. 4.23. The time-averaged normalised cavity radius (defined based on a vapour volume fraction $\alpha_v = 0.1$) is $r_c/c_0 \approx 0.01$ for both PANS closures.

In wetted flow conditions the PANS-KSKL model predicts a higher axial velocity at the viscous core radius than the PANS-SST model. Both models show a reduction in axial velocity at the vortex core ($r/c_0 \leq 0.05$), which is an indication of increased physics in the simulation. Evidence for this behaviour can be observed in the experimental results reported by Bosschers [13]. The increase in axial velocity towards in the region $r/c_0 \leq 0.02$ is also an improvement compared to the wetted flow results obtained using DDES and IDDES, reported by Liebrand et al. [190]. For those results $\max\left(\overline{u_x}/U_\infty\right) \approx 1.1$, which is a significant underprediction compared to the experimentally observed values. The maximum azimuthal velocity is underpredicted by 20% by both PANS models. In

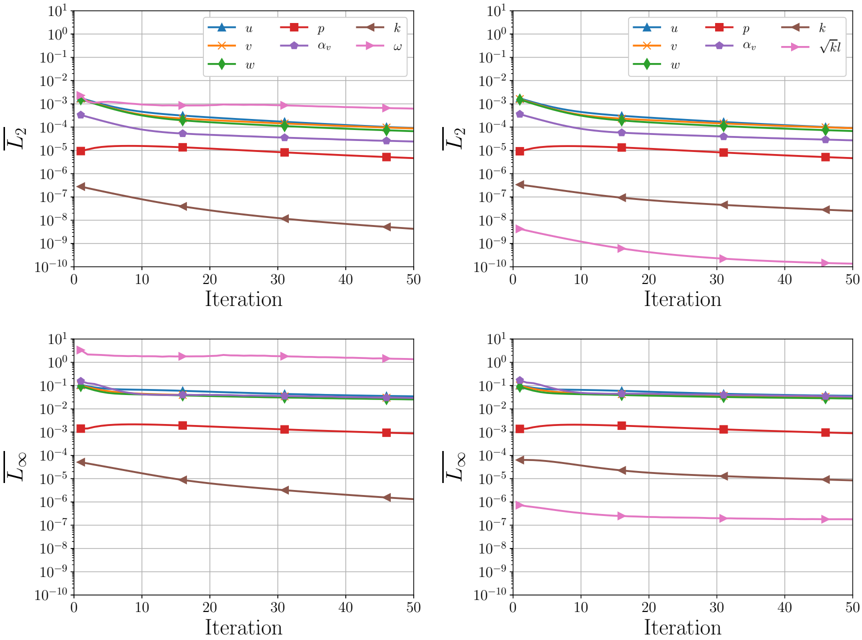

Figure 4.21: Elliptical wing. Time-averaged iterative convergence for the different equations, using PANS-SST (left) and PANS-KSKL (right) with $f_k = 0.1$.

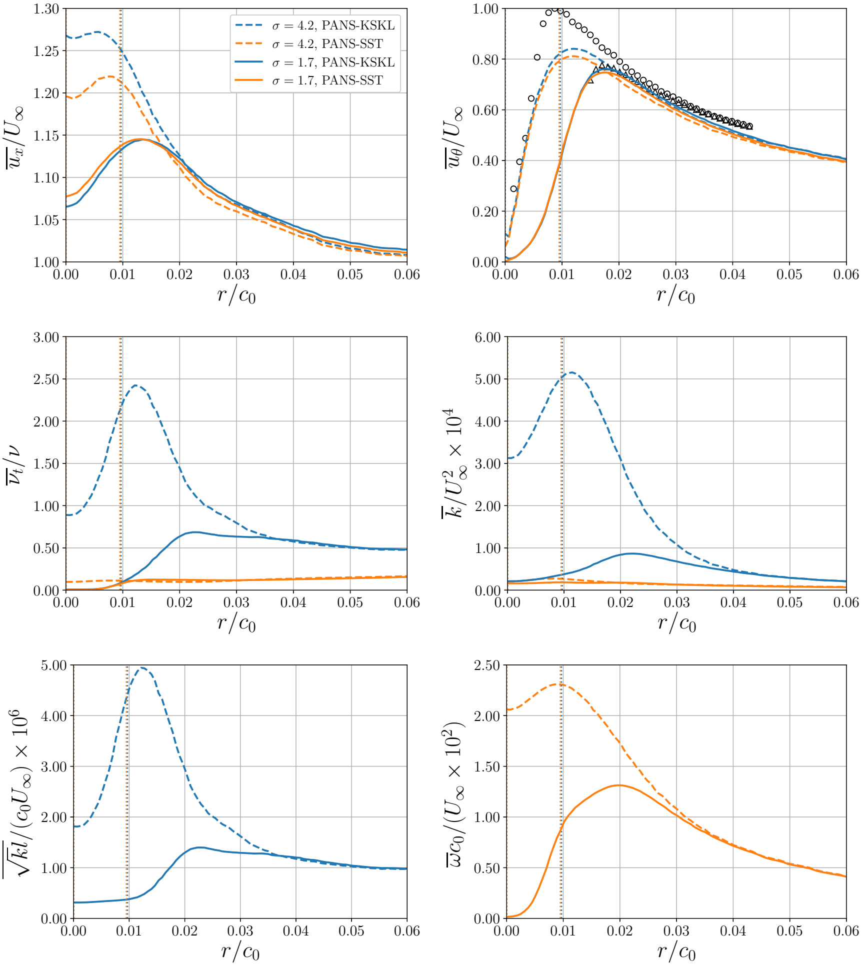

Figure 4.22: Elliptical wing. Radial distribution of time-averaged axial and azimuthal velocity, eddy-viscosity ratio, turbulence kinetic energy and second turbulence variable at $x/c_0 = 0.5$ downstream of the wing tip. Dashed lines indicate wetted flow, and solid lines indicate cavitating flow. Vertical dashed lines correspond to the cavity radius r_c. Experimental data from Pennings, Westerweel, et al. [43].

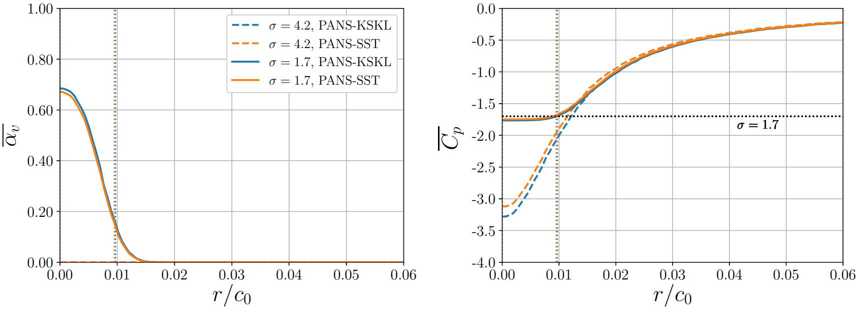

Figure 4.23: Elliptical wing. Radial distribution of vapour volume fraction and pressure coefficient at $x/c_0 = 0.5$ downstream of the wing tip. Dashed lines indicate wetted flow, and solid lines indicate cavitating flow. Vertical dashed lines correspond to the cavity radius r_c.

cavitating conditions, the predicted viscous core radii ($r_v = \arg\max(u_\theta)$) and azimuthal velocity magnitudes match the experimental values. The inclusion of cavitation reduces the axial velocity at the vortex core and increases the viscous core radius, compared to wetted flow.

As expected, the eddy-viscosity levels for $f_k = 0.1$ are orders of magnitude lower than for a full RANS ($f_k = 1.0$) solution (not shown in this work). The inclusion of cavitation reduces the eddy-viscosity to zero inside the cavity radius. In line with the expectations formulated in Sec. 4.3.1, the eddy-viscosity in the far-field predicted by PANS-KSKL – for this f_k – is approximately three times larger than the eddy-viscosity produced by PANS-SST. In wetted flow conditions, the PANS-KSKL eddy-viscosity also shows a large peak at the viscous core radius, which is absent for PANS-SST. Technically, the assumptions of a uniform, steady flow, made in the derivation of eddy-viscosity decay, are not valid in this case, due to the inclusion of synthetic inflow turbulence. Despite this, it does explain the higher ν_t/ν in the far-field. The effect of varying f_k on the eddy-viscosity decay is outside of the scope of this work, but was investigated in Chapter 6 for PANS-SST. It is important to note that for cavitating conditions, at the cavity radius, the eddy-viscosity ratios are similar in magnitude, implying similar cavitation dynamics. Compared to PANS-SST, higher levels of k are observed for PANS-KSKL. The peak in k coincides with the peak in ν_t/ν and is just outside the viscous core radius.

Comparing the values for the second turbulence variable, obtained by two different turbulence closures, is not straightforward, due to the different formulations. For both models, the inclusion of cavitation reduces the magnitude in the region $r/c_0 \leq 0.03$. In line with expectations, PANS-SST predicts high diffusion in the entire field (with the exception of the vortex core). From RANS modelling it is known that the SST model performs poorly in strongly rotating flows, leading to the use of curvature corrections, see e.g. [202]. In contrast, in cavitating conditions, PANS-KSKL shows a constant, low, diffusion inside the cavity radius, with a peak at a higher radius compared to PANS-SST. In wetted flow conditions, there is a large difference in $\sqrt{k}l$ between the vortex core and viscous core radius. This reduction outside the vortex core also occurs for PANS-SST, but the difference in magnitude is significantly smaller, again highlighting the difficulties of applying the SST model for rotational flows.

The PANS-KSKL model predicts a lower pressure coefficient in the vortex core in wetted flow conditions, compared to PANS-SST. This is related to the increased axial velocity. In cavitating conditions, both models show identical pressure profiles, but the vapour volume fraction is slightly higher for the PANS-KSKL model.

Fig. 4.24 shows – for cavitating conditions – the distribution of the instantaneous normalised eddy-viscosity, modelled turbulence kinetic energy and second turbulence values at the same location as Fig. 4.22. The distribution of $\sqrt{k}l$ clearly shows the roll-up process of the vortex. These differences in the second turbulence variables also contribute to the differences in eddy-viscosities. For PANS-KSKL, the eddy-viscosity is defined as the minimum of two terms, $C_\mu^{1/4}\sqrt{k}l$ and $a_1 k/\langle S\rangle$ (see Eq. C.10). Inside the cavity radius, ν_t is defined by term II, due to the high strain rate caused by the rotation, while outside of this radius, it is determined by term I. This can seen by comparing the distributions of ν_t/ν and $\sqrt{k}l$ in Fig. 4.24. In contrast, for PANS-SST, the eddy-viscosity is given by

$$\nu_t = \frac{a_1 k}{\max\left(a_1\omega, \langle S\rangle F_2\right)}. \tag{4.19}$$

As for PANS-KSKL, at the vortex core, ν_t is defined by the second term in the max function, due to the high strain rate caused by the rotation. Further outwards the dissipation rate dominates. The high diffusion rate around the vortex leads to a lower eddy-viscosity.

From these definitions, it is easily observed that the limiters depend on the used f_k value. When the eddy-viscosity in the RANS turbulence kinetic energy length scale and dissipation rate is expressed, the following relations can be obtained:

$$\nu_t = \min\left(C_\mu^{1/4}\frac{f_k^2}{f_\varepsilon}\sqrt{K}L; \frac{a_1 f_k K}{\langle S\rangle}\right) \tag{4.20}$$

for PANS-KSKL, and

$$\nu_t = \frac{a_1 f_k K}{\max\left(a_1\frac{f_\varepsilon\Omega}{f_k}, \langle S\rangle F_2\right)} \tag{4.21}$$

for PANS-SST. Both of the limiters in these functions show a similar trend: with decreasing f_k, the region depending on term II (depending on the strain rate) decreases in size, while the eddy-viscosity in a larger part of the domain is depends on either $\sqrt{k}l$ or ω. Interestingly, the trends are not identical. For PANS-KSKL term I decreases quadratically, and term II linearly; for PANS-SST however, term I decreases linearly, and term II is independent on f_k. This partly explains why the secondary turbulence transport equation for PANS-KSKL (with lower f_k values) is better suited for rotational flows than the ω equation, since the ω equation requires more arbitrary limiting.

4.3.3. CONCLUSIONS

A new PANS closure has been derived based on the KSKL model. Simulations using low f_k values show that the favourable properties of decreased eddy-viscosity and improved iterative convergence exhibited by the KSKL model compared to $k-\omega$ models are carried over to the PANS model. It is shown that the improvement in iterative convergence

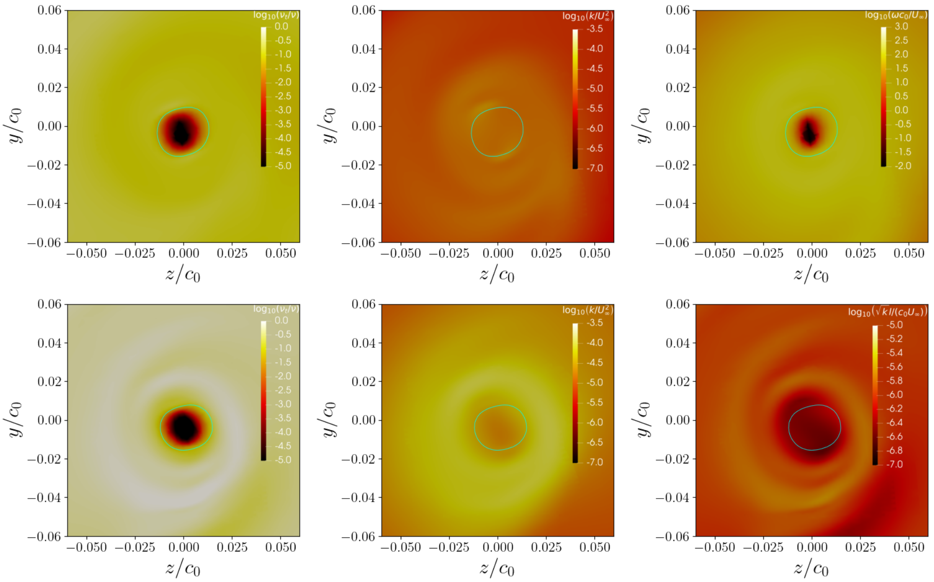

Figure 4.24: Elliptical wing. Instantaneous ν_t/ν, k and $\sqrt{k}l$ or ω, for PANS-SST (top row) and PANS-KSKL (bottom row), at $x/c_0 = 0.5$ downstream of the wing tip. The cavity radius, $\alpha_v = 0.1$, is indicated in cyan ($r_c/c_0 \approx 0.01$).

holds for multiphase flows, for which the ω equation is well known for being difficult to converge, making this model suitable for cases such as simulating cavitation dynamics and underwater radiated noise. In common engineering practice, higher f_k values than those values used in this work might be more typical, although the benefits demonstrated here are expected to be maintained, since they largely derive from the parent RANS model. It was also shown – theoretically and numerically – that the PANS-KSKL model exhibits a low decay of eddy-viscosity downstream of the inlet boundary condition for $f_k < 1.0$, potentially simplifying practical application compared to the PANS-SST model. The influence of f_k on the decay of the eddy-viscosity prescribed at the inlet, and the effect this has on the results, requires further numerical investigation.

4.4. CONCLUSIONS

Two questions concerning the use of PANS were investigated, both related with how to select the input parameters, f_k and f_ε. Based on the results for a channel flow and a circular cylinder, it is concluded that the most reliable results can be obtained with $f_\varepsilon = 1.0$, i.e. the high Reynolds number approach, and with a *Constant, a priori* determined, f_k. These settings will be used in the remainder of this thesis.

A new PANS-KSKL model is derived, investigated and tested. For several flows in the remainder of this thesis, this model will be applied.

5

TURBULENT CHANNEL FLOW AT $Re_\tau = 395$

Different variable resolution turbulence modelling approaches (hybrid, bridging models and LES) are evaluated for turbulent channel flow at $Re_\tau = 395$*, for cases using either streamwise periodic boundary conditions or the inflow turbulence generator (ITG). The effect of iterative, statistical and discretisation errors is investigated. For LES, little difference between the different sub-filter modelling approaches is found on the finer grids, while on coarser grids ILES deviates from explicit LES approaches. The results for hybrid models are strongly dependent on their formulation, and the corresponding blending between the RANS and LES regions. The application of PANS with different ratios of modelled-to-total kinetic energy,* f_k*, shows that there is no smooth transition in the results between RANS and DNS. Instead, a case-dependent threshold which separates two solution regimes is observed:* f_k *values below* 0.2 *yield a proper turbulent solution, similar to LES results; higher* f_k *values lead to a laminar flow due to filtering of the smallest scales in the inverse energy cascade. The application of the ITG is observed to yield similar performance for all models. The reduced computational cost and increased flexibility makes it a suitable approach to enable the usage of SRS for industrial flow cases which depend on the development of a turbulent boundary layer. It ensures that sufficient large-scale structures develop over the full boundary layer height, thereby negating the problem of relying on the inverse energy cascade for the development of turbulence. Both LES and PANS with ITG yield a better match with the reference data than hybrid models; of these methods PANS is preferable due to the separation of modelling and discretisation errors.*

5.1. INTRODUCTION

Linked to the increased physics in SRS is the requirement of more physical inflow boundary conditions. It has been repeatedly shown that the results of LES or DNS can be dependent on inflow conditions, e.g. [26, 27]. For SRS of turbulent flows which do not

---

This chapter has been published in Computers & Fluids **209**, 104636 (2020) [193].

exhibit strong separated vortical structures, it is necessary that the inflow contains time-varying fluctuations which resemble turbulence. If this is not addressed, laminar [1] solutions can be obtained, and consequently integral quantities, such as mean forces, can be underpredicted [29]. For attached, weakly unsteady flows, unphysical laminar separation may occur easily since transition to turbulence is significantly delayed. Ironically, this implies that for computing mean forces RANS methods often yield the best results for such flows. Hybrid methods also better predict mean forces, due to the use of RANS inside the boundary layer, resulting for example in superior prediction of velocity gradients close to the wall, when using steady inflow. However, at the interface between RANS and LES regions not all the modelled turbulence is transferred directly into resolved turbulence, leading to an overly laminar flow field. In such cases, inflow turbulence might still be necessary. While this problem has been known for a number of years, many publications using SRS still do not apply a proper inflow. These works often focus on turbulent structures and dynamics which appear satisfactory, yet the forces simultaneously show a large mismatch with experimental data. This discrepancy in integral quantities leads to difficulties in the validation of numerical results, and deteriorates the credibility of SRS for practical applications. Currently, the need for synthetic turbulence generation hampers the usage of SRS for industrial cases, such as cavitation and noise research for ship propellers.

Inflow turbulence can be generated either by precursor methods (such as a channel flow), or by synthetic methods, which do not rely on flow recycling. Precursor methods are generally noted for their accuracy, although they are more expensive to use due to the need to generate turbulence in a second, separate, domain. Their use is also often limited to canonical flows. Synthetic methods are cheaper to use, easier to tune to a desired set of turbulent inflow statistics, and more generally applicable [28]. These properties make a synthetic method preferable for industrial CFD, despite the requirement of a development length to allow the introduced fluctuations to develop into 'real' turbulence. In the case of cavitation and noise prediction, a further requirement is that the inflow velocity fluctuations are divergence-free, thereby avoiding spurious pressure fluctuations which can pollute the entire domain for incompressible computations.

It is well known that the choice of SRS model affects the flow prediction around the object of interest, although a subject less well addressed in the literature is the model interaction with the propagation of inflow turbulence. Consequently, an evaluation of different SRS methods in combination with inflow turbulence is necessary. This chapter attempts to provide a systematic overview of the effect of SRS turbulence modelling approaches, both with streamwise periodic boundary conditions and with the ITG. Full comparisons between different SRS approaches, including higher order moments, are rare in literature [184]; often, different codes, grids and solver settings are used, which makes it difficult to assess the modelling error of the turbulence modelling approaches. Models included in this chapter are hybrid (DDES [53], IDDES [203]) and XLES [104]); bridging (PANS [51] with $f_k \in [0.05, 1.00]$); and LES (Smagorinsky [47], Lilly [108, 109], WALE [111], KSGS [112] and ILES). Attention is paid to the assessment of iterative, discretisation and statistical errors.

---

[1] In this context laminar flow is defined as the absence of resolved velocity fluctuations, i.e. the Reynolds stresses $Re_{ij} = \overline{u'_i u'_j}/u_\tau^2 \approx 0$.

The chosen test case is a turbulent channel flow at $Re_\tau = 395$, a canonical test case for the study of wall-bounded turbulence, due to the simple geometry and abundance of reference data. Experimental results are first published ninety years ago, and numerical studies have been performed using LES and DNS since the 1980s. Fig. 5.1 shows an overview of numerical results available in the open literature. It is observed that a range in total number of grid cells is applied for LES/DNS approaches at lower Re_τ values. DES and PANS results have been published for significantly higher Re_τ, but often without refining the grid. Most results shown are obtained using a finite volume approach, with second-order accurate discretisation schemes. Fig. 5.1 also shows an overview of the usage of synthetic turbulence generation methods available in the open literature, sorted per test case.

In this chapter, Sec. 5.2 describes the test case, numerical setup and turbulence-generating method. After an assessment of the numerical errors in Sec. 5.3, the results for hybrid, bridging and LES approaches using streamwise periodic boundary conditions (i.e. flow recycling) and the ITG are compared in Sec. 5.4 and 5.5, respectively. Finally, Sec. 5.6 discusses the implications of the results for industrial test cases, followed by the conclusions in Sec. 5.7.

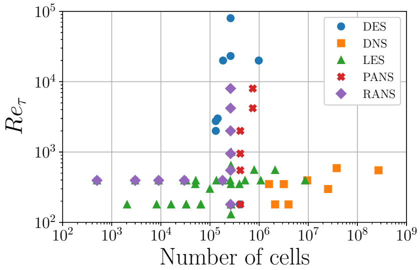

Test case	DFM	FSM	FM	SEM
Decaying homogeneous	1	1	2	2
Channel flow	5	1		4
Airfoil	1		1	
Airfoil trailing edge				1
Square duct				1
Plane jet	1			
Staggered cube array	1			

Figure 5.1: Literature overview with a selection of the available numerical results. Turbulent channel flow results (left) as function of the number of grid cells, N_c, and the turbulence modelling approach (left) [169, 171, 204–216]. Usage of synthetic turbulence generation (right) sorted by test case and method (Digital Filtering (DFM), Forward Stepwise (FSM), Fourier (FM) and Synthetic Eddy method (SEM) [26, 27, 124–126, 217–223].

5.2. NUMERICAL SETUP AND SOLVER

Computations are made using a rectangular domain, with two no-slip walls oriented normal to the y-direction and periodic boundary conditions in spanwise direction. (see Fig. 5.2). The remaining boundaries are either connected using periodic boundary conditions in order to approximate an infinite channel; or alternatively, an inflow and outflow boundary condition is specified if the ITG is applied. Cartesian grids with hyperbolic tangent clustering towards the walls are used, as described in Sec. 5.3.3. The non-dimensional time step for the grid used for comparing turbulence modelling approaches, *G4*, is $\Delta t^* = 1/2 u_\tau \Delta t/\delta \approx 1 \times 10^{-3}$. This leads to $\Delta t^+ = u_\tau^2 \Delta t/\nu \approx 0.08$ and a maximum Courant number below 0.2 (2000 time steps per flow-through time). To maintain the proper bulk and friction Reynolds numbers, $Re_b = U_b 2\delta/\nu$ and $Re_\tau = u_\tau \delta/\nu$ respectively, a body-force is applied which is proportional to the streamwise pressure gradient

$\mathrm{d}p/\mathrm{d}x = -\tau_w/\delta$, with $\tau_w = \rho u_\tau^2$ [52].

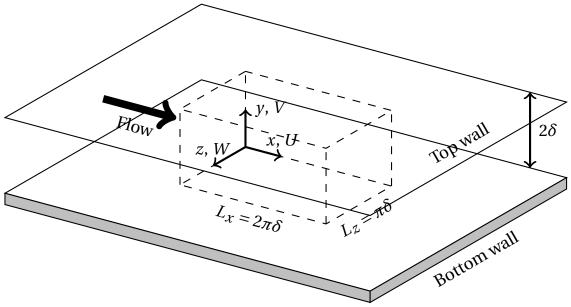

Symbol	Value
δ [m]	0.1
U_b [m/s]	6.928×10^{-2}
u_τ [m/s]	3.966×10^{-3}
τ_w [N/m^2]	1.570×10^{-1}
ν [m^2/s]	1.004×10^{-6}
Re_τ	395
Re_b	13 800

Figure 5.2: Schematic overview of the domain and physical parameters. The dashed lines indicate the computational domain. The figure is based on the drawing of de Villiers [171].

For the simulations reported here time integration is performed using a second-order implicit three time level scheme, and the convection terms in the momentum equations are discretised using a second-order accurate central differencing scheme (the Péclet number has a magnitude of $\mathcal{O}(10)$). An investigation into the effect of the convection scheme for the momentum equation can be found in Sec. 5.3.3. The turbulence equations are discretised using a first-order upwind scheme. Due to the fine grid resolution employed, the effect of discretisation on the sub-filter stresses is limited.

The use of scale-resolving turbulence methods for a turbulent channel yields a so-called supercritical laminar solution for which many flow-through times are needed to trigger transition to the turbulent regime [171]. To this end in the current work to speed up the transition, the method suggested by Schoppa and Hussain [172] is used. This method is only applicable to cases where periodic boundary conditions can be used, and is tuned for a turbulent channel flow; it is therefore not a general approach. The flow is initialised as a laminar parabolic flow profile, u_0^+, on which near-wall parallel streaks of slower and faster moving fluid are superimposed according to the equation

$$u^+\left(y^+,z^+\right) = u_o^+\left(y^+\right) + \frac{\Delta u_0^+}{2}\cos\left(\beta^+ z^+\right)\frac{y^+}{30}\exp\left(-\sigma y^{+2}+0.5\right)\cdot(1+0.2X). \tag{5.1}$$

Here Δu_0^+ is the streak's normal ($y-$ direction) circulation per unit length, taken as $1/4U_b$, $\beta^+ = 2\pi/z^+$ is the spanwise wave number, chosen to produce a sparse streak spacing ($z^+ \approx 200$), $\sigma = 0.00055$ and X is an added random signal, $X \in [0,1]$, to enhance symmetry breaking. To generate instabilities, based on linear stability analysis the streaks are perturbed according to the relation

$$w^+\left(y^+,z^+\right) = \varepsilon\sin\left(\alpha^+ x^+\right)y^+\exp\left(-\sigma y^{+2}\right)\cdot(1+0.2X), \tag{5.2}$$

with a linear perturbation amplitude $\varepsilon = U_b/200$ and an axial wave number $\alpha^+ = 2\pi/500$.

5.3. NUMERICAL ERRORS

The input error is assumed to be negligible due to the well controlled conditions in the computations, and either the periodic nature of the solution, or the reliability of the DNS results reported in the open literature. The round-off error is negligible due to the use of double precision arithmetic. Therefore, in this chapter, only the iterative, discretisation and statistical error are assessed.

The results are obtained along a line perpendicular to the wall at the centre of the channel (see Sec. 5.3.2). Computations are performed using grid *G4* (see Sec. 5.3.3) and using PANS ($f_k = 0.10$) unless indicated otherwise. Only half the channel height is shown.

5.3.1. ITERATIVE ERROR

The iterative convergence is assessed based on the residuals, normalised by the diagonal element of the left-hand-side matrix of the linearised system of equations. This is of particular interest since if the iterative error would be of the same order of magnitude as the turbulence fluctuations, the results would be strongly affected. Despite this, the influence of iterative error is rarely studied in the open literature. Following the approach advocated by Eça, Vaz, et al. [154], a PANS computation with $f_k = 0.10$ was performed using different iterative convergence criteria ($L_2 = 10^{-3}$, 10^{-4}, 10^{-5}, 10^{-6}, 10^{-7} and 10^{-8}). The effect on the mean velocity ($\overline{u}^+$), Reynolds stresses ($Re_{ij} = \overline{u'_i u'_j}/u_\tau^2$) and turbulence kinetic energy spectra ($E_u(f)$ at $y^+ \approx 20$) along a wall-normal line at the centre of the domain is shown in Fig. 5.3. For values of $L_2 = 10^{-3}$ and 10^{-4}, the mean velocity shows an underprediction in the buffer layer ($5 < y^+ < 30$), while for $L_2 \leq 10^{-5}$ the results are converged. The Reynolds stresses and spectra also show a large mismatch with the reference data for $L_2 = 10^{-3}$ and 10^{-4}. The magnitude of the peak value Re_{uu} and the turbulence kinetic energy spectra converge for stricter convergence criteria. As a compromise between cost and accuracy, the criterium $L_2 = 10^{-6}$ is used in the remainder of this chapter. Applying this criterium leads to a residual of $L_\infty = 10^{-5}$ in each time step for momentum; the residuals for pressure and turbulence equations are at least one order of magnitude smaller. In this manner, the iterative error is smaller than the turbulence fluctuations of interest.

5.3.2. STATISTICAL ERROR

A potentially dominating error in unsteady and especially turbulence resolving simulations is the statistical error. In order to remove the start-up effects and estimate the magnitude of this source of uncertainty, the Transient Scanning Technique (TST) is employed [160]. This technique allows an estimation of the statistical uncertainty based on a signal of finite length. The uncertainty is expanded to obtain a 95% confidence interval. The TST is applied to the velocity signals and Reynolds stresses at measurement points along the height of the channel. Based on the TST, it is found that the first 11 flow-through times (≈ 30000 time steps) must be removed to eliminate the start-up effects. This conclusion is independent of the wall-normal distance of the measurement point. In the remainder of this chapter, the mean values are then computed based on approximately 45 flow-through times, resulting in a statistical uncertainty for the mean streamwise velocity below 2%, and for the Reynolds stress components below 10%.

These uncertainties are in agreement with the sampling errors as obtained from the engineering approaches suggested by Ries et al. [224]. The estimates of the sampling

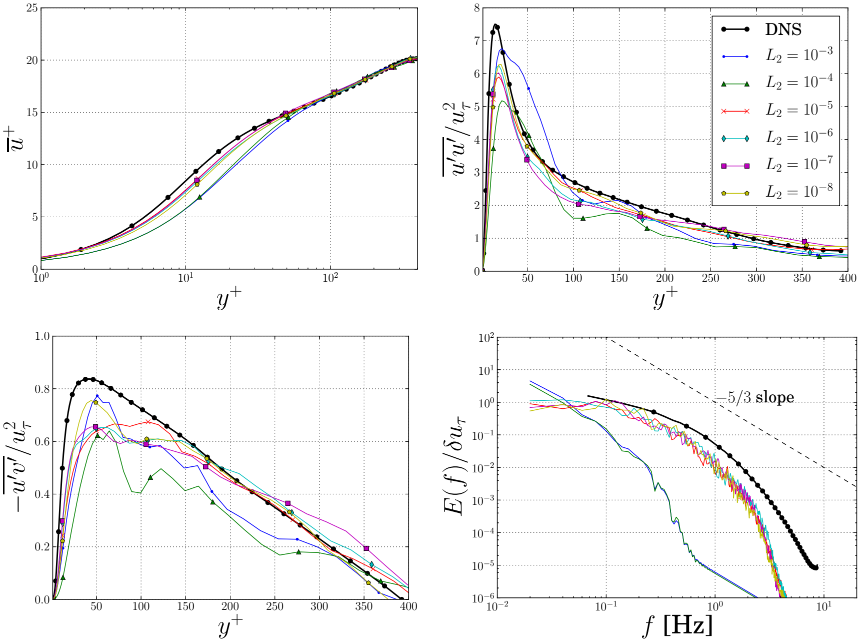

Figure 5.3: Mean velocity ($\overline{u}^+$) profiles, Reynolds stress (Re_{uu} and Re_{uv}) profiles and turbulence kinetic energy spectra ($E_{u,y^+\approx 20}(f)$) using different iterative convergence criteria.

error e for $\overline{u}^+$, u' and u^2_{rms} are given as:

$$e = \sqrt{\frac{2\delta I^2}{U_b t_{av}}}, \qquad e = \sqrt{\frac{\delta}{U_b t_{av}}} \qquad \text{and} \qquad e = \sqrt{\frac{4\delta}{U_b t_{av}}}. \tag{5.3}$$

Here t_{av} indicates the averaging time and I the turbulence intensity $I = u'/\overline{u}$. These estimates give sampling errors of 1%, 5% and 10% for $\overline{u}$, u' and u'^2 respectively when applied to the results of the present study.

In order to reduce these errors more flow-through times should be computed. It must be noted that in literature spatial averaging is often applied to the results since the flow is statistically homogeneous [224]. In this way a low statistical uncertainty is achieved using fewer flow-through times. However this implies that the flow is statistically converged in the entire domain, but not at every location. In this chapter spatial averaging is explicitly not applied, to ensure a statistically converged solution at all locations, and to properly compare with results obtained with the ITG.

5.3.3. DISCRETISATION ERROR

In order to assess the discretisation error, four different grids (with refinement ratios $r_i = h_i/h_1 = \Delta t_i/\Delta t_1 = 1.00$, 1.25, 1.57 and 1.97) were employed. Details of the grids are given in Tab. 5.1. The grid designated *G4* is equal to the one used for the DNS reference data [169]. Note that all these grids are well within LES guidelines, in terms of wall resolution, found in literature, and have resolutions typical of DNS [55, 225]. It is commonly assumed in literature, when grids with DNS resolution, in conjunction with second-order schemes, are used for LES, that discretisation errors are negligible and do not have to be assessed. However, discretisation errors depend on both the number of cells and the accuracy of the schemes employed, and assessment of these errors is still necessary.

The effect of grid refinement is shown in Fig. 5.4. Both the mean velocity and Reynolds stresses appear reasonably insensitive to grid resolution, however Re_{uu} and Re_{uv} deviate slightly on the finest grid. The main differences are observed for the turbulence kinetic energy spectra. Grid refinement leads to a slightly increased cut-off frequency, since the smaller cells allow for higher wavenumbers to be resolved. This indicates that the employed f_k (0.10) is below the grid cut-off, i.e. the grid and numerical settings do not result in DNS resolution. Nevertheless, based on the similarity between the results it is concluded that the coarsest grid has a sufficient resolution. For this reason, grid refinement for the LES models was not pursued, since due to the fine grid resolution, little effect of the sub-filter model is expected. Instead, to compare the effect of grid resolution on the sub-filter modelling, grid coarsening was performed. To this end, two additional grids (with refinement ratios $r_i = 2.63$ and 3.97) are employed, in combination with PANS ($f_k = 0.10$), LES KSGS and ILES. Fig. 5.5 shows that even the coarsest grid still has sufficient resolution to predict the mean velocity profiles well, in the cases of PANS and ILES. For Re_{uu} both ILES and PANS overpredict the peak near the wall, especially on coarser grids. This overprediction is absent for LES KSGS, due to the sub-filter model. On finer grids however, the peak is underpredicted, indicating that the SGS is too dissipative. The peak on the coarsest grid is also shifted away from the wall. For Re_{uv}, again LES KSGS predicts the magnitude better on a coarse grid than ILES and PANS. This difference is absent on finer grids. In terms of turbulence kinetic energy spectra, it is clear that grid refinement leads to an increase in energy at higher frequencies, i.e. the cut-off frequency increases. The effect of the sub-filter model is also clear for LES KSGS, the cut-off on all grids being at a lower frequency than for ILES and PANS. This effect is most significant on the coarsest grid.

To conclude, the grid designated *G4* has a sufficient resolution to be able to compare the different models. Grid coarsening shows that, although the results obtained by ILES appear reasonable, the absence of a sub-filter model can lead to an overprediction of turbulent stresses on coarse grids. In addition, similarity in results indicates that PANS with a low f_k is comparable to LES without a sub-filter model (ILES).

Table 5.1: Details of used grids. r_i ($= h_i/h_1 = \Delta t_i/\Delta t_1$) indicates the refinement ratio , N the number of cells in different directions, Δy_1 the initial wall-normal spacing, $x^+ = u_\tau \Delta x/\nu$, $y^+ = u_\tau \Delta y/\nu$ and $z^+ = u_\tau \Delta z/\nu$ the average non-dimensional wall units in different directions and the maximum Courant number, Co_{max}.

Grid	r_i	N_x	N_y	N_z	$N/10^6$	$\Delta y_1 \cdot 10^4$	x^+	y^+	z^+	Co_{max}
G6	3.97	63	47	47	0.14	2.1	24	0.2	20	0.07
G5	2.63	95	71	71	0.48	1.4	16	0.13	13	0.12
G4	**1.95**	**127**	**95**	**95**	**1.18**	**1.0**	**12**	**0.10**	**10**	**0.20**
G3	1.56	159	119	119	2.30	0.8	9.6	0.08	8	0.21
G2	1.25	199	149	149	4.50	0.6	7.7	0.06	6.4	0.22
G1	1.0	249	187	187	8.84	0.5	6.1	0.05	5.1	0.25

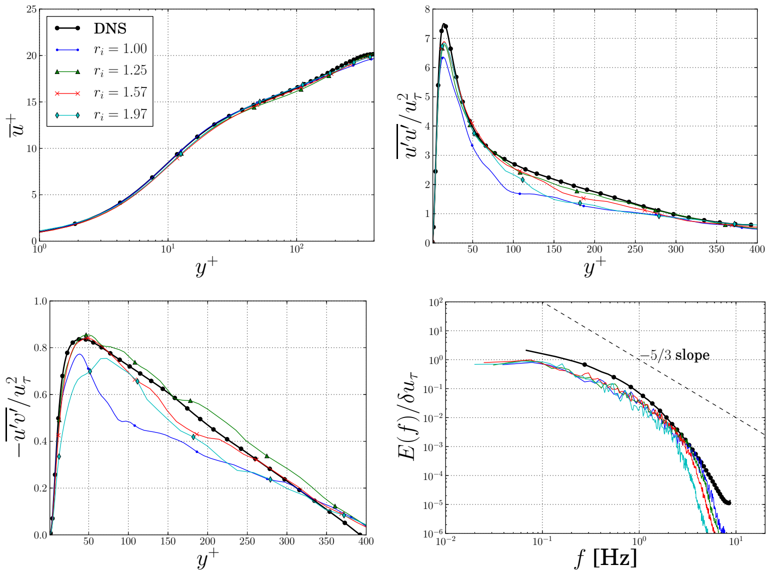

Figure 5.4: Mean velocity ($\overline{u}^+$) profiles, Reynolds stress (Re_{uu} and Re_{uv}) profiles and turbulence kinetic energy spectra ($E_{u,y^+\approx 20}(f)$) using different grids and PANS ($f_k = 0.10$).

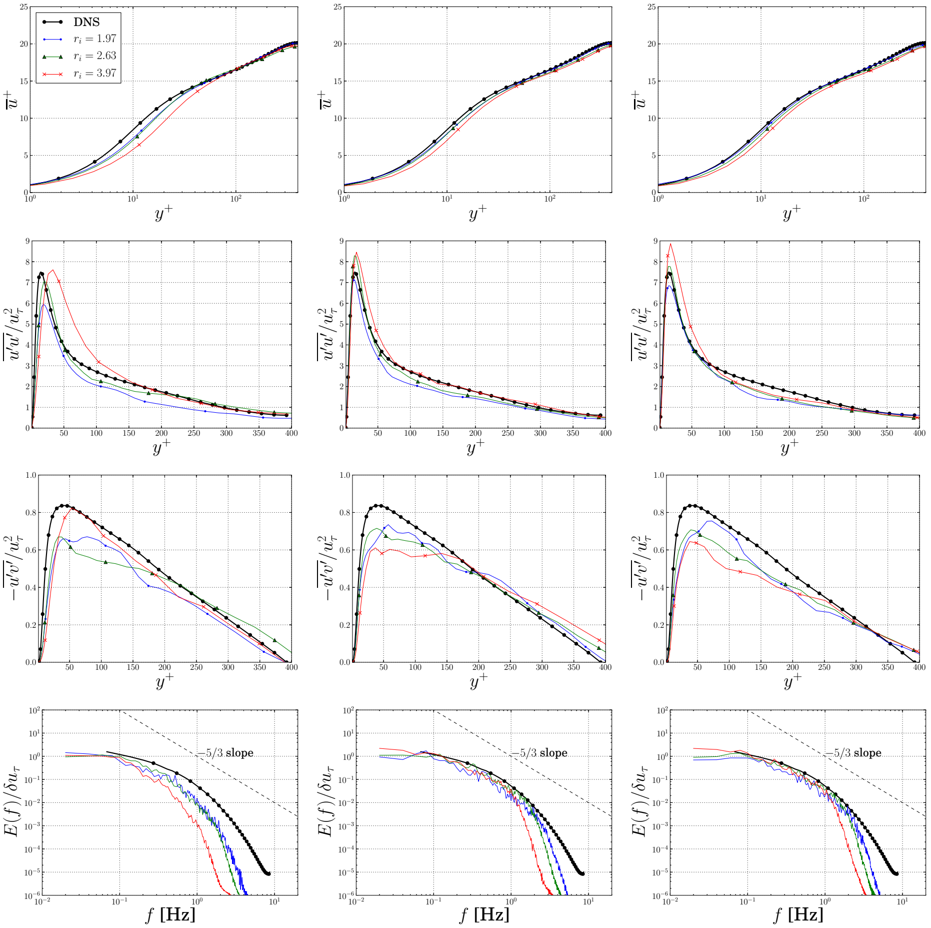

(a) LES KSGS (b) ILES (c) PANS ($f_k = 0.10$)

Figure 5.5: Mean velocity ($\overline{u}^+$) profiles, Reynolds stress (Re_{uu} and Re_{uv}) profiles and turbulence kinetic energy spectra ($E_{u,y^+\approx 20}(f)$) using different grids.

A second source of discretisation error is the discretisation of the convection terms in the equations. Due to the use of a unstructured finite volume CFD code, users are limited to second-order accurate schemes. For the Reynolds number studied here, the discretisation of the momentum equations is dominant. Basara et al. [226] investigated blended upwind-CD schemes for finite volume LES and hybrid methods. They state that 'results obtained with a blending factor lower than 0.98 or 0.96 are treated as suspicious', and that the use of a second-order accurate Central-Differencing scheme is preferred. However in industrial high Reynolds number flows this is often not possible, meaning that (lower-order) upwinding, or blended schemes are used [226]. In order to investigate this effect, the convection scheme for the momentum equation is varied between First Order Upwind (FOU), Central Differencing (CD), a blended upwind-CD with a blending factor of 0.5 (FOU-CD) and the approximately second-order QUICK (Quadratic Upstream Interpolation for Convective Kinematics [227]) scheme. The investigation is performed for ILES, LES KSGS and PANS with $f_k = 0.10$. The computations are deliberately performed on the coarser grid *G6* to highlight the difference between different convection schemes and different sub-filter models [226]. These differences are expected to be smaller on finer grids. The non-dimensional time step $\Delta t^* = u_\tau \Delta t / 2\delta \approx 2 \times 10^{-3}$ leads to $\Delta t^+ = u_\tau^2 \Delta t / \nu \approx 0.5$ and a maximum Courant number of 0.1.

Fig. 5.6 shows the normalised mean velocity ($\overline{u}^+$) and Reynolds stress profiles (Re_{uu} and Re_{uv}), together with the turbulence kinetic energy spectra $E(f)$. In terms of velocity profiles, the CD scheme yields the best match with the reference data for all turbulence approaches. The QUICK scheme captures the trend, but overpredicts the velocity in the range $0.1 < y/\delta < 0.4$ and underpredicts the velocity in the outer layer ($y^+ > 50$), especially for the PANS model. FOU clearly yields a laminar, parabolic, velocity profile. Both the mean velocity and Reynolds stresses indicate that FOU and FOU-CD yield no fluctuations, i.e. a laminar flow; CD and QUICK yield a turbulent solution. Generally the magnitude of the Reynolds stresses are larger for QUICK than for CD. Finally the spectra are compared. Due to the laminar flow predicted using FOU and FOU-CD the energy contained in the spectrum is much lower for all models. Both CD and QUICK show the correct shape, but for all models CD contains more energy across the entire frequency range. There appears to be little difference between ILES and PANS. The spectrum for LES KSGS shows a cut-off at a lower frequency, since part of the turbulence is modelled by the sub-filter model.

To conclude it is clear that for all SRS, first order schemes add too much discretisation error and lead to a mismatch in flow profile. Fully second-order schemes yield the best results, while using QUICK (a commonly used scheme in industrial applications), reasonable results are obtained. With a QUICK scheme less energy is resolved than by the CD scheme, which is in line with literature [216, 228]. In the remainder of this chapter the convection terms in the momentum equation are discretised using a second-order accurate CD scheme. For industrial cases the application of CD is typically not possible, due to high local cell Péclet numbers [90], although reasonable results can still be obtained using QUICK.

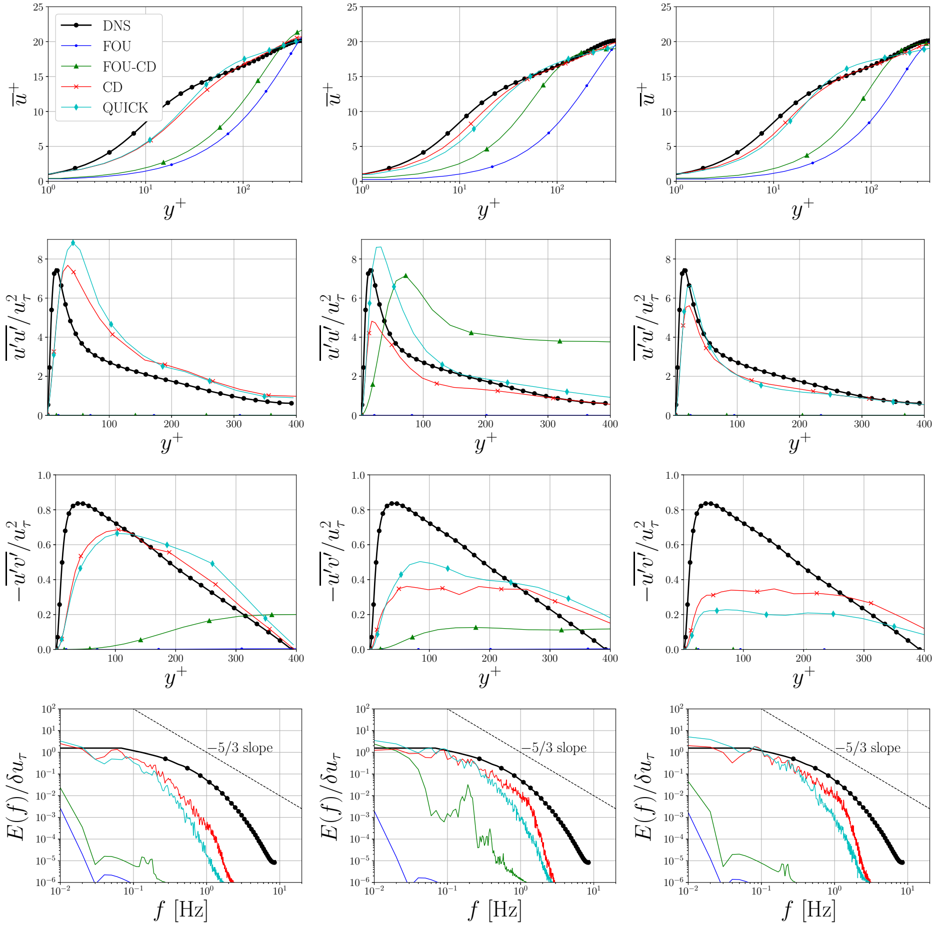

(a) LES KSGS

(b) ILES

(c) PANS ($f_k = 0.10$)

Figure 5.6: Comparison of normalised mean velocity ($\overline{u}^+$), Reynolds stress (Re_{uu}) profiles and turbulence kinetic energy spectra ($E_{u,y^+\approx 20}(f)$) using different convection schemes for the momentum equations.

5.4. TURBULENCE APPROACHES WITH FLOW RECYCLING

5.4.1. LES

Fig. 5.7 shows the mean velocity profiles, Reynolds stresses and turbulence kinetic energy spectra of the streamwise velocity at $y^+ \approx 20$. The mean velocity profiles for all models capture the trend of the DNS data. In terms of Reynolds stresses, it is clear that all models capture the trend, but deviate in terms of magnitude. The highest Reynolds stress terms are generally obtained for the ILES and KSGS, followed by the Smagorinsky, Lilly and WALE model. The Lilly model performs adequately for Re_{uu}, but underpredicts Re_{uv}, Re_{vv} and Re_{ww}. For all models the magnitude of the Reynolds stress terms is generally underpredicted, with Re_{ww} an exception. For Re_{vv}, the peak is shifted towards the right for all models indicating that the strongest turbulence fluctuations occur further from the wall. The turbulence kinetic energy spectra for the LES models are comparable, although as shown in Sec. 5.3.3 this is grid dependent. For the resolution employed here, there is little difference between the models. Only ILES shows a slightly higher cut-off frequency due to the absence of a sub-filter model. Generally it appears that ILES yields the best results, which has been observed before for a channel flow on a fine grid. This is related to excessive diffusion and non-monotonic grid convergence for LES, i.e. on fine grids ILES can give better results than LES with a sub-filter model [229, 230].

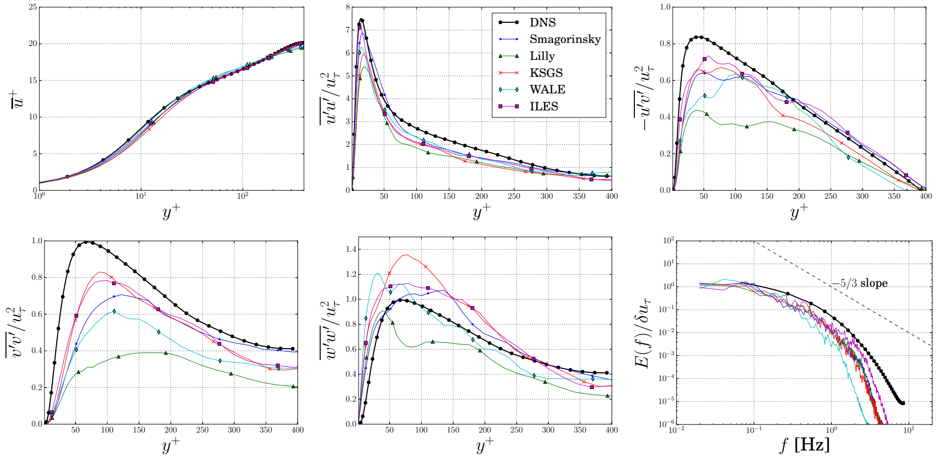

Figure 5.7: Normalised mean velocity and Reynolds stress profiles and turbulence kinetic energy spectra using LES and DNS [169]. From left to right, and top to bottom $\overline{u}^+$, Re_{uu}, Re_{uv}, Re_{vv}, Re_{ww} and $E_{u,y^+\approx 20}(f)$.

Turbulent structures in the flow are visualised in Fig. 5.8, using iso-contour plots of Q, based on the instantaneous flow field. Q is defined as $Q = 1/2\left(|\langle\Omega\rangle| - |\langle S\rangle|\right)$, with $\langle\Omega\rangle$ defined as the anti-symmetric part of ∇u, representing local flow rotation [231]. The iso-contours and the sides of the domain are coloured by the normalised streamwise velocity ($u^* = u/U_b$). Based on a visual observation, it appears that the Lilly and WALE model predict larger structures than the other models. For the Lilly model, this is related to the application of the 'test' filter, which is larger than the grid size; for the WALE model, this is a result of the inclusion of wall distance in the determination of the length scale

L_s.

To conclude, the comparison shows that the best match for the Reynolds stresses is obtained with ILES, although this is strongly grid dependent. Smagorinsky, KSGS and WALE perform comparably, and the Lilly model shows the poorest performance due to the larger test filter. The WALE model should perform better for flows involving complex geometries, meaning its advantages do not show up here.

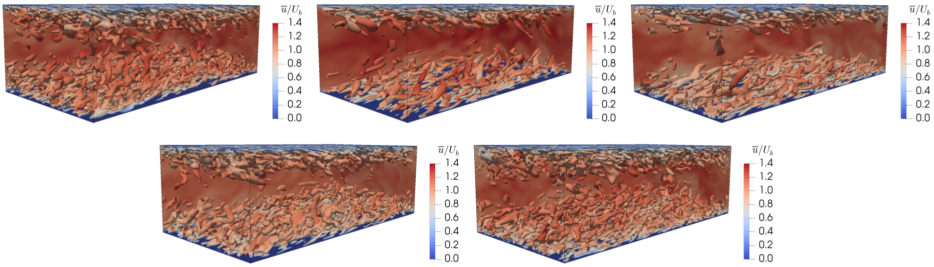

Figure 5.8: LES instantaneous turbulent flow fields ($Q = 0.3$), coloured by $u^* = u/U_b$. First row from left to right Smagorinsky, Lilly and WALE, second row KSGS and ILES.

5.4.2. HYBRID MODELS

Fig. 5.9 shows the flow field statistics for the hybrid models. For the mean velocity, XLES shows an underprediction in the buffer-layer ($5 \leq y^+ \leq 30$). DDES shows an overprediction in the log-law region and an underprediction near the centreline. IDDES matches the reference data well. In terms of Reynolds stresses, XLES captures the trend but underpredicts the magnitude for all components. The peak in the Re_{vv} and Re_{ww} distribution is significantly shifted away from the wall, an indication of the hybrid nature of the model. The DDES model has a more interesting behaviour. The shielding function of the model is formulated such that close to the wall, inside the boundary layer, RANS should be used. In the far-field LES should be employed, with the RANS model acting as sub-filter model [213]. Since a turbulent channel flow consists solely of a boundary layer, with no far-field region, one might expect the solution to be fully RANS. This explains the good match for the averaged velocity. However the Reynolds stress components show that turbulence is fully modelled only in the region $y^+ < 50$, while closer to the centre turbulence is resolved. The employed grid resolution leads to $l_t^{SRS} < l_t^{RANS}$, thereby forcing the switch to occur inside the boundary layer. The division between RANS and LES regions, is visible in Fig. 5.10. Note that even though this is the same behaviour which lead to the development of DDES as a replacement of DES, this can still occur for DDES under certain circumstances (i.e. combinations of test case and grid density). An effect of using LES only close to the centreline is an underprediction of the energy contained in the spectrum at the investigated location ($y^+ \approx 20$). In IDDES and XLES, the RANS region is much smaller (see Fig. 5.10), which is reflected in the magnitude of the Reynolds stresses. Due to the use of RANS close to the wall an underprediction occurs in this region. For IDDES and XLES models the turbulence kinetic energy spectrum also matches well with the other LES results. Note that the underprediction for DDES is related to the location of the probe ($y^+ \approx 20$), which is inside the RANS layer. The fluctuations at this point are LES fluctuations which influence the RANS layer. The turbulence kinetic energy spectrum match the DNS data better for spectra closer to the centreline (not shown in this study).

The turbulent structures in the flow are visualised in Fig. 5.11. The effect of using RANS near the walls in the DDES formulation is obvious, only larger structures in the centre of the channel exist. The structures in the IDDES and XLES model are similar to the LES Smagorinsky, KSGS and ILES results.

The results indicate that for cases where the instantaneous near wall flow field is of importance (for instance sheet cavitation), hybrid models are less suitable than LES or PANS. DDES is not able to properly resolve the boundary layer. In contrast, IDDES performs better for the mean velocity and Reynolds stresses but with the exception of Re_{vv}. XLES underpredicts the all components of the Reynolds stress tensor.

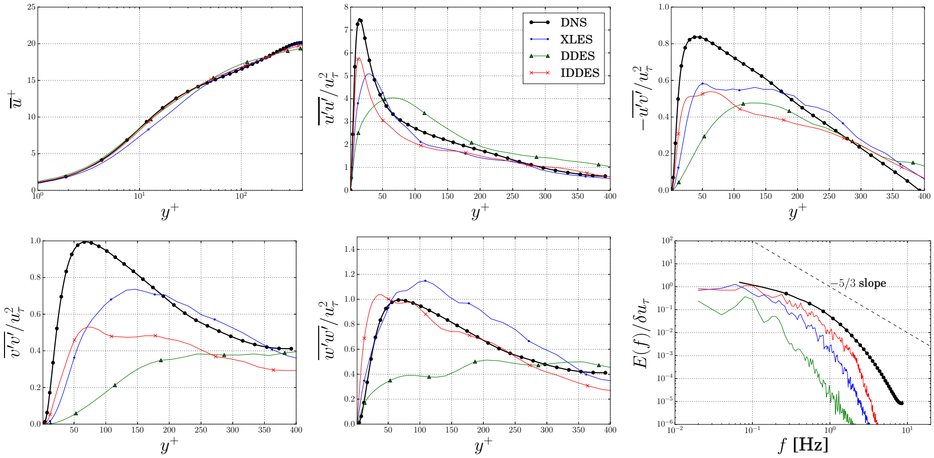

Figure 5.9: Normalised mean velocity and Reynolds stress profiles and turbulence kinetic energy spectra using hybrid models and DNS [169]. From left to right, and top to bottom $\overline{u}^+$, Re_{uu}, Re_{uv}, Re_{vv}, Re_{ww} and $E_{u,y^+\approx 20}(f)$.

5.4.3. PANS

The PANS model is applied with $f_k = 0.75$, 0.50, 0.25, 0.20, 0.15, 0.10 and 0.05. Fig. 5.12 clearly shows the effect of reducing the f_k parameter on the mean velocity profile: $f_k = 1.00$ yields a RANS result as expected, while when moving from $f_k = 0.75$ to 0.20 the modelled turbulence kinetic energy is reduced and more turbulence kinetic energy should be resolved. However, by reducing f_k the flow profile becomes more laminar. Rather than resolving turbulence the velocity perturbations are damped and the flow remains laminar. The highest f_k values still have a reasonable match with the DNS, since these yield mostly turbulent RANS solutions. Below $f_k = 0.20$ the fluctuations are not damped and a fully turbulent flow develops. The results for $f_k = 0.15$, 0.10 and 0.05 match the DNS data velocity almost perfectly. The same behaviour occurs if PANS is applied to a fully

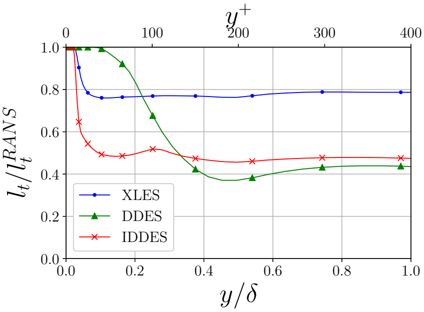

Figure 5.10: Instantaneous, spatially averaged, LES regions (l_t/l_t^{RANS}) for the DDES and IDDES models (right). 1 indicates RANS, 0 LES.

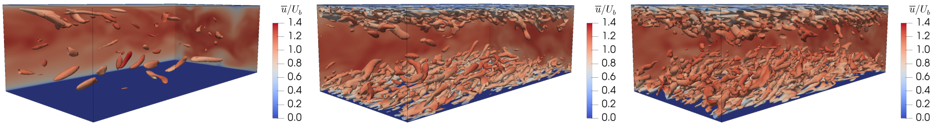

Figure 5.11: Hybrid models instantaneous turbulent flow fields ($Q = 0.3$), coloured by $u^* = u/U_b$. From left to right DDES, IDDES and XLES.

developed turbulent flow (for instance obtained from a LES computation); for higher f_k values the fluctuations are damped after between five and seven flow-through times. The normalised Reynolds stress profiles and turbulence kinetic energy spectrum yield additional insight into this behaviour. It is clear that for computations with f_k in the range 0.75 – 0.20 a laminar solution is obtained; the Reynolds stress tensor components equal zero. The Reynolds stress profiles and turbulence kinetic energy spectra $f_k = 0.15$, 0.10 and 0.05 are comparable and obtain the proper trends and order of magnitude. Interestingly, the peaks for $f_k = 0.10$ are higher than for $f_k = 0.15$ and 0.05. This is an indication of the need for finer grids and iterative convergence criteria for lower f_k values. For both $f_k = 0.10$ and 0.05 the match is better than for explicit LES, which is related to the increased turbulence resolution.

The turbulent structures in the flow are visualised in Fig. 5.13 for the lower f_k values. There is little difference between the different simulations. It appears that the results for cases with low f_k are identical to ILES. This is not true when looking at the eddy-viscosity, however. The maximum eddy-viscosity ratio, ν_t/ν, in the field for $f_k = 0.15$ has a magnitude of $\mathcal{O}(10^2)$, whereas for $f_k = 0.05$ this is $\mathcal{O}(10)$, and for ILES it is zero by definition. For comparison, for a turbulent RANS solution $\nu_t/\nu = \mathcal{O}(10^5)$. It is clear that the magnitude of eddy-viscosity has little effect on the results, provided that f_k is below the threshold to allow a turbulent flow.

The observed strong dependence on f_k, resulting in distinct laminar and turbulent flow regimes, is related to the physics of the problem. In a wall-bounded turbulent flow, such as a turbulent channel or flat plate, the small scales near the wall move away from the wall, and merge into increasingly larger scales away from the wall. The large scales

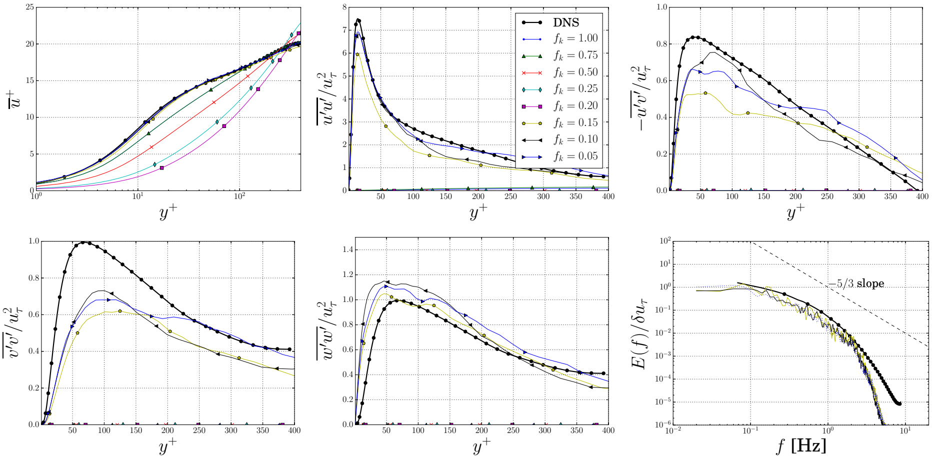

Figure 5.12: Normalised mean velocity and Reynolds stress profiles and turbulence kinetic energy spectra using PANS and DNS [169]. From left to right, and top to bottom $\overline{u}^+$, Re_{uu}, Re_{uv}, Re_{vv}, Re_{ww} and $E_{u,y^+\approx 20}(f)$.

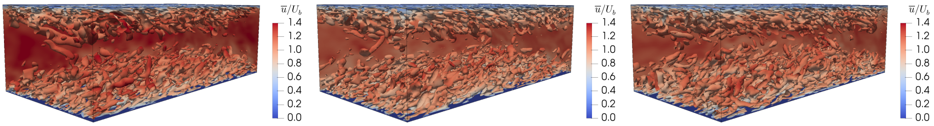

Figure 5.13: PANS instantaneous turbulent flow fields ($Q = 0.3$), coloured by $u^* = u/U_b$. From left to right $f_k = 0.15$, 0.10 and 0.05.

then break up into small scales and are dissipated. This process is known as energy backscatter, or the inverse energy cascade [214]. A turbulent flow only develops if the filter length is smaller than the length scales of the small scales, otherwise the mechanism responsible for creating a fully turbulent flow is filtered out. This can occur on a coarse grid for all methods, or, in the case of PANS, when using a large f_k value. This hypothesis is confirmed by the guideline that for SRS the effective computational Reynolds number,

$$Re_e = \frac{U\delta}{\nu + \nu_{modelled}} = \frac{U\delta}{\nu + f_k^2 \nu_t}, \tag{5.4}$$

must exceed the critical transition Reynolds number needed for the onset of instability, Re_c [175]. For a turbulent channel flow, this guideline is satisfied for the cases with $f_k < 0.20$ ($Re_c \approx 2300$, obtained from experiments [199]). To enable turbulent results for f_k values in the range 0.20 − 1.00 the ITG is needed, which not only feeds the small scales, but also feeds energy directly into the larger scales to allow a turbulence cascade to develop. Note that the synthetic turbulence is inserted across the height of the channel, in contrast to the physics where turbulence develops parallel to the walls.

5.5. TURBULENCE APPROACHES WITH ITG

The second set of results is obtained by applying the ITG described in Sec. 2.4. The turbulent fluctuations are added to the mean turbulent velocity profile, which is prescribed at the inlet. The domain is initialised with the mean turbulent flow profile, while the ITG is located just behind the inlet. The body-force terms are added over $L_{tg} = 0.1\delta$ which corresponds to two cells in the streamwise direction. In this case periodic boundary conditions are only applied in the spanwise direction. Based on the TST (see Sec. 5.3.2), temporal averaging of the results is performed over 7 flow-through times, after removing two flow-through times. The resulting statistical uncertainty for the mean streamwise velocity is below 3%, and for the Reynolds stress components below 12%. The mean velocity and Reynolds stress profiles prescribed are taken from the DNS reference data. The prescribed integral length scales are anisotropic but a homogeneous approximation is made based on the length scales given by Y. Kim et al. [124]; in the streamwise direction the length scale is taken as 0.9δ, in the spanwise and wall perpendicular direction as 0.045δ. It is noted that, due to this assumption, the prescribed length scales at the wall are too large.

The application of the ITG based on Eq. 2.51 affects the iterative convergence; the L_2 and L_∞ norms are shown in Tab. 5.2. The ratio L_∞/L_2 is $\mathcal{O}(10^1)$ for synthetic cases compared to $\mathcal{O}(10^2)$ for recycling results, indicating that the residuals stagnate in a considerable part of the domain. Fig. 5.15 shows that this occurs in the cells close to the location at which the body-force terms are applied, due to the local, explicit, addition of these terms, which also vary per time step. The close proximity of the ITG to the inflow (where velocity is prescribed) also contributes to this situation. To remedy this issue, for Chapter 6 onwards, an additional source term is added to the velocity field (see Eq. 2.51).

Table 5.2: Average residual norms for recycling and synthetic cases.

Equation	Recycling		Synthetic	
	L_∞	L_2	L_∞	L_2
Momentum:	10^{-5}	10^{-6}	10^{-2}	10^{-4}
Pressure:	10^{-6}	10^{-7}	10^{-4}	10^{-6}
Turbulence:	10^{-6}	10^{-7}	10^{-7}	10^{-9}

It is observed that a streamwise development length is needed to allow the added perturbations to develop into a turbulent flow profile, and obtain a reasonable match with the input values. With the current implementation of the ITG, after 6δ the results for $\overline{u}$ and Re_{uu} are self similar, as shown in Fig. 5.14. At this location, Re_{uv} is still underpredicted, Re_{uv} keeps developing until approximately 10δ. This is comparable to Y. Kim et al. [124] and Z.-T. Xie and Castro [126], who both give a required development length of 10δ. The results shown in the remainder of this section are obtained at a location 6δ behind the ITG.

In order to compare the results obtained from recycling and synthetic computations, Fig. 5.16 shows the resolved turbulence intensity versus the channel height for all models. As shown in Sec. 5.4, for the recycling cases, the LES models show the best match with the reference data, together with the PANS results with $f_k < 0.2$. The synthetic results however, are similar for all models. With the exception of PANS, I is overpredicted

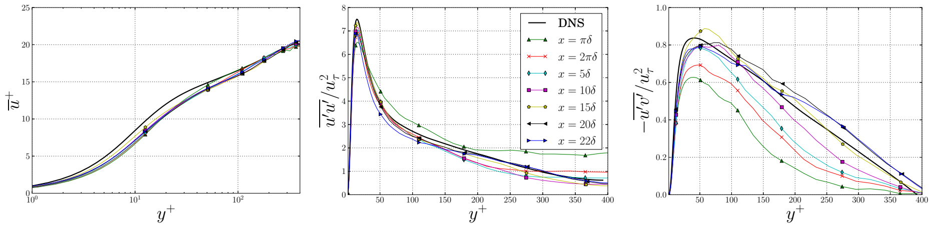

Figure 5.14: Normalised mean velocity and Reynolds stress profiles at different downstream locations using PANS with $f_k = 0.05$ and the ITG. From left to right, $\overline{u}^+$, Re_{uu} and Re_{uv}.

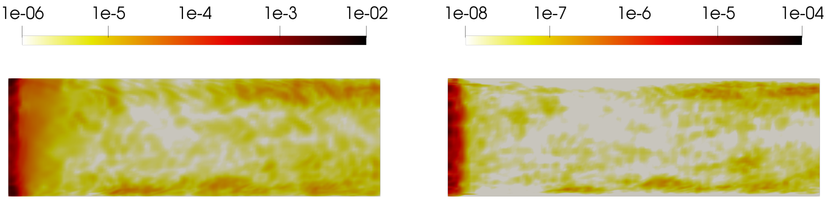

Figure 5.15: Velocity (left) and pressure (right) residuals in the domain for a PANS computation with ITG (f_k = 0.05). The ITG is located at the left of the images.

at the centre of the domain. Both DDES and PANS with higher f_k show an underprediction of I at the wall. The PANS results show an increase in I with decreasing f_k, as might be expected. Nevertheless the results show that the application of the ITG can prevent the occurrence of laminar flow for cases where the critical transition Reynolds number exceeds the effective computational Reynolds number (as is the case for $f_k \geq 0.20$, see Section 5.4.3).

5.5.1. LES

Fig. 5.17 shows the results obtained using different LES models. As expected the shape of the mean velocity profiles matches the DNS data well, however an underprediction occurs across the channel height. For Re_{uu}, ILES and WALE have the correct peak value, with the other models showing the correct shape but a lower peak. In contrast to the recycling results (Fig. 5.7), where all models underpredicted Re_{uv} and Re_{vv}, the results lie on or above the DNS data for all models except the Lilly model. This model *does* accurately predict Re_{ww} however, which is overpredicted by the other models. For the turbulence kinetic energy spectrum, the ILES and WALE model contain the most energy, while the spectrum for the Lilly model shows less energy than for the recycling cases. The underprediction by the Lilly model is similar to that already shown in Fig. 5.7 and is again related to the application of the larger ‘test’ filter, which filters out synthetic turbulence.

5.5.2. HYBRID MODELS

The results obtained using different hybrid models are shown in Fig. 5.18. For the mean velocity, the same underprediction occurs as for the LES models. The results for the DDES model are improved with respect to recycling cases (Fig. 5.9): the magnitude is

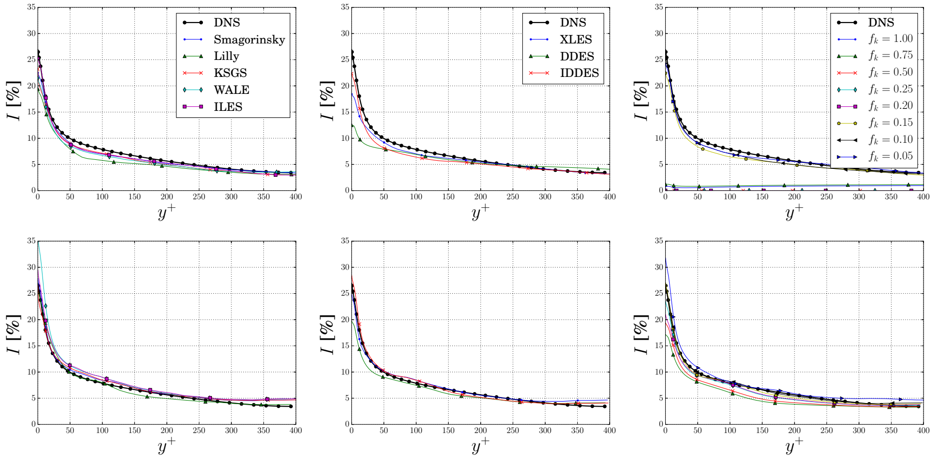

(a) LES (b) Hybrid (c) PANS

Figure 5.16: Resolved turbulence intensity ($I = 1/3\sqrt{\overline{u_i' u_i'}}/\overline{u}$) for recycling (top row) and ITG (bottom row) for LES, hybrid and PANS models. Results obtained at $x = 2\delta$ and averaged in transverse direction.

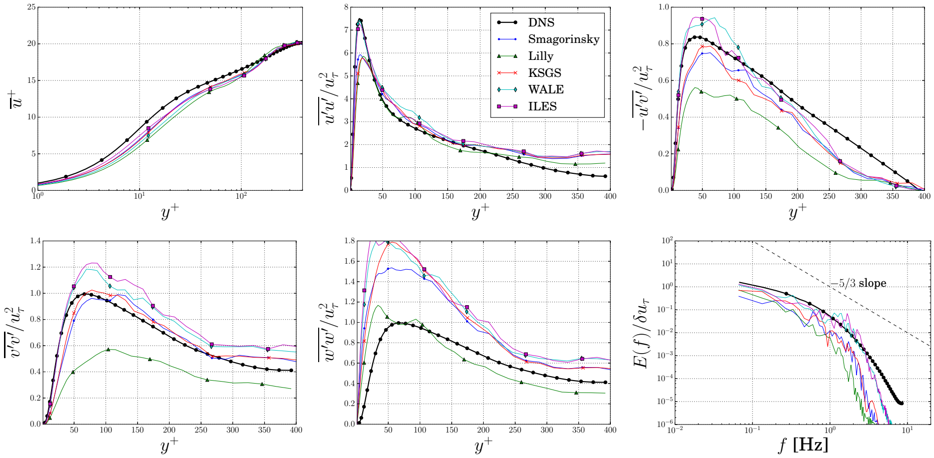

Figure 5.17: Normalised mean velocity and Reynolds stress profiles and turbulence kinetic energy spectra using LES and the ITG. From left to right, and top to bottom $\overline{u}^+$, Re_{uu}, Re_{uv}, Re_{vv}, Re_{ww} and $E_{u,y^+\approx 20}(f)$. Results obtained at $x = 2\delta$ and averaged in transverse direction.

still significantly underpredicted but the distribution of the Reynolds stress components is closer to the DNS data, and there is more energy in the spectrum. For the IDDES model, the Reynolds stresses are also higher compared to the recycling results. The peak of Re_{uu}, Re_{uv} and Re_{vv} is better captured, but Re_{ww} is overpredicted. The XLES results are similar to the IDDES results, with the exception of an underprediction of Re_{uu} near the wall which was also observed for recycling cases. The energy in the turbulence kinetic energy spectrum is lower for XLES than for IDDES, exhibiting a magnitude similar to DDES. For all models Re_{uv} is underpredicted at the centre, which was not the case for the recycling results.

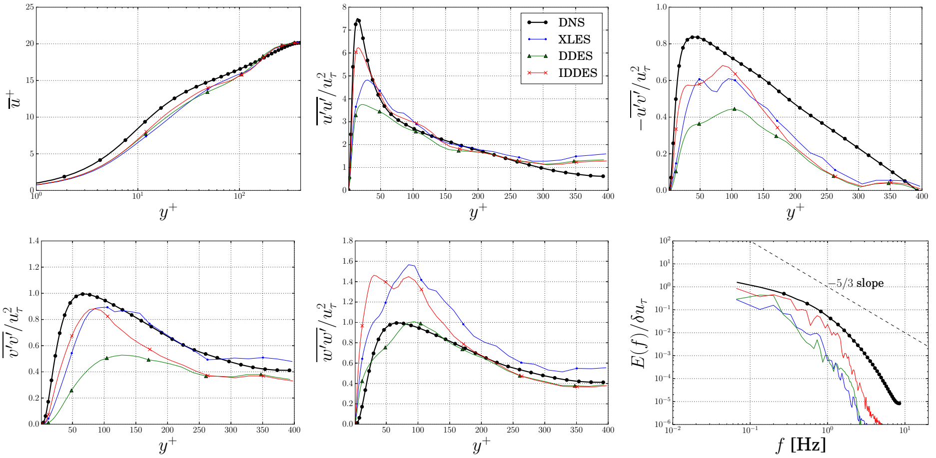

Figure 5.18: Normalised mean velocity and Reynolds stress profiles and turbulence kinetic energy spectra using hybrid models and the ITG. From left to right, and top to bottom $\overline{u}^+$, Re_{uu}, Re_{uv}, Re_{vv}, Re_{ww} and $E_{u,y^+\approx 20}(f)$. Results obtained at $x = 2\delta$ and averaged in transverse direction.

5.5.3. PANS

Fig. 5.19 shows the results obtained using PANS with different f_k values. As seen for the other synthetic results, the mean velocity is underpredicted. For all components of the Reynolds stresses a similar behaviour is observed; with decreasing f_k the results converge towards the DNS data with decreasing f_k. Re_{uu} is overpredicted at the centre with $f_k = 0.05$. The same occurs for Re_{ww} when $f_k \leq 0.25$, but then across the full channel height. The increase in fluctuations with decreasing f_k can be related to the results obtained without the ITG: the addition of synthetic turbulence leads to a turbulent profile, yet computations with higher f_k values add dissipation, thereby damping the resolved turbulence. Consequently, the resolved Reynolds stresses decrease in magnitude. This is most visible in the turbulence kinetic energy spectra, where the cut-off frequency increases with decreasing f_k.

Fig. 5.20 visualises the turbulent structures from PANS, based on Q. The most important difference with the results presented in Sec. 5.4.3 (Fig. 5.13) is that for $f_k > 0.15$ turbulent structures now exist in the flow. However for these higher f_k values the fluctu-

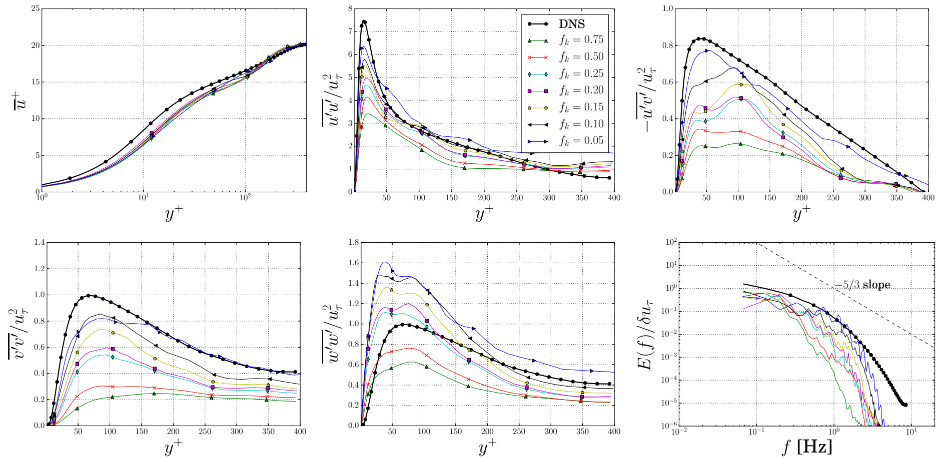

Figure 5.19: Normalised mean velocity and Reynolds stress profiles and turbulence kinetic energy spectra using PANS and the ITG. From left to right, and top to bottom $\overline{u}^+$, Re_{uu}, Re_{uv}, Re_{vv}, Re_{ww} and $E_{u,y^+\approx 20}(f)$. Results obtained at $x = 2\delta$ and averaged in transverse direction.

ations are filtered by the model as they propagate downstream of the ITG, as can be most clearly seen near the walls. The images are similar to the recycling results for the lower f_k values ($f_k \leq 0.15$), however close to the ITG more structures can be seen in the centre of the channel.

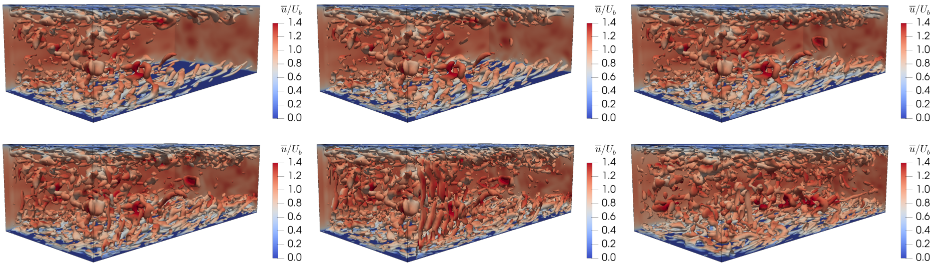

Figure 5.20: PANS with ITG, instantaneous turbulent flow fields ($Q = 0.3$), coloured by $u^* = u/U_b$. From left to right, and top to bottom $f_k = 0.75$, 0.50, 0.25, 0.15, 0.10 and 0.05. The ITG is located at the left of the images.

5.6. DISCUSSION

In this chapter turbulence is generated both using streamwise periodic boundary conditions and a pressure gradient, i.e. as precursor (Sec. 5.4), and using the ITG (Sec. 5.5). For industrial CFD it is shown that, independent of the selected turbulence simulation approach, the synthetic method can produce a turbulent inflow at significantly lower computational cost. Only two flow-through times from ITG to object of interest have to be computed before statistics can be collected based on the TST, in contrast to the precursor computations for which 11 flow-through times were required (Sec. 5.3.2). The ability to more easily tune the method to obtain the desired Reynolds stresses and length scales is also attractive for industrial applications for which these quantities may already be known. Finally, it is noted that for a range of industrial test cases, such as foils, wings or propellers, only homogeneous inflow turbulence is required. For such cases, the advantages of the ITG clearly show; no flow recycling is required, and the grid only needs to be refined around the object of interest and upstream.

A cause of concern is the possible introduction of additional numerical errors by the ITG. The main error sources are: not satisfying mass conservation, interpolation, and iterative errors. In the present study, the pressure fluctuations introduced by the ITG were observed to be of the same order of magnitude as the pressure fluctuations in recycling cases (results not shown in this study), indicating that the introduced turbulence satisfies mass continuity. Interpolation errors occur between the grid on which random numbers are generated, and the CFD grid. However, due to the finer density of the CFD grid compared to the density of the random number grid (which is a consequence of the desired length scales), this error is small. It is also important to keep in mind that the velocity fluctuations themselves are not interpolated to the CFD grid, but rather the body-force terms which perturb the flow, thereby decreasing the sensitivity to the interpolation. Note that a precursor turbulence generator may also not be entirely free from interpolation errors, depending on the two grids used.

The application of the ITG does significantly worsen the convergence behaviour when compared to recycling cases (Sections 5.3.1 and 5.5). The solver does not converge in the cells near the ITG where the body-force terms are added. If the ITG is located further from the inflow, the residuals can be reduced by about one order of magnitude, but stagnation still occurs (results not shown in this study). However the residuals show that the lack of convergence is a local effect (Fig. 5.15), and by definition the object of interest must be located far from the ITG to allow for a sufficient development length [28]. It is expected that the ITG has little effect on the iterative error at the object of interest, and therefore these cells could be excluded from the reported maximum residuals in the domain.

While potentially introducing numerical errors, it is clear that the ITG significantly reduces modelling errors by improving the similarity between computations and experimental setups. This is beneficial not only for SRS techniques such as LES and PANS which yield unphysical laminar and/or separating flows without proper inflow conditions [29], but also for hybrid models where the problems tend to be more concealed. Finally, while both precursor and synthetic turbulence generation methods are independent of the turbulence simulation approach, it should be emphasised that recycling in combination with PANS using insufficiently low f_k values does not lead to a turbulent flow (see Fig. 5.12). To enable the use of this model with these settings, the synthetic method is required.

5.7. CONCLUSIONS

A turbulent channel flow at $Re_\tau = 395$ is simulated using two approaches for generating inflow turbulence. The interaction of these methods with several SRS models is investigated, and the results are compared to DNS reference data. For recycling cases the numerical errors are also evaluated. Based on the normalised residuals it is shown that the iterative error was negligible. The statistical uncertainty based on 45 flow-through times was below 2% for the mean values, and below 10% for the Reynolds stresses. The grids employed satisfy LES recommendations from the open literature. It is shown that the discretisation error due to the grid is negligible, the discretisation of the convective terms in the momentum equations having a larger effect. Best results are obtained with a second-order accurate CD scheme.

For LES, the magnitude of the turbulent fluctuations depends on the sub-filter modelling. Due to the fine grid resolution however, the difference between the LES models was found to be small. The Lilly and WALE model predict larger turbulent structures than the other models. On coarser grids explicit LES predicts the Reynolds stresses more accurately than ILES. In contrast, hybrid models, which are often favoured in industrial applications, show less satisfactory results. Both XLES and IDDES have a reasonable match; the velocity profiles are close to the reference data, and the Reynolds stresses, although underpredicted in magnitude, show the correct shape. Due to the formulation of the IDDES model, the Reynolds stresses are especially underpredicted close to the wall. While the formulation of the DDES model should lead to a full RANS behaviour, in the centre of the domain a LES behaviour was observed. Finally the application of PANS showed that there is a case-dependent threshold which separates two solution regimes: $0.20 \leq f_k < 1.0$ yields a laminar solution regardless of the initialisation of the flow, while if $f_k < 0.20$ a turbulent flow can develop. The results are then very similar to ILES, since due to the low f_k the RANS formulation in the PANS model has little effect. This finding is supported by the visualised turbulent structures and an investigation into the effect of grid coarsening, where PANS with $f_k = 0.10$ and ILES follow the same trend.

The application of the ITG shows that results comparable to recycling computations can be obtained at reduced computational cost. In this case, the PANS model with higher f_k values also results in a turbulent flow. Ease of usage and tuning makes the use of the ITG promising in order to obtain a representative inflow for industrial CFD applications. In the following chapters a method to improve the iterative convergence behaviour is assessed, and the method is applied to more industrially orientated test cases, including cavitation. Also the effect on the far-field radiated noise is investigated.

6

DELFT TWIST 11 HYDROFOIL

The Delft Twist 11 Hydrofoil is a common test case for investigating the interaction between turbulence and cavitation modelling in computational fluid dynamics. Despite repeated investigations, results reported for the lift and drag coefficient are accompanied by significant uncertainties, both in experimental and numerical studies. When using scale-resolving approaches, it is known that turbulent fluctuations must be inserted into the domain in order to prevent the flow from remaining laminar around the body of interest, although this has been overlooked until now for the present test case. This chapter investigates the errors occurring when a laminar inflow is applied for mildly separated or attached flows, by employing the partially averaged Navier-Stokes equations with varying values for the ratio of modelled-to-total turbulence kinetic energy, and with varying grid densities. It is shown that depending on the grid resolution laminar leading edge separation can occur. When turbulent fluctuations are added to the inflow, the leading edge separation is suppressed completely, and the turbulent separation zone near the trailing edge reduces in size. The inflow turbulence has a large effect on the skin friction, which increases with increasing turbulence intensity to a limit determined by the grid resolution. In cavitating conditions the integral quantities are dominated by the shedding sheet cavity. The turbulence intensity has little effect on the pressure distribution, leading to a largely unaffected sheet cavitation, although the shedding behaviour is affected. It is shown that, especially in wetted flow conditions, with scale-resolving methods inflow turbulence is necessary to match the experimental flow field.

6.1. INTRODUCTION

This chapter aims to explore the reduction in modelling errors when using resolved inflow turbulence, and the application of the ITG for simulating cavitation dynamics. Such a methodology can result in an increased physical resolution while using smaller domains, i.e. less computational cells. Potential use cases include: simulating a propeller in a cavitation tunnel, simulating a propeller in behind condition without resolving the

---

This chapter has been published in Ocean Engineering **228**, 1088602 (2021) [201].

entire flow around the hull upstream, or predicting the interaction between two wings, while only simulating the downstream wing. The test case of choice in the current chapter, is the 3D twisted wing studied by Foeth et al. [232]. This is a well documented test case, exhibiting a shedding sheet cavity representative of a ship propeller, while avoiding the additional complications due to a rotating body. The test case was experimentally studied in both wetted and cavitating conditions, and is a common numerical test case [233]. Due to the cavitation occurring inside the boundary layer, the cavitation behaviour is strongly dependent on the interaction between turbulence and cavitation modelling, emphasizing the need for proper inflow boundary conditions. An overview of previous investigations into this test case is given in Sec. 6.2.2.

The test case was designed to study cavitation behaviour, which naturally has led to a focus on attempting to capture the cavitating behaviour. Unfortunately, an effect of this is that some of the difficulties in simulating this test case have been overlooked. Although it is known from literature that inflow turbulence is necessary for SRS methods, all SRS results in the open literature for this test case do not employ such methods. Indeed, they obtain reasonable results for the cavity length and shedding behaviour. It seems that the presence of a sheet cavity on the wing surface obscures some of the difficulties in simulating this flow. The laminar [1] inflow leads to an incorrect boundary layer prediction, but still the presence of cavitation leads to a production of turbulence and vorticity due to the occurrence of shear layers in the flow. Due to these turbulent perturbations, turbulence-like structures arise when solving the Navier-Stokes equations, masking the modelling errors due to the laminar inflow. Due to the complex interaction between modelling and numerical error such results strongly depend on the used grid, time step and turbulence model. Commonly, coarser grids results in lower eddy-viscosity levels (see e.g. Diskin et al. [234]), leading to the occurrence of increased dynamics. In such cases grid refinement can suppress dynamics, thereby leading to an increasing comparison error with grid refinement. In contrast, under wetted flow conditions, the lack of inflow turbulence structures can lead to unrealistic flow results when using SRS approaches.

In the current chapter an attempt is made to show the mismatch between computations and experiments which can occur for this case when using a steady inflow for SRS. The focus will therefore be on wetted flow conditions, to prevent the presence of turbulence due to cavitation obscuring the errors. Nevertheless, results for cavitating conditions are also presented. All results are obtained using PANS, in order to be able to systematically vary the turbulence resolution between RANS and (underresolved) direct numerical simulation (DNS), while simultaneously utilising several grid densities. Iterative, statistical and discretisation errors are assessed.

The chapter is organised as follows. Sec. 6.2 describes the test case and numerical setup, while Sec. 6.3 details the estimation of the numerical errors. After this, the results are addressed in two sections: wetted flow in Sec. 6.4, and cavitating flow in Sec. 6.5. The Discussion and Conclusions in Sections 6.6 and 6.7 complete the study.

---

[1] In this context laminar flow is defined as the absence of resolved velocity fluctuations, i.e. the Reynolds stresses $Re_{ij} = \overline{u'_i u'_j}/u_\tau^2 \approx 0$.

6.2. TEST CASE AND SETUP

6.2.1. TEST CASE DESCRIPTION

The Delft Twist 11 Hydrofoil is a NACA0009 profile with a spanwise-varying angle of attack from 0° at the sides to 11° at midspan, mounted with an angle of attack at the wall $\alpha_{wall} = -2°$. The chord length $c = 0.15$ m and the span $s = 2c$. The spanwise twist is given by [232, 235]

$$\alpha = \alpha_{max}\left(2\frac{|y|}{c}^{3} - 3\frac{y}{c}^{2} + 1\right) + \alpha_{wall}. \tag{6.1}$$

The Reynolds number is $Re = U_\infty c/\nu = 1 \times 10^6$, leading to an inflow velocity of $U_\infty = 6.97$ m/s. In cavitating conditions, the cavitation number is $\sigma = \left(p_\infty - p_v\right)/q_\infty = 1.07$ with the dynamic pressure $q_\infty = 1/2\rho U_\infty^2$. In the experiments sand roughness with a grain size of 10^{-4} m was applied at the leading edge at $x/c = 0.04$ to force transition to turbulence, but also leading to an increase in drag.

Foeth [235] measured the lift force, the pressure at different locations on the suction side and applied particle image velocimetry (PIV) to analyse the developing cavity shape and shedding behaviour. The drag was not measured. For the lift and pressures, the calibration errors of the sensors are reported, but no total uncertainties are given. Regarding the setup, an uncertainty of 2.7% is reported for the inflow velocity, and 5% for the cavitation number. Inflow turbulence levels of the cavitation tunnel were 2-3% at the location of the wing. This is higher than the more recent values reported for the same cavitation tunnel by Varadharajan [236] (≈ 1.5%), but those were obtained with a 50% lower mean tunnel velocity. From both sources no information is available on the integral length scale, which makes matching the experimental setup and quantitative validation difficult. For more details the reader is referred to Foeth [235].

In the present study, for the cavitation model the bubble radius and concentration were set to $n_b = 1 \times 10^8$ m^{-3} and $R_b = 1 \times 10^{-5}$ m, respectively, based on [79]. Time integration is performed using a second-order implicit three time level scheme, the convection terms in the momentum equations are discretised using a second-order accurate flux limited Quadratic Upstream Interpolation for Convective Kinematics (QUICK) scheme, the turbulence and cavitation equations are discretised using a first-order upwind scheme. Diffusion is central second-order accurate, and non-orthogonality and eccentricity of the grid are considered by extra deferred corrections.

6.2.2. LITERATURE OVERVIEW

The Delft Twist 11 Hydrofoil is a common test case for investigating the interaction between turbulence and cavitation modelling in CFD. In literature, a number of different turbulence modelling approaches for this case have been applied, such as Euler equations [237, 238], unsteady RANS [79, 239–243], unsteady RANS with an ad-hoc eddy-viscosity correction (such as the so-called Reboud correction [244]) [79, 240, 245, 246], Reynolds Stress Models (RSM) [242], LES [240, 243, 247–251], hybrid models [79, 240, 242, 243] and PANS [252]. The use of unsteady RANS typically suppresses the cavity dynamics, while LES results show a shape and shedding behaviour which is more in agreement with the experiments, although the cavity length is underpredicted. hybrid models, such as DES, shed less cavity structures due to the sheet cavity being close to the wing surface, i.e. in a RANS region. The use of the Reboud correction leads to increased cavity dynamics and cavity length, however its ad hoc empirical nature introduces additional modelling error in the results. The PANS results reported show a shedding behaviour comparable to experiments, however only one ratio of modelled-to-total turbulent kinetic energy was investigated. From literature it is know that the results can vary significantly based on this ratio [57, 164, 193]. Most investigations ([79, 239–243, 245, 249, 253]) make use of the Schnerr-Sauer cavitation model, which is also employed in the current chapter.

An overview of the reported mean lift coefficient $\overline{C_L} = \overline{L}/(q_\infty cs)$ and Strouhal number $St = fc/U_\infty$ as function of the number of grid cells N_c in cavitating conditions can be found in Fig. 6.1. The coefficients are defined using the lift force L and the shedding frequency f, and divided by the turbulence model. The mean lift coefficient is underpredicted by every simulation found in the open literature, which indicates that the cavitation extent is underestimated [253]. A wide variety of grid types and densities is employed in the literature. It must be noted that, in general, the grids are relatively coarse considering the Reynolds number, with high wall-normal resolutions. The stream- and spanwise resolutions are regularly not reported, and the sensitivity of the results towards the grid is often not investigated. This leads to few reported uncertainties for integral values.

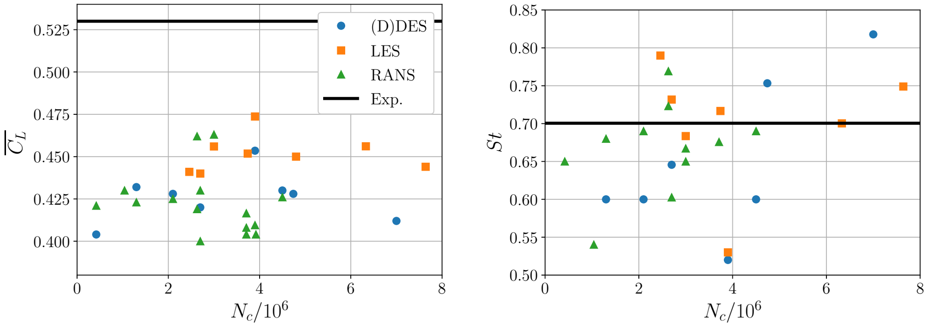

Figure 6.1: Literature overview of integral quantities in cavitating conditions as function of the number of cells and turbulence model [79, 239–243, 245, 246, 249, 250, 253, 254].

As mentioned in the introduction, the literature focusses on cavitation conditions. Nevertheless, some results for wetted flow are reported [79, 233, 243, 253, 254]. These results are mostly limited to the forces and the pressure distribution on the centreline, no flow visualisations are given. Hoekstra et al. [233] do report that within their workshop 'all participants report an attached boundary layer on the entire foil', i.e. no boundary layer separation is observed on the wing surface. See Fig. 6.2 for an overview of the reported mean lift $\overline{C_L}$ and drag coefficient $\overline{C_D} = \overline{D}/(q_\infty cs)$ as function of the number of grid cells and turbulence model. Some results match the experimental lift coefficient well, however again the spread in results is significant.

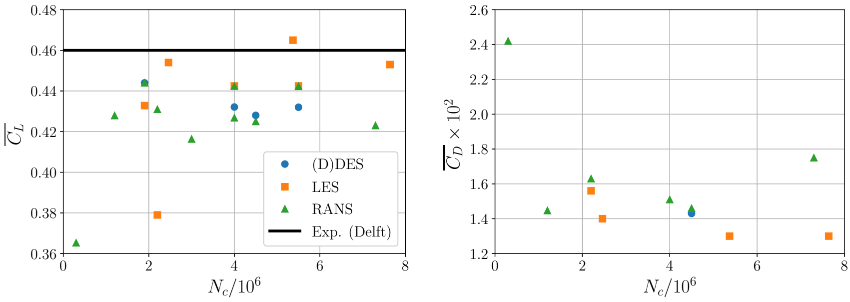

Figure 6.2: Literature overview of integral quantities in wetted flow conditions as function of the number of cells and turbulence model [79, 233, 239, 243, 253, 254].

6.2.3. NUMERICAL SETUP

The computational domain extends two chord lengths upstream of the leading edge and five chord lengths downstream. Half of the wing is modelled with a symmetry plane at the centre of the wing. The use of a symmetry plane in the setup can lead to modelling errors when attempting to resolve turbulence using SRS and when adding synthetic turbulence. Nevertheless, it was employed to reduce numerical cost. It must be remarked that most results in literature, including the LES results, employ the same simplification. The top and bottom of the domain are located one chord length from the wing, matching the dimensions of the cavitation tunnel used by Foeth et al. [232]. The boundaries of the domain are modelled as slip-walls, whereas on the wing a no-slip boundary condition is applied. At the inlet an inflow boundary condition is used, fixed pressure is defined at the outlet.

Fig. 6.3 shows the wing geometry, computational domain and grid topology. The boundary conditions at the inlet are a Dirichlet condition for all velocity components and turbulence quantities, and at the outlet a Dirichlet condition for the pressure. The wing's surface is modelled as a non-slip wall, with a symmetry boundary condition at the centre of the wing. All other domain boundaries are modelled as slip walls. Four geometrically similar, multi-block hexahedral structured grids ($G1$, $G2$, $G3$ and $G4$) are used, but for comparison purposes also an additional grid ($G0^*$) is employed. This grid is identical to grid $G1$, but it includes a local refinement box with dimensions $4/3c \times c \times 2/3c$ surrounding the wing. In this refinement box the grid is refined by a factor 2 with respect to grid $G1$. The average values of the non-dimensional wall cell-sizes x_n^+, x_c^+ and x_s^+ (normal, chordwise and spanwise) on the suction side centreline of the different grids are given in Tab. 6.1. Due to the 3D geometry and grid topology, the averaged values do not give a good indication of the cell distribution over the wing. Fig. 6.4 shows the x_n^+, x_c^+ and x_s^+ distribution over the chord at the wing centreline on the suction side. Over the entire wing x_n^+ is well below 1 for all grids. On the suction side, x_c^+ reaches high values at the leading edge, drops immediately after the leading edge and then increases again. It remains relatively constant but decreases again towards the trailing edge. Finally, x_s^+ is high at the leading edge, and decreases along the wing. The values for x_s^+ at the wing midspan are lower than the values towards the wall of the cavitation tunnel (where $\alpha =$

−2°).

When comparing these resolutions to guidelines from literature for a well-resolved LES or PANS, $x_n^+ < 1$, $50 < x_c^+ < 150$ and $15 < x_s^+ < 40$, [225], it is clear that in wall-normal direction, all grids are sufficiently fine. Grids $G0^*$ and $G1$ do comply with the required x_c^+, however none of the applied grids reaches the required resolution in spanwise direction. Due to the computational cost, the grids are not refined below these levels.

For computations with a resolved turbulent inflow, the ITG is located at $x_{TG} = -2c$ with respect to the leading edge of the wing, which is close to the inflow boundary condition.

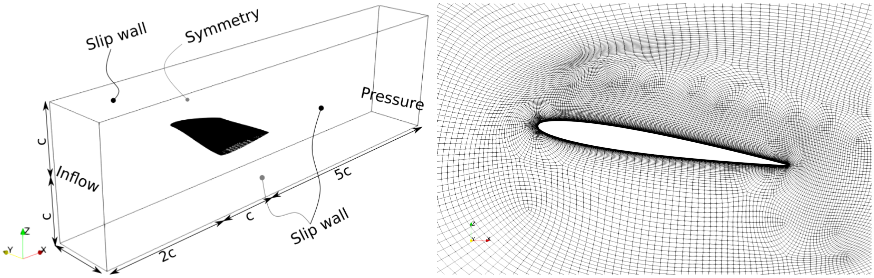

Figure 6.3: The Delft Twist 11 Hydrofoil and grid $G3$ at the symmetry plane. In the left figure, the boundary conditions are indicated with lines, black dots refer to planes at the front of the image, while grey dots refer to planes at the back of the image.

Table 6.1: Number of cells N_c, grid refinement factor h_i, and non-dimensional wall units $x^+ = u_\tau x/\nu$ based on the friction velocity at the wall u_τ, in normal, $\overline{x}_n^+$, chordwise, $\overline{x}_c^+$, and spanwise, $\overline{x}_s^+$, directions, averaged on the wing suction side at the centreline and obtained from a steady state, wetted flow, RANS computation. The * indicates a grid with local refinement surrounding the wing.

Grid	$N_c/10^6$	h_i	$\overline{x}_n^+$	$\overline{x}_c^+$	$\overline{x}_s^+$
$G4$	1.30	2.00	0.32	320	550
$G3$	2.10	1.70	0.25	260	460
$G2$	4.50	1.32	0.20	225	330
$G1$	10.31	1.00	0.15	150	290
$G0^*$	55.13	0.50	0.08	80	150

6.3. NUMERICAL ERRORS

As is generally accepted, numerical errors can be divided into input, round-off, iterative, discretisation, and, in the case of unsteady computations, statistical errors [149]. The round-off error is assumed to be negligible due to the use of double precision arithmetic [255]. One of the sources of input error are boundary conditions. The effect of changing the inflow boundary condition is assessed in Sec. 6.4. In this section, the iterative, discretisation and statistical error are assessed.

The iterative convergence is assessed based on the residuals, normalised by the diagonal element of the left-hand-side matrix of the linearised system of equations. All

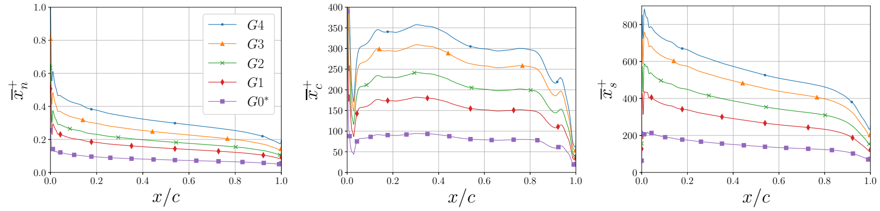

Figure 6.4: Non-dimensional wall units $x^+ = u_\tau x/\nu$, based on the friction velocity at the wall u_τ, versus the chord length at the wing centreline on the suction side only, in normal, $\overline{x}_n^+$, chordwise, $\overline{x}_c^+$, and spanwise, $\overline{x}_s^+$, directions. Obtained from a steady state, wetted flow, RANS computation.

wetted flow calculations with steady inflow condition are converged until L_∞ is below 10^{-6}. Computations with a resolved turbulent inflow are converged until L_2 is below 10^{-4} and L_∞ below 10^{-2}. The largest residuals occur near the ITG and the wing leading edge. Residuals can be reduced further by increasing the number of outerloops, with the exception of the ω equation which stagnates. For cavitating computations, the L_2-norm is generally in the order of 10^{-3}, while the L_∞-norm is in the order of 10^{-1} for all equations except for the ω equation. For this equation the L_2-norm is in the order of 10^{-3} and the L_∞-norm in the order of $10^0 - 10^{-1}$.

The finite length of a CFD simulation introduces a random uncertainty in the mean of the signal. To estimate the statistical uncertainty, and to remove the start-up effect, the Transient Scanning Technique (TST) is used (see Sec. 3.2.5). For wetted flow cases with a steady inflow or low levels of inflow turbulence intensity ($\mathscr{I}_{LE} < 10\%$), the statistical uncertainty for integral quantities is below 1%, for higher inflow turbulence intensities ($\mathscr{I}_{LE} > 10\%$) it is below 5%. For cavitating computations, the statistical uncertainty for the mean lift and drag forces is below 3%.

The discretisation error, $E_d(\phi)$, is estimated using a power series expansion [57, 149]

$$E_d(\phi) = \phi_1 - \phi_0 = \frac{\phi_{i+1} - \phi_1}{r_{i+1}^p - 1}. \tag{6.2}$$

where ϕ_0 indicates the estimated solution for zero discretisation error and r is the refinement ratio, based on

$$\frac{r_i}{r} = \frac{h_i}{h_1}. \tag{6.3}$$

with h the cell length. Based on the data it is not possible to obtain an accurate estimation of p, so both a value of 1.0 and 2.0 are used. $p = 1.0$ leads to a conservative estimate, $E_{d,max}$ whereas $p = 2.0$ yields a lower value, $E_{d,min}$.

6.4. WETTED FLOW RESULTS

This section describes the results for wetted flow simulations, i.e. without cavitation. Among the results reported are the lift coefficient $C_L = L/(q_\infty cs)$, the drag coefficient $C_D = D/(q_\infty cs)$, the pressure coefficient $C_p = (p - p_\infty)/q_\infty$ and the streamwise skin friction coefficient $C_{f,x} = \tau_{w,x}/q_\infty$ at the wing midspan. The results are compared against experimental results by Aït Bouziad [256] (designated EPFL), and against results obtained with the panel code XFoil [257]. With XFoil the 2D NACA0009 cross-section was computed at an angle of attack at the centreline (α =9°). Since the 3D effects due to the twist are not included in XFoil, differences in the magnitude of C_p are to be expected. Nevertheless, it gives a good indication of the pressure distribution along the chord.

6.4.1. STEADY INFLOW CONDITION

Most of the computations with a steady inflow converge to a steady solution, with the exception of flow solutions which show leading edge separation extending along the chord. Consequently, the results in this section are obtained with a larger time step which is kept fixed to $\Delta t^* = U_\infty \times \Delta t / c = 6.97 \times 10^{-3}$, leading to a maximum and average Courant number of 48 and 2.3 on the finest grid, and 22 and 1.2 on the coarsest grid, respectively. These large Courant numbers were deemed acceptable based on preliminary computations with a smaller time step, which showed the same solutions with a similar iterative convergence.

Fig. 6.5 shows the lift and drag coefficient as a function of the grid refinement h_i/h_1 and the physical resolution f_k, together with the discretisation error as error bars. Both the lift and drag have a low grid dependency, leading to small discretisation errors. f_k has little influence on the lift coefficient in the range 1.00 – 0.50, however the lift coefficient suddenly drops by almost 10% for $f_k = 0.25$. For $f_k = 0.00$, lift increases again. This will be commented upon later. The drag coefficient shows a linear decrease with decreasing f_k, with the exception for $f_k = 0.25$ on the two finest grids, and $f_k = 0.00$, where the drag suddenly increases. A division of the drag into pressure and friction drag shows that the friction drags linearly decreases with f_k. However for $f_k = 0.00$ and 0.25 on the fine grids the pressure drag doubles, due to flow separation occurring at the leading edge, as will be explained later based on flow visualisations.

The effect of reducing f_k is visualized in Fig. 6.6 by showing the time-averaged streamwise skin friction coefficient, limiting streamlines and time-averaged normalized streamwise velocity $\overline{u}/U_\infty$. With a reduction in f_k, the streamwise skin friction decreases. For $f_k = 0.25$, the flow starts to change. Depending on the grid resolution, two solution regimes are predicted. For the coarser grids ($G3$ and $G4$), turbulent separation is observed in the streamlines near the trailing edge along the entire span of the wing. Along the spanwise position the angle of attack varies, the separation region moves towards the leading edge with increasing angle of attack. This is accompanied by a negative friction coefficient on the wing surface, indicating recirculating flow over the wing. On the finer grids ($G1$ and $G2$), the separation location moves further upstream, and the flow exhibits laminar separation close to the leading edge. The flow solution is now also unsteady, which together with the separation at the leading edge, is a clear indication of a stall condition. After the laminar separation bubble the flow periodically detaches and reattaches, leading to a time-averaged positive skin friction, which increases the pressure drag as observed in Fig. 6.5. The grid sensitivity of the flow separation is likely related to the $\overline{x}_c^+$ resolution behind the leading edge (see Fig. 6.4). While it is low at the leading edge, on grids $G3$ and $G4$ it more than doubles over a chordwise distance of $\approx c/30$, thereby suppressing the flow separation. On the finer grids, $\overline{x}_c^+$ still increases, but the increase is less drastic, allowing the grid to resolve the flow separation. The results for

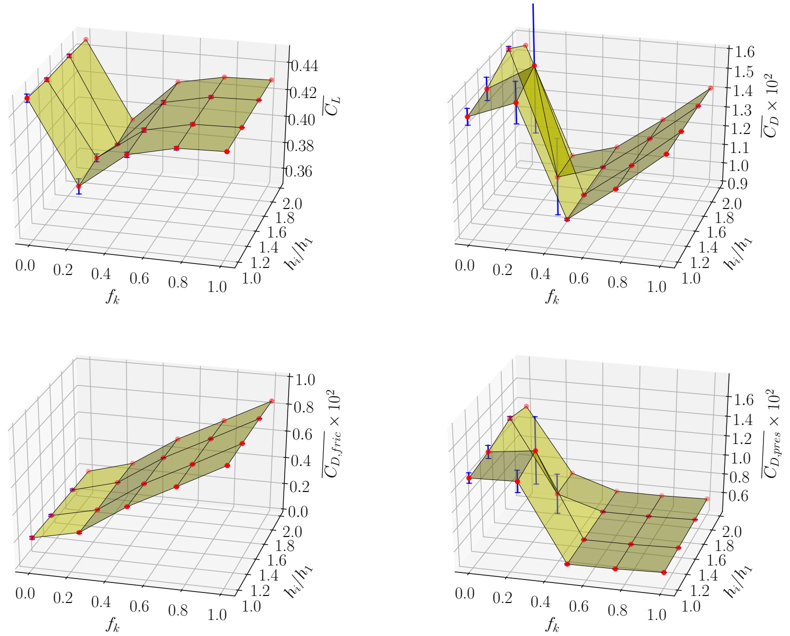

Figure 6.5: Time-averaged lift and drag coefficient (top row), and friction and pressure drag (bottom row) as function of the refinement ratio h_i/h_1 and f_k, for wetted flow simulations with steady inflow. The dots are the results, the blue vertical lines indicate the uncertainty $E_{d,min}$.

$f_k = 0.00$ show this stall condition on all grids; due to the absence of a turbulence model, the flow instability is not suppressed by any eddy-viscosity. Again the time-averaged skin friction is positive behind the separation bubble at the leading edge, leading to an increased pressure drag. For this f_k value, the largest differences occur more towards the tunnel side wall where the angle of attack is lower. On the coarse grid there is a large region with negative friction, which decreases in size on the finer grids.

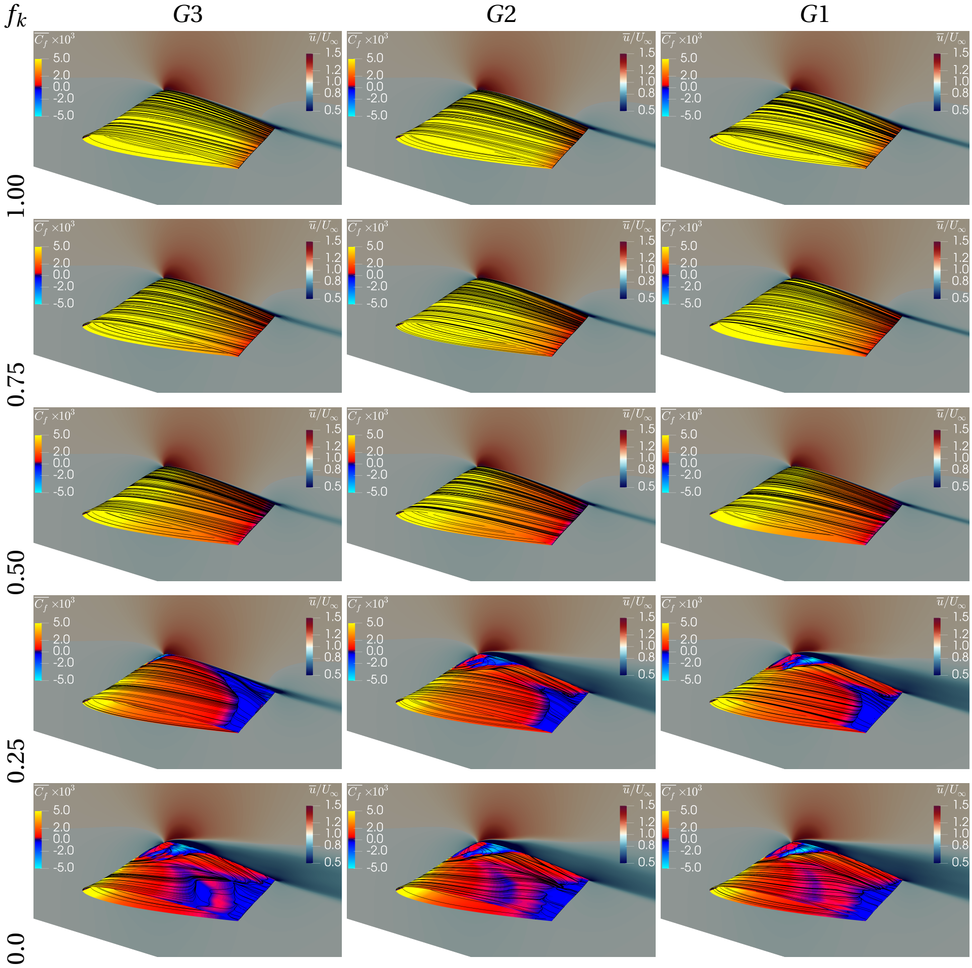

Figure 6.6: Limiting streamlines and time-averaged skin friction coefficient $\overline{C_{f,x}}$ on the wing surface, and streamwise velocity $\overline{u}/U_\infty$, for different f_k values, using different grids with steady inflow. Results for $G4$ are similar to $G3$ and are therefore not shown. Flow from left to right.

To quantify the differences in time-averaged skin friction coefficient, Fig. 6.7 shows $\overline{C_{f,x}}$ at the wing centreline. $\overline{C_{f,x}}$ decreases with decreasing f_k. For $f_k = 1.00$, $\overline{C_{f,x}}$ is close to the XFoil prediction, the deviation in slope is likely related to 3D effects which are not included in the XFoil prediction. The trend remains the same in the range $0.5 \leq f_k \leq 1.0$, only the magnitude varies. For $f_k = 0.25$ on the coarse grids, $\overline{C_{f,x}}$ shows a trough for $0.05 < x/c < 0.1$, after which it increases until $x/c = 0.2$ and then decreases again until it becomes negative for $x/c > 0.4$. On these coarser grids, the low $\overline{C_f}$ values are likely related to an absence of transition, i.e. the flow remains laminar along the chord. On the finer grids, the flow separates at the leading edge, so $\overline{C_{f,x}}$ shows a peak at $x/c \approx 0.05$, after which it becomes negative until $x/c \approx 0.4$, and then remains positive until the trailing edge. The leading edge separation induces transition at $x/c \approx 0.4$, leading to a higher $\overline{C_f}$ than observed for $f_k = 0.25$ on the coarser grids. Fig. 6.6 already showed that this pattern varies significantly along the span of the wing. Finally for $f_k = 0.00$, the pattern is similar on all grids. There is a large separation region at the leading edge, inducing transition. $\overline{C_{f,x}}$ on the fine grids ($G2$ and $G1$) equals the $\overline{C_{f,x}}$ predicted by $f_k = 0.25$, which is in line with the earlier visual observations.

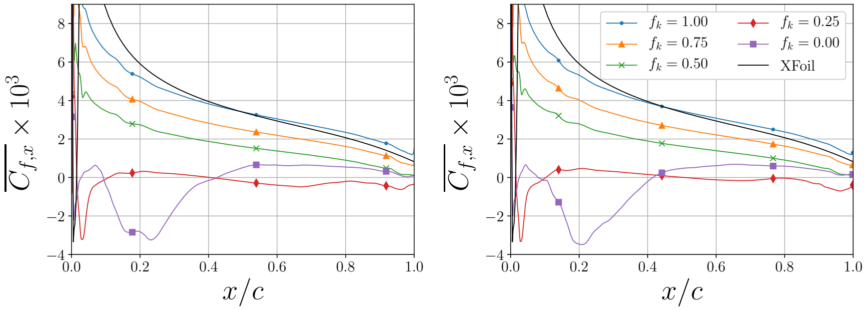

(a) $G4$ (b) $G3$

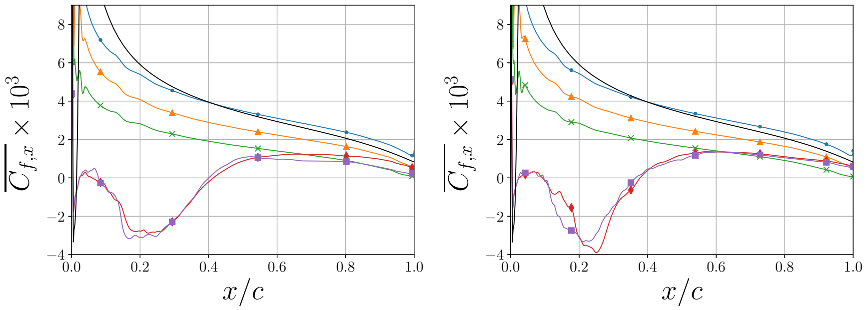

(c) $G2$ (d) $G1$

Figure 6.7: Time-averaged streamwise skin friction coefficient with steady inflow, for varying f_k using different grids.

The pressure distribution at the wing surface is less affected by the flow pattern, as shown in Fig. 6.8. The different computations show little difference, with the exception of the $f_k = 0.00$ and 0.25 on grids $G2$ and $G1$, which is of course directly linked to the unsteady flow separation. The other computations predict similar $\overline{C_p}$ distributions, but for $f_k = 0.25$, $\overline{C_p}$ is slightly lower in the range $0.2 \lesssim x/c \lesssim 0.7$, and higher for $x/c \gtrsim 0.7$. Two observations can now be made. Firstly, both $\overline{C_{f,x}}$ and $\overline{C_D}$ are strongly affected by f_k, and vary for each f_k value; while $\overline{C_p}$ and $\overline{C_L}$ show two sets of solutions based on f_k being above or below a certain threshold. Secondly, in the range $x/c \leq 0.4$, $\overline{C_p}$ does not depend on f_k, which is favourable for cavitation inception predictions. The cavitation behaviour and attached sheet cavity extent will be insensitive to f_k, and consequently to the lack of inflow turbulence.

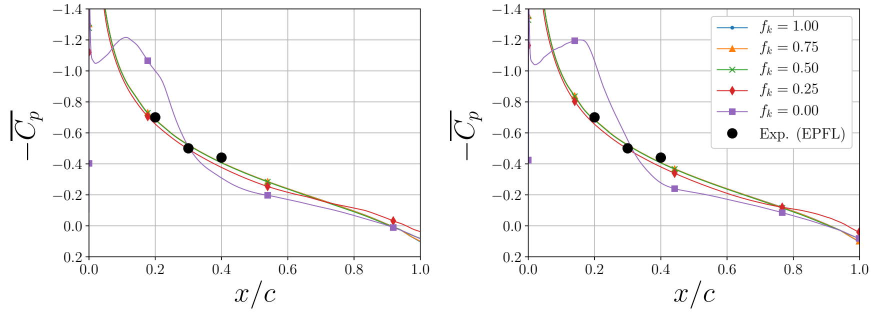

(a) *G4*

(b) *G3*

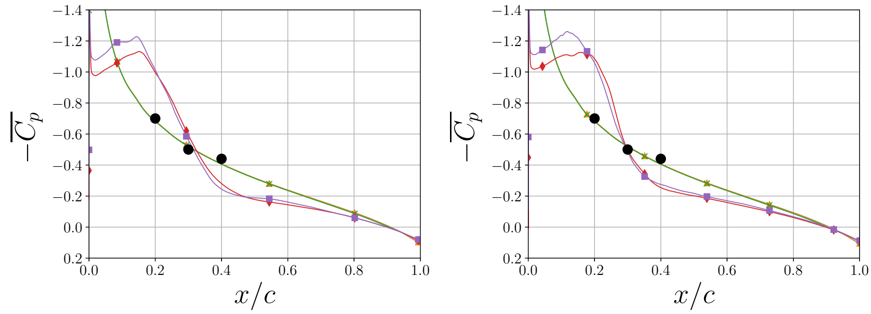

(c) *G2*

(d) *G1*

Figure 6.8: Time-averaged surface pressure coefficient $\overline{C_p}$ for varying f_k using different grids with steady inflow.

What happens when f_k is reduced? The change in the flow is related to changes in the turbulence intensity, both modelled and resolved. Due to the reduction of f_k the effect of modelled turbulence is reduced, while due to the steady inflow boundary condition the resolved flow is laminar (i.e. the resolved turbulence intensity is zero). This is clearly visible in Fig. 6.9, which shows k, ω and ν_t/ν between the location where later resolved inflow turbulence will be inserted, and the leading edge. Both k and ω decrease downstream, but since ν_t/ν depends on the ratio of k and ω (Eq. 2.28), ν_t/ν is relatively constant along the streamwise direction. However with decreasing f_k, ν_t/ν decreases, leading to the flow becoming laminar with decreasing f_k. Note that for $f_k = 0.00$, $\nu_t/\nu = 0$ by definition. Due to low inflow turbulence level, by pass transition on the wing surface is delayed, and the flow separates at the trailing edge. For even lower f_k, the flow becomes completely laminar and separates at the leading edge. This was already observed by Foeth [235], who recognised that for the limited Reynolds numbers typical for model scale wings transition to turbulence does not occur at the leading edge unless the boundary layer is locally disturbed, hence the application of surface roughness in the experiments. It is known from literature that laminar boundary layers separate earlier than turbulent boundary layers [258]. The occurrence of turbulent trailing edge separation leads to the decrease in lift coefficient, and the decrease in drag coefficient is proportional to the reduction in skin friction due to the laminar boundary layer along the chord. With leading edge separation the lift and drag coefficient increase again, due to a different pressure distribution. Unsteady structures can be observed (e.g. based on the $Q-$criterion), potentially leading to a wrong conclusion that the approach is resolving a turbulent boundary layer.

Up to now, with the exception of the work by Foeth [235] who employed surface roughness, separation has not been reported in literature for this test case. A number of reasons can be identified to explain this. Simulations using RANS or hybrid models do not show flow separation due to the inherent assumptions employed in RANS in the boundary layer, leading to transition to turbulent flow at the leading edge. For SRS results, such as LES and PANS, it is shown that for intermediate f_k values, such as 0.25, the behaviour is grid sensitive and only occurs on fine grids. The literature overview in Fig. 6.1 and Fig. 6.2 showed that most LES results reported in literature are obtained using coarser grids than the ones here, thereby potentially hiding this behaviour. It must also be remarked that most investigations in literature focus on cavitation dynamics. However, due to the nature of the test case, when cavitation is included, this separation is again masked since due to the cavitation inception criterion used in CFD, the sheet cavity occurs at the same location as the flow separation at the leading edge. The use of XFoil further confirms the hypothesis that the leading edge separation with a laminar inflow is physical. When using a turbulent inflow, similar $\overline{C_{f,x}}$ and $\overline{C_p}$ distributions are found, however when reducing the inflow turbulence (when moving from what is known in XFoil as a 'dirty' towards a 'clean' wind tunnel) the solution becomes more and more difficult to converge, again pointing to unsteady flow separation at the leading edge.

To ensure that further grid refinement does not yield different flow behaviour, additional $f_k = 0.25$ and 0.00 computations were performed on a grid with a local refinement box surrounding the wing (grid $G0^*$). The integral values are $\overline{C_L} = 0.35$ and 0.42, $\overline{C_D} \times 10^2 = 1.00$ and 0.85 for $f_k = 0.25$ and 0.00 respectively. The drag appears to continue to increase with increasing simulation time. Fig. 6.10 shows $\overline{C_{f,x}}$ and $\overline{C_p}$ at the midspan, along with a flow visualisation for $f_k = 0.00$. For this additionally refined grid, the wing does not show such a large region of recirculating flow at the leading edge, as for grid $G1$, leading to a pressure distribution closer matching the experiments. At a first glance it appears that refining the grid to this level solves the problems observed previously in this section. However, investigation of $\overline{C_f}$ shows that leading edge separation still occurs. The difference is that here $\overline{C_f}$ becomes positive again at $x/c \approx 0.1$, after which it remains positive until close towards the trailing edge. On grid $G1$, $\overline{C_f}$ also seemed to recover at $x/c \approx 0.07$, but then decreases again and does not become positive until $x/c \approx 0.4$. The increased grid resolution, decreases the leading edge separation, and therefore leads to a reasonable prediction of the drag. The lift however, is even lower than for the PANS results on coarser grids. Potentially, the leading edge separation is reduced even more on a further refined grid, however it is important to realise that this grid is already re-

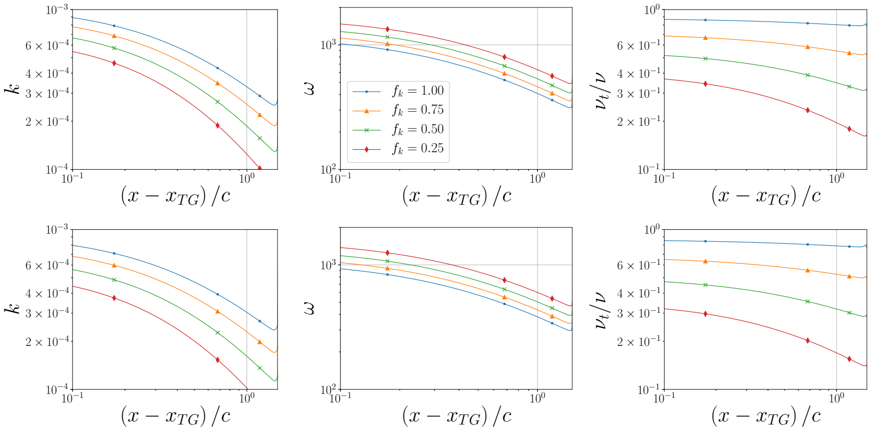

Figure 6.9: Time- and $y-z$ plane spatially-averaged modelled turbulence kinetic energy k (left), dissipation rate ω (centre) and eddy-viscosity ratio ν_t/ν (right) decay for steady inflow. The inlet boundary is located at the left of the figures, the leading edge at the right. Results obtained on grid $G4$ (top row) and $G1$ (bottom row) for varying f_k. Recall that for $f_k = 0.00$, k and ν_t/ν are, by definition, zero.

fined to a level which is currently unaffordable for industrially oriented cases. This grid is significantly finer than LES grids employed in the literature for this test case.

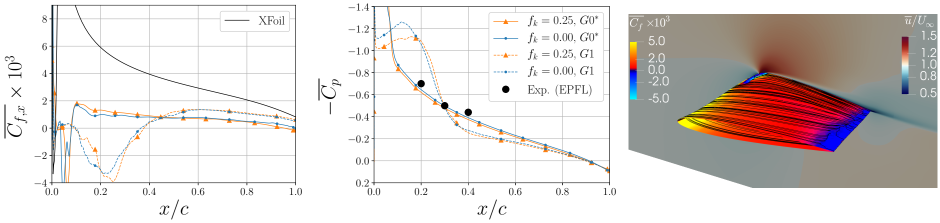

Figure 6.10: $\overline{C_{f,x}}$ (left), $\overline{C_p}$ (centre), and flow visualisation for $f_k = 0.00$ on grid $G0^*$ (right) for steady inflow.

To summarise, it is clear that flow predictions with SRS with a steady inflow do not match experimental conditions, but it could be argued that this would have little effect on cavitation predictions due to the inception criterion used in CFD. $\overline{C_p}$ does not vary, so the inception behaviour will be the same. However, it should be emphasized that the laminarization of the flow is a problem, as also known from literature [28, 193]. Firstly, $\overline{C_p}$ does change towards the trailing edge, potentially affecting the development and dynamics of shed cavities. Secondly the integral quantities (lift and drag) differ significantly from experiments, making validation impossible. It is interesting to note that the lift decreases with f_k, away from the experimental value, with the exception of $f_k = 0.00$, which gives higher values than $f_k = 1.00$. From this, the incorrect conclusion could be made that $f_k = 0.00$, also known as ILES, does not suffer from these problems and yields the best match for experimental values. Nevertheless, as shown, $\overline{C_D}$, $\overline{C_{f,x}}$ and $\overline{C_p}$ are different, and in fact the entire flow changes, from a steady attached flow to an unsteady flow separating at the leading edge. Indeed, the lift is better predicted, but for the wrong reasons. Instead it is necessary to introduce synthetic inflow turbulence to obtain a turbulent boundary layer from the leading edge onwards, to better match the experimental results.

6.4.2. RESOLVED TURBULENT INFLOW CONDITION

To trigger the flow to become turbulent and suppress unphysical separation, synthetic turbulence is added at the inflow. The need for such boundary conditions is well known for LES and PANS [28, 193], however LES results in the open literature for this specific test case do not employ such methods.

The ITG is located at $x_{TG} = -2c$, with turbulent fluctuations inserted in a plane perpendicular to the flow with dimensions $c \times c$ and a thickness in primary flow direction of $c/15$, which corresponds to $2-3$ cells in streamwise direction. A number of conditions with varying levels of turbulence intensity and integral length scale are investigated, the settings at the location of the ITG are summarized in Tab. 6.2. The decay in turbulence kinetic energy is compared to the slope of theoretical decay of isotropic homogeneous turbulence [259]

$$\frac{\overline{u_i u_i}}{U_\infty^2} \propto \left(\frac{x - x_{TG}}{\mathscr{L}}\right)^{-n}. \tag{6.4}$$

In this equation x indicates the measurement location and n is approximately equal to 1.27, based on experiments. Tab. 6.2 also shows the turbulence intensity, $\mathscr{I} = \sqrt{2/3\langle K\rangle}/U_\infty = \sqrt{\overline{u_i u_i}}/U_\infty$, expected at the leading edge based on the theoretical decay. For Case A and C the turbulence intensity is comparable to the experimental setup; no integral length scale was reported for the experiments.

From a theoretical perspective, it is incorrect to insert velocity fluctuations in a computation with $f_k = 1.00$, since for such a f_k value all turbulence should be modelled. In this chapter it is still done, to investigate the trends. Due to the use of pseudo-random numbers the curves for the different computations overlap.

The time step for these computations is kept fixed to $\Delta t^* = U_\infty \times \Delta t/c = 6.97 \cdot 10^{-4}$, with maximum Courant numbers of approximately 5 occurring close to the leading edge. In the remainder of the domain the Courant number is well below 1. The L_2 norms of the residuals are $\mathcal{O}(10^{-4})$, $\mathcal{O}(10^{-6})$, $\mathcal{O}(10^{-7})$ and $\mathcal{O}(10^{-7})$, for momentum, pressure, turbulence kinetic energy and dissipation, respectively. Of these equations only the ω equation stagnates, the other equations keep on converging and decrease at least one order of magnitude during a time step. The L_∞ norms for the same equations are $\mathcal{O}(10^{-2})$, $\mathcal{O}(10^{-3})$, $\mathcal{O}(10^{-4})$ and $\mathcal{O}(10^{-3})$. The largest residuals occur in the cells where the ITG is located. During the computation the flow passes the chord seven times, with averaging applied during the final four time units ($T_{wf} = c/U_\infty$), leading to a maximum statistical error of 5%, which occurs for the case with highest inflow turbulence intensity.

First, cases A and B are compared on all grids with $0.0 \leq f_k \leq 1.0$. The streamwise development of the synthetic isotropic turbulence between the ITG and the leading edge, is shown for $f_k = 0.25$ in Fig. 6.11. The Reynolds stresses decrease around two orders of magnitude on the coarse grid, while on the fine grid the decrease is about one order of magnitude, which is comparable to Eq. 6.4. An initially surprising observation is that the decay of resolved turbulence is almost insensitive to the f_k value (not shown in the

Table 6.2: Settings for the homogeneous, isotropic, inflow turbulence at the ITG $\overline{u_i u_i}/U^2_{\infty TG}$, and theoretically expected inflow turbulence at the leading edge $\overline{u_i u_i}/U^2_{\infty LE}$ and turbulence intensity $\mathscr{I}_{LE}$, following the slope defined by Eq. 6.4.

Case	$\mathscr{L}/c$	$\overline{u_i u_i}/U^2_{\infty TG}$	$\overline{u_i u_i}/U^2_{\infty LE}$	$\mathscr{I}_{LE}/\%$
A	0.033	0.01	0.0004	2.0
B	0.013	0.10	0.004	6.3
C	0.013	0.01	0.0004	2.0
D	0.033	0.10	0.004	6.3
E	0.013	0.20	0.008	8.9
F	0.013	0.30	0.012	11.0
G	0.013	0.40	0.016	12.7
H	0.013	0.60	0.024	15.5

graph), suggesting no effect of the chosen f_k on the computations. However, the statistical representation of turbulence (the ‘RANS’ contribution) does vary with f_k, a higher f_k leads to a higher eddy-viscosity. As observed earlier, on finer grids the eddy-viscosity levels also increase.

These results, in combination with results from literature [168, 193] suggest that while the selected value of f_k strongly affects the production of modelled turbulence, it does not affect the decay of resolved turbulence in this streamwise range. While this might seem counterintuitive, it can be explained from the equations which are being solved. The filtered Navier-Stokes equations are independent of f_k, f_k only affects the turbulence transport equations for k and ω. Due to the formulation of the ITG fluctuations are introduced regardless of f_k, which can lead to the unphysical combination of $f_k = 1.00$, i.e. RANS, with resolved turbulent fluctuations. After their addition to the flow, the development of the fluctuations is described by the Navier-Stokes equations. The difference between computations with different f_k values, is the level of ν_t/ν. However in this short range the effect of the increased eddy-viscosity is too small to significantly dampen the velocity fluctuations, and therefore the decay of resolved turbulence is comparable. A similar observation was made when using synthetic turbulence for a channel flow in Chapter 5, close to the ITG the solutions for different f_k values are comparable, and velocity fluctuations are being dampened only further downstream. The comparable decay is also an indication that the grids are fine enough to not add excessive diffusion.

In Fig. 6.12 and 6.13, the flow is visualized using the time-averaged streamwise velocity and friction coefficient at the wing surface, for different f_k values on grids $G4$ and $G1$. The visualisation shows that while the flow at the surface is affected by the inflow turbulence, for $f_k = 0.25$ a region of separated flow still occurs near the trailing edge. The size of the separated flow region is reduced compared to the results obtained with a steady inflow, especially on the finer grid. The separation is also smaller for Case B than for Case A. When $f_k = 0.00$, the region of separation is larger, especially on the coarser grid. This is an indication of the increased grid sensitivity of ILES, due to the absence of a sub-filter model. Note that for both these levels of inflow turbulence, for all f_k values, the large flow separation at the leading edge as observed for low f_k values without inflow turbulence (Fig. 6.6) disappears.

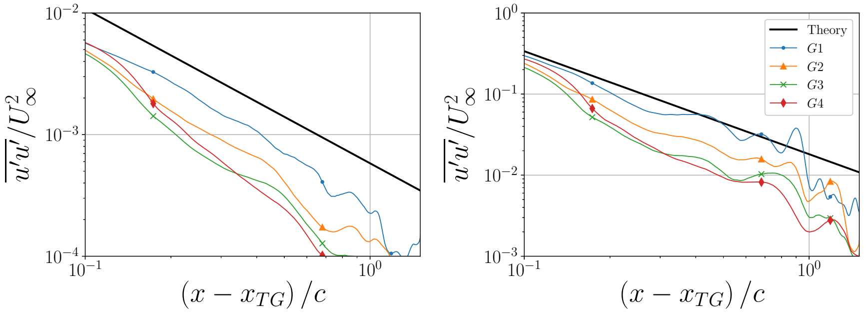

Figure 6.11: Time- and $y-z$ plane spatially-averaged resolved streamwise Reynolds stresses for Case A (left) and B (right) between ITG and the leading edge, on different grids for $f_k = 0.25$. The results show little dependence on f_k.

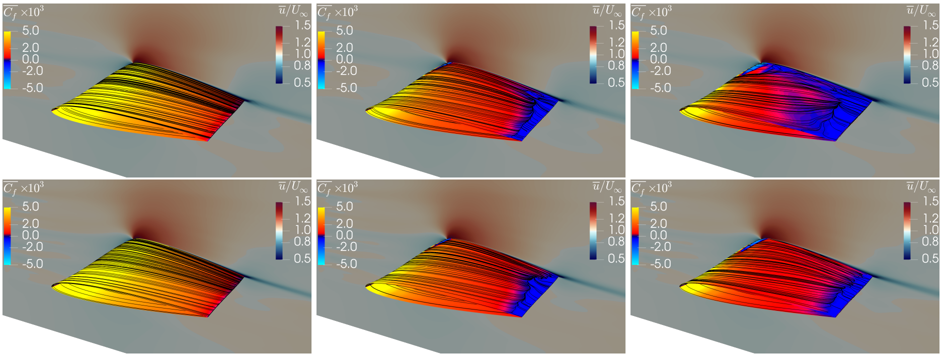

Figure 6.12: Limiting streamlines and time-averaged streamwise skin friction coefficient $\overline{C_{f,x}}$ and time-averaged streamwise velocity $\overline{u}/U_\infty$, on grid $G4$ (top row) and grid $G1$ (bottom row) with a resolved turbulent inflow, Case A. From left to right $f_k = 0.50$, 0.25 and 0.00. Results for $f_k = 1.00$ and 0.75 are similar to $f_k = 0.50$.

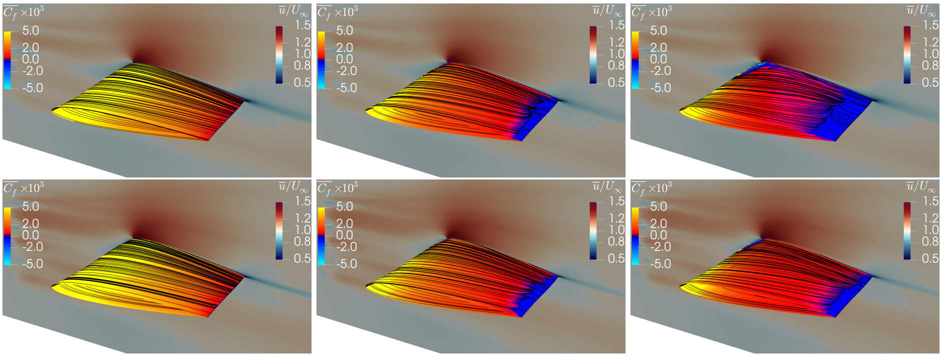

Figure 6.13: Limiting streamlines and time-averaged streamwise skin friction coefficient $\overline{C_{f,x}}$, and time-averaged streamwise velocity $\overline{u}/U_\infty$, on grid $G4$ (top row) and grid $G1$ (bottom row) with a resolved turbulent inflow, Case B. From left to right $f_k = 0.50$, 0.25 and 0.00. Results for $f_k = 1.00$ and 0.75 are similar to $f_k = 0.50$.

The effect on the skin friction coefficient is further analysed in Fig. 6.14, by plotting $\overline{C_{f,x}}$ versus x/c at midspan for varying f_k for the two cases. A comparison with the steady inflow results shows that $\overline{C_{f,x}}$ increases with the addition of inflow turbulence. An increase in Re_{ii} also leads to an increase in $\overline{C_{f,x}}$, independent of f_k used in the computation. As expected, $f_k = 1.00$ gives a RANS distribution, where $\overline{C_{f,x}}$ has a peak at the leading edge and then decreases along the chord, while remaining positive. The magnitude is comparable to the XFoil prediction. With decreasing f_k, the magnitude of $\overline{C_{f,x}}$ decreases along the chord. For $f_k = 0.50$, there is a slight kink at $x/c = 0.1$, but the profile remains similar to the RANS results. However the result for $f_k = 0.25$ clearly shows not only a much lower $\overline{C_{f,x}}$, but also drops after the leading edge to a negative value, after which it increases again to a constant value along the wing. This shows that the flow is still laminar at the leading edge, but transitions to turbulent flow at $x/c = 0.1$, indicating that the inflow turbulence is not sufficient to trigger a turbulent flow at the leading edge. For Case A, it can also be observed that for $x/c > 0.9$, $\overline{C_{f,x}}$ still becomes negative, indicating turbulent flow separation. It is noteworthy that on finer grids $\overline{C_{f,x}}$ always increases, independent of f_k. For $f_k = 0.25$, this has the effect that, while still present, the separation region at the trailing edge is reduced (as was observed previously in Fig. 6.12). On the coarse grid, $\overline{C_{f,x}}$ for $f_k = 0.00$ remains close to zero for both cases, indicating that transition does not occur and that the flow remains laminar. On the finer grid it increases, but remains close to zero along the chord.

When comparing Case B to Case A, it can be observed that the increase in inflow turbulence leads to an increase in $\overline{C_{f,x}}$ along the chord for all f_k values, except for $f_k = 0.00$ on the coarse grid. For Case B, on the coarse grid there is still a small region where $\overline{C_{f,x}} < 0$ close to the leading edge, while on the fine grid $\overline{C_{f,x}}$ remains positive along the wing.

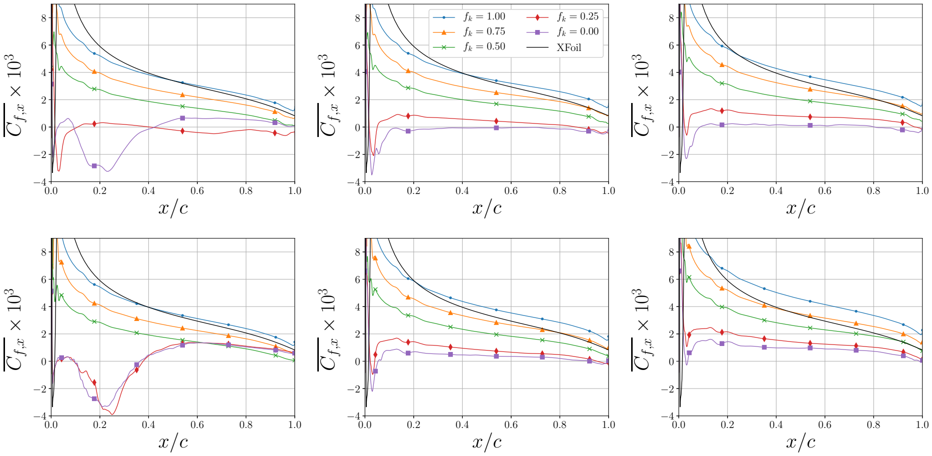

(a) Steady inflow (b) Case A (c) Case B

Figure 6.14: Time-averaged streamwise skin friction coefficient $\overline{C_{f,x}}$ for a steady inflow and resolved turbulent inflows Case A and Case B, on grid $G4$ (top row) and $G1$ (bottom row) for varying f_k.

The effect on the pressure coefficient is limited, and is therefore not shown. There is no difference between different f_k values, except at the trailing edge ($x/c > 0.9$) in the location of turbulent flow separation. As expected, this difference is larger on the coarse grid, $G4$, and larger for Case A than for Case B. For Case A, there is a still a difference between $f_k = 0.25$ and 0.00 and the other f_k values on the finest grid; for Case B there is no longer an observable difference between the different f_k values on the finest grid.

The effect on the integral quantities is presented in Fig. 6.15, where the time-averaged lift and drag coefficient are given as a function of the grid refinement and f_k. The predicted trend for the lift for Case A is similar to what was observed without inflow turbulence (Fig. 6.5). There is a sudden decrease in $\overline{C_L}$ for $f_k = 0.25$, but the predicted lift by $f_k = 0.00$ is again approximately 5% larger than for $f_k = 1.00$, which is caused by a higher pressure on the pressure side of the wing between the leading edge and midchord, close to the tunnel wall. For Case B the decrease at $f_k = 0.25$ is smaller, and $\overline{C_L}$ is more constant across the f_k range, especially on the finest grid. The addition of inflow turbulence leads to a temporally varying lift coefficient, since now the effective angle of attack varies in time. As expected the standard deviation σ_{C_L} for Case B is larger than for Case A due to the higher turbulence intensity. For Case A, $\sigma_{C_L} \times 10^3 \approx 6$ while for Case B, $\sigma_{C_L} \times 10^3 \approx 23$. For the drag coefficient, in both cases A and B, the trend is the same as for the case with a steady inflow: $\overline{C_D}$ decreases with decreasing f_k. For both cases, $\overline{C_D}$ increases across the f_k range compared to the steady inflow, and $\overline{C_{f,x}}$ for Case B is larger than for Case A. Again the standard deviation in the drag coefficient is larger for Case B than for Case A, i.e. $\sigma_{C_D} \times 10^3 \approx 1.3$ versus $\sigma_{C_D} \times 10^3 \approx 0.4$.

It is again emphasized, that, while ILES ($f_k = 0.00$) theoretically should involve the least modelling of turbulence, it is not the best approach. It does yield the highest lift coefficient, but at the same time the predicted drag force is lower than all other results. The skin friction shows that the flow is still laminar, but due to the now absent leading edge separation the lift coefficient is reduced compared to the results with steady inflow. The use of a different convection scheme in the momentum equation might improve these results. It is known from literature that ILES requires a convection scheme which adds enough dissipation to act as a sub-filter model. In the current chapter QUICK is used, which might not fulfil that requirement by either adding too much, or not sufficient dissipation. An investigation into different convection schemes is outside of the scope of the current chapter. The difficulties in predicting integral quantities do indicate that the use of ILES is rather sensitive to the setup, next to the entanglement of modelling and discretisation errors, which is inherent to the method (see Chapter 5. Consequently, in the remainder of this chapter $f_k = 0.25$ is employed.

6.4.3. INCREASING $\mathscr{L}$ VERSUS $\mathscr{I}_{LE}$

When varying both $\mathscr{L}$ and $\mathscr{I}_{LE}$ systematically (cases A, B, C and D), a distinction can be made between the effect of $\mathscr{L}$ versus $\mathscr{I}_{LE}$. These variations are only investigated for $f_k = 0.25$, on the finest grid, since here the largest difference between results from cases with and without inflow turbulence occur. Varying $\mathscr{L}$ has almost no effect on the time-averaged lift and drag coefficient. However, with a smaller integral length scale, the standard deviation of the signal increases, see Tab. 6.3. Increasing $\mathscr{I}_{LE}$ leads to an increase of 5 – 10% in time-averaged quantities; as expected the increase in standard

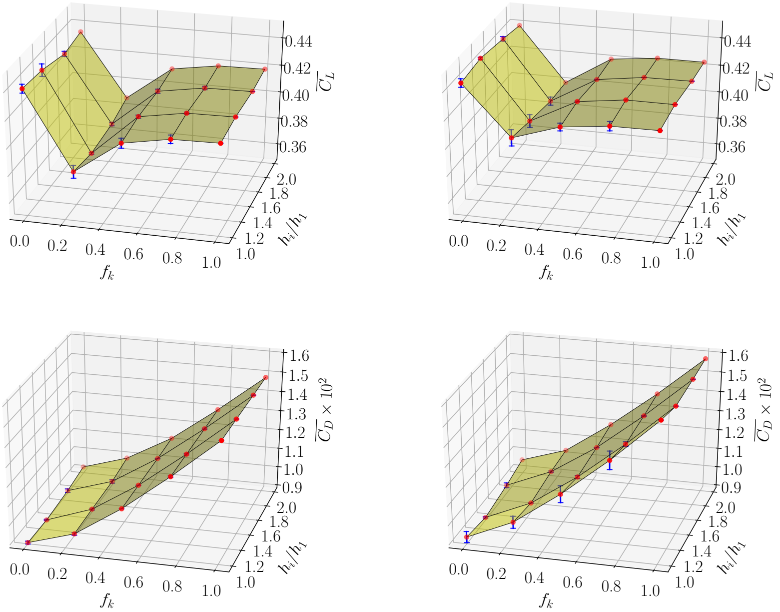

Figure 6.15: Time-averaged lift (top row) and drag coefficient (bottom row) as function of the refinement ratio, h_i/h_1, and f_k, for wetted flow simulations with a resolved turbulent inflow, Case A (left) and Case B (right). The dots are the results, the blue vertical lines indicate the uncertainty $E_{d,min}$.

deviation is again significantly larger (between 2 and 3 times larger). The streamwise decay of $\mathscr{I}_{LE}$ (not shown) is as expected comparable for all computations, but varies in magnitude depending on the inflow $\mathscr{I}_{LE}$.

Table 6.3: Overview of integral quantities as function of the inflow turbulence level at the ITG and integral length scale on grid $G1$ with $f_k = 0.25$.

$\mathscr{L}/c$	0.013		0.033	
$\mathscr{I}_{LE}$	$\overline{C_L}$	$\sigma_{C_L} \times 10^3$	$\overline{C_L}$	$\sigma_{C_L} \times 10^3$
2.0	0.38	7.6	0.38	4.1
6.3	0.41	25.3	0.39	10.8
	$\overline{C_D} \times 10^2$	$\sigma_{C_D} \times 10^3$	$\overline{C_D} \times 10^2$	$\sigma_{C_D} \times 10^3$
2.0	0.98	0.5	0.98	0.3
6.3	1.03	1.5	1.03	0.7

The flow visualisation in Fig. 6.16 is in line with previous results, modifying $\mathscr{L}$ shows only small differences, while increasing $\mathscr{I}_{LE}$ decreases the size of separation region at the trailing edge. This is also clearly visible in Fig. 6.17, where $\overline{C_{f,x}}$ increases with $\mathscr{I}_{LE}$. It is important to realise that the location of transition is not affected by the settings of the ITG, only the magnitude of the skin friction. For $\mathscr{I}_{LE} = 2.0\%$, there is only a difference between $\mathscr{L}/c = 0.013$ and 0.033 near the trailing edge, whereas for $\mathscr{I}_{LE} = 6.3\%$, $\mathscr{L}/c = 0.013$ yields a higher skin friction along the chord. The increase in $\overline{C_{f,x}}$ manifests itself already at the leading edge. All computations show a trough at $x/c \approx 0.05$, but the minimum $\overline{C_{f,x}}$ varies. For $\mathscr{I}_{LE} = 2.0\%$, for both integral length scales $\min\left(\overline{C_{f,x}}\right) \times 10^3 \approx -1$, indicating locally recirculating flow. The lack of difference between the two integral values indicates that while the inflow turbulence intensity is high enough to prevent leading edge separation on the wing, due to the turbulence decay it is too low at the leading edge to further affect the boundary layer flow. When the inflow turbulence intensity is increased to $\mathscr{I}_{LE} = 6.3\%$, $\min\left(\overline{C_{f,x}}\right)$ increases. When $\mathscr{L}/c = 0.033$ the minimum is close to 0, while for the smaller integral length scale the minimum is approximately +1. Here the inflow turbulence intensity does affect the boundary layer flow, the smaller integral length is closer in magnitude to the turbulent length scales occurring closer to the wing surface, leading to an increasingly turbulent boundary layer and therefore increased skin friction. For the pressure distribution, again no differences are observed, except near the trailing edge.

These observations imply that a sufficiently small integral length scale can trigger transition directly at the leading edge, similarly to roughness applied to the wing. However, such a small length scale must be supported by the grid to be convected from the ITG until the leading edge and enter the boundary layer. Due to the employed grid resolutions in this chapter, no integral length scales below $\mathscr{L}/c = 0.013$ are investigated. For the remainder of this chapter, this smaller length scale is employed.

6.4.4. THE EFFECT OF INCREASING INFLOW TURBULENCE INTENSITY

To investigate the effect of increasing the inflow turbulence intensity, cases B, C, E, F, G and H are compared. The integral length scale is kept fixed to $\mathscr{L}/c = 0.013$, and only

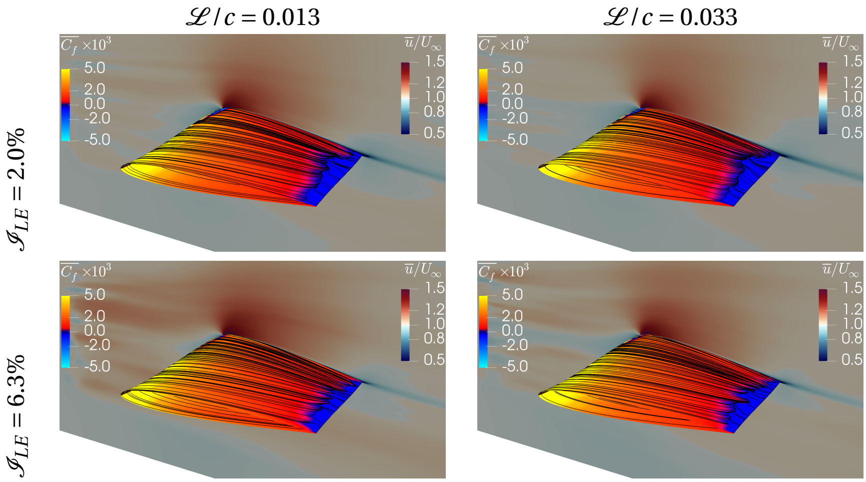

Figure 6.16: Limiting streamlines and time-averaged streamwise skin friction coefficient on the wing surface, and streamwise velocity, for $f_k = 0.25$ on grid $G1$ with a resolved turbulent inflow.

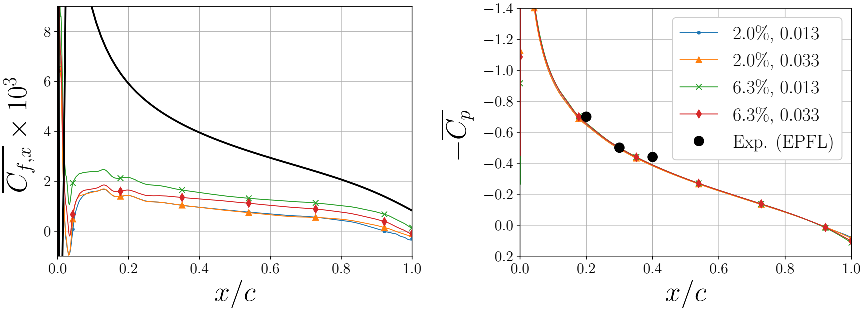

Figure 6.17: Time-averaged streamwise skin friction (left) and surface pressure coefficient (right) for $f_k = 0.25$ on grid $G1$ with a resolved turbulent inflow, as function of the inflow turbulence level and integral length scale. The legend indicates $\mathscr{I}_{LE}$ and $\mathscr{L}/c$.

grid $G1$ with $f_k = 0.25$ is investigated. The streamwise development of Re_{ii} follows the theoretical decay for all cases, and an increase in Re_{ii} also leads to an increase in ν_t/ν.

The effect on the integral quantities is shown in Fig. 6.18. Both the time-averaged lift and drag increase with increasing inflow turbulence, and both quantities increase by approximately 10% between the lowest and the highest inflow turbulence levels. However the difference between a RANS solution and a SRS solution without inflow turbulence is much larger for the drag than for the lift, as seen in previous sections. So while the increase in inflow turbulence results in a lift force which is comparable to the RANS solution, the drag force is still significantly underpredicted. Note also that for both lift and drag, the increase with increasing $\mathscr{I}_{LE}$ seems to converge, meaning even higher inflow turbulence intensities will likely not result in a significantly higher mean force value. Note that for $\mathscr{I}_{LE} = 15.5\%$, $\overline{u_i u_i}/U^2_{\infty TG} = 0.60$, which is very high, but it is employed for the sake of completeness. The standard deviation of the signal has not converged. Furthermore, the large value for $\overline{C_D}$ at $\mathscr{I}_{LE} = 0.0\%$ is caused by the separation at the leading edge, so this should not be interpreted as the ‘correct’ result.

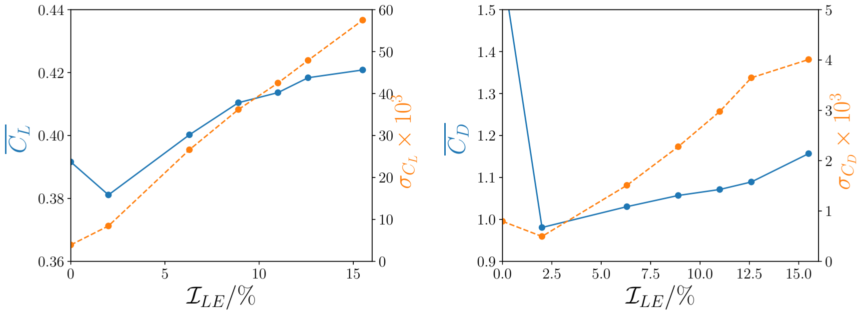

Figure 6.18: Time-averaged (solid lines) and standard deviation (dashed lines) of lift (left) and drag coefficient (right), for $f_k = 0.25$ on grid $G1$ with a resolved turbulent inflow, as function of the inflow turbulence level. The legend indicates $\mathscr{I}_{LE}$.

Finally, the effect of increasing inflow turbulence intensity on $\overline{C_{f,x}}$ and $\overline{C_p}$ is investigated in Fig. 6.19. The $\overline{C_{f,x}}$ profiles show a small separation at the leading edge for non-zero $\overline{u_i u_i}/U^2_{\infty}$, leading to transition. This transition location does not vary with the inflow turbulence intensity, although an increase in $\mathscr{I}_{LE}$ does lead to an increase in skin friction along the wing, which is also observed in RANS computations in literature [260]. For $\overline{C_{f,x}}$, the results with the highest $\mathscr{I}_{LE}$ seem to converge, indicating a limit to the skin friction which can be obtained using the ITG on this grid, with this value for the integral length scale. The minimum value of $\overline{C_{f,x}}$ at $x/c \approx 0.05$ also increases, until a limit is reached at approximately $\overline{C_{f,x}} \times 10^3 = 1.1$. A consequence of the increasing inflow turbulence intensity is a change of the slope of $\overline{C_{f,x}}$, in the range $0.1 \leq x/c \leq 0.7$. The peak at $x/c \approx 0.1$ reaches a maximum for $\mathscr{I}_{LE} = 6.3\%$, after which it decreases again, while at $x/c \approx 0.7$ the $\overline{C_{f,x}}$ keeps increasing with increasing $\mathscr{I}_{LE}$. Finally, again for $\overline{C_p}$, there is little difference between the computations with inflow turbulence.

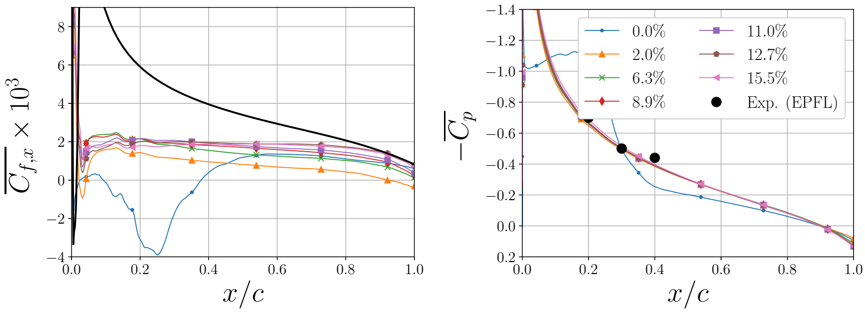

Figure 6.19: Time-averaged streamwise skin friction (left) and surface pressure coefficient (right) for $f_k = 0.25$ on grid $G1$ with a resolved turbulent inflow, as function of the inflow turbulence level.

6.4.5. INFLOW TURBULENCE CONCLUSIONS

Based on these comparisons, the use of synthetic turbulence at the inflow can suppress the large leading edge separation as observed for PANS with a low f_k value and usual steady inflow conditions. Provided that the grid can support the selected integral length scale, a decrease in integral length scales increases the skin friction. The effect of varying $\mathscr{I}_{LE}$ is larger. No inflow turbulence leads to either a large leading edge separation zone, or a laminar flow along the wing. A small amount of inflow turbulence already suppresses the leading edge separation, and leads to a small separation at the leading edge, inducing transition. To increase the lift and drag coefficient, higher inflow turbulence intensities are required. $\overline{C_{f,x}}$ shows that even with the highest levels of turbulence attempted in this chapter, still laminar to turbulent transition is visible downstream of the leading edge. To trigger transition further towards the leading edge, the integral length scale should be reduced. This does require the grids to be refined further, due to the computational costs this was not attempted in the current chapter. The application of inflow turbulence does also decrease the turbulent separation region at the trailing edge, however it was not completely removed. Separation at the trailing edge is never mentioned in literature, however there is an indication that this phenomenon was also present in the experiments. When one of the few reported wetted flow velocity fields obtained with PIV by Foeth [235] is compared with the current computations using the same colour scale, it becomes clear that the turbulent separation at the leading edge also occurred in the experiments. Fig. 6.20 shows the same wavy region of low velocity at the trailing edge, although the velocity scale prohibits the observation of negative velocities at the trailing edge. This implies that turbulent separation at the trailing edge is a feature of this test case, and the removal of this by increasing the inflow turbulence intensity should not be a goal.

$\overline{C_p}$ is only affected near the trailing edge; closer to the leading edge it matches the limited experimental data well. This indicates that the presence of synthetic turbulence should have little effect on cavitation inception (this will be investigated in the next section). This does not mean that cavitation is not affected at all. The presence of resolved turbulence in the flow can potentially disturb the formed cavity, leading to additional dynamics, varying wing loading or noise. Together with the ability to tune the turbu-

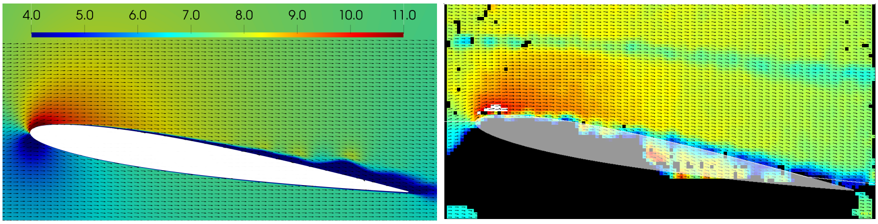

Figure 6.20: Magnitude of velocity at the wing centreline, obtained using PANS with $f_k = 0.25$ on $G4$ (left) and PIV (right). The PIV field is reproduced from Foeth [235], both figures use the same colour scale.

lence inflow statistics, the procedure here used is a promising method to compute noise due to cavitation dynamics, or dynamically varying blade loading for cavitating or non-cavitating propellers in a non-uniform wake field.

6.5. CAVITATING RESULTS

The final investigation in this chapter concerns the application of inflow turbulence to a case with cavitation. Thus far in literature PANS is rarely combined with multi-phase flows, a notable exception being the work by Ji, X. Luo, Y. Wu, et al. [252]. However this work focusses on analysing the cavity dynamics, only a single f_k is attempted with a steady inflow, and the associated modelling errors are not investigated. To the knowledge of the authors the combination of cavitation with inflow turbulence has not been attempted before. The computations are compared against numerical results obtained with DDES and IDDES; and against experimental results by Aït Bouziad [256] and Foeth [235], designated EPFL and Delft, respectively.

In the computations the cavitation number, $\sigma = 1.07$ is matched, while the settings for the inflow turbulence correspond to Case B of the wetted flow computations, meaning $\mathscr{L}/c = 0.013$ and $\mathscr{I}_{LE} = 6.3\%$; the turbulence intensity is comparable to the experiments. For this level of inflow turbulence, the lift coefficient is relatively insensitive to the selected f_k value. The relatively low turbulence intensities limit the risk of numerical instabilities when cavitation modelling is included. Higher inflow turbulence intensities lead to improved drag predictions, but in cavitating computations can also lead to increased computational instability due to the combination of shedding sheet cavitation and inflow turbulence. The integral length scale in the experiments is unknown, the currently employed value is selected based on numerical reasons. The Courant number is well below 1, with the exception of some cells at the trailing edge where a maximum value of 4 is reached. The computations are started from a wetted flow computation with cavitation introduced over a period corresponding to around 0.5 shedding cycles. Based on the TST it is found that the first five shedding cycles must be removed to eliminate the start-up effects. Computations are then continued for an additional six cycles in the stationary range, reducing the statistical uncertainty for the mean lift and drag forces below 3%. A shedding cycle T_s is $1/St$ larger than the wetted flow time unit, so $T_s = T_{wf}/St$. The normalised residuals reach at least 10^{-3} for L_2 for all equations. The L_∞ norms are higher, and occur near the leading edge.

Fig. 6.21 shows the developed time signal and power spectral density (PSD) of the lift coefficient and vapour volume, compared with DDES and IDDES results, following removal of the start-up effects, as discussed in Sec. 6.3. The PSD is computed using the pwelch algorithm and applying a Hann window with 50% overlap, resulting in averaging over 6 segments [261]. Note the significantly larger variations in V_v for IDDES. The PSDs for the PANS computations show no clear dominant shedding frequency due to the windowing, but show that the resolved turbulent inflow leads to a higher PSD at higher frequencies.

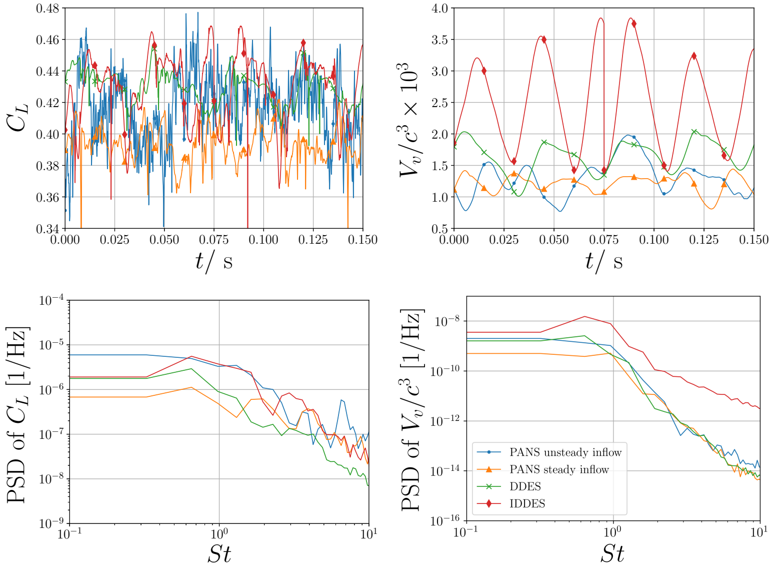

Figure 6.21: Time signal and PSD with windowing of lift coefficient (left) and vapour volume (right), for $f_k = 0.25$ on grid $G1$ without and with inflow turbulence ($\mathscr{L}/c = 0.013$, $\mathscr{I}_{LE} = 6.3\%$). Time axis shifted following removal of start-up effects. DDES results from Vaz et al. [79].

The integral values can be found in Tab. 6.4. As for wetted flow, the application of a resolved turbulent inflow condition increases the lift for the PANS computations; $\overline{C_L}$ is below the lift predicted by the hybrid models (DDES and IDDES). When comparing to experiments, all models underpredict the lift. Fig. 6.1 already showed that this is common in literature, indicating that the discrepancy might also be attributed to unknown experimental uncertainty. It is remarkable that the fluctuations in lift are also significantly smaller for PANS than for the hybrid models, this will be commented upon later. Note that the standard deviation of the lift coefficient is an order of magnitude larger than for the wetted flow computations (Sec. 6.4), indicating that the fluctuations in the lift due to the inflow turbulence are negligible compared to the cavitation induced fluctuations. Unsurprisingly, the predicted drag is higher for all models which employ RANS close the the wall, the fluctuations in drag however are comparable for all models. For PANS, the standard deviation of the drag has increased by a factor 2 compared to wetted flow, again indicating that the fluctuations due to cavitation are dominant. This is confirmed by the observation that the standard deviation for a steady inflow condition is slightly higher than for a resolved turbulent inflow. The average vapour volume increases for PANS when the resolved turbulent inflow condition is employed, but the mean and standard deviation of the vapour volume remain below the predictions done by DDES and IDDES. Finally, the Strouhal number is computed from a single segment PSD of the lift coefficient and vapour volume to emphasize the lower frequencies of the shedding sheet cavity (not shown here). For PANS without inflow turbulence, St_{V_v} is larger than St_{C_L}, implying different mechanisms are responsible for the vapour and lift fluctuations respectively, and indicating additional dynamics in the sheet cavity. For PANS with a resolved inflow, the shedding frequency halves although it must be remarked that this shedding frequency is difficult to discern.

Table 6.4: Integral values of cavitating computations with PANS with a steady and a resolved turbulent inflow and $f_k = 0.25$ on $G1$. DDES results were previously reported in Vaz et al. [79]. St computed from PSDs without windowing (not shown in this chapter).

	Experiment	Steady inflow			Resolved turbulent inflow
Quantity		DDES	IDDES	PANS ($f_k = 0.25$)	PANS ($f_k = 0.25$)
$\overline{C_L}$	0.53	0.43	0.43	0.39	0.41
$\sigma_{C_L} \times 10^3$	-	11.19	19.27	1.56	2.33
$\overline{C_D}$	-	2.28	2.36	1.71	1.74
$\sigma_{C_D} \times 10^3$	-	2.07	3.52	2.26	2.21
$\overline{V_v}/c^3 \times 10^3$	-	1.69	2.42	1.16	1.30
$\sigma_{V_v}/c^3 \times 10^4$	-	2.95	6.90	1.79	2.72
St_{C_L}	0.70	0.56	0.72	0.63	0.37
St_{V_v}	0.70	0.56	0.72	0.81	0.85

Fig. 6.22 shows both the instantaneous and time-averaged streamwise skin friction and velocity at the centreline for both cases with PANS. The trailing edge separation can still be observed towards the tunnel wall, where the angle of attack is smaller, but in the regions downstream of the sheet cavity it is absent. The size decreases again when inflow turbulence is added. An interesting observation is that the low momentum inside the cavity leads to a time-averaged velocity field, which looks similar to the time-averaged velocity field for wetted flow with low f_k without inflow turbulence, i.e. when flow separation occurs at the leading edge (see Fig. 6.6). In this case the presence of cavitation masks the leading edge separation which was observed in the wetted flow computation.

Similar observations can be made from the time-averaged skin friction and pressure coefficients at midspan, see Fig. 6.23. The skin friction coefficient is based on the density of the liquid to enable comparing to the wetted flow results. Again the similarity with wetted flow cases without inflow turbulence is clear in the shape of $\overline{C_{f,x}}$ (compare for example Fig. 6.23 to Fig. 6.7). The application of inflow turbulence leads to a higher $\overline{C_{f,x}}$ in the range $x/c > 0.5$, but towards the leading edge (in the cavitation region), little differences occur. This is not surprising, since in this region the local flow is dominated by the presence of the low momentum fluid inside the cavity. In the range $0.25 \le x/c \le 0.35$, the steady inflow results show more re-circulation than the resolved turbulent inflow results, indicating that the application of inflow turbulence affects the boundary layer in the region where the cavity is periodically being shed.

The time-averaged pressure coefficient clearly shows the presence of cavitation com-

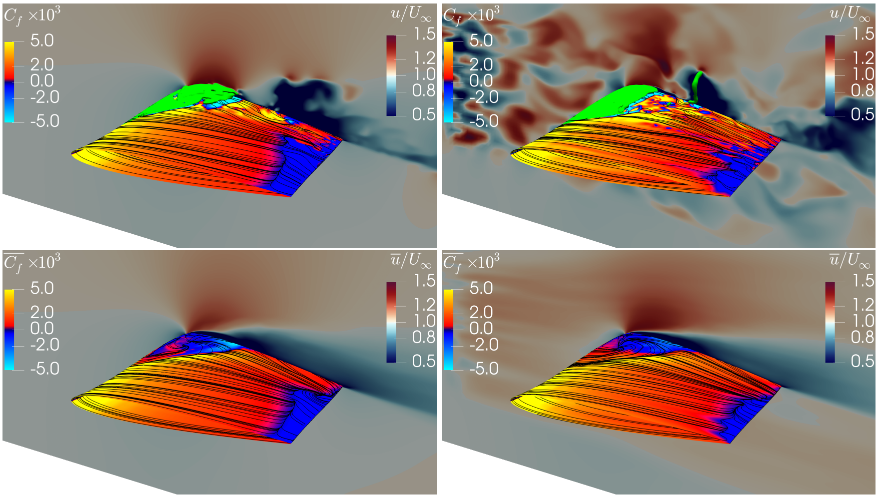

Figure 6.22: Instantaneous (top row) and time-averaged (bottom row) limiting streamlines and friction coefficient $C_{f,x}$, on the wing surface, and streamwise velocity, u/U_∞, for $f_k = 0.25$ on grid $G1$, for steady (left) and a resolved turbulent inflow (right) ($\mathscr{L}/c = 0.013$, $\mathscr{I}_{LE} = 6.3\%$). The instantaneous iso-contour of the vapour volume is indicated in green ($\alpha_v = 0.1$).

pared to the results obtained for wetted flow. At the leading edge, the pressure coefficient shows the suction peak due to the presence of a stagnation point. The magnitude of this peak depends on the value of n_0 chosen in the Schnerr-Sauer cavitation model, but does not affect the dynamic cavitation behaviour [79]. Downstream of the suction peak the pressure coefficient has a constant value approximately equal to the cavitation number (until $x/c \approx 0.3$). The length of this horizontal plateau indicates the mean length of the cavity. When comparing to the experimental results, the cavity length is underpredicted by all numerical approaches. The application of a resolved turbulent inflow has little effect on the mean cavity length, however, the mean cavity length predicted by PANS is lower than the cavity length predicted by DDES or IDDES, related to the higher shedding frequency. This also explains the lower predicted vapour volume. Again note the similarity between C_p for cavitating conditions, with the laminar wetted flow condition on grid $G1$ which also exhibits a horizontal plateau at $-\overline{C_p} \approx -1.1$ in the range $0 < x/c \leq 0.2$ (see Fig. 6.8).

The effect of the resolved turbulent inflow is most visible in the standard deviation of the streamwise skin friction and pressure coefficients near the leading edge. For the skin friction in the region $x/c \leq 0.2$, the standard deviation fluctuates but is at some points almost 30% higher, while the standard deviation of the pressure coefficient increases almost 50% in the same region. Along the remainder of the chord the standard deviation for both PANS computations is similar, and in magnitude, σ_{C_p} is comparable to the results obtained with DDES and IDDES. However, the chordwise variation is sensitive to the model choice. For IDDES two clear peaks can be observed, the largest is related to the varying length of the sheet, while the peak at the leading edge is due to the cavity detaching from the leading edge and growing again. A somewhat similar behaviour is observed for PANS with a steady inflow. However, for the resolved turbulent inflow σ_{C_p} reduces at the the leading edge, indicating a different shedding behaviour. Instead of the periodically growing and detaching cavity as observed in experiments and obtained with IDDES, for PANS only parts of the sheet are shed, similar to what was observed for DDES [79]. For PANS, this happens at a higher shedding frequency, leading to a lower standard deviation of the lift coefficient and a lower time-averaged vapour volume.

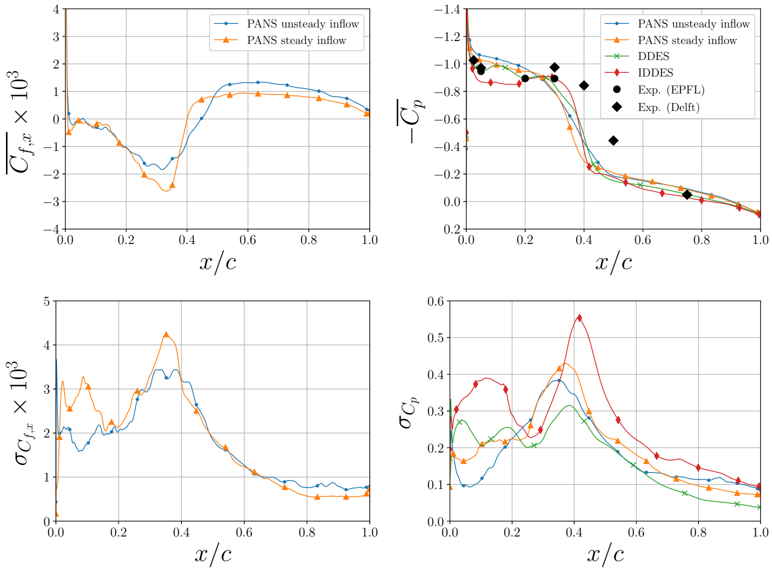

Figure 6.23: Time-averaged (top row) and standard deviation (bottom row) of streamwise skin friction (left) and surface pressure coefficient (right), for $f_k = 0.25$ on grid $G1$ with inflow turbulence, $\mathscr{L}/c = 0.013$, $\mathscr{I}_{LE} = 6.3\%$. DDES results from Vaz et al. [79].

6.6. DISCUSSION

In this chapter, the ITG is used to reduce the modelling errors in SRS incurred by using a steady (RANS-like) inflow, both in wetted and cavitating conditions. For the test case considered, when applying $f_k \leq 0.5$, it is necessary to insert turbulent fluctuations upstream of the wing in order to obtain a flow field predicted by SRS which is close to the experimentally observed flow field. Since lowering f_k reduces the amount of modelled inflow turbulence, this must be replaced by resolved turbulence in order to maintain a physically correct flow field approaching the object of interest. When a steady inflow is applied, the flow around the object remains laminar along most or all of the chord, and – for certain combinations of sufficiently fine grid resolution and low f_k – separates already at the leading edge. Flow separation was not previously reported for numerical results found in literature, although an indication of this phenomenon can be found in the experimental work by Foeth [235]. The reasons for this oversight vary: the results obtained with RANS or hybrid models do not exhibit flow separation, due to the RANS assumption of a fully-developed turbulent boundary layer. The LES results reported in literature also did not exhibit this, although this could be related to the employed grid resolution at the wall; not just in wall-normal direction, but also in the directions parallel to the wall (which is in literature much coarser than the ones here used). In the current chapter it is observed that the inclusion of cavitation in the computation tends to mask the leading edge separation, which is likely also the case for the LES results from literature.

Using synthetic inflow turbulence, transition is triggered closer to the leading edge, resulting in turbulent flow along the wing, thereby avoiding laminar flow separation. This behaviour is reminiscent of the application of vortex generators on aerofoils, where the vortex generators energize the boundary layer, thereby improving the stall behaviour by preventing leading edge separation [258, 262, 263]. The turbulent flow separation at the trailing edge seen in certain simulations is, however, thought to be physically correct, since this was also observable in the experiments. It is noted that the sensitivity to inflow turbulence quantities for SRS is analogous to what is commonly observed when using RANS with transition models, where modest differences in inflow turbulence intensity can dramatically affect boundary layer development (see e.g. [190, 260, 264]).

An alternative approach for obtaining a turbulent boundary layer in the simulations is to trip the boundary layer close to the leading edge. This is commonly applied for measurements of turbulent boundary layers performed at moderate Reynolds numbers ($10^4 - 10^5$) or for flow control purposes, in order to reduce the size of laminar separation bubbles, and reduce the associated drag. Applications include aircraft wings, wind turbines or blades of turbomachinery [258, 263]. The sand grain roughness applied in the experiments of the present test case could be reproduced numerically in a number of ways: by geometrically resolving the roughness [265], applying a simplified trip in the geometry (e.g. [263, 266]), or by adding wall-normal velocity fluctuations (e.g. [258, 267, 268]). An advantage of a trip is that there is no need to tune the ITG to obtain a turbulent boundary layer. Nevertheless, there are several challenges involved in applying this type of approach. Geometrically resolved sand grain roughness is far from standard practice in CFD, and will in any case only quantitatively agree with what is used in experiments, while wall-normal velocity fluctuations and a trip – despite the much simpler geometry – must also be tuned to obtain a flow disturbance equivalent to the roughness applied in the experiments. Wall-normal velocity fluctuations could also have a detrimental effect on iterative convergence. Although these approaches do reduce the need for a refined grid upstream of the object, leading to slightly reduced numerical cost per simulation, the required modification to the grid makes it a less general methodology, which is more difficult to apply across a range of test cases or operating conditions ([263]). In real-life engineering applications it can be expected that inflow turbulence is present. Consequently, the use of a steady inflow in combination with SRS always introduces a certain level of modelling error. When trips are used, there is also the risk that a too thick turbulent boundary layer develops, which may affect the flow prediction downstream. It can also introduce a pressure jump [263], which can have implications for numerical cavitation inception (which is typically based on the simplified criterion $C_p < -\sigma$).

Therefore, when the development of a turbulent boundary layer is the primary goal, applying leading edge roughness is probably the better approach. However, should the focus of simulations be more on large-scale dynamics, such as noise generation of propellers due to inflow turbulence [269] or cavitation dynamics, the development of the boundary layer is of less importance compared to the interaction of turbulence with the leading edge. In such cases the ITG is the more appropriate choice.

It was shown in this chapter that, despite specifying unphysically high inflow turbulence intensities in the simulations (significantly higher than the reported $2-3\%$ in the experiments), it was not possible to obtain transition directly at the leading edge, since the inflow turbulence fluctuations do not enter the boundary layer due to insufficient (spanwise) grid resolution. This agrees with the findings of Tangermann and Klein [270], who studied the effect of inflow turbulence for a NACA profile at moderate angle of attack using DDES. While using inflow turbulence with similar $\mathscr{L}/c$ to that used in the present chapter, they observed that smaller integral length scales are needed to enter the boundary layer and cause transition, while larger length scales mainly affect loading, as they induce angle of attack fluctuations. However, to be able to properly resolve a fully turbulent boundary layer from the leading edge onwards, the grid resolution has to be increased by several orders of magnitude to support these smaller length scales, as well as the transition process they initiate. The lack of resolution leads to a limit in skin friction: for computations with low f_k values, the skin friction remains significantly lower than the results with higher f_k values. It is noted, however, that when applying a trip it might also be difficult to numerically reproduce the transition behaviour behind the trip due to the fine grid resolution required.

As already mentioned in the Introduction, the Delft Twist 11 Hydrofoil was used as a test case representative of a simplified propeller. The results in this chapter indicated that the fundamental shedding frequency of the sheet cavity was not affected by the synthetic inflow turbulence. For a propeller operating in a wake field, this finding likely holds, since the dynamics of a sheet cavity at the blade passage frequency are governed by the rotation of the blade in a non-uniform mean velocity field, although cavity shedding and higher-frequency dynamics are expected to be somewhat sensitive to inflow turbulence. Simulating a non-uniform wake field in SRS leads to the additional requirement of specifying inhomogeneous anisotropic inflow turbulence.

6.7. CONCLUSION

The Delft Twist 11 Hydrofoil was evaluated in wetted and cavitating flow conditions, using the PANS methodology with a varying ratio of modelled-to-total kinetic energy, on different grids and using both a steady and a resolved turbulent inflow. It was shown that modelling errors can occur when applying a steady inflow condition, as used for RANS, due to the flow around the object remaining laminar. This leads to underpredicted lift and drag forces, making validation impossible. Depending on the grid resolution, the wing can even exhibit laminar leading edge separation, i.e. stall.

When employing a resolved turbulent inflow, where homogeneous isotropic turbulence is inserted into the flow, the leading edge separation disappears regardless of the chosen input values for the ITG. The region of trailing edge separation is reduced by increasing the inflow turbulence intensity, which also increases the skin friction along the wing. The separation at the trailing edge is also observed in the experimental results, meaning that, although this was not reported previously, a proper match with the experimental flow field is obtained. Increasing the inflow turbulence intensity also increases the mean lift and drag force, though only till a certain limit. The fluctuations in lift and drag keep increasing. An important observation is that the inflow turbulence has almost no effect on the pressure distribution. This implies that inception remains unaffected when using the – in CFD and the maritime world – commonly applied cavitation inception criterion. Varying the integral length scale has less effect on the flow separation. When using a resolved turbulent inflow, it is necessary that SRS grids are refined upstream to support the convection and development of inflow turbulence.

For cavitating conditions, the variations in lift and drag due to inflow turbulence are significantly smaller than the fluctuations due to the shedding sheet cavity. The addition of inflow turbulence does affect the shedding behaviour: smaller parts of the sheet cavity are being shed at a higher frequency. The predicted mean lift and drag match the numerical results reported in the literature, while the predicted Strouhal number is higher than the experimental value. To the knowledge of the authors, this is the first application of synthetic inflow turbulence to a test case including cavitation.

As part of future work it is desirable to improve the iterative convergence of the computations, which was seen to reduce due to the interaction of cavitation and inflow turbulence. Secondly, the influence of applying a symmetry plane at the foil midspan in order to reduce the domain size (and thereby also the required number of grid cells) should be further investigated. When resolving turbulence, the symmetry plane introduces a modelling error, and with the inclusion of inflow turbulence this error becomes even larger, being already present upstream of the wing. It is also clear that further refined grids are a necessity to obtain a proper resolved boundary layer and properly capture transition behaviour with SRS methods. With respect to the validation, the inclusion of more physics in the CFD computations leads to more stringent demands for experimental data. It is recommended to not only measure integral quantities, but also characteristics of the setup such as turbulence intensity and integral length scale, and the flow in the boundary layer. The absence of this information for the Delft Twist foil highlights the need for new experimental test cases aimed at validation of SRS investigations of multiphase flows.

In this chapter the ITG is successfully combined with cavitation. The next chapters will focus on the inclusion of an acoustic analogy in such setups.

ACKNOWLEDGEMENTS

The authors would like to thank Maarten Kerkvliet and Bart Schuiling of MARIN for their help with the grid generation.

7

ELLIPTICAL WING

A tip vortex generated by an elliptical wing is simulated in wetted and cavitating conditions, using scale-resolving simulations. The vortex is excited by synthetic inflow turbulence with varying inflow turbulence intensities. Vortex kinematics and cavity dynamics are analysed, and validated against experiments and a semi-analytical model from literature. The far-field radiated noise is analysed using an acoustic analogy. Using a background noise correction, the sound due to inflow turbulence is removed, and the sound due to cavity dynamics is isolated. Based on the sound spectra, the main noise generating mechanisms are identified. Cavitating simulations predict a broadband increase of approximately 15 dB in the far-field radiated noise, while doubling the inflow turbulence intensity results in an increase of approximately 10 dB.

7.1. INTRODUCTION

Historically, when investigating cavity vortex dynamics, there is – both for experiments and simulations – a preference for using stationary wings representative of propeller blades, instead of using the full propeller geometry. The absence of rotation leads to a simplified measurement setup and reduced computational requirements since only a single blade has to be resolved. Such a case is the canonical case of a vortex generated by a three-dimensional wing with an elliptical planform [13, 190, 272, 273], commonly referred to as the 'Arndt' wing. With respect to the cavity dynamics, several vortex deformation modes can be identified [13, 273], each of which contribute to the noise produced by the wing.

In numerical investigations in literature, a range of turbulence models are applied, resulting in different reported lift coefficients, as shown in Fig. 7.1. Formulations relying on the Boussinesq hypothesis are not sufficient, as shown by Schot et al. [23]. Curvature corrections are found to improve results, but modelling errors of the velocity profiles in the vortex were still found to be large [23, 274]. The application of LES and ILES decreases the modelling error for the integral quantities compared to experiments and the

---

This chapter has been submitted for publication [271].

models avoided early decay of vorticity [274]. However, it is unclear whether turbulent velocity fluctuations are properly developed, meaning that the predicted vortex could be excessively laminar. Paskin [25] obtained velocity fluctuations in the wake of the foil, using DES. However, due to grid induced separation the lift coefficient did not match the experimental results of [43]. The work by Liebrand et al. [190] showed that the usage of SRS, such as DDES, can lead to improved vortex predictions compared to traditional Reynolds averaged Navier-Stokes (RANS) methods. However – due to the steady inflow – the results obtained converged to a steady solution, exhibiting a significant modelling error when compared to experiments. Remarkably, most numerical investigations in literature focus on either predicting cavitation inception (e.g., Asnaghi, Svennberg, Gustafsson, et al. [274]), or capturing the time-averaged flow kinematics (e.g., [23, 25]). There are few attempts at simulating the cavity dynamics and noise generating mechanisms, for which this test case was designed.

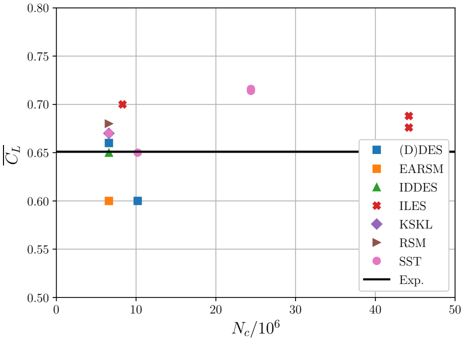

Figure 7.1: Literature overview of lift coefficients ($\overline{C_L} = \overline{L}/\left(1/2\rho U_\infty^2 A\right)$, with the overline indicating a time-average, L the lift force, ρ the density and A the wing surface area) in wetted flow conditions, as function of the number of grid cells (N_c) and turbulence model. Results at 9° angle of attack at $Re \approx U_\infty c_0/\nu = 8.95 \times 10^5$. Experimental results from Pennings, Bosschers, et al. [273], numerical results from [25, 190, 202].

The aim of this chapter is to investigate whether the vortex dynamics observed in experiments for this test case can be reproduced by applying SRS together with synthetic inflow turbulence, and whether this can be related to far-field noise. Simulations are performed with PANS [51] and IDDES [54]. A theoretical advantage of PANS is that due to the explicit setting of the filter between RANS and DNS, the discretisation and modelling errors are decoupled [57]. The use of a single formulation ranging from RANS to DNS prevents ad hoc behaviour when switching between resolving and modelling turbulence, as can occur for hybrid methods, such as (I)DDES [79]. In this chapter the PANS-KSKL model, designed for multiphase flows, is used. Iterative, statistical and discretisation errors are assessed. The postprocessing consists of:

1. analysing and validating the vortex kinematics;
2. analysing the vortex dynamics based on 2D fast Fourier transforms, and comparing the dynamics against the semi-analytical formulation by Bosschers [13],

which was validated with experimental measurements by Pennings, Bosschers, et al. [273];

3. analysing the predicted noise, computed using an acoustic analogy.

The chapter is structured as follows. Sec. 7.2 describes the test case, theoretical dispersion relationship by Bosschers [13] and numerical setup. After a discussion of the numerical uncertainty in Sec. 7.3, the main results are presented in Sec. 7.4, followed by the discussion and conclusions in Sec. 7.5 and 7.6, respectively.

7.2. TEST CASE AND SETUP

The ‘Arndt’ wing is an elliptical planform with a NACA66_2-415 cross-section, a root-chord of $c_0 = 0.1256$ m, a wingspan of $b = 0.15$ m and a surface area $A = 0.01465$ m^2. The most widely considered test condition in literature for this wing is for a root-chord based Reynolds number of 8.95×10^5. Using $\nu = 1.002 \times 10^{-6}$ m^2/s and $\rho = 998$ kg/m^3, this yields an inflow velocity of 7.15 m/s.

Numerical results in the literature often exhibit a premature decay of vorticity, and therefore an underpredicted cavity size, compared to experiments. This is primarily attributed to numerical diffusion, and overprediction of eddy viscosity. Liebrand et al. [190] recently argued that this can also partly be attributed to the assumption of a fully turbulent boundary layer, while the Reynolds number is in the transitional regime. Following those results the wing is investigated only at 9° angle of attack, to mitigate this laminar-turbulent transition issue.

Pennings, Westerweel, et al. [43] measured the lift force and applied particle image velocimetry (PIV) in wetted and cavitating conditions to analyse the cavity dynamics and measure cavity radius for different cavitation numbers. For the same cavitation tunnel Foeth [235] reported typical levels of inflow turbulence intensity at the location of the wing of 2-3%, while Varadharajan [236] observed $\approx 1.5\%$ at a 50% lower mean tunnel velocity. Neither source provides information on the integral length scale.

7.2.1. DISPERSION RELATION FOR A 3D VORTEX

The goal of the current study is to compare the simulated cavity dynamics with the experimental observations by Pennings, Westerweel, et al. [43]. Based on those results, three vortex deformation modes were identified: the breathing mode (a volume variation), the serpentine mode (a centre line displacement) and the double helix mode (an rotating elliptical cross-section of the vortex), as visualised in Fig. 7.2.

Bosschers [13] extended this idea, and derived a dispersion relation using a small-perturbation analysis for the kinematic and dynamic boundary conditions, to describe these dynamics and to analyse resonance frequencies in the radiated noise. Under the assumption that the phase velocity of the axial deformation is much smaller than the speed of sound, the non-dimensional dispersion relation for low frequencies can be formulated as

$$\tilde{\omega}^{\pm}\left(\tilde{k}_x, n\right) = \tilde{U}_{x,c}\tilde{k}_x + \tilde{U}_{\theta,c}n \pm \sqrt{K_\sigma}\sqrt{\frac{-\tilde{k}_x K_n'\left(|\tilde{k}_x|\right)}{K_n\left(|\tilde{k}_x|\right)}}T_\omega. \tag{7.1}$$

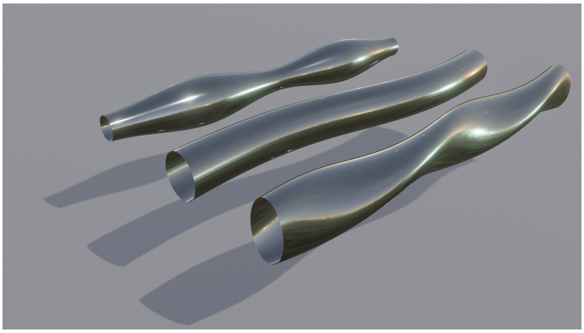

Figure 7.2: Deformation modes of the vortex cavity. From top till bottom the breathing mode ($n = 0$), the serpentine mode ($n = 1$) and the double helix mode ($n = 2$), based on Bosschers [13].

The vibration modes all contain two branches and therefore two frequencies. This is indicated by the plus-minus sign, and also used in the mode identification (e.g. $n = 0^+$ and $n = 0^-$). In Eq. 7.1, non-dimensional quantities are indicated with a tilde. K is a modified Bessel function of the second kind (also known as a MacDonald function), and K' is its first derivative with respect to the argument; n indicates an integer, representing the mode ($n = 0, \pm 1, \pm 2$, for breathing, serpentine mode and double helix mode, respectively), $\tilde{k}_x = k_x r_c$ is the normalised wavenumber, with $k_x = 2\pi/\lambda$ with λ the wavelength, and $\tilde{\omega} = 2\pi f r_c / U_\infty$. T_ω indicates the contribution of surface tension. Due to the absence of surface tension modelling in the present study, this is neglected, i.e. $T_\omega = 1.0$. The expression depends furthermore on the normalised axial and azimuthal velocities at the cavity interface, $\tilde{U}_{x,c} = u_{x,c}/U_\infty$ and $\tilde{U}_{\theta,c} = u_{\theta,c}/U_\infty$, respectively.

In the current study Eq. 7.1 is used as validation of the cavitation dynamics predicted by the simulations. $\tilde{U}_{x,c}$ and $\tilde{U}_{\theta,c}$ will be compared against the values obtained by Pennings, Bosschers, et al. [273] and Bosschers [13]. Due to limitations in the PIV measurements, in the experimental results $\tilde{U}_{\theta,c}$ was obtained using

$$\tilde{U}_{\theta,c} = \begin{cases} \sqrt{\sigma}, & \text{potential flow vortex,} \\ \sqrt{\sigma}\sqrt{\frac{r_c^2}{r_v^2 + r_c^2}}, & \text{cavitating Lamb-Oseen vortex,} \end{cases} \tag{7.2}$$

with σ as the cavitation number. The stiffness term was defined as

$$K_\sigma = \begin{cases} \sigma, & \text{potential flow vortex,} \\ \sigma\left(\frac{r_c^2}{r_v^2 + r_c^2}\right), & \text{cavitating Lamb-Oseen vortex.} \end{cases} \tag{7.3}$$

The dispersion relation (Eq. 7.1), with the relative sensitivities to the different parameters, is visualised in Fig. 7.3

7.2.2. COMPUTATIONAL DOMAIN AND GRID

The computational domain corresponds to the cavitation tunnel of Delft University of Technology [43], with an inlet located $5c_0$ upstream of the wing and an outlet located $10c_0$ downstream. The domain is visualised in Fig. 7.4.

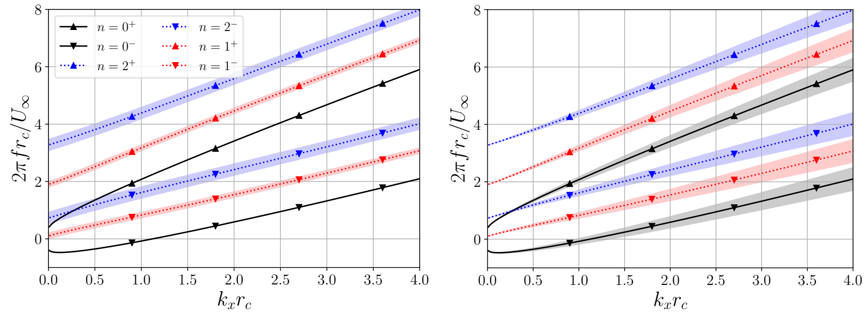

(a) $\tilde{U}_{\theta,c}$ (b) $\tilde{U}_{x,c}$

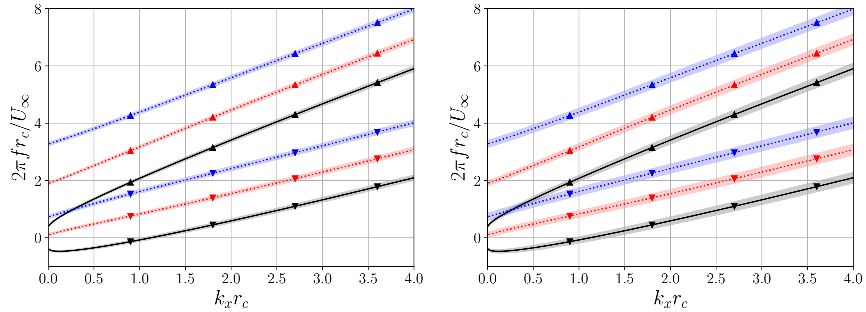

(c) K_σ (d) T_ω

Figure 7.3: Non-dimensional dispersion diagram for the cavity deformation modes $n = 0^\pm$ and $n = 2^\pm$ (left) and $n = 1^\pm$ (right) described by Eq. 7.1. The parameters are taken as $\tilde{U}_{x,c} = 1.0$, $\tilde{U}_{\theta,c} = 1.0$ and $K_\sigma = 1.0$. Shaded regions indicate uncertainty bands obtained by varying the parameter in the subcaption by ±10%.

The grid consists of multi-block hexahedral structured grid, with additional refinement around the wing's edges. To minimise numerical diffusion, *a priori* grid refinement was employed to increase the resolution in the vortex and wake regions [275]. For the resolution in the vortex, the recommendation by Asnaghi, Svennberg, and Bensow [202] of an in-plane and streamwise resolution of $r_v/8$ and $r_v/4$ was met for the finest grid, with r_v the viscous core radius. Upstream of the wing – between the ITG and the wing – an additional refinement box is located to resolve the inserted synthetic inflow turbulence. The computational grid contains 7.44×10^6 cells, and has non-dimensional wall cell sizes ($x^+ = u_\tau x/\nu$, with u_τ the wall friction velocity and x the cell size) of $\overline{x_n^+} = 0.1$, $\overline{x_t^+} = 160$ and $\overline{x_s^+} = 330$ in normal (n), tangential (t) and spanwise (s) direction, respectively. The numerical grid, with the porous data surfaces used for the acoustic analysis (see Sec. 2.6.1) are shown in Fig. 7.5. The PDS passes through several regions of varying grid densities, which is not ideal with respect to the accuracy of the FWH method. Nevertheless, given the computational cost of the simulations, and the need to refine the grid in the region encompassing the vortex, this is considered inevitable.

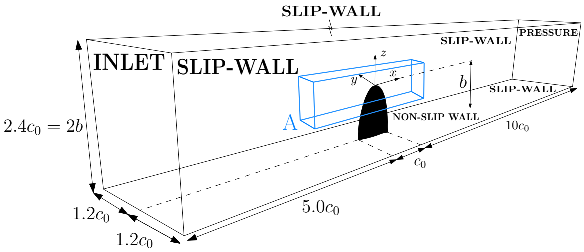

Figure 7.4: Schematic visualisation of computational domain including geometrical parameters expressed in c_0, and boundary conditions. Reproduced from Liebrand et al. [190].

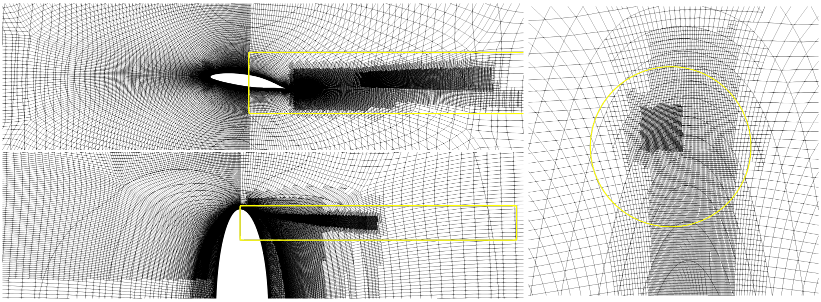

Figure 7.5: Numerical grid. The PDS for the acoustic analysis is indicated in yellow.

7.2.3. COMPUTATIONAL SETUP

Two experimental conditions were matched, one wetted flow and one cavitating condition. The wetted flow condition corresponds to a cavitation number of $\sigma = 4.2$, while for the cavitating condition $\sigma = 1.7$ [13, 273]. The condition $\sigma = 1.7$ is common in numerical investigations of this test case in literature, since in this way tip vortex cavitation is obtained, while avoiding sheet cavitation [23] which could dominate the vortex dynamics due to its shedding behaviour. This case was also investigated without inflow turbulence using ReFRESCO by Liebrand et al. [190].

Although the specified number of seeds and bubble radius are expected to affect the liquid-vapour interface, their effect was considered to be out of the scope of this research. These were set to $n_b = 1 \times 10^9$ m^{-3} and $R_B = 3 \times 10^{-5}$ m respectively, based on [23, 64, 80]. For the PANS-KSKL model, a fixed f_k value of 0.1 is employed, based on the experience for simulating sheet cavitation (see Chapter 6.

The boundary condition at the inlet is a Dirichlet condition for all velocity components and a Neumann condition for pressure. Next to the resolved turbulence, at the inflow a RANS turbulence intensity of 1% and an eddy-viscosity ratio of 1.0 is prescribed. A Dirichlet condition for the pressure is prescribed at the outlet, with Neumann conditions for velocity and turbulence quantities. The tunnel walls were modelled as slip walls, and the wing's surface as a non-slip wall. The timestep for these computations is kept fixed to $\Delta t^* = \Delta t U_\infty / c_0 = 0.01$.

Homogeneous isotropic turbulence was inserted at $x/c_0 = -2.4$ using three different turbulence intensity levels, resulting in a turbulence intensity ($\mathscr{I} = \sqrt{\overline{u'^2}}/U_\infty$, with $u' = \langle U_i \rangle - U_\infty$) at the location of the wing tip of $\mathscr{I}_{tip} \approx 1.3\%$, 0.7% or 0.3%. The integral length scale is selected taking several considerations into account. Firstly, the energy-containing scales should be sufficiently large such that about 80% of the TKE can be resolved using the chosen grid resolution. This requirement derives from guidelines for LES [52], and is also necessary when selecting a low f_k value (< 0.2). Furthermore, and importantly for the present case, since the ITG introduces numerical background noise into the simulation, it is desirable to select the integral length scales such that a frequency shift relative to the anticipated cavity dynamics is present. From literature it is known that the non-dimensional cavity resonance frequency ($2\pi f r_c / U_\infty$) at $\sigma = 1.7$ lies in the range 0.4 – 0.6 [273]. Therefore an integral length scale of $L_{\mathrm{tip}}/r_c \approx 80$ is chosen, corresponding to $f_{\mathscr{L}} = U_\infty / \mathscr{L} = 0.07$, or at least six times below the cavity resonance frequency. We note that the selected inflow parameters do not correspond to measured conditions in the cavitation tunnel, although there is a complete lack of information regarding the integral length scale in the facility. For test cases where the integral length scale is known, meaning that a frequency shift between cavitation dynamics and inflow turbulence cannot necessarily be guaranteed, additional attention should be given to ensuring sufficient signal-to-noise ratio in the simulations.

The streamwise development of inflow turbulence based on a line monitor $b/3$ above the wing tip in z direction is shown in Fig. 7.6. The integral length scale was determined using the first local minimum of the temporal autocorrelation function.

The inflow intensities remain relatively constant in the region $(x - x_{TG})/c_0 \geq 0.5$, after the initial disturbances due to the ITG. For all turbulence intensities, the wetted flow $\mathscr{I}$ is slightly higher for than the cavitating results. This is likely related to an interaction between the ITG and the cavitation model. Assuming a quadratic dependency of the (non-cavitating) noise on the turbulence intensity, a 10% difference between the cases results in an effect below 1 dB, which for the current studies is considered acceptable.

To evaluate the inflow turbulence characteristics, the spectra are compared against

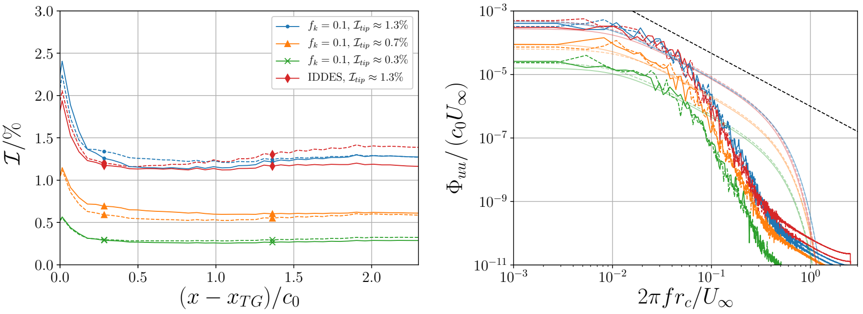

Figure 7.6: Streamwise development of inflow turbulence intensity and turbulence kinetic energy spectra at the streamwise position close to the wing tip. Dashed lines indicate $\sigma = 4.2$ (wetted flow), solid lines correspond to $\sigma = 1.7$. Translucent lines indicate the von Kármán fits. The wing tip is located at $x/c_0 = 0.0$, which corresponds to $\left(x - x_{TG}\right)/c_0 = 2.4$. Cavity radius obtained from results described in Sec. 7.4.3. For $\sigma = 4.2$ results, the frequency axis is normalised by the r_c obtained from the corresponding $\sigma = 1.7$ simulation.

theoretical von Kárman spectra (shown with translucent lines in Fig. 7.6), given by

$$\Phi_{uu} = \frac{\mathscr{L}_{tip}\overline{u'^2}}{\pi U_\infty} \frac{2\pi}{\left(1+\hat{k}_x^2\right)^{5/6}} \exp\left(-\frac{9}{4}\left(\frac{2\pi f}{U_\infty R_\lambda}\right)^2\right)^2, \tag{7.4}$$

with

$$\hat{k}_x = \frac{2\pi f / U_\infty}{\sqrt{\pi}\Gamma\left(5/6\right) / \left(\mathscr{L}_{tip}\Gamma\left(1/3\right)\right)}. \tag{7.5}$$

Here Φ_{uu} indicates the power spectral density, Γ the gamma function, and R_λ the Taylor scale Reynolds number, here assumed to be 500 [276]. For this fit, the integral length scale $\mathscr{L}_{tip}$ and $\overline{u'^2}$ are taken from the simulation. To enable comparison against the results from the analysis of the cavitation dynamics, and results from literature, the horizontal axis is normalised based on the cavity radius r_c. For the $\sigma = 4.2$ results, r_c is obtained from the corresponding $\sigma = 1.7$ simulation.

Taking the ratio of the integral of the numerical resolved and theoretical von Kármán spectra results in an estimate that 80-90% of the turbulence kinetic energy is resolved in the simulations, which satisfies guidelines for LES [52]. It is also clear from Fig. 7.6 that the energy-containing range lies well below the cavity resonance frequency, confirming that the desired frequency separation has been achieved. The cut-off at lower wavenumbers in the numerical results compared to the theoretical spectra should help to further reduce the numerical background noise at frequencies at which cavity dynamics are expected.

Cavitating computations are started at a higher cavitation number to increase stability of the simulation during the initial timesteps. By increasing the vapour pressure using a cosine function, the required cavitation number is reached after 0.0193 s, or in non-dimensional time-units $tU_\infty/c = 1.1$. The inflow turbulence reaches the tip of the wing after 0.07 s, or $tU_\infty/c = 4.0$. Each full computation simulates 1.93 s, or $tU_\infty/c = 110$.

7.2.4. POSTPROCESSING METHOD

From the simulations several different types of data are extracted, and combined. The postprocessing method is schematically shown in Fig. 7.7, with the remainder of this and the next subsection going into more detail regarding the determination of the relevant quantities.

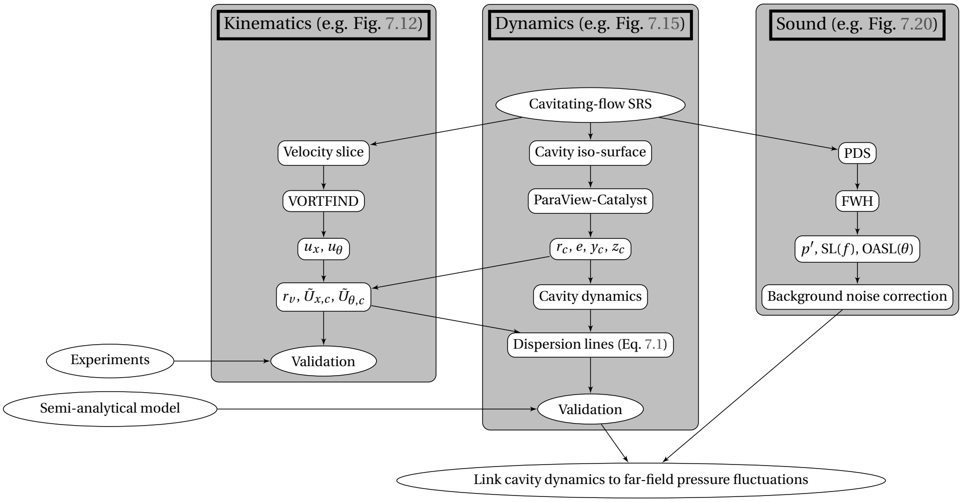

Figure 7.7: Postprocessing flow chart indicating the data flow.

To compute the viscous core radius and obtain the parameters for the dispersion relationship, the improved VORTFIND algorithm [277, 278] is applied to cross-sections of the velocity field around the vortex at $x/c_0 = 0.50$ downstream of the tip. From this velocity slice, the vortex centre, velocity profiles, and consequently the viscous core radius, can be obtained.

The vortex dynamics are analysed using a modified version of the method developed by van den Boogaard [279] which was based on the work of Bosschers [13]. In those studies the cavity centreline and radius are obtained from the cavity projection to two planes (y and z, also designated 'top' and 'side' view). The centreline and radius are then analysed by means of a 2D fast Fourier transform (FFT) to obtain Cross-Power Spectral Density (CPSD) and the phase difference between the planes. These results can then be compared against the theoretical dispersion relation (Eq. 7.1). Bosschers [13] applied the methodology to experimental results, while van den Boogaard [279] attempted to reproduce this for a numerical test case.

The restriction to two projection planes derives from the limited data available from the experiments, in which a stereo camera setup was used. Theoretically, the projection to two planes should yield all the required information to distinguish the different modes: variations in radius lead to the $n = 0$ mode, variation in centreline give the $n = 1$ mode, and from differences between r_y and r_z the $n = 2$ mode can be obtained. However, some problems with this approach can be observed. The main issue is that due to the setup it is assumed that the cavity cross-section is always convex, and can be described by an ellipse. Due to the projection, any other shape will always reduce to this ellipse, meaning that modes $n = 0$, 1 and 2 are the only modes which can be observed. Higher modes are commonly assumed to be irrelevant with respect to noise generation, due to their lower acoustic radiation efficiency [280], since it is expected that the $n = 0$ acts as a monopole, $n = 1$ as a dipole, and $n = 2$ as a quadrupole. It does however mean that more elaborate vortex features cannot be obtained with this postprocessing. Even when this assumption is made deliberately, the approach based on projections can still lead to problems. Consider the hypothetical case of an elliptical cross-section, with its main axis oriented 45° with respect to the projection coordinate system. Based on the projections, $r_y = r_z$, meaning that no distinction can be made between a circular and elliptical cross-section. This means that in the CPSD there is a data bleed of the $n = 2$ mode to the $n = 0$ mode. Due to the temporal rotation of the $n = 2$ mode this phenomenon will always occur, however at varying locations along the vortex. In the work of Bosschers [13], this was circumvented by identifying the modes of the dispersion lines based on their phase difference, yet an approach which does not suffer from this problem is preferable. The current approach makes use of different parameters. The modes are identified using the cavity centroid, effective radius, eccentricity and angle, which are defined later in this subsection.

ReFRESCO co-processing, which is based on the ParaView Catalyst library [281], is used to obtain this data and manage the amount of data which needs to be written to file. The procedure is schematically shown in Fig. 7.8. In the simulation, the iso-surface of $\alpha_v = 0.1$ is extracted at every timestep, thereby preventing the need to store the full solution at every timestep. These iso-surfaces are sliced in the streamwise direction, oriented perpendicular to a quadratic fit of the time-averaged cavity trajectory. The intersection between the slice and iso-surface yields a polygon. Using the method by Fitzgibbon et al. [282], an ellipsoid with the centroid $\left(y_c, z_c\right)$ and a width of $2a$ and a height of $2b$, according to the formulation

$$\frac{\left(y-y_c\right)^2}{a^2}+\frac{(z-z_c)^2}{b^2}=1, \tag{7.6}$$

is fitted onto the cross-section. The effective radius is computed with

$$r_{eff}=\sqrt{ab}, \tag{7.7}$$

when assuming that the area of the ellipse is equivalent to a circle with radius r_{eff} ($\pi r_{eff}^2 = \pi ab$). The eccentricity is defined as

$$e=\begin{cases}\sqrt{1-\frac{a^2}{b^2}}, & \text{if } b>a;\\ \sqrt{1-\frac{b^2}{a^2}}, & \text{if } a<b.\end{cases} \tag{7.8}$$

The angle of the fitted ellipse with respect to a Cartesian coordinate system is also analysed to check whether the cross-section rotates in time. Note that by fitting an ellipse, the results are still limited to the second modal deformation. This makes for easy comparison against the results by Bosschers [13], but using this method an extension can be easily realised in the future by modifying the fitting function.

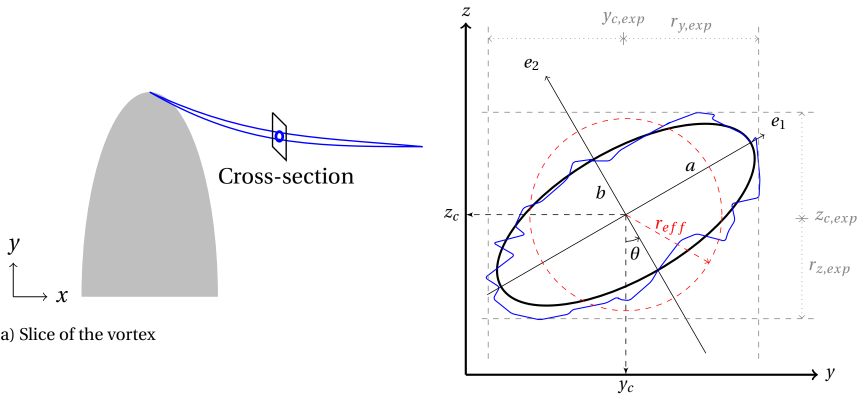

(a) Slice of the vortex

(b) Cavity cross-section and fitted ellipse

Figure 7.8: Extraction of vortex parameters. Fig. 7.8a shows the cavity with a slice of the iso-surface. Fig. 7.8b shows the fitting procedure and extraction of variables. Onto each cross-section of the cavity (in blue), is an ellipse fitted (black) with the parameters x_c, y_c, a, b, e, and the angle, indicated by θ. The effective radius is computed using a circle with the same area as the fitted ellipse (red). For comparison, the method used in the experiments by [43] is indicated in grey with the subscript exp.

The availability of these three quantities allows for a clear distinction between the different modes: the centroid should yield $n = 1$, the effective radius $n = 0$ and the eccentricity $n = 2$. For all quantities, following Bosschers [13] the Power Spectral Density (PSD) is computed with

$$PSD = 120 + 10\log_{10}\left(\frac{S \odot S^*}{r_c^2}\right), \tag{7.9}$$

with S is the single-sided 2D spectrum of the quantity ϕ, and S^* is its complex conjugate. The spectrum and its conjugate are multiplied using an element-wise matrix multiplication, i.e. the Hadamard product, indicated by $\odot$. For the centroid and fitted ellipse, the Cross-Power Spectral Density (CPSD) is also computed based on the y and z coordinates or a and b of the ellipse respectively, using

$$CPSD = 120 + 10\log_{10}\left(\frac{G_{y_c} \odot G^*_{z_c}}{r_c^2}\right) \tag{7.10}$$

where G_{y_c} indicates the 2D spectrum of y_c, and $G^*_{z_c}$ the complex conjugate of the 2D spectrum of z_c, or G_a and G_b respectively. These results are presented in decibels (dB), and can be compared against the theoretical dispersion relation (Eq. 7.1).

The far-field acoustics are obtained using the FWH method, as explained in Sec. 2.6.1. In the current study the far-field receiver arrays are placed at 3° intervals by revolving around the x-axis (blue), y-axis (orange), and z-axis (green). Receivers are located in the acoustic far-field, at a distance of $r_{rec} = 5$ m, i.e. $\approx 40c_0$. The setup is visualised in Fig. 7.9. The PDS is a cylinder with a radius of 0.25 m and a length of 0.4 m, extending from the wing tip downstream, containing 71840 cell faces (see also Fig. 7.5). The PDS is constructed from the faces of the numerical grid, thereby avoiding interpolation [148]. At the location of the wing, the cylinder ends on the wing surface. The intersection with the boundary layer introduces spurious noise, due to the quadrupole source volume integral being ignored [82, 86, 148, 283]. Nevertheless, it was deemed necessary to encapsulate the cavity attached to the wing tip.

In literature it is observed that for flows containing strong vortical structures, such as propellers, the inclusion of end caps can lead to spurious noise, again originating from the quadrupole source volume integral being ignored. A common solution is to omit the downstream part of the PDS, provided that the PDS is long enough to enclose as much of the relevant flow physics as possible [82, 86]. A similar problem is expected to occur here as well due to the inflow turbulence generation, however in this case both the up- and downstream parts of the PDS (i.e. the top and bottom, or end caps, of the cylinder) must be removed. This is not a full solution, since the PDSes lie inside the region where upstream turbulence is being generated. This leads to vortices passing through the sides of the cylinders, and consequently spurious noise. A method to address this is by computing the quadrupole sources and correcting the predicted noise [283], which remains to be done in future work. In the current study, it is anticipated that this noise will be dominated by the cavitation noise. The background noise due to the ITG-PDS setup will be investigated in Sec. 7.4.4.

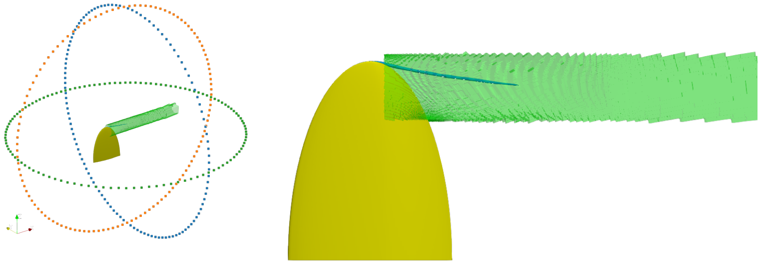

Figure 7.9: Left figure: Locations of the far-field receiver arrays placed at 3° intervals by revolving around x-axis (blue), y-axis (orange), and z-axis (green). Distance from the wing was scaled down by a factor of 10 in the figure for readability. Right figure: side view of the PDS and wing.

7.3. NUMERICAL ERRORS

To assess the iterative convergence, the residuals, normalised by the diagonal element of the left-hand-side matrix of the linearised equation, are used. For PANS-KSKL wetted flow computations with inflow turbulence, the obtained residuals are $L_2 \approx 10^{-4}$ ($L_\infty \approx 10^{-2}$) for the momentum equations, $L_2 \approx 10^{-6}$ ($L_\infty \approx 10^{-3}$) for pressure and $L_2 \approx 10^{-8}$ ($L_\infty \approx 10^{-5}$) and $L_2 \approx 10^{-10}$ ($L_\infty \approx 10^{-8}$) for k and $\sqrt{k}L$, respectively. When cavitation is included, similar convergence is obtained, while the vapour volume fraction equation reaches $L_2 \approx 10^{-5}$ ($L_\infty \approx 10^{-2}$). These residuals show the superior convergence behaviour of the KSKL closure, as observed in Chapter 4. For the IDDES computations, based on a SST model, similar convergence is reached for all equations, except the turbulence equation. For k, $L_2 \approx 10^{-7}$ ($L_\infty \approx 10^{-4}$), but ω stagnates at $L_2 \approx 10^{-3}$ ($L_\infty \approx 10^{0}$).

With respect to the discretisation error, a grid based on previous verification studies by Liebrand et al. [190], is employed with additional grid refinement zones. It was shown that the resolution used by Liebrand et al. [190] was sufficient to achieve acceptable discretisation errors (below 10%) for the prediction of the vortex kinematics.

Finally, the finite length of a CFD simulation introduces a random uncertainty in the mean of the signal. To estimate the statistical uncertainty, and to remove the start-up effect, the Transient Scanning Technique (TST) is used. As start up effect, the time corresponding to the flow moving from the inlet to the wing tip is removed, corresponding to 5.5 non-dimensional time units ($T = c_0/U_\infty$). After the start up, the simulation is continued for another 6 flow-through times of the entire domain, corresponding to approximately 100 non-dimensional time units. Due to the need to obtain a sufficient time-trace to analyse the cavity dynamics, the resulting statistical uncertainty is negligible for the integral quantities. For quantities describing the cavity dynamics, such as the effective radius and eccentricity, the statistical uncertainty is below 3%.

7.4. RESULTS

Cavitating and wetted flow conditions are investigated, both with and without inflow turbulence, using PANS and IDDES (see Tab. 7.1 for the different conditions). From the experimental results described in Bosschers [13] a relatively small vortex ($r_c/c_0 = 0.0038$) with a mostly circular cross-section is expected. In all results in this section, PANS-KSKL computations are indicated by $f_k = 0.1$.

7.4.1. OVERVIEW

Fig. 7.10 shows an overview of the simulations, with the normalised, instantaneous, vorticity in the background, together with the cavity iso-surface and skin friction coefficient and limiting streamlines on the wing surface. The variations in vorticity in the background are a result of the synthetic inflow turbulence. In the wake and surrounding the vortex higher levels of vorticity are present. The limiting streamlines and skin friction coefficient show turbulent separation at $x/c_0 \approx 0.6$ on both the pressure and suction side, which was also observed experimentally [284]. For more details on this phenomenon, and the sensitivity to the inflow characteristics, the reader is referred to Liebrand et al. [190].

Tab. 7.1 reports the time-average and standard deviation of the lift and drag coefficient, together with the mean viscous core and cavity radius. The results show that IDDES predicts a lower time-averaged lift and drag, and a lower standard deviation of these quantities, both in wetted and cavitating flow. The standard deviation of the lift and drag for IDDES without inflow turbulence is 0, which is in line with the results obtained in [190], namely that these computations converge to a steady state. The addition of inflow turbulence leads to small variations in the instantaneous lift and drag, but does not alter the viscous core radius.

The use of PANS without ITG leads to leading edge flow separation, similar to what was observed in in Chapter 6. Consequently, PANS is only used in combination with ITG. IDDES is applied with and without ITG, since it does not suffer from this issue due to the fact that the inner part of the boundary layer is solved using RANS.

Fig. 7.11 shows an instantaneous side and top view of the vortex at $\sigma = 1.7$. The $n = 0$ and $n = 1$ modes are not clearly discernible, although it should be noted that this

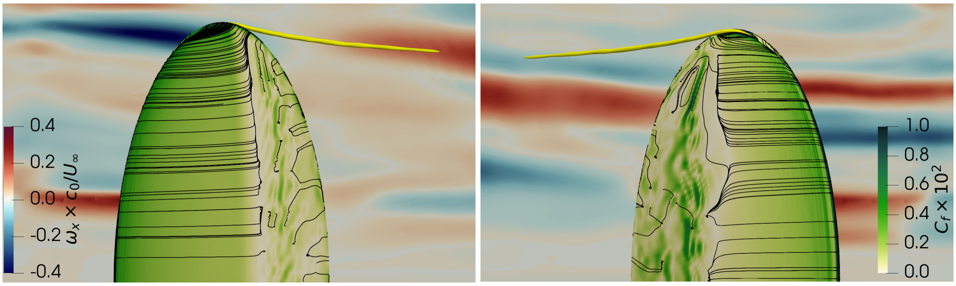

(a) Pressure side

(b) Suction side

Figure 7.10: PANS ($f_k = 0.1$), $\sigma = 1.7$, $\mathscr{I}_{tip} \approx 0.7\%$. Limiting streamlines and skin friction coefficient ($C_f = |\tau_{w,x}|/\left(0.5\rho U_\infty^2\right)$, with $\tau_{w,x}$ the skin friction in streamwise direction), on the wing surface. Cavity is indicated in yellow. The background shows a slice of the normalised, instantaneous, x component of the vorticity ($\omega = \nabla \times \langle U_i \rangle$) at $y/c_0 = 0.4$ in the pressure side image, and $y/c_0 = -0.4$ in the suction side image. The flow is from left-to-right for the pressure side, and from right-to-left for the image of the suction side.

Table 7.1: Time average and standard deviation of lift and drag forces; and mean radii, obtained at $x/c_0 = 0.50$.

σ	Computation	$\mathscr{I}_{tip}/\%$	$\overline{C_L}$	σ_{C_L}	$\overline{C_D}$	σ_{C_D}	$\overline{r_v}/c_0$	$\overline{r_c}/c_0$
4.2	$f_k = 0.1$	1.3	0.714	0.029	0.059	0.002	0.012	-
	$f_k = 0.1$	0.7	0.712	0.012	0.060	0.002	0.012	-
	$f_k = 0.1$	0.3	0.710	0.009	0.060	0.002	0.012	-
	IDDES	1.3	0.639	0.020	0.054	0.001	0.013	-
	IDDES	0.0	0.646	0.000	0.054	0.000	0.013	-
1.7	$f_k = 0.1$	1.3	0.713	0.024	0.060	0.002	0.018	0.010
	$f_k = 0.1$	0.7	0.714	0.013	0.060	0.002	0.018	0.010
	$f_k = 0.1$	0.3	0.712	0.009	0.060	0.002	0.017	0.009
	IDDES	1.3	0.644	0.023	0.054	0.002	0.017	0.009
	IDDES	0.0	0.648	0.000	0.054	0.000	0.017	0.008

is expected due to the small amplitude of the fluctuations. It is possible to discern the ribbon-like structure in the cavity downstream of the tip, indicative of the $n = 2$ mode.

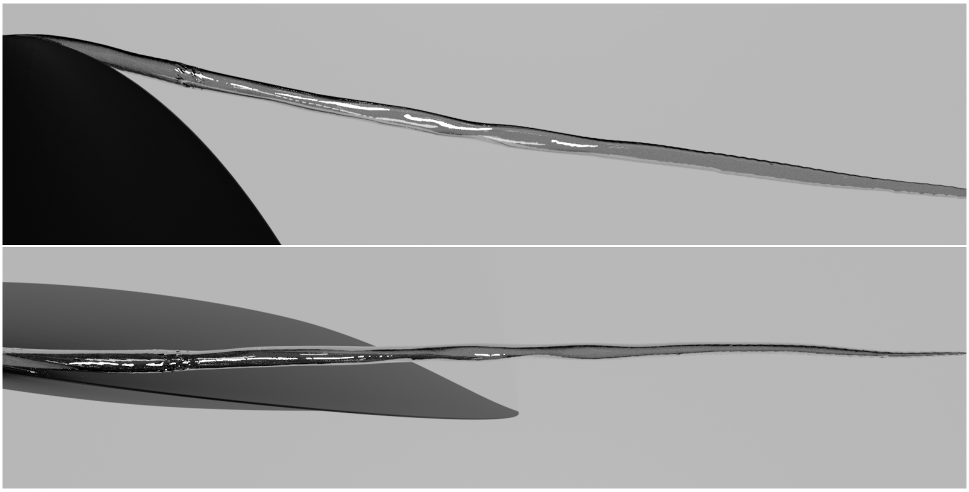

Figure 7.11: PANS ($f_k = 0.1$), $\sigma = 1.7$, $\mathscr{I}_{tip} \approx 0.7\%$. Instantaneous top and side view images of the vortex cavity. The side view shows the wing pressure side, the flow is from left to right.

The description of the results follows the workflow as described in Fig. 7.7. The velocity distributions are determined in Sec. 7.4.2, Sec. 7.4.3 focuses on the analysis of the cavity dynamics, while Sec. 7.4.4 shows the acoustic results and compares those to the cavity dynamics.

7.4.2. VORTEX KINEMATICS

Using the VORTFIND algorithm the velocity field is analysed at $x/c_0 = 0.5$. Fig. 7.12 shows the time-averaged profiles of axial and azimuthal velocity along the radius, compared to the data obtained using PIV by [43]. In both graphs, also the cavity radius r_c is indicated, this being obtained based on the results described in Sec. 7.4.3.

The axial velocity for wetted flow shows a clear difference between IDDES and PANS. For IDDES the axial velocity decreases inside the viscous core radius, having a maximum at the viscous core radius for both wetted and cavitating conditions. This was also observed in Liebrand et al. [190] for RANS models (KSKL, SST and EARSM) and DDES. For PANS however, for wetted flow, the axial velocity increases to a maximum which is constant in the region $r/c_0 \lessapprox 0.08$. The inclusion of cavitation leads to a decrease in axial velocity in the core for all computations, but again PANS predicts a higher velocity than IDDES. The axial velocity is reduced even further for lower cavitation numbers (simulations at $\sigma = 1.2$ were performed but are not presented here).

The increase in inflow turbulence intensity leads to a small reduction in axial velocity in the vortex core in wetted flow conditions. This reduction is in line with the observation of Varadharajan [236], who investigated experimentally the effect of inflow turbulence on a wetted vortex at a lower Reynolds number. Several turbulence intensities (up to 6%) were employed. A reduction in axial velocity of up to 20% was measured, however the currently considered range in turbulence intensities (up to 1.3%) is smaller.

The azimuthal velocity profiles for $\sigma = 1.7$ with PANS match the experiments well, both in terms of viscous core radius and velocity magnitude. The IDDES predictions show a slightly reduced azimuthal velocity and a smaller viscous core radius. In wetted flow conditions, for both models the azimuthal velocity is underpredicted at the viscous core radius. The PANS results show a higher maximum velocity compared to IDDES, but this is still approximately 20% lower than the experimental values. Increasing $\mathscr{I}$ increases the maximum velocity for IDDES, but for PANS there is no observable difference.

From these figures, the viscous core radius is obtained, as well as the axial and azimuthal velocities at the cavity interfaces. These values – obtained at this downstream location – are used as input for the semi-analytical dispersion relationship (Eq. 7.1). It is known from literature (e.g. [190]) that the viscous core size and cavity radius depend on the downstream distance, due to the counteracting effects of roll-up and vortex diffusion. Generally, the cavity radius decreases somewhat linearly, while the viscous core size keeps increasing downstream. This downstream location is a compromise between downstream distance of the wing tip, and the limited length of the cavity in the simulations. It does introduce an error in the determination of the dispersion lines (Eq. 7.1); based on Fig. 7.3 the effect of this error can be approximated.

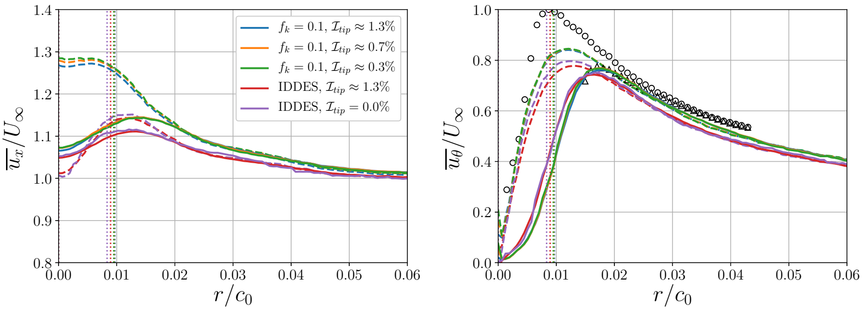

Figure 7.12: Radial distribution of axial (left) and azimuthal (right) velocity at $x/c_0 = 0.5$. Dashed lines and circles indicate $\sigma = 4.2$ (wetted flow), solid lines and triangles correspond to $\sigma = 1.7$. Vertical dotted lines indicate the cavity radius r_c ($\alpha_v = 0.1$). Experimental data from Pennings, Westerweel, et al. [43].

7.4.3. CAVITY DYNAMICS

Secondly, the cavity dynamics are analysed based on the cavity iso-surfaces ($\alpha_v = 0.1$) extracted at every timestep (as described previously in Sec. 7.2.4). All results shown here are obtained with a PANS model, $f_k = 0.1$, with $\mathscr{I}_{tip} = 0.7\%$.

To select which part of the vortex to analyse, space-time diagrams, are used. In these contour plots, the cavity radius is shown with the downstream distance off the tip (x) on the horizontal axis, and time (t) on the vertical axis. Downstream propagating phenomena can be observed as diagonal lines. Fig. 7.13 shows $x-t$ diagrams for IDDES with and without inflow turbulence, leading to a dynamic and steady cavity, respectively. In the derivation of the dispersion relation (Eq. 7.1) it is assumed that the vortex is an infinitely long 2D vortex. This requires theoretically that the vortex should be analysed where the cavity size no longer grows (after the roll-up, $x/c_0 > 1.0$), nor decays. However, in computational results it is commonly observed that the cavity diffuses after $\approx 1c_0$ downstream of the tip [190]. Consequently, in the current study, the vortex is analysed from directly behind the tip until the point where it diffuses, so the effect of the roll-up is not removed. This is also a clear discrepancy between simulations and experiments. In experimental results, the cavity extends all the way until the end of the test section, i.e. $\mathcal{O}(10c_0)$.

From Fig. 7.13 the effect of ITG is clearly visible. Both results are obtained with IDDES, but while the results with ITG show dynamics and a vortex increasing and decreasing in length and radius, the results without ITG converge indeed to a steady solution for $t/s \gtrapprox 0.1$.

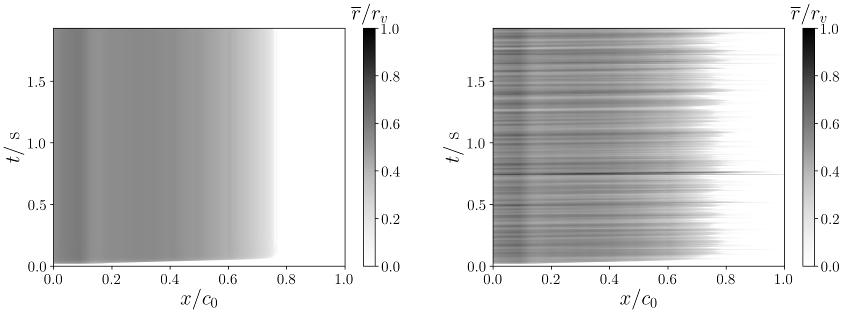

Figure 7.13: Space-time diagram of cavity radius normalised with viscous core radius. Left IDDES without ITG ($\mathscr{I}_{tip} = 0.0\%$), right with ITG ($\mathscr{I}_{tip} \approx 1.3\%$).

RESOLUTION

The resolution of the cavity dynamics analysis can be computed from the sampling resolution in time and space. In this analysis the timestep is $\Delta t = 1.93 \cdot 10^{-4}$ s, so the sampling frequency is $f_{s,time} = 1/\Delta t = 5.81 \cdot 10^3$ Hz, and consequently the Nyquist frequency is $f_{N,time} = f_{s,time}/2 = 2.91 \cdot 10^3$ Hz. The number of temporal samples is 1×10^4, while the number of spatial samples is 500 over a length of $2c_0$ behind the tip, leading to $\Delta s = 6 \cdot 10^{-4}$ m, $f_{s,space} = 1/\Delta s = 1.67 \cdot 10^3$ m^{-1} and $f_{N,space} = f_{s,space}/2 = 8.35 \cdot 10^2$ m^{-1}. The distance between two slices corresponds to $2-3$ cells, so the spatial resolution is slightly undersampled.

Based on Fig. 7.13, the cavity is commonly analysed in the range $0.0 < x/c_0 < 0.8$, leading to 10^2 spatial and 10^4 temporal samples. Following the approach of Bosschers [13], the time-averaged data for each streamwise location station is subtracted to obtain the fluctuations with respect of the mean. For the FFT a single segment is used to obtain the best resolution.

This leads to a spatial resolution of $\Delta k_x = 9.95$ m^{-1} and a temporal resolution of $\Delta f = 2.07$ Hz. For PANS ($f_k = 0.1$) with $\mathscr{I}_{tip} \approx 0.7\%$, this results in the non-dimensional resolutions of $\Delta(k_x r_c) = 2.6 \times 10^{-3}$ and $\Delta\left(2\pi f r_c/U_\infty\right) = 1.1 \times 10^{-2}$. For comparison, van den Boogaard [279] obtained $\Delta k_x = 36-84$ m^{-1} and $\Delta f = 4-8$ Hz, while Bosschers [13] had a resolution of $\Delta k_x = 31.6$ m^{-1} and $\Delta f = 0.15$ Hz. Bosschers [13] indicated that while his temporal resolution was sufficient, his spatial resolution was not. The resolution in the current analysis therefore uses a coarsened temporal resolution, and a refined spatial resolution.

1D ANALYSIS

Following Bosschers [13] a 1D analysis is first performed, where an averaging operator in time or space is applied, followed by a FFT in space or time, respectively. Fig. 7.14 shows the 1D PSD for the effective radius, eccentricity, centroid location and angle.

The PSD of the time-averaged effective radius, centroid locations and angle decrease after $k_x r_c \approx 0.04$. For the time-averaged angle and eccentricity there is a peak at $k_x r_c \approx 0.1$. In the space-averaged PSDes, there is a peak in the spectrum at $2\pi f r_c / U_\infty \approx 0.01$, after which the spectra decrease. For the effective radius and y and z centroids there is a slight hump at $2\pi f r_c / U_\infty \approx 0.2$. The eccentricity and angle show a clear peak at $2\pi f r_c / U_\infty \approx 0.3 - 0.4$, and for the eccentricity there is another peak at $2\pi f r_c / U_\infty \approx 1.0$. These peaks are an indication that the helical mode is present in the cavity. At a slightly lower frequency, $2\pi f r_c / U_\infty \approx 0.2$, there is also a peak for the y and z centroids for PANS with $\mathscr{I}_{tip} = 0.7$ and 0.3%, pointing to the serpentine mode. The effective radius does not show a clear peak, indicating that the breathing mode is difficult to discern from the simulations. The spectra will be related to the produced sound in Sec. 7.4.4, where a physical interpretation will be given.

For PANS, increasing the inflow turbulence intensity generally also increases the PSD of the space-averaged quantities. For the y and z centroids, for $\mathscr{I}_{tip} = 1.3\%$ there is a much higher broadband spectrum at higher frequencies, thereby obscuring the secondary peaks which can be observed for the lower intensities. A possible explanation for this is that in this case the inflow turbulence disturbs the vortex to such a degree that the vortex no longer oscillates in a natural frequency.

2D ANALYSIS

Secondly a 2D analysis is applied, where a FFT in time and in space is applied simultaneously, resulting in a wavenumber-frequency diagram in which dispersion relationships should appear as diagonal lines (as detailed in Sec. 7.2.1). The contour plots of the 2D PSD and CPSD are also smoothed using a bilinear filter to remove noise.

In the 2D PSD plots the fitted dispersion relations (Eq. 7.1) are shown, using the values given in Tab. 7.2. The tables shows the fitting parameters obtained from the computations, and from the theoretical relations given by Bosschers [13] (Eq. 7.2 and Eq. 7.3). $\tilde{U}_{x,c}$ has no theoretical counterpart. $\tilde{U}_{\theta,c}$ from the computations is lower than the potential flow and Lamb-Oseen values. For K_σ the Lamb-Oseen values are used in the plots. $\tilde{U}_{x,c}$ is slightly lower than the experimentally observed value, while $\tilde{U}_{\theta,c}$ matches the experimental value well. As expected based on the results in Sec. 7.4.2, there is little difference between the parameters for the different simulations. Compared to the experimental values from Bosschers [13], $\tilde{U}_{x,c}$ is 20% lower, while $\tilde{U}_{\theta,c}$ is comparable.

In line with the experimental analysis, convection lines, defined by

$$\tilde{\omega} = c_g \left(\tilde{k}_x - \tilde{k}_{x,0} \right), \tag{7.11}$$

are drawn at constant group velocity c_g and using $\tilde{k}_{x,0} = 0.42m$, with $m = 0$. Bosschers [13] used $c_g = 0.95 U_\infty$, but in the current study, a better match was obtained using $c_g =$

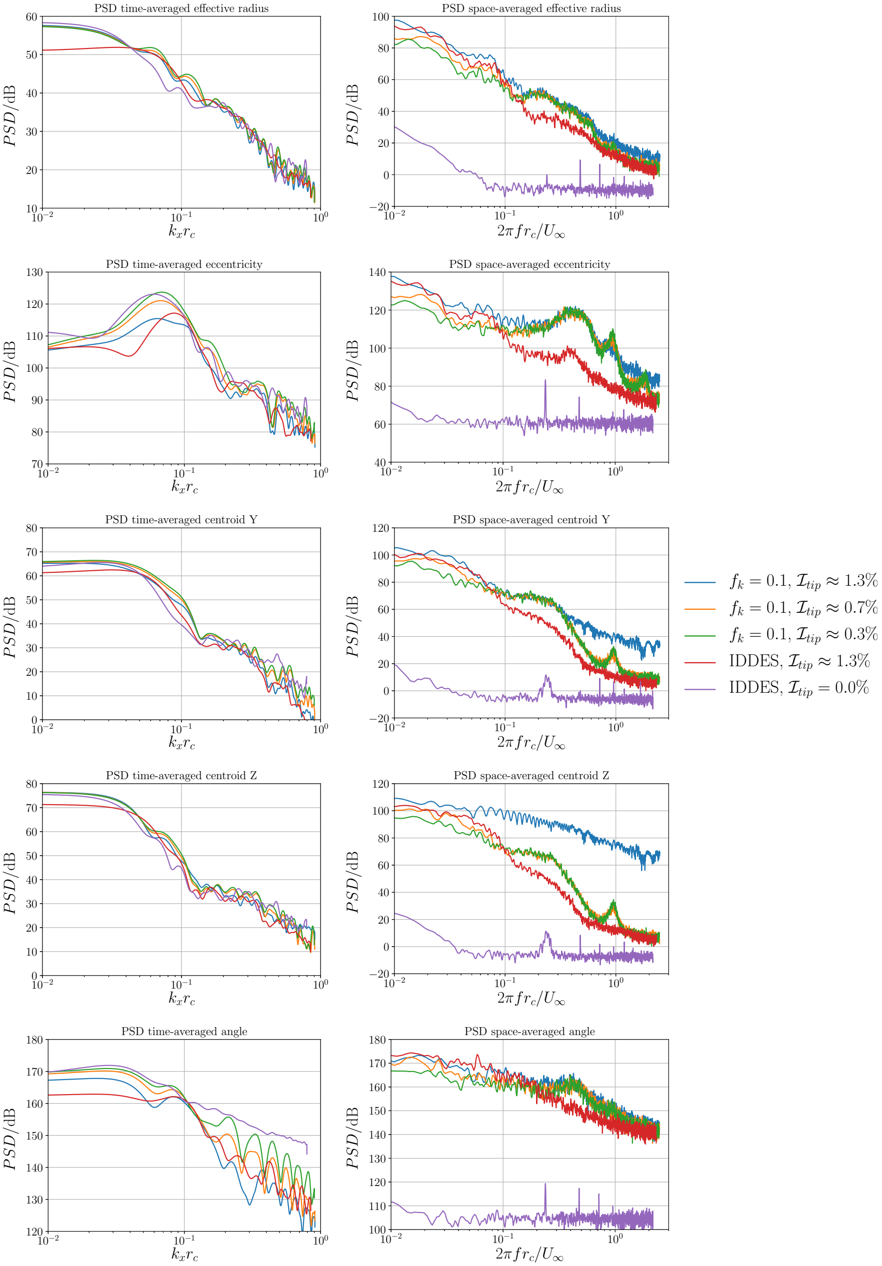

Figure 7.14: Frequency domain analysis of the temporally- (left) and spatially-averaged (right) effective radius, eccentricity, centroid and angle of the cavity. The resolution is given in Sec. 7.4.3.

$1.25U_\infty$. This value is closer to the value $c_g = 1.19U_\infty$ employed by Pennings, Bosschers, et al. [273].

Table 7.2: Values of non-dimensional velocities and stiffness coefficient at the cavity interface for $\sigma = 1.7$, based on Equations 7.2 and 7.3 for potential flow and Lamb-Oseen, respectively (see Section 7.4.2), and based on computations. The values used for the lines in Figs. 7.15 and 7.16 are indicated in **bold**. Cavity radius and viscous core size are given in Table. 7.1. For $\sigma = 1.7$, Bosschers [13] gives experimental values of $\tilde{U}_{x,c} = 1.25$ and $\tilde{U}_{\theta,c} = 0.4$.

Computation	$\mathscr{I}_{tip}/\%$	Coefficient	Potential flow	Lamb-Oseen	Computation
PANS($f_k = 0.1$)	1.3	$\tilde{U}_{x,c}$	-	-	**1.013**
		$\tilde{U}_{\theta,c}$	1.30	0.622	**0.387**
		K_σ	1.70	**0.387**	-
PANS($f_k = 0.1$)	0.7	$\tilde{U}_{x,c}$	-	-	**1.012**
		$\tilde{U}_{\theta,c}$	1.30	0.616	**0.387**
		K_σ	1.70	**0.379**	-
PANS($f_k = 0.1$)	0.3	$\tilde{U}_{x,c}$	-	-	**1.011**
		$\tilde{U}_{\theta,c}$	1.30	0.630	**0.385**
		K_σ	1.70	**0.397**	-
IDDES	1.3	$\tilde{U}_{x,c}$	-	-	**1.002**
		$\tilde{U}_{\theta,c}$	1.30	0.620	**0.365**
		K_σ	1.70	**0.384**	-
IDDES	0.0	$\tilde{U}_{x,c}$	-	-	**1.002**
		$\tilde{U}_{\theta,c}$	1.30	0.587	**0.369**
		K_σ	1.70	**0.344**	-

Fig. 7.15 shows the PSD of eccentricity, effective radius, y centroid and angle for a PANS simulation with $\mathscr{I}_{tip} \approx 0.7\%$. Fig. 7.16 shows the CPSD and phase difference for the $y-z$ centroid and $a-b$ of the fitted ellipse. Following the results by Bosschers [13], the phase differences are only shown for a coherence larger than 0.4. Results for the $\mathscr{I}_{tip} \approx 0.3\%$ are similar, and not shown in this thesis. The 1D analysis in Fig. 7.14 showed a lot of noise in the space-averaged PSDes of the y and z centroids coordinates for $\mathscr{I}_{tip} \approx 1.3\%$. This reduces the coherence and makes both the trends for the z centroid and the phase differences more difficult to observe, again pointing to the conclusion that the vortex is no longer oscillating according to a dispersion relation, and instead is dominated by the inflow turbulence. As expected, the reduced dynamics and cavity length for the IDDES simulation make observing the dispersion relation more difficult. Consequently, these results are not presented.

The PSD of the effective radius shows a diagonal lines in the wavenumber-frequency diagram, but this does not match the theoretical lines for the $n = 0^\pm$ modes. The slope does match the dispersion lines, as is to be expected, since it depends on the axial flow speed. The same occurs for the PSD of the y and z centroids. The diagonal lines visible in the PSD of the effective radius and y and z centroids match the convection line $c_g\,(m = 0)$. The PSD of the eccentricity and angle do match the $n = 2^-$ and $n = -2^+$ modes.

The CPSD of the $y-z$ centroid and $a-b$ ellipse show a similar behaviour. Again the

$n = \pm 1^{\pm}$ modes are not distinguishable, but the $n = 2^{-}$ and $n = -2^{+}$ modes can be clearly observed in the CPSD of the $a - b$ ellipse. In contrast, the phase difference of the $y - z$ centroid does match the theoretical dispersion lines for the $n = -1^{+}$ and $n = 1^{-}$ modes. For the CPSD of the $y - z$ centroid clearly shows the convection line c_g $(m = 0)$.

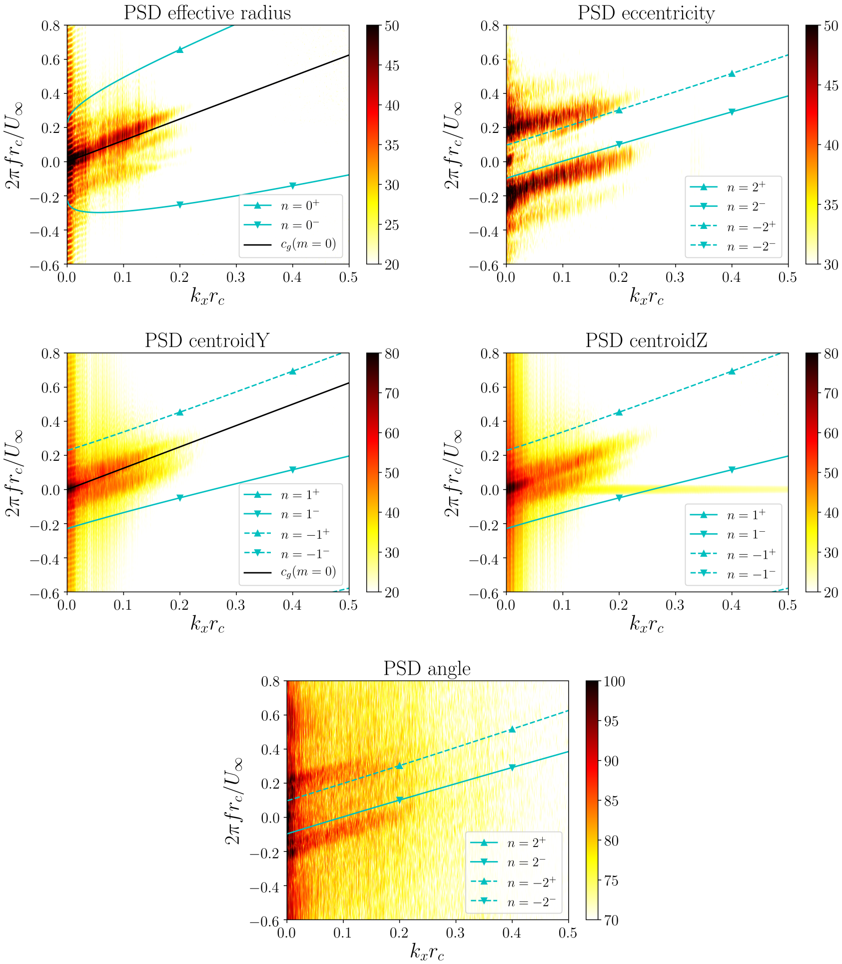

Figure 7.15: PANS ($f_k = 0.1$), $\sigma = 1.7$, $\mathscr{I}_{tip} \approx 0.7\%$. Wavenumber-frequency diagrams (PSD) of the variation of the effective radius, y and z centroids, eccentricity and angle, based on a single segment FFT. Theoretical dispersion lines shown in cyan, and convection line in black.

What can be concluded from these results? The match with the theoretical predictions shows that the helical mode shape can be clearly distinguished from the PSDes, while the serpentine mode can be distinguished from the phase difference, but not in the PSD. This is in line with the observations by Bosschers [13] based on experiments by Pennings, Bosschers, et al. [273]. In contrast, the breathing mode (volume variation) is difficult to distinguish. Two reasons for this can be identified. First, when comparing the

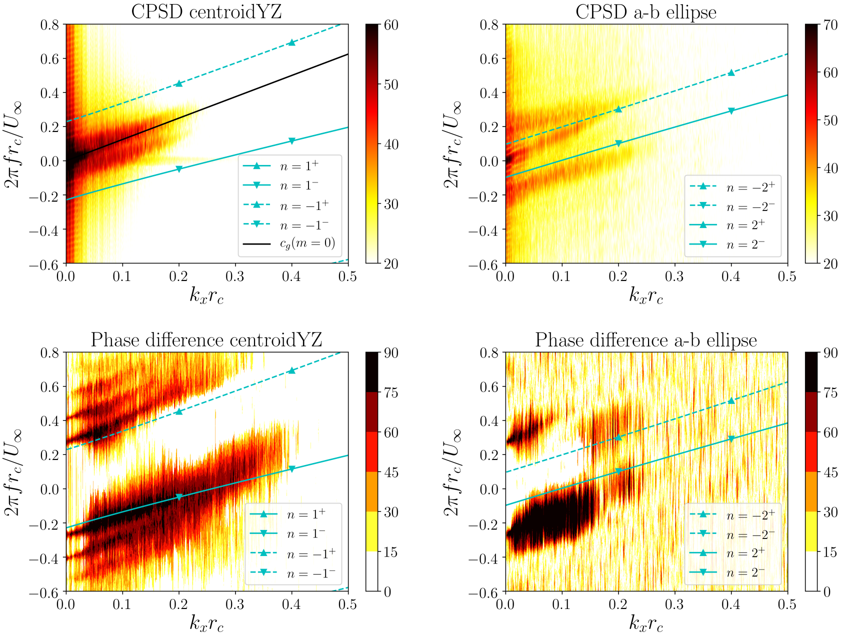

Figure 7.16: PANS ($f_k = 0.1$), $\sigma = 1.7$, $\mathscr{I}_{tip} \approx 0.7\%$. Wavenumber-frequency diagrams (CPSD) and phase difference of the $a - b$ ellipse and the $y - z$ centroid coordinates, based on FFT with 4 segments in time and 2 in space, with a 75% overlapping Hann window. Phase differences with a coherence below 0.4 are masked. Theoretical dispersion lines shown in cyan, and convection line in black.

cavity radius with the experimental result, it is clear that the numerically predicted cavity length is both significantly smaller from the experimental cavity, and fluctuates. This was already observed in Fig. 7.13. The fluctuations can cause shrinking of the cavity along the entire cavity length in a short timespan, instead of a fluctuation propagating along the cavity with approximately the free-stream velocity. This results in a large peak at zero wavenumber and frequency, making observing the dispersion relationship difficult. Secondly, while the time-averaged numerical cavity radius is larger ($r_c/c_0 \approx 0.01$) compared to the experimental value ($r_c/c_0 = 0.0038$ [13]), it also varies more along the cavity length. This invalidates the assumption of an infinite vortex, made in the derivation of the dispersion relation. An alternative explanation would insufficient excitation of the breathing mode, either in amplitude or frequency. However, the wavelength corresponding to the resonance criterion of zero group speed (at $\partial\tilde{\omega}/\partial\tilde{k}_x = 0$ [13]) is $\lambda = 2\pi r_c/\tilde{k}_x$, with $\tilde{k}_x = 0.05$, leading to $\lambda \approx 0.078$ m. This wavelength is close to the turbulence integral length scale of the inflow turbulence ($\mathscr{L} = 0.6c_0 = 0.075$ m). This suggests that a lack of excitation does not cause the absence of the $n = 0$ mode.

The reduced cavity dynamics for IDDES can be related to the model formulation, which blends RANS with LES depending on the location (in contrast to PANS). Fig. 7.17 shows the RANS/LES regions around the wing tip. As expected, the area close to the wing is solved using RANS. The local refinements in the grid are also clearly visible, since they directly affect the RANS/LES interface (see Sec. 7.3). While most of the tip vortex is in a LES region, the vortex originates in a RANS region at the wing tip. This is also the location where the inflow turbulence is most likely to interact with the vortex, since the remainder of the vortex is locating in the wake of the wing. The use of RANS at the wing tip reduces the resolved turbulent velocity fluctuations, which are transferred to modelled turbulence. Consequently, the excitation of the vortex is reduced, leading to less cavity dynamics.

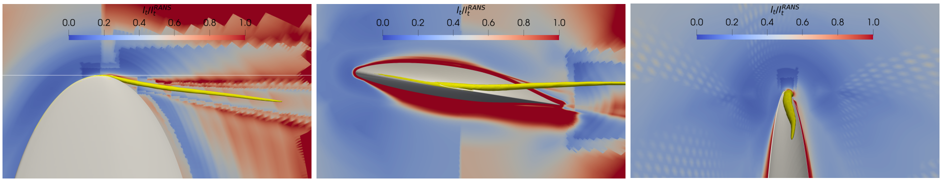

(a) Chordwise-normal ($y/c_0 = 0.0$) (b) Spanwise-normal ($z/c_0 = 0.8$) (c) Streamwise-normal ($x = x_{tip}$)

Figure 7.17: Instantaneous LES regions (l_t/l_t^{RANS}) for the IDDES model close to the wing tip. 1 indicates RANS, 0 LES. The cavity is indicated in yellow.

7.4.4. FAR-FIELD NOISE

Finally, the far-field radiated noise is investigated using the results of the FWH acoustic analogy. The results are presented as source levels (SL) at one metre, assuming spherical spreading,

$$\mathrm{SL}(f) = \mathrm{SPL}(f) + 20\log_{10}(|\mathbf{r}|) \tag{7.12}$$

with SPL(f) the sound pressure level, defined as

$$\mathrm{SPL}(f) = 10\log_{10}\left(\frac{\phi_{pp}(f)}{p_{ref}^2}\right) \tag{7.13}$$

where ϕ_{pp} is the acoustic pressure power spectral density and p_{ref} the acoustic reference pressure, $p_{ref} = 1\times10^{-6}$ Pa; and the overall SL,

$$\mathrm{OASL} = 10\log_{10}\left(\frac{\int_{f_1}^{f_2}\phi_{pp}\mathrm{d}f}{p_{ref}^2}\right) + 20\log_{10}(|\mathbf{r}|), \tag{7.14}$$

indicating the decibel level of the normalised acoustic energy across the frequency range $f_1 - f_2$.

The source levels have been smoothed using a top hat filter based on one-third octave (OTO) bandwidths, according to

$$\hat{\phi}(f_c) = \int_{f_l}^{f_u}\phi(f)\mathrm{d}f - \Delta f_{OTO}, \tag{7.15}$$

which is then corrected to recover the narrowband spectrum level. Here f_c are the OTO bandwidth centre frequencies, resulting in $f_l = 2^{-1/6}f_c$ and $f_u = 2^{1/6}f_c$.

Following common practise for sound measurements [285], a background noise correction is applied [18]:

- if the difference between signal and background noise is more than 10 dB, the results are not adjusted;
- if the difference is between 3 and 10 dB, the background noise is subtracted from the signal;
- if the difference is below 3 dB, the source level data in the corresponding OTO band is discarded due to an insufficient signal-to-noise ratio.

WETTED FLOW

Fig. 7.18 shows the SL spectra for the furthest downstream receiver for the wetted flow computations, and the OTO SL corrected using the IDDES simulation without inflow turbulence for the background noise levels. All spectra show a peak at $2\pi f r_c/U_\infty \approx 0.02 - 0.04$, after which the spectrum decays. For PANS the SL is proportional to inflow turbulence intensity in the frequency range $10^{-2} < 2\pi f r_c/U_\infty < 10^{-1}$; doubling the intensity results in an increase at the spectral peak of approximately 10 dB. In the range $2\pi f r_c/U_\infty > 0.2$ the spectra converge.

In contrast, the IDDES spectrum shows the same peak at lower frequencies, but is significantly lower in the region $2\pi f r_c/U_\infty > 0.2$. For IDDES without ITG ($\mathscr{I}_{tip} = 0.0\%$), the SL is, as expected, even lower. Across the frequency range the difference is around 150 dB. Consequently, in the largest part of the frequency range, the results are not adjusted by the background noise correction.

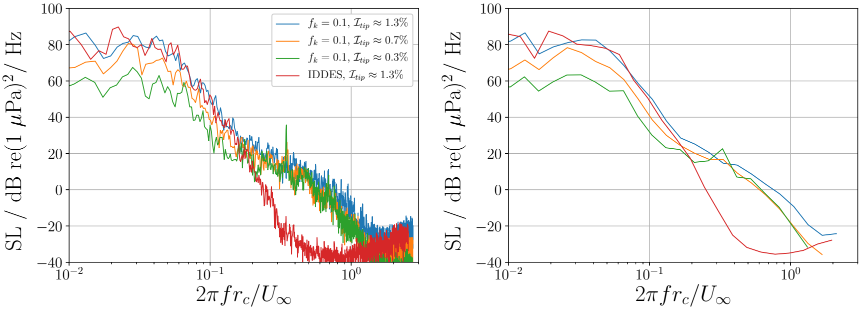

Figure 7.18: Wetted flow spectra (left) and OTO bandwidth filtered spectra, corrected with the IDDES $\mathscr{I}_{tip} = 0.0\%$ result (right), obtained at the furthest downstream receiver.

From the sensitivity of the spectrum to varying inflow turbulence intensities, and the fact that the frequency range overlaps with the energy-containing frequency range in the inflow spectrum (see Fig. 7.6), it can be concluded that the peak at lower frequencies is directly related to the inflow turbulence. The peak at lower frequencies is also present in pressure spectra made at locations close to the wing tip (not shown). This frequency range should therefore not be considered in the following, cavitating, investigations to assess the overall sound level (OASL). This will be ensured by performing the background noise correction.

Fig. 7.19 shows gives the OASL, integrated over the frequency range $0.01 \leq 2\pi f r_c/U_\infty \leq 0.1$. In this frequency range the inflow turbulence intensity has the largest effect, based on Fig. 7.18. The results for $\mathscr{I}_{tip} = 1.3\%$ for IDDES and PANS are almost identical. There is a an increase of approximately 120 dB between simulations with $\mathscr{I}_{tip} = 0.0\%$ and $\mathscr{I}_{tip} = 0.3\%$. For PANS, doubling the turbulence intensity leads to a subsequent increase of 10 dB. The results for the different planes are almost identical, pointing to a monopole behaviour. This implies that the first term in Eq. 2.68 dominates, likely since the ITG introduces a large varying velocity normal to the PDS.

CAVITATING FLOW

Fig. 7.20 shows the SL spectra at the furthest downstream receiver in cavitating conditions, and compares it against wetted flow computations. Again the observation can be made that – compared to IDDES – the PANS simulations predict a higher SL in the region $2\pi f r_c/U_\infty > 0.2$, while having a comparable magnitude at lower frequencies. The SL of IDDES without ITG ($\mathscr{I}_{tip} = 0.0\%$) is again not visible in the graph due to its low magnitude.

Comparing the cavitating results to the wetted flow results shows that for frequencies in the range $2\pi f r_c/U_\infty > 0.05$, the cavitating simulations predict a SL which is 10-20 dB higher. The SL of PANS wetted flow is approximately the same as the SL for IDDES with cavitating flow. This increase in SL for PANS can be related to the increased cavity dynamics as observed in Sec. 7.4.3.

Fig. 7.21 shows the SL spectra for only the cavitating simulations, and the SL for each simulation corrected using the corresponding wetted flow spectrum. The PANS simula-

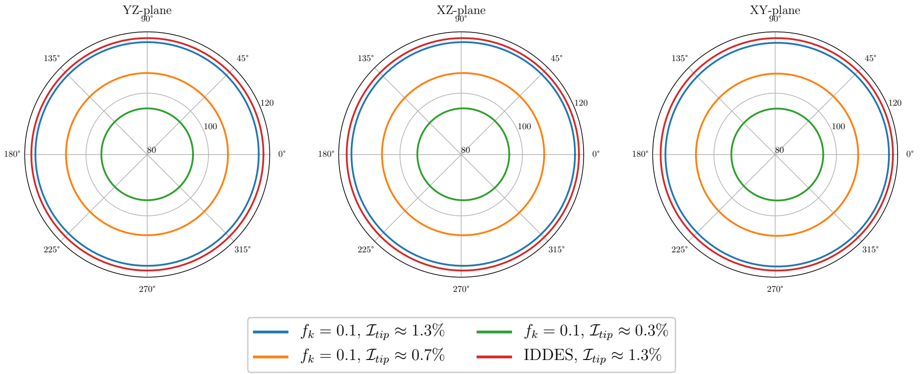

Figure 7.19: OASL for wetted flow computations at receivers in the different planes, integrated over $0.01 \leq 2\pi f r_c / U_\infty \leq 0.1$. For the YZ-plane, 0° is in the lift direction, and 90° in the spanwise direction. For the XZ-plane, 0° is in the flow direction, and 90° in the spanwise direction. For the YZ-plane, 0° is in flow direction, and 90° in the lift direction.

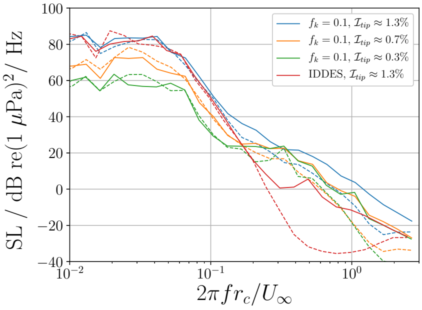

Figure 7.20: OTO bandwidth filtered spectra, for cavitating and wetted flow computations. Spectra obtained for the furthest downstream receiver. Dashed lines indicate $\sigma = 4.2$ (wetted flow), solid lines correspond to $\sigma = 1.7$.

tions with $\mathscr{I}_{tip} = 0.3\%$ and $\mathscr{I}_{tip} = 0.7\%$ show a broadband hump in the frequency range $0.2 \lessapprox \pi f r_c / U_\infty \lessapprox 0.5$, matching the hump in the PSD of the space-averaged effective radius.

There is also a peak observable at $2\pi f r_c / U_\infty \approx 0.5$, and at $2\pi f r_c / U_\infty \approx 1.0$. These peaks are more clearly observable in the uncorrected spectra, shown in Fig. 7.22, since the OTO filtering reduces the amplitude and shifts the frequency. In the uncorrected spectra, the peaks have an amplitude of approximately 10 dB. The frequency of the first peak matches the peak in the PSD of the space-averaged eccentricity, while the second one matches the peak in the space-averaged centroid. This implies that the $n = 0$ mode is responsible for broadband hump, while the $n = 1$ or $n = 2$ lead to the secondary peaks in the SL spectra. The first peak also overlaps with the cavity resonance observed in experimental measurements [273]. The increased PSD at higher frequencies in the cavity dynamics as observed for $\mathscr{I}_{tip} = 1.3\%$ manifests itself in the SL spectra by an increased SL across the frequency range $2\pi f r_c / U_\infty > 0.2$. The background noise correction clearly shows that the lower frequencies ($2\pi f r_c / U_\infty \leq 0.2$) should not be considered for determining the OASL due to cavitation, as expected based on the previous section.

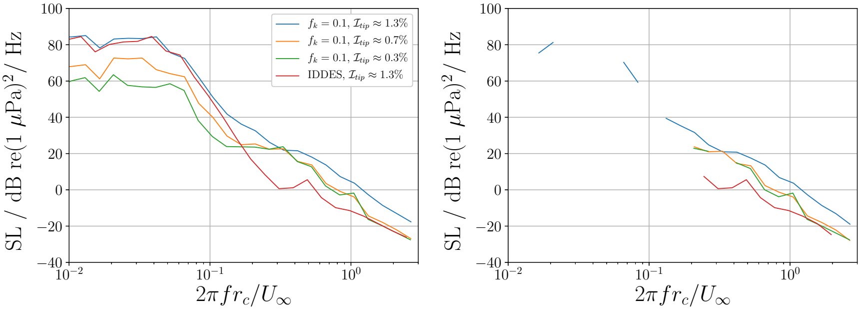

Figure 7.21: Uncorrected (left) and background noise corrected (right) OTO bandwidth filtered spectra. For the background noise corrected spectra, each cavitating spectrum is corrected by its corresponding wetted flow spectrum. The corrected spectra are discontinuous where data is discarded due to an insufficient signal-to-noise ratio. Spectra obtained at the furthest downstream receiver.

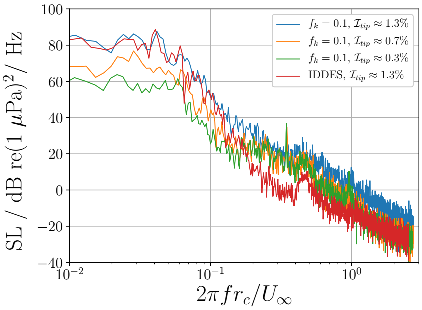

Figure 7.22: Spectra for cavitating simulations, obtained for the furthest downstream receiver.

Fig. 7.23 shows the OASL at the different receiver planes, determined in the frequency range based on the background noise correction. The OASL predicted by PANS and IDDES with cavitation and $\mathscr{I}_{tip} = 1.3\%$ is comparable, and is approximately 15 dB higher than the wetted flow OASL. Again, for PANS doubling the inflow turbulence intensity leads to an increase of approximately 10 dB, despite the different frequency range compared to Fig. 7.19. The directionality plots show that the far-field radiated noise has a monopole behaviour, which is agreement with theory and measurements for most cavitating cases (see e.g. [13]).

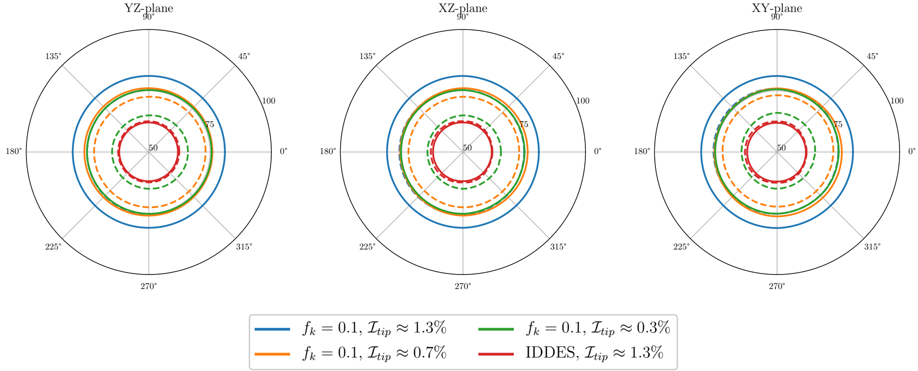

Figure 7.23: OASL at receivers in the different planes, integrated over $0.2 \leq 2\pi f r_c / U_\infty \leq 2.0$. For the YZ-plane, 0° is in the lift direction, and 90° in the spanwise direction. For the XZ-plane, 0° is in the flow direction, and 90° in the spanwise direction. For the YZ-plane, 0° is in flow direction, and 90° in the lift direction. Dashed lines indicate $\sigma = 4.2$ (wetted flow), solid lines correspond to $\sigma = 1.7$.

7.5. DISCUSSION

The cavity dynamics and associated far-field pressure fluctuations originating from a cavitating tip vortex were analysed. The results are sensitive to the choice of turbulence model, inflow turbulence characteristics, method to solve multiphase flows and the method to extract the acoustics. These aspects are discussed further.

In the cavity dynamics the oscillation modes from theory can be discerned. The slope and trend of the lines is correct, but the match between theory and simulations is less good. With additional tuning of the parameters of the semi-analytical equations it is possible that a better match can be obtained between theory and simulations. Currently, this is not done for reasons of consistency. The cavity is analysed at its interface, and hence the values for the azimuthal and axial velocity at that location are used. This points to one of the error sources. In a VOF method, there is no clear definition of an interface [65], meaning that the results are sensitive to the choice of interface used. Currently, the (common) assumption of $\alpha_v = 0.1$ (10% of vapour) is employed to locate the interface. Since the velocity distributions are proportional to the definition of the cavity radius (inside the viscous core radius), the parameters defining the dispersion lines are sensitive to this choice. An alternative method would be to fit the dispersion lines, and check at which iso-surface these values can be obtained. However, this could lead to a discrepancy between the interface used for the analysis of the cavity dynamics, and the one used for the fitting parameters. Alternatively the cavity dynamics should be analysed at a range of vapour volume fractions. Due to the associated additional computational cost and storage requirements this would entail, this was not attempted in the current study. That being said, it is important to realise that the value of vapour volume fraction does strongly affect the size of the cavity which can be analysed. While for $\alpha_v = 0.1$, the length is approximately $1c_0$, this decreases to $0.6c_0$ for $\alpha_v = 0.5$, and even to $0.2c_0$ for $\alpha_v = 0.9$. The cavity radius approximately halves with each of these steps. Since part of the discrepancies between simulations and theory can be related to the underpredicted cavity length, a higher vapour volume fraction to extract the iso-surface is not likely to improve the results.

Compared to experimental investigations, the dynamics – especially of the effective radius and centreline – are less pronounced. Since the inclusion of inflow turbulence introduces cavity dynamics, it is logical to attribute this difference to the level of inflow turbulence intensity. It must be remarked that the current levels of turbulence intensity are a compromise between numerical stability and cavitation dynamics. Higher levels of inflow turbulence intensity do lead to increased cavity dynamics, but also result in higher numerical background noise levels. It can also lead to parts of the cavity being shed, invalidating the assumption of an infinite vortex. It is hypothesised that the mechanism of the cavity dynamics is as follows: the inflow turbulence acts as a disturbance, which triggers the cavitating tip vortex at the leading edge to start oscillating. Due to this excitation, the cavity starts to oscillate in its natural frequency, leading to the observable oscillation modes. Evidence for this can be found in the mismatch in frequencies between inflow turbulence and cavity dynamics.

In this study, two methods of SRS were applied: IDDES and PANS. IDDES has two clear advantages, due to its hybrid formulation it is cheaper to apply, and it allows for running the case without inflow turbulence (which was not possible when using PANS). Nevertheless, to resolve cavity dynamics inflow turbulence is required, whatever SRS method is used. When comparing the results to PANS, it is clear that both the differences in dynamics, as well as in acoustics are significant. For IDDES, there are less cavity dynamics, and it is more difficult to discern the oscillation modes. This in turn makes it more difficult to understand the noise generating mechanics. One of the reasons for this is likely related to the RANS region close to the wing, from which the vortex originates. It seems that in the PANS simulations, the vortex is mostly affected by the inflow turbulence at the wing tip. However in IDDES this is handled by RANS. This leads to reduced cavity dynamics compared to PANS, for which part of the turbulence spectrum is resolved throughout the entire domain.

A final comment concerns the method of processing the results. A coupled CFD-solver and co-processor is used to speed up the workflow, and even more importantly, reduce the storage requirements. The cavity iso-surface is computed at runtime, at every timestep, and stored to a file by the co-processor. This results in approximately 40 Gb of iso-surface data per simulation. To put this into perspective, storing the full solution file containing all fields, to extract the iso-surface *a posteriori*, would require approximately 80 Tb of data per simulation, i.e. an increase of a factor 2000. Even when only the grid data and vapour volume fraction field would be saved, this would still result in approximately 20 Tb of data per simulation. It is clear that that standard approach would make the study here performed unfeasible.

7.6. CONCLUSIONS

A tip vortex originating from an elliptical wing is simulated with SRS in conjunction with synthetic inflow turbulence. Reported results include kinematics, 3D cavity dynamics, and far-field pressure levels. The dynamics are compared to a modal decomposition based on theory for an infinitely long, 2D, cavitating vortex.

The comparison of the velocity profiles showed that the results match the experiments reasonably well in cavitating conditions. In wetted flow results, the peak azimuthal velocity is underpredicted by 20%. The application of synthetic inflow turbulence leads to observable cavity dynamics, which is a significant improvement compared to previous results reported in literature, for which the simulations converge to a steady state solution, even when using SRS. The mean velocity profiles are little affected by in the inflow turbulence, in the range of turbulence intensities employed in this study. In general, increasing the inflow turbulence intensity leads to increased cavity dynamics. However, it was shown that a too high inflow turbulence intensity can disturb the vortex to such a degree that observing the dispersion relation is no longer possible.

The cavity dynamics are analysed using 1D and 2D FFT's of the effective radius, centroid, angle, eccentricity and coefficients of the fitted ellipse. It was not possible to observe the breathing mode, likely due to the violation of the assumption of an infinite vortex, and because the variations in cavity length affected the cavity radius. The serpentine mode could be observed in the phase difference of the y and z centreline coordinates, while the helical mode could be observed in the angle, eccentricity and the CPSD of the fitted ellipse. To the knowledge of the authors, this is the first time that it was possible to numerically reproduce the semi-analytical dispersion relationship of a cavitating vortex. In contrast to the experimental observations from literature, in the current study the dispersion relation is matched against the numerical data using fitting parameters obtained from the simulations itself, thereby validating this relation.

Far-field pressure levels were obtained using an acoustic analogy. There is a clear difference for far-field radiated noise between wetted and cavitating flow. The inclusion of cavitation leads to an increase of 10 – 20 dB in the far-field SL, as long as dynamics are introduced by synthetic inflow turbulence. The variability in the inflow introduces the broadband hump in the sound spectrum. In the spectra the effect of inflow turbulence is also present, but the sound sources can be separated based on their frequency range. When comparing the acoustic spectra to the spectra of the cavity dynamics, it seems that especially the effective radius and the eccentricity in the non-circular cross-section contributes to the acoustics for this case. These are described by the $n = 0^{\pm}$ and $2^{\pm}$ modes of the dispersion relationship. The peaks in the sound spectra match the resonance frequency observed in literature. Since the acoustic behaviour is a monopole, it is clear that the variations in effective radius dominate the radiated noise, as was expected.

For future work, it would be desirable to capture the $n = 0^{\pm}$ modes, since these dominate the produced far-field noise. Several lines of work could be investigated. Firstly, it would be desirable to obtain a longer cavity – by using finer grids or modifications to the cavitation model – to better comply with the assumptions made in the derivation semi-analytical model. This way the match with experimental data could also be improved. Alternatively, varying inflow turbulence integral length scales could be considered. Finally, there is the option to use an inflow which more closely resembles a wake field affecting a ship propeller. Such a wake field results in different excitation frequencies affecting the vortex, since the wake is dominated by the blade passage frequency. This could be achieved for a wing by varying the inflow speed or angle of attack. With respect to noise predictions, it would be preferable to have the PDS inside a constant grid density region, which requires an increased cell count in the wake.

In this study a co-processing method is used to manage the amount of data being generated. With the increase in available computational power such large data flows will become even more of an issue in the future. This means that performing data analysis during the simulation runtime – although requiring more work to setup the simulation – is the only scalable future option.

8

CONCLUSIONS

This chapter summarises the main conclusions and recommendations.

8.1. INTRODUCTION

This thesis aims to give a better understanding of simulating cavitating tip vortices, in order to predict sources of URN. To this end, SRS were applied to several test cases, including wetted and cavitating conditions. Conclusions concern both the simulation of noise sources, as well as the general application of SRS. Based on the findings several recommendations are given for further research directions, as well as for the use of SRS.

8.2. THE NEED FOR AN UNSTEADY INFLOW CONDITION

It is repeatedly shown in literature that the results of LES or DNS can be dependent on inflow conditions, e.g. [26, 27]. For SRS of attached turbulent flows it is necessary that the inflow contains time-varying stochastic fluctuations which resemble turbulence. In the field of maritime engineering, this has mostly not been addressed until now. The following problems associated with not using a resolved turbulent inflow were observed in this study for the different test cases:

- Turbulent channel flow: when using PANS, there is a case-dependent threshold based on the ratio of modelled-to-total turbulence kinetic energy f_k, which separates two solution regimes: $0.2 \leq f_k < 1.0$ yields a laminar solution regardless of the initialisation of the flow, while if $f_k < 0.2$, a turbulent flow can develop. A resolved turbulent inflow therefore is necessary.
- Delft Twist 11 hydrofoil: the boundary layer flow remains laminar, and depending on the grid resolution and f_k, leading edge separation can be seen at the angle of attack investigated. In the experiments, this was circumvented by adding leading edge sand roughness. The inclusion of cavitation in the computation tends to mask the leading edge separation, thereby partly explaining reported agreement between numerical and experimental results in literature.

- Elliptical wing: the boundary layer flow remains laminar, and depending on the grid resolution and f_k, can also show leading edge separation. More importantly, this test case was experimentally used to investigate cavitation dynamics. However without inflow turbulence all simulations converge to a steady solution resulting in a lack of noise generating mechanisms. This conclusion is in line with that of Pennings [36], who concluded that a cavitating vortex only acts as a noise source when the natural frequencies of the cavity are excited.

For the channel flow with periodic boundary conditions and a low enough f_k value, a turbulent flow, matching DNS results, can be obtained. However, for the other cases – simulating an object in the centre of a cavitation tunnel – it is common to employ slip walls for the domain walls to reduce the computational cost. It is also not desirable to use periodic boundary conditions, to prevent the wake of the object interacting with the object. These two reasons make the use of synthetic inflow turbulence a necessity in order to obtain a SRS flow prediction matching the experimental results.

8.3. SRS WITH A TURBULENT INFLOW

It is shown that, independent of the selected turbulence simulation approach, the synthetic method can produce a turbulent inflow at significantly lower computational cost than using a precursor method. The ability to more easily tune the method to obtain the desired Reynolds stresses and length scales is also attractive for industrial applications for which these quantities may already be known. Despite the proposed improvements, the possible introduction of additional numerical errors – such as interpolation and iterative errors (especially occurring in multi-phase flow conditions) – remains a concern. Nevertheless, the modelling errors are significantly reduced by improving the similarity between computations and experimental setups.

The main findings per test case are:

- Turbulent channel flow: synthetic inflow turbulence can deliver a turbulent flow for PANS computations with higher f_k values.

- Delft Twist 11 Hydrofoil: when employing a resolved turbulent inflow, the leading edge separation disappears regardless of the chosen input values for the turbulence generator. The flow field matches the experimentally observed flow field better, and the mean lift and drag force are increased, though still underpredicted compared to the experimental values. Importantly, the pressure distribution is not affected, thereby not changing the cavitation inception behaviour when using the cavitation inception criterion $C_p < -\sigma$.

- Elliptical wing: the introduction of synthetic inflow turbulence again suppresses leading edge separation. It also leads to observable cavitation dynamics, whereas these dynamics were lacking in the case of a steady inflow. This indicates that the synthetic inflow turbulence acts as an disturbance for the tip vortex, which then oscillates at its natural frequencies.

8.4. CAVITATION DYNAMICS AND NOISE GENERATION

For the Twist foil in cavitating conditions, the variations in lift and drag due to resolved inflow turbulence are significantly smaller than the fluctuations due to the shedding sheet cavity. This indicates that for this test case the dynamics of the sheet cavity are relatively unaffected by the inflow turbulence.

For a cavitating tip vortex, the introduction of synthetic inflow turbulence leads to cavitation dynamics that match the theoretical predictions based on a modal decomposition for an infinitely long, two-dimensional, cavitating vortex. The serpentine and helical modes were clearly observed, but it was not possible to discern the breathing mode in the wavenumber-frequency diagrams. It is hypothesised that this is due to the limited and fluctuating cavity length in the simulations, invalidating the assumption of an infinite vortex in the dispersion relation. The fluctuation in cavity length also cause a decrease of the cavity radius along the length, instead of a fluctuation propagating along the cavity length, making observing the dispersion relationship difficult.

The acoustic analysis showed that the inclusion of cavitation leads to an increase of 10-20 dB in the acoustic source level, as long as cavity dynamics are introduced. Far-field pressure fluctuations occur at similar frequencies as the variations in effective radius and eccentricity in the non-circular cross-section. The acoustic behaviour is a monopole, since it is dominated by variations in the effective radius. Numerical noise due to the inflow turbulence is also present in the sound spectra. Using wetted flow computations with inflow turbulence, it was possible to perform a frequency-dependent background noise correction, and separate the predicted cavitation noise from other spurious contributions.

8.5. FINDINGS RELATED TO PANS

8.5.1. EFFECT OF f_ε

When using PANS, two settings determine the turbulence resolution: the modelled-to-total ratio of turbulence kinetic energy and dissipation, f_k and f_ε, respectively. In literature, PANS is applied almost exclusively using $f_k < 1.0$ and $f_\varepsilon = 1.0$ (known as the ‘high Reynolds number’ approach), assuming that dissipation occurs entirely at the modelled scales.

This assumption was tested using simulations of a turbulent channel flow at varying Reynolds numbers. When reducing f_ε, under the condition $f_k < f_\varepsilon < 1$, the results show a larger dependency on f_k. Due to the reduction of f_ε, the turbulence dissipation is no longer confined to the smallest scales, leading to excessive diffusion and a suppression of the smaller scales. In the case of a channel flow, this can lead to a laminar-like solution, independent of the flow initialisation or Reynolds number. Only when using a very low f_k (in the DNS limit) can reasonable results for the mean velocity and Reynolds stress profiles be obtained, although in that case the results for $f_\varepsilon = 1.0$ also match the reference data well. Consequently, for industrial flow cases at high Reynolds number, the recommendation to use $f_\varepsilon = 1.0$ was found to be valid.

8.5.2. SELECTING f_k

For the usage of PANS two approaches can be distinguished: 1) the *Constant* f_k approach, where a constant value of f_k is used in the domain and throughout the simulation time; and 2) the approach where f_k can vary. This approach can be further subdivided into *Static*, where f_k is fixed in time, or *Dynamic* for which f_k can also vary in time. At the time of writing, there is no consensus on how to estimate f_k from a given flow field on a given grid, both *Static* and *Dynamic* PANS. The results obtained using either of these approaches are strongly dependent on this estimate, potentially leading to significant modelling errors. Due to differences in the definition of the characteristic grid dimension and the application of empirical constants, it is clear that the absolute values of the estimates should be treated with care, and more emphasis should be placed on the predicted trends instead. An issue unaddressed in literature is that *Static* estimates should be applied to steady flow solutions; however for statistically unsteady flows, such solutions are not obtainable. In this thesis this issue was circumvented by using the time-averaged quantities.

In this work, the estimates were compared against the *a posteriori* computed ratio of modelled-to-total turbulence kinetic energy $\tilde{f}_k$. It was shown that, in general, $\tilde{f}_k$ is smaller that the constant f_k, which was used in the computation. Several issues were observed with the in literature published estimates:

- Most estimates are constructed such that $f_k = 1$ in the entire boundary layer. *Constant* f_k computations show that $\tilde{f}_k = 1.0$ only in the first row of cells near the wall. This indicates that the estimates should not be applied inside boundary layers, and a consequence of this behaviour is that the PANS model behaves more like a DES model. This is sometimes described in literature as an advantage or a aim in the derivation of the estimate, although this does imply that the unfavourable properties of DES, such as error entanglement, are then also incorporated.

- All estimates yield $f_k = 1.0$ if the flow is laminar (upstream and in the far-field), implying that in those regions the PANS model resorts to the RANS parent model. For *Static* computations this can be a problem, if during a subsequent PANS computation synthetic turbulence is added at the inflow. Due to the high f_k value upstream, the introduced fluctuations might already be largely dissipated before they reach the object.

- *Dynamic* PANS computations potentially show an oscillatory behaviour for f_k due to the strong spatial variation of the estimates. This spatial variation is analogous to DES computations, where the flow can also suddenly transition from a LES zone to a RANS zone, thereby introducing commutation errors. Not only is f_k temporally and spatially varying, but also the flow field upon which it is based, thereby potentially introducing artificial unsteadiness in the computation.

These issues combined lead to the conclusion that despite potential theoretical advantages of the usage of *Dynamic* PANS, the *Constant* PANS approach, with a f_k fixed in time and space, is still preferable in order to minimise errors in CFD results and increase the reliability of industrial CFD.

8.5.3. PANS-KSKL MODEL

A new PANS closure was derived based on the KSKL model aimed at multiphase flows. It was shown that the favourable properties of decreased eddy-viscosity and improved iterative convergence exhibited by the KSKL model compared to $k-\omega$ models, are carried over to the PANS model. The improvement in iterative convergence holds for multiphase flows, thus making the new model attractive for the accurate simulation of cavitation dynamics and noise. For such cases the ω equation is difficult to converge. It was also shown that for $f_k < 1.0$ the PANS-KSKL model exhibits a low decay of eddy-viscosity downstream of the inlet boundary condition. This simplifies practical application, but can make the PANS-KSKL model more sensitive to the eddy-viscosity prescribed at the inlet. The influence of varying the eddy-viscosity at the inflow for varying f_k requires further numerical investigation.

8.6. RECOMMENDATIONS FOR FUTURE WORK

The use of CFD to predict URN depends on the modelling and/or resolving of turbulence, cavitation and acoustics, and their interaction. Within this thesis there was a focus on resolving and modelling turbulence, and the associated inflow boundary condition. For future work it is recommended to focus on the other two components.

A recurring observation, both in literature and in this thesis, is that numerically predicted cavities have a smaller size compared to experimental observations. In this thesis, this is most apparent for cavitating tip vortex of the elliptical wing. While the experimentally observed vortex propagates beyond the end of the test section, the numerically predicted vortex diffuses after approximately one root chord length. The application of adaptive grid refinement in the vortex region could extend the cavity size, but will not address this discrepancy entirely. In literature, the underprediction of cavity sizes is often related to excessive diffusion due to high eddy-viscosity levels in simulations (see e.g. [190]). However, while the use of SRS with inflow turbulence does slightly increase the cavity length, it is still significantly underpredicted despite reduced eddy-viscosity levels. This finding suggests that solutions to address the underprediction of the cavity length should be sought for in the modelling of multiphase flow, i.e. volume of fluid (VOF) together with the cavitation model.

In VOF the vapour-liquid interface is not clearly defined, and is usually algebraically reconstructed based on a scalar field (the vapour volume fraction α_v). VOF is known for not being able to keep a sharp interface (see e.g. [66–73]). This implies that the results for cavity dynamics can strongly depend on the chosen definition of the interface (in this thesis $\alpha_v = 0.1$), and leads to early dissipation of the vortex. Alternative methods to describe the interface, such as geometric reconstructions methods [286], level-set [287], coupled level-set VOF [288] and phase field methods [289–291] exist, but are currently not widely applied for industrial test cases. Reasons for this include not satisfying mass conservation, or difficulties in the application on unstructured grids (for example due to the need for high-order derivatives [291]). It is recommended to look into the application of such methods for cavitation predictions.

Related to the method of modelling multiphase flow, is the modelling of phase change, i.e. the cavitation model. In this thesis the Schnerr-Sauer cavitation model [80] is employed. This method is widely used in literature, with generally favourable results despite using a simplified inception criterion. However, in the context of tip vortex cavitation it must be noted that the influence of non-condensible gas is neglected. Recent research in the TU Delft cavitation tunnel suggests that the tip vortex cavity size is largely dominated by gas diffusion into the vortex [292], which is an effect currently not included in the simulations. In order to better match experimental observation such effects should be included in the modelling.

With respect to noise predictions, from the elliptical wing simulations it is clear that the application of inflow turbulence leads to a high sound level at lower frequencies. While turbulence produces sound, it is likely that part of the numerically predicted sound is due to an interaction between the inflow turbulence and the Ffowcs Williams-Hawkings (FWH) acoustic analogy. Currently, it is not possible to distinguish between physical and spurious artificial sound. This should be looked into, and if possible corrected. In this thesis this was partly addressed by the application of a background noise correction to the predicted sound levels. While this requires extra (wetted flow) simulations, it is a important step to distinguish between sound introduced by cavitation and sound due to other sources, such as the inflow turbulence. It is advisable to apply such a correction to cavitating sound preditions.

8.7. GUIDELINES FOR THE USE OF SRS

Following the investigations described in this thesis, several recommendations can be made for the use of SRS for industrial test cases:

- It is crucial that SRS of attached flows include a resolved turbulent inflow. The implemented turbulence generator can deliver such an inflow, at a small increase in computational cost compared to SRS simulations without inflow turbulence, while significantly reducing modelling errors.
- When using a resolved turbulent inflow, it is necessary that SRS grids are refined upstream to support the convection and development of inflow turbulence. This is one of the main reasons for the increase in computational cost compared to SRS simulations without inflow turbulence.

Based on the verification and validation processes, some further observations can be made:

- The traditional, RANS based, assumption that discretisation errors are dominant is no longer valid in the context of SRS. Consequently, for validation purposes, the total numerical error should be used. A consequence of this is that in a research context all error sources should be examined, even though some of these examinations are expensive or difficult.
- The inclusion of more physics in the CFD computations leads to more stringent demands for experimental data. It is recommended to measure characteristics of the setup such as inflow turbulence intensity and integral length scale, and also the flow inside the boundary layer to enable validation of SRS.
- The absence of such information about the setup for the cases addressed in this work highlights the need for new experimental test cases aimed at validation of

SRS investigations of multiphase flows. Typical test cases include wings and propellers exhibiting sheet or tip vortex cavitation.

ACKNOWLEDGEMENTS

I could not have achieved this thesis on my own. Three people in particular have contributed greatly to this work.

Firstly, Thomas Lloyd. Many, many thanks for the endless rereading and giving comments to all my work (and checking all the references!). There were times where I was a bit annoyed, but you have made my work so much better. I highly doubt if I'll ever find someone as critical as you again, I will miss it.

Secondly, Guilherme Vaz. Thanks for the support and feedback, and your knowledge about CFD in general. I also really appreciate you staying involved, even after moving to Portugal during the project.

And thirdly, my promotor Tom van Terwisga. Thanks for offering this PhD position to me while I was doing my masters thesis, always being available for a chat, and always being concerned with my well-being.

Also my second promotor, Jerry Westerweel, is acknowledged for his feedback on the draft thesis. All my colleagues, either at TU Delft, or at MARIN, have also been very supportive. I would like to thank in particular: Benoît LeBlanc, Carlo Negrato, Chiara Wielgosz, Stefano Levato, Rui Lopes, João Muralha, Gem Rotte, Soren Schenke, Hugo Verhelst, Marco ten Eikelder, Reinier Bos, Swaraj Nanda, Pranav Sumanth, Lina Nikolaidou, Sarjoon Alkhateeb and Filipo Riccioli. Artur Lidtke should receive special mention for helping me out with the turbulence generator, testing and improving the code, and assisting in general. Also Sébastien Lemaire, thanks for all the support with handy scripts, coding and Linux. Your efforts have made my work so much more efficient. Finally, a word for my two amazing students: Rens Liebrand and Maurits van den Boogaard. You both have greatly helped me, either with testing ideas for different test cases, or writing code for postprocessing data. Thanks!

I also would like to thank NWO for funding this research, and everyone attending to the NWO meetings for their comments and feedback. This includes: Swaraj Nanda, Gerrit Elsinga, Johan Bosschers, Tjakko Keizer, Norbert Bulten, Joop van Son, Izak Goedbloed and Petra Stoltenkamp. Special thanks in particular to MARIN, for the opportunity to perform part of the work there, and for allowing me to use their computational resources.

On a more personal note, I would like to thank Marina van Oord, Niek Teeuwen, Erik van Duin, Salomon Voorhoeve, my brother, Gert-Jan Klapwijk and my parents, Ellen Vernij and Pieter Jan Klapwijk, for always supporting me. And finally, of course, my lovely wife Kirsten, who is always available to distract me, and usually has made some more cake.

Maarten Derk Klapwijk
Bodegraven, October 17, 2021

REFERENCES

[1] Hildebrand, J. (2009). Anthropogenic and natural sources of ambient noise in the ocean. *Marine Ecology Progress Series*, *395*, 5–20. https://doi.org/10.3354/meps08353

[2] Frisk, G. (2012). Noiseonomics: The relationship between ambient noise levels in the sea and global economic trends. *Scientific Reports*, *2*, 437–441. https://doi.org/10.1038/srep00437

[3] Rolland, R., Parks, S., Hunt, K., Castellote, M., Corkeron, P., Nowacek, D., Wasser, S., & Kraus, S. (2012). Evidence that ship noise increases stress in right whales. *Proceedings of the Royal Society B: Biological Sciences*, *279*(1737), 2363–2368. https://doi.org/10.1098/rspb.2011.2429

[4] Wittekind, D., & Schuster, M. (2016). Propeller cavitation noise and background noise in the sea. *Ocean Engineering*, *120*, 116–121. https://doi.org/10.1016/j.oceaneng.2015.12.060

[5] Duarte, C., Chapuis, L., Collin, S., Costa, D., Devassy, R., Eguiluz, V., Erbe, C., Gordon, T., Halpern, B., Harding, H., Havlik, M., Meekan, M., Merchant, N., Miksis-Olds, J., Parsons, M., Predragovic, M., Radford, A., Radford, C., Simpson, S., ... Juanes, F. (2021). The soundscape of the anthropocene ocean. *Science*, *371*, Article 6529. https://doi.org/10.1126/science.aba4658

[6] DNV GL. (2021, July 1). *Rules for classification, ships: Part 6 additional class notations, Chapter 8 living and working conditions, Section 1 comfort class.* (2021st ed.). Classification rules. DNV GL. Høvik, Norway. Retrieved July 2, 2021, from https://rules.dnv.com/docs/pdf/DNV/RU-SHIP/2021-07/DNV-RU-SHIP-Pt6Ch8.pdf

[7] Kaplan, M., & Solomon, S. (2016). A coming boom in commercial shipping? The potential for rapid growth of noise from commercial ships by 2030. *Marine Policy*, *73*, 119–121. https://doi.org/10.1016/j.marpol.2016.07.024

[8] Bureau Veritas, & DNV GL. (2015, November 30). *Guidelines for regulation on UW noise from commercial shipping: Fp7 - grant agreement no. 314227 and no. 314394* (Tech. report) [Sonic deliverable 5.4].

[9] Rodríguez, A., Mullor, R., Palomo, P., Baudin, E., & Lamaison, V. (2015, May 18). New European underwater noise measurement standard developed in the AQUO project, In *Proc. of OCEANS MTI/IEEE*. Genova, Italy. https://doi.org/10.1109/OCEANS-Genova.2015.7271336

[10] IMO. (2021, June 17). *Marine environment protection committee (MEPC 76), 10 to 17 June 2021 (remote session)* [Meeting summaries]. Retrieved July 7, 2021, from https://www.imo.org/en/MediaCentre/MeetingSummaries/Pages/MEPC76meetingsummary.aspx

[11] van Wijngaarden, E., Bosschers, J., & Kuiper, G. (2005, June 19). Aspects of the cavitating propeller tip vortex as a source of inboard noise and vibration, In *Proc.*

of ASME fluids engineering division summer meeting and exhibition. American Society of Mechanical Engineers. Houston, Texas, United States.

[12] Urick, R. (1984). *Ambient noise in the sea*. Undersea Warfare Technology Office, Naval Sea Systems Command, Department of the Navy.

[13] Bosschers, J. (2018). *Propeller tip-vortex cavitation and its broadband noise* (Doctoral dissertation). University of Twente, the Netherlands. https://doi.org/10.3990/1.9789492679529

[14] Carlton, J. (2018). *Marine propellers and propulsion*. Oxford, United Kingdom, Elsevier Butterworth-Heinemann.

[15] ITTC. (2017a). *Underwater noise from ships, full scale measurements* (Recommended Procedures and Guidelines No. 7.5-04-04-01).

[16] Sponagle, N. (1998, June). *Variability of ship noise measurements* (Tech. memorandum No. 88-210). Defence Research Establishment Atlantic.

[17] AQUO. (2012). *Achieve quieter oceans by shipping noise footprint reduction: Fp7 - collaborative project no. 314227* (A. Moreno, Ed.; Tech. report No. D 3.1) [WP 3: Measurements task t3.1] [European URN Standard Measurement Method]. European URN Standard Measurement Method.

[18] ISO. (2016). *Iso 17208-1:2016: Underwater acoustics - quantities and procedures for description and measurement of underwater sound from ships - part 1: Requirements for precision measurements in deep water used for comparison purposes*. Geneva, Switzerland, International Organization for Standardization. https://www.iso.org/standard/39752.html

[19] ITTC. (2017b). *Model-scale propeller cavitation noise measurements* (Recommended Procedures and Guidelines No. 7.5-02-01-05).

[20] Bertschneider, H., Bosschers, J., Choi, G., Ciappi, E., Farabee, T., Kawakita, C., & Tang, D. (2014). Specialist committee on hydrodynamic noise. *Final report and recommendations to the 27th ITTC*, *45*.

[21] Lloyd, T. (2013). *Large eddy simulations of inflow turbulence noise: Application to tidal turbines* (Doctoral dissertation). University of Southampton, United Kingdom.

[22] Lidtke, A. (2017, June 1). *Predicting radiated noise of marine propellers using acoustic analogies and hybrid Eulerian-Lagrangian cavitation models* (Doctoral dissertation). University of Southampton, United Kingdom.

[23] Schot, J., Pennings, P., Pourquie, M., & Van Terwisga, T. (2014, July 20). Modelling of tip vortex cavitation for engineering applications in OpenFOAM, In *WCCM XI: 11th world congress on computational mechanics*. CIMNE. Barcelona, Spain.

[24] Asnaghi, A. (2018). *Computational modelling for cavitation and tip vortex flows* (Doctoral dissertation). Chalmers University of Technology, Sweden.

[25] Paskin, L. (2018). *A numerical assessment of turbulence modeling in tip vortex flows at cavitating conditions* (Master thesis). École Centrale de Nantes, France.

[26] Jarrin, N., Benhamadouche, S., Laurence, D., & Prosser, R. (2006). A synthetic-eddy-method for generating inflow conditions for large-eddy simulations. *International Journal of Heat and Fluid Flow*, *27*(4), 585–593. https://doi.org/10.1016/j.ijheatfluidflow.2006.02.006

[27] Klein, M., Sadiki, A., & Janicka, J. (2003). A digital filter based generation of inflow data for spatially developing direct numerical or large eddy simulations. *Journal of Computational Physics*, *186*(2), 652–665. https://doi.org/10.1016/S0021-9991(03)00090-1

[28] Tabor, G., & Baba-Ahmadi, M. (2010). Inlet conditions for large eddy simulation: A review. *Computers & Fluids*, *39*(4), 553–567. https://doi.org/10.1016/j.compfluid.2009.10.007

[29] Lund, T., Wu, X., & Squires, K. (1998). Generation of turbulent inflow data for spatially-developing boundary layer simulations. *Journal of Computational Physics*, *140*(2), 233–258. https://doi.org/10.1006/jcph.1998.5882

[30] Brennen, C. (2014). *Cavitation and bubble dynamics*. Cambridge University Press.

[31] Franc, J., & Michel, J. (2006). *Fundamentals of cavitation*. Springer Science & Business Media.

[32] Leighton, T. (2012). *The acoustic bubble*. Elsevier Science.

[33] Young, F. (1999). *Cavitation*. World Scientific Publishing Company.

[34] Lloyd, T., Foeth, E., Lafeber, F., & Bosschers, J. (2020, November 16). Progress in the prediction and mitigation of propeller cavitation noise and vibrations, In *Proc. of 26th international virtual hiswa symposium*. Amsterdam, the Netherlands.

[35] ITTC. (2002). *Testing and extrapolation methods propulsion; cavitation: Description of cavitation appearances* (Recommended Procedures and Guidelines No. 7.5-02-03-03.2).

[36] Pennings, P. (2016). *Dynamics of vortex cavitation* (Doctoral dissertation). Delft University of Technology, the Netherlands.

[37] Ballard, R., Archbold, R., & Marshall, K. (2005). *The lost ships of Robert Ballard*. Thunder Bay Press.

[38] ICES. (1995). Underwater noise of research vessels: Review and recommendations (R. Mitson, Ed.). *ICES Cooperative Research Report, No. 209*. https://doi.org/10.17895/ices.pub.5317

[39] Götz, T., Hastie, G., Hatch, L., Raustein, O., Southall, B., Tasker, M., Thomsen, F. Et al. (2009). Overview of the impacts of anthropogenic underwater sound in the marine environment. *OSPAR Biodiversity Series*, *441*, 1–134.

[40] Higuchi, H., Arndt, R., & Rogers, M. (1989). Characteristics of tip vortex cavitation noise. *Journal of Fluids Engineering*, *111*(4), 495–501. https://doi.org/10.1115/1.3243674

[41] Dacles-Mariani, J., Zilliac, G., Chow, J., & Bradshaw, P. (1995). Numerical/experimental study of a wingtip vortex in the near field. *AIAA Journal*, *33*(9), 1561–1568. https://doi.org/10.2514/3.12826

[42] Raestad, A. (1996). Tip vortex index-an engineering approach to propeller noise prediction. *The Naval Architect*, 11–14.

[43] Pennings, P., Westerweel, J., & Van Terwisga, T. (2015). Flow field measurement around vortex cavitation. *Experiments in Fluids*, *56*(11), 206. https://doi.org/10.1007/s00348-015-2073-9

[44] Gassmann, M., Wiggins, S., & Hildebrand, J. (2017). Deep-water measurements of container ship radiated noise signatures and directionality. *The Journal of the*

Acoustical Society of America, *142*(3), 1563–1574. https://doi.org/10.1121/1.5001063

[45] Mahesh, K., Kumar, P., Gnanaskandan, A., & Nitzkorski, Z. (2015). LES applied to ship research. *Journal of Ship Research*, *59*(04), 238–245. https://doi.org/10.5957/JOSR.59.4.150049

[46] Reyes, D., Cooper, J., & Girimaji, S. (2014). Characterizing velocity fluctuations in partially resolved turbulence simulations. *Physics of Fluids*, *26*, Article 085106. https://doi.org/10.1063/1.4892080

[47] Smagorinsky, J. (1963). General circulation experiments with the primitive equations: I. The basic experiment. *Monthly Weather Review*, *91*(3), 99–164. https://doi.org/10.1175/1520-0493(1963)091<0099:GCEWTP>2.3.CO;2

[48] Rezaeiravesh, S., Liefvendahl, M., & Fureby, C. (2016, June 5). On grid resolution requirements for LES of wall-bounded flows, In *Eccomas congress 2016*. European Community on Computional Methods in Applied Sciences. Crete, Greece.

[49] Bose, S., & Park, G. (2018). Wall-modeled large-eddy simulation for complex turbulent flows. *Annual Review of Fluid Mechanics*, *50*(1), 535–561. https://doi.org/10.1146/annurev-fluid-122316-045241

[50] Spalart, P. (1997, August 4). Comments on the feasibility of LES for wings, and on a hybrid RANS/LES approach, In *Proc. of 1st AFOSR international conference on DNS/LES*. Greyden Press. Ruston, Louisiana, United States.

[51] Girimaji, S., & Abdol-Hamid, K. (2005, January 10). Partially averaged Navier-Stokes model for turbulence: Implementation and validation, In *Proc. of 43rd AIAA aerospace sciences meeting and exhibit*. Reno, Nevada, United States.

[52] Pope, S. (2000). *Turbulent flows*. Cambridge University Press.

[53] Spalart, P., Deck, S., Shur, M., Squires, K., Strelets, M., & Travin, A. (2006). A new version of detached-eddy simulation, resistant to ambiguous grid densities. *Theoretical and Computational Fluid Dynamics*, *20*(3), 181–195. https://doi.org/10.1007/s00162-006-0015-0

[54] Gritskevich, M., Garbaruk, A., Schütze, J., & Menter, F. (2012). Development of DDES and IDDES formulations for the $k-\omega$ shear stress transport model. *Flow, Turbulence and Combustion*, *88*(3), 431–449. https://doi.org/10.1007/s10494-011-9378-4

[55] Georgiadis, N., Rizzetta, D., & Fureby, C. (2010). Large-eddy simulation: Current capabilities, recommended practices, and future research. *AIAA journal*, *48*(8), 1772–1784. https://doi.org/10.2514/1.J050232

[56] Eça, L., & Hoekstra, M. (2014). A procedure for the estimation of the numerical uncertainty of CFD calculations based on grid refinement studies. *Journal of Computational Physics*, *262*, 104–130. https://doi.org/10.1016/j.jcp.2014.01.006

[57] Pereira, F., Vaz, G., Eça, L., & Girimaji, S. (2018). Simulation of the flow around a circular cylinder at Re = 3900 with partially-averaged Navier-Stokes equations. *International Journal of Heat and Fluid Flow*, *69*, 234–246. https://doi.org/10.1016/j.ijheatfluidflow.2017.11.001

[58] Ghosal, S., & Moin, P. (1995). The basic equations for the large eddy simulation of turbulent flows in complex geometry. *Journal of Computational Physics*, *118*(1), 24–37. https://doi.org/10.1006/jcph.1995.1077

[59] Hamba, F. (2011). Analysis of filtered Navier-Stokes equation for hybrid RANS/LES simulation. *Physics of Fluids*, *23*(1), Article 015108. https://doi.org/10.1063/1.3549933

[60] Mockett, C., Haase, W., & Thiele, F. (2015). Go4Hybrid: A European initiative for improved hybrid RANS-LES modelling. In *Progress in hybrid RANS-LES modelling* (pp. 299–303). Springer.

[61] Pereira, F., Grinstein, F., Israel, D., Rauenzahn, R., & Girimaji, S. (2021). Modeling and simulation of transitional Taylor-Green vortex flow with partially averaged Navier-Stokes equations. *Physical Review Fluids*, *6*, Article 054611. https://doi.org/10.1103/PhysRevFluids.6.054611

[62] Luo, D., Yan, C., Liu, H., & Zhao, R. (2014). Comparative assessment of PANS and DES for simulation of flow past a circular cylinder. *Journal of Wind Engineering and Industrial Aerodynamics*, *134*, 65–77. https://doi.org/10.1016/j.jweia.2014.08.014

[63] Zhang, J., Minelli, G., Rao, A., Basara, B., Bensow, R., & Krajnović, S. (2018). Comparison of PANS and LES of the flow past a generic ship. *Ocean Engineering*, *165*, 221–236. https://doi.org/10.1016/j.oceaneng.2018.07.023

[64] Vaz, G., Jaouen, F., & Hoekstra, M. (2009, June 1). Free-surface viscous flow computations: Validation of URANS code FRESCO, In *Proc. of 28th international conference on ocean, offshore and arctic engineering*. American Society of Mechanical Engineers. Honolulu, Hawaii, United States.

[65] Hirt, C., & Nichols, B. (1981). Volume of Fluid (VoF) method for the dynamics of free boundaries. *Journal of Computational Physics*, *39*(1), 201–225. https://doi.org/10.1016/0021-9991(81)90145-5

[66] Kubota, A., Kato, H., & Yamaguchi, H. (1992). A new modelling of cavitating flows: A numerical study of unsteady cavitation on a hydrofoil section. *Journal of Fluid Mechanics*, *240*, 59–96. https://doi.org/10.1017/S002211209200003X

[67] Kunz, R., Boger, D., Stinebring, D., Chyczewski, T., Lindau, J., Gibeling, H., Venkateswaran, S., & Govindan, T. (2000). A preconditioned Navier–Stokes method for two-phase flows with application to cavitation prediction. *Computers & Fluids*, *29*(8), 849–875. https://doi.org/10.1016/S0045-7930(99)00039-0

[68] Sauer, J., & Schnerr, G. (2001). Development of a new cavitation model based on bubble dynamics. *Journal of Applied Mathematics and Mechanics / Zeitschrift für Angewandte Mathematik und Mechanik*, *81*(S3), 561–562. https://doi.org/10.1002/zamm.20010811559

[69] Singhal, A., Athavale, M., Li, H., & Jiang, Y. (2002). Mathematical basis and validation of the full cavitation model. *Transactions-American Society of Mechanical Engineers Journal of Fluids Engineering*, *124*(3), 617–624. https://doi.org/10.1115/1.1486223

[70] Bensow, R., & Liefvendahl, M. (2008, June 13). Implicit and explicit subgrid modeling in LES applied to a marine propeller, In *Proc. of 38th fluid dynamics conference and exhibit*. Seattle, Washington, United States.

[71] Wikström, N. (2006). *Approaching large eddy simulation of cavitating flows for marine applications* (Doctoral dissertation). Chalmers University of Technology, Sweden.

[72] Huuva, T. (2008). *Large eddy simulation of cavitating and non-cavitating flow* (Doctoral dissertation). Chalmers University of Technology, Sweden.

[73] Lu, N. (2013). *Modelling cavitation mechanisms using large eddy simulation* (Doctoral dissertation). Chalmers University of Technology, Sweden.

[74] Salvatore, F., Streckwall, H., & Van Terwisga, T. (2009, June 22). Propeller cavitation modelling by CFD-results from the VIRTUE 2008 Rome workshop, In *Proceedings of the 1st international symposium on marine propulsors*. Trondheim, Norway.

[75] Vaz, G., Hally, D., Huuva, T., Bulten, N., Muller, P., Becchi, P., Herrer, J., Whitworth, S., Macé, R., & Korsström, A. (2015, May 31). Cavitating flow calculations for the E779A propeller in open water and behind conditions: Code comparison and solution validation, In *Proc. of 4th international symposium on marine propulsors*. Austin, Texas, United States.

[76] Kanfoudi, H., Lamloumi, H., & Zgolli, R. (2012). Numerical investigation for steady and unsteady cavitating flows. *Advances in Modeling of Fluid Dynamics*, 87–96. https://doi.org/10.5772/48421

[77] Roohi, E., Zahiri, A., & Passandideh-Fard, M. (2013). Numerical simulation of cavitation around a two-dimensional hydrofoil using VOF method and LES turbulence model. *Applied Mathematical Modelling*, *37*(9), 6469–6488. https://doi.org/10.1016/j.apm.2012.09.00

[78] Shin, K. (2010). *Cavitation simulation on marine propellers* (Doctoral dissertation). Technical University of Denmark, Denmark.

[79] Vaz, G., Lloyd, T., & Gnanasundaram, A. (2017, June 15). Improved modelling of sheet cavitation dynamics on Delft Twist 11 hydrofoil, In *Proc. of VII international conference on computational methods in marine engineering*. Nantes, France.

[80] Schnerr, G., & Sauer, J. (2001, May 27). Physical and numerical modeling of unsteady cavitation dynamics, In *Proc. of ICMF, 4th international conference on multiphase flow*. New Orleans, Louisiana, United States.

[81] Crighton, D. (1975). Basic principles of aerodynamic noise generation. *Progress in Aerospace Sciences*, *16*(1), 31–96. https://doi.org/10.1016/0376-0421(75)90010-X

[82] Ianniello, S., Muscari, R., & Mascio, A. (2013). Ship underwater noise assessment by the acoustic analogy. Part I: Nonlinear analysis of a marine propeller in a uniform flow. *Journal of Marine Science and Technology*, *18*(4), 547–570. https://doi.org/10.1007/s00773-013-0227-0

[83] Ianniello, S., Muscari, R., & Di Mascio, A. (2014). Ship underwater noise assessment by the acoustic analogy part II: Hydroacoustic analysis of a ship scaled model. *Journal of Marine Science and Technology*, *19*(1), 52–74. https://doi.org/10.1007/s00773-013-0236-z

[84] Ffowcs Williams, J., & Hawkings, D. (1969). Sound generation by turbulence and surfaces in arbitrary motion. *Philosophical Transactions of the Royal Society of London. Series A, Mathematical and Physical Sciences*, *264*(1151), 321–342. https://doi.org/10.1098/rsta.1969.0031

[85] Di Francescantonio, P. (1997). A new boundary integral formulation for the prediction of sound radiation. *Journal of Sound and Vibration*, *202*(4), 491–509. https://doi.org/10.1006/jsvi.1996.0843

[86] Lloyd, T., Lidtke, A., Rijpkema, D., Van Wijngaarden, E., Turnock, S., & Humphrey, V. (2015, September 28). Using the FW-H equation for hydroacoustics of propellers, In *Proc. of the 18th numerical towing tank symposium*. Cortona, Italy.

[87] Batchelor, G. (2000). *An introduction to fluid dynamics*. Cambridge University Press. https://doi.org/10.1017/CBO9780511800955

[88] Klaij, C., Hoekstra, M., & Vaz, G. (2018). Design, analysis and verification of a volume-of-fluid model with interface-capturing scheme. *Computers & Fluids*, *170*, 324–340. https://doi.org/10.1016/j.compfluid.2018.05.016

[89] Versteeg, H., & Malalasekera, W. (2007). *An introduction to computational fluid dynamics: The finite volume method*. Pearson Education Limited.

[90] Ferziger, J., Perić, M., & Street, R. (2019). *Computational methods for fluid dynamics*. Springer International Publishing.

[91] Patankar, S., & Spalding, D. B. (1972). A calculation procedure for heat, mass and momentum transfer in three-dimensional parabolic flows. *International Journal of Heat and Mass Transfer*, *15*, 1787. https://doi.org/10.1016/B978-0-08-030937-8.50013-1

[92] Klaij, C. M., & Vuik, C. (2013). SIMPLE-type preconditioners for cell-centered, colocated finite volume discretization of incompressible Reynolds-averaged Navier-Stokes equations. *International Journal for Numerical Methods in Fluids*, *71*(7), 830–849. https://doi.org/10.1002/fld.3686

[93] Courant, R., Friedrichs, K., & Lewy, H. (1928). Über die partiellen differenzengleichungen der mathematischen physik. *Mathematische annalen*, *100*(1), 32–74. https://doi.org/10.1007/BF01448839

[94] Issa, R. I. (1986). Solution of the implicitly discretised fluid flow equations by operator-splitting. *Journal of Computational Physics*, *62*(1), 40–65. https://doi.org/10.1016/0021-9991(86)90099-9

[95] Eça, L., Klaij, C., Vaz, G., Hoekstra, M., & Pereira, F. (2016). On code verification of RANS solvers. *Journal of Computational Physics*, *310*, 418–439. https://doi.org/10.1016/j.jcp.2016.01.002

[96] Pereira, F., Eça, L., & Vaz, G. (2017). Verification and validation exercises for the flow around the KVLCC2 tanker at model and full-scale Reynolds numbers. *Ocean Engineering*, *129*, 133–148. https://doi.org/10.1016/j.oceaneng.2016.11.005

[97] *ReFRESCO theory manual* (Tech. report). (2017, October 26). MARIN, Wageningen, the Netherlands.

[98] Hawkes, J., Vaz, G., Philips, A., Cox, S., & Turnock, S. (2018). On the strong scalability of maritime CFD. *Journal of Marine Science and Technology*, *28*, 81–93. https://doi.org/10.1007/s00773-017-0457-7

[99] Hawkes, J., Vaz, G., Phillips, A., Klaij, C., Cox, S., & Turnock, S. (2019). Chaotic multigrid methods for the solution of elliptic equations. *Computer Physics Communications*, *237*, 26–36. https://doi.org/10.1016/j.cpc.2018.10.031

[100] Pereira, F. (2018). *Towards predictive scale-resolving simulations of turbulent external flows* (Doctoral dissertation). Universidade de Lisboa, Instituto Superior Técnico, Portugal.

[101] Germano, M. (1992). Turbulence: The filtering approach. *Journal of Fluid Mechanics*, *238*, 325–336. https://doi.org/10.1017/S0022112092001733

[102] Menter, F., Kuntz, M., & Langtry, R. (2003). Ten years of industrial experience with the SST turbulence model. *Turbulence, Heat and Mass Transfer, 4*(1), 625–632.

[103] Menter, F., Egorov, Y., & Rusch, D. (2006). Steady and unsteady flow modelling using the $k-\sqrt{k}L$ model, In *ICHMT digital library online*, Danburry, Connecticut, United States. Begell House Inc.

[104] Kok, J., Dol, H., Oskam, B., & van der Ven, H. (2004, January 5). Extra-large eddy simulation of massively separated flows, In *Proc. of 42nd AIAA aerospace sciences meeting and exhibit*. Reno, Nevada, United States.

[105] Kok, J. (2000). Resolving the dependence on freestream values for the $k-\omega$ turbulence model. *AIAA journal, 38*(7), 1292–1295. https://doi.org/10.2514/2.1101

[106] Girimaji, S. (2006). Partially-averaged Navier-Stokes model for turbulence: A Reynolds-averaged Navier-Stokes to direct numerical simulation bridging method. *Journal of Applied Mechanics, 73*(3), 413–421. https://doi.org/10.1115/1.2151207

[107] Eça, L., Pereira, F., & Vaz, G. (2018). Viscous flow simulations at high Reynolds numbers without wall functions: Is $y^+ \approx 1$ enough for the near-wall cells? *Computers & Fluids, 170*, 157–175. https://doi.org/10.1016/j.compfluid.2018.04.035

[108] Germano, M., Piomelli, U., Moin, P., & Cabot, W. (1991). A dynamic subgrid-scale eddy viscosity model. *Physics of Fluids A: Fluid Dynamics, 3*(7), 1760–1765. https://doi.org/10.1063/1.857955

[109] Lilly, D. (1992). A proposed modification of the Germano subgrid-scale closure method. *Physics of Fluids A: Fluid Dynamics, 4*(3), 633–635. https://doi.org/10.1063/1.858280

[110] Nicoud, F., Toda, H., Cabrit, O., Bose, S., & Lee, J. (2011). Using singular values to build a subgrid-scale model for large eddy simulations. *Physics of Fluids, 23*(8), 085106. https://doi.org/10.1063/1.3623274

[111] Nicoud, F., & Ducros, F. (1999). Subgrid-scale stress modelling based on the square of the velocity gradient tensor. *Flow, Turbulence and Combustion, 62*(3), 183–200. https://doi.org/10.1023/A:1009995426001

[112] Davidson, L. (1997, September 8). Large eddy simulation: A dynamic one-equation subgrid model for three-dimensional recirculating flow, In *Proc. of 11th international symposium on turbulent shear flow*. Grenoble, France.

[113] Grinstein, F., Margolin, L., & Rider, W. (2007). *Implicit Large Eddy Simulation: Computing turbulent fluid dynamics*. Cambridge University Press.

[114] Mockett, C., Haase, W., & Schwamborn, D. (2017). *Go4Hybrid: Grey area mitigation for Hybrid RANS-LES methods: Results of the 7th framework research project Go4Hybrid, funded by the European Union, 2013-2015*. Springer International Publishing. https://doi.org/10.1007/978-3-319-52995-0

[115] Haase, W., Braza, M., & Revell, A. (2009). *DESider – a European effort on Hybrid RANS-LES modelling: Results of the European-Union funded project, 2004-2007*. Springer Berlin Heidelberg. https://doi.org/10.1007/978-3-540-92773-0

[116] Aider, J.-L., & Danet, A. (2006). Large-eddy simulation study of upstream boundary conditions influence upon a backward-facing step flow. *Comptes Rendus Mécanique, 334*(7), 447–453. https://doi.org/10.1016/j.crme.2006.05.004

[117] Aider, J.-L., Danet, A., & Lesieur, M. (2007). Large-eddy simulation applied to study the influence of upstream conditions on the time-dependant and averaged

characteristics of a backward-facing step flow. *Journal of Turbulence*, *8*(N51). https://doi.org/10.1080/14685240701701000

[118] Mathey, F., Cokljat, D., Bertoglio, J., & Sergent, E. (2006). Assessment of the vortex method for large eddy simulation inlet conditions. *Progress in Computational Fluid Dynamics, An International Journal*, *6*(1-3), 58–67. https://doi.org/10.1504/PCFD.2006.009483

[119] Fung, J., Hunt, J., Malik, N., & Perkins, R. (1992). Kinematic simulation of homogeneous turbulence by unsteady random Fourier modes. *Journal of Fluid Mechanics*, *236*, 281–318. https://doi.org/10.1017/S0022112092001423

[120] Janin, J., Duval, F., Friess, C., & Sagaut, P. (2021). A new linear forcing method for isotropic turbulence with controlled integral length scale. *Physics of Fluids*, *33*(4), 045127. https://doi.org/10.1063/5.0045818

[121] Perret, L., Delville, J., Manceau, R., & Bonnet, J.-P. (2006). Generation of turbulent inflow conditions for large eddy simulation from stereoscopic PIV measurements. *International Journal of Heat and Fluid Flow*, *27*(4), 576–584. https://doi.org/10.1016/j.ijheatfluidflow.2006.02.005

[122] Perret, L., Delville, J., Manceau, R., & Bonnet, J.-P. (2008). Turbulent inflow conditions for large-eddy simulation based on low-order empirical model. *Physics of Fluids*, *20*(7), 075107. https://doi.org/10.1063/1.2957019

[123] Benhamadouche, S., Jarrin, N., Addad, Y., & Laurence, D. (2006). Synthetic turbulent inflow conditions based on a vortex method for large-eddy simulation. *Progress in Computational Fluid Dynamics, an International Journal*, *6*(1-3), 50–57. https://doi.org/10.1504/PCFD.2006.009482

[124] Kim, Y., Castro, I., & Xie, Z. (2013). Divergence-free turbulence inflow conditions for large-eddy simulations with incompressible flow solvers. *Computers & Fluids*, *84*, 56–68. https://doi.org/10.1016/j.compfluid.2013.06.001

[125] Kröger, H., & Kornev, N. (2018). Generation of divergence free synthetic inflow turbulence with arbitrary anisotropy. *Computers & Fluids*, *165*, 78–88. https://doi.org/10.1016/j.compfluid.2018.01.018

[126] Xie, Z.-T., & Castro, I. (2008). Efficient generation of inflow conditions for large eddy simulation of street-scale flows. *Flow, Turbulence and Combustion*, *81*(3), 449–470. https://doi.org/10.1007/s10494-008-9151-5

[127] Lidtke, A., Klapwijk, M., & Lloyd, T. (2021). *Effect of inflow turbulence on sound radiated by a circular cylinder in a low mach number flow* [Submitted for publication].

[128] Peters, A. (2020, January 1). *Numerical modelling and prediction of cavitation erosion using Euler-Euler and multi-scale Euler-Lagrange methods* (Doctoral dissertation). Germany: Universität Duisburg-Essen. https://doi.org/10.17185/duepublico/71156

[129] Vaz, G., & Hoekstra, M. (2008, January 8). *Cavitation modelling in FRESCO* (Tech. report). MARIN, Wageningen, the Netherlands.

[130] Merkle, C., Feng, J., & Buelow, P. (1998, April 10). Computational modeling of the dynamics of sheet cavitation, In *Proc. of 3rd international symposium on cavitation.* Grenoble, France.

[131] Iben, U. (2002). Modeling of cavitation. *Systems Analysis Modelling Simulation, 42*(9), 1283–1307. https://doi.org/10.1080/716067218

[132] Frobenius, M., Schilling, R., Bachert, R., Stoffel, B., & Ludwig, G. (2003, November 1). Three-dimensional unsteady cavitating effects on a single hydrofoil and in a radial pump measurement and numerical simulation, In *Proc. of the 5th international symposium on cavitation*. Osaka, Japan.

[133] Saito, Y., Nakamori, I., & Ikohagi, T. (2003, November 1). Numerical analysis of unsteady vaporous cavitating flow around a hydrofoil, In *Proc. of the 5th international symposium on cavitation*. Osaka, Japan.

[134] Zwart, P., Gerber, A., & Belamri, T. (2004, May 30). A two-phase flow model for predicting cavitation dynamics, In *Proc. of 5th international conference on multiphase flow*. Yokohama, Japan.

[135] Senocak, I., & Shyy, W. (2004). Interfacial dynamics-based modelling of turbulent cavitating flows, Part-1: Model development and steady-state computations. *International Journal for Numerical Methods in Fluids, 44*(9), 975–995. https://doi.org/10.1002/fld.692

[136] Wu, J., Wang, G., & Shyy, W. (2005). Time-dependent turbulent cavitating flow computations with interfacial transport and filter-based models. *International Journal for Numerical Methods in Fluids, 49*(7), 739–761. https://doi.org/10.1002/fld.1047

[137] Merkle, C., Li, D., & Sankaran, V. (2006, June 9). Multi-Disciplinary Computational Analysis in Propulsion, In *Proc. of 42nd AIAA/ASME/SAE/ASEE joint propulsion conference & exhibit*. Sacramento, California, United States.

[138] Huang, B., & Wang, G. (2011). A modified density based cavitation model for time dependent turbulent cavitating flow computations. *Chinese Science Bulletin, 56*(19), 1985–1992. https://doi.org/10.1007/s11434-011-4540-x

[139] Goncalvès, E. (2013). Numerical study of expansion tube problems: Toward the simulation of cavitation. *Computers & Fluids, 72*, 1–19. https://doi.org/10.1016/j.compfluid.2012.11.019

[140] Konstantinov, S., Tselischev, D., & Tselischev, V. (2014). Numerical cavitation model for simulation of mass flow stabilization effect in ANSYS CFX. *Modern Applied Science, 9*(4), 21–30. https://doi.org/10.5539/mas.v9n4p21

[141] Niedźwiedzka, A., Schnerr, G., & Sobieski, W. (2016). Review of numerical models of cavitating flows with the use of the homogeneous approach. *Archives of Thermodynamics, 37*(2), 71–88. https://doi.org/10.1515/aoter-2016-0013

[142] Curle, N., & Lighthill, M. (1955). The influence of solid boundaries upon aerodynamic sound. *Proceedings of the Royal Society of London. Series A. Mathematical and Physical Sciences, 231*(1187), 505–514. https://doi.org/10.1098/rspa.1955.0191

[143] Lighthill, M. (1952). On sound generated aerodynamically I. General theory. *Proc. of the Royal Society of London. Series A. Mathematical and Physical Sciences, 211*(1107), 564–587. https://doi.org/10.1098/rspa.1952.0060

[144] Salvatore, F., & Ianniello, S. (2003). Preliminary results on acoustic modelling of cavitating propellers. *Computational Mechanics, 32*(4-6), 291–300. https://doi.org/10.1007/s00466-003-0486-4

[145] Seol, H., Suh, J.-C., & Lee, S. (2005). Development of hybrid method for the prediction of underwater propeller noise. *Journal of Sound and Vibration*, *288*(1-2), 345–360. https://doi.org/10.1016/j.jsv.2005.01.015

[146] Brentner, K., & Farassat, F. (1997, April 29). An analytical comparison of the acoustic analogy and Kirchhoff formulation for moving surfaces, In *American helicopter society 53rd annual forum*. CIMNE. Virginia Beach, Virgina, United States.

[147] Brentner, K., & Farassat, F. (2003). Modeling aerodynamically generated sound of helicopter rotors. *Progress in Aerospace Sciences*, *39*(2-3), 83–120. https://doi.org/10.1016/S0376-0421(02)00068-4

[148] Lidtke, A., Lloyd, T., & Vaz, G. (2019, May 26). Acoustic modelling of a propeller subject to non-uniform inflow, In *Proc. of 6th international symposium on marine propulsors*. Rome, Italy.

[149] Roache, P. (2009). *Fundamentals of verification and validation*. Hermosa Publishers.

[150] Roache, P. (1998). *Verification and Validation in Computational Science and Engineering*. Hermosa Publishers.

[151] Katsuno, E., Lidtke, A., Düz, B., Rijpkema, D., & Vaz, G. (2019, September 29). Parameter uncertainty quantification applied to the Duisburg propeller test case, In *Proc. of 22nd numerical towing tank symposium*. Tomar, Portugal.

[152] Dou, Y., Lei, Y., Wu, G., Guo, S., Zhou, J., & Shen, L. (2010). FPGA accelerating double/quad-double high precision floating-point applications for ExaScale computing, In *Proc. of the 24th acm international conference on supercomputing*, Tsukuba, Ibaraki, Japan, Association for Computing Machinery. https://doi.org/10.1145/1810085.1810129

[153] Nagaraju, M., & Shekar, G. (2012). FPGA based quadruple precision floating point arithmetic for scientific computations. *International Journal of Advanced Computer Research*, *2*(3), 7–12.

[154] Eça, L., Vaz, G., & Hoekstra, M. (2018, October 1). On the role of iterative errors in unsteady flow simulations, In *Proc. of 21st numerical towing tank symposium*. Cortona, Italy.

[155] Stern, F., Wilson, R., Coleman, H., & Paterson, E. (2001). Comprehensive approach to verification and validation of CFD simulations—part 1: Methodology and procedures. *Journal of Fluids Engineering, 123*(4), 793–802. https://doi.org/10.1115/1.1412235

[156] Celik, I., Ghia, U., Roache, P., Freitas, C., Coleman, H., & Raad, P. (2008). Procedure for estimation and reporting of uncertainty due to discretization in CFD applications. *Journal of Fluids Engineering, 130*(7), Article 078001. https://doi.org/10.1115/1.2960953

[157] Xing, T., & Stern, F. (2010). Factors of safety for Richardson extrapolation. *Journal of Fluids Engineering, 132*(6), Article 061403. https://doi.org/10.1115/1.4001771

[158] Rider, W., Witkowski, W., Kamm, J., & Wildey, T. (2016). Robust verification analysis. *Journal of Computational Physics, 307*, 146–163. https://doi.org/10.1016/j.jcp.2015.11.054

[159] Brouwer, J., Tukker, J., Klinkenberg, Y., & van Rijsbergen, M. (2019). Random uncertainty of statistical moments in testing: Mean. *Ocean Engineering, 182*, 563–576. https://doi.org/10.1016/j.oceaneng.2019.04.068

[160] Brouwer, J., Tukker, J., & Van Rijsbergen, M. (2015, October 7). Uncertainty analysis and stationarity test of finite length time series signals, In *Proc. of the 4th international conference on advanced model measurement technology for the maritime industry*. Istanbul, Turkey.

[161] Lemaire, S., & Klapwijk, M. (2021). *PyTST* (Version v1.0). Zenodo. https://doi.org/10.5281/zenodo.4428158

[162] ASME. (2009). Standard for verification and validation in computational fluid dynamics and heat transfer. *ASME V&V 20-2009*.

[163] Klapwijk, M., Lloyd, T., Vaz, G., & Van Terwisga, T. (2019, May 13). PANS simulations: Low versus high Reynolds number approach, In *Proc. of VIII international conference on computational methods in marine engineering*. Gothenborg, Sweden.

[164] Klapwijk, M., Lloyd, T., & Vaz, G. (2019). On the accuracy of partially averaged Navier-Stokes resolution estimates. *International Journal of Heat and Fluid Flow, 80*, Article 108484. https://doi.org/10.1016/j.ijheatfluidflow.2019.108484

[165] Klapwijk, M., Lloyd, T., & Vaz, G. (2021). The development of a partially sveraged Navier-Stokes KSKL model. *Journal of Fluids Engineering*. https://doi.org/10.1115/1.4052484

[166] Frendi, A., Tosh, A., & Girimaji, S. (2007). Flow past a backward-facing step: Comparison of PANS, DES and URANS results with experiments. *International Journal for Computational Methods in Engineering Science and Mechanics*, *8*(1), 23–38. https://doi.org/10.1080/15502280601006207

[167] Lakshmipathy, S., Reyes, D., & Girimaji, S. (2011, June 27). Partially averaged Navier-Stokes method: Modeling and simulation of low Reynolds number effects in flow past a circular cylinder, In *Proc. of 6th AIAA theoretical fluid mechanics conference*. Honolulu, Hawaii, United States.

[168] Pereira, F., Vaz, G., & Eça, L. (2015, September 15). An assessment of scale-resolving simulation models for the flow around a circular cylinder, In *Proc. of the 8th international symposium on turbulence, heat and mass transfer*. Sarajevo, Bosnia and Herzegovina.

[169] Moser, R., Kim, J., & Mansour, N. (1999). Direct numerical simulation of turbulent channel flow up to $Re_\tau = 590$. *Physics of fluids*, *11*(4), 943–945. https://doi.org/10.1063/1.869966

[170] Patankar, S. (1980). *Numerical heat transfer and fluid flow*. Taylor & Francis.

[171] de Villiers, E. (2007). *The potential of Large Eddy Simulation for the modelling of wall bounded flows* (Doctoral dissertation). University of London, United Kingdom.

[172] Schoppa, W., & Hussain, F. (2000). Coherent structure dynamics in near-wall turbulence. *Fluid Dynamics Research*, *26*(2), 119–139. https://doi.org/10.1016/S0169-5983(99)00018-0

[173] Girimaji, S., & Wallin, S. (2013). Closure modeling in bridging regions of variable-resolution (VR) turbulence computations. *Journal of Turbulence*, *14*(1), 72–98. https://doi.org/10.1080/14685248.2012.754893

[174] Davidson, L. (2016). Zonal PANS: Evaluation of different treatments of the RANS–LES interface. *Journal of Turbulence*, *17*(3), 274–307. https://doi.org/10.1080/14685248.2015.1093637

[175] Pereira, F., Eça, L., Vaz, G., & Girimaji, S. (2018). Challenges in scale-resolving simulations of turbulent wake flows with coherent structures. *Journal of Computational Physics*, *363*, 98–115. https://doi.org/10.1016/j.jcp.2018.02.038

[176] Abdol-Hamid, K., & Girimaji, S. (2004). *A two-stage procedure toward the efficient implementation of PANS and other hybrid turbulence models*. NASA Langley Research Center.

[177] Jeong, E., & Girimaji, S. (2010). Partially averaged Navier-Stokes (PANS) method for turbulence simulations - flow past a square cylinder. *Journal of Fluids Engineering*, *132*(12), Article 121203. https://doi.org/10.1115/1.4003153

[178] Han, X., Krajnović, S., & Basara, B. (2013). Study of active flow control for a simplified vehicle model using the PANS method. *International Journal of Heat and Fluid Flow*, *42*, 139–150. https://doi.org/10.1016/j.ijheatfluidflow.2013.02.001

[179] Foroutan, H., & Yavuzkurt, S. (2014). A partially-averaged Navier-Stokes model for the simulation of turbulent swirling flow with vortex breakdown. *International Journal of Heat and Fluid Flow*, *50*, 402–416. https://doi.org/10.1016/j.ijheatfluidflow.2014.10.005

[180] Elmiligui, A., Abdol-Hamid, K., Massey, S., & Pao, S. (2004, August 16). Numerical study of flow past a circular cylinder using RANS, hybrid RANS/LES and PANS formulations, In *Proc. of 22nd applied aerodynamics conference and exhibit*. Providence, Rhode Island, United States.

[181] Basu, D., Hamed, A., & Das, K. (2007, July 30). Assessment of partially averaged Navier Stokes (PANS) multiscale model in transonic turbulent separated flows, In *ASME/JSME 5th joint fluids engineering conference*. American Society of Mechanical Engineers. San Diego, California, United States.

[182] Song, C.-S., & Park, S.-O. (2009). Numerical simulation of flow past a square cylinder using partially-averaged Navier-Stokes model. *Journal of Wind Engineering and Industrial Aerodynamics*, *97*(1), 37–47. https://doi.org/10.1016/j.jweia.2008.11.004

[183] Basara, B., Krajnovic, S., Girimaji, S., & Pavlovic, Z. (2011). Near-wall formulation of the partially averaged Navier Stokes turbulence model. *AIAA journal*, *49*(12), 2627–2636. https://doi.org/10.2514/1.J050967

[184] Luo, D. (2019). Numerical simulation of turbulent flow over a backward facing step using partially averaged Navier-Stokes method. *Journal of Mechanical Science and Technology*, *33*(5), 2137–2148. https://doi.org/10.1007/s12206-019-0416-9

[185] Davidson, L., & Friess, C. (2019). A new formulation of f_k for the PANS model. *Journal of Turbulence*, *20*, 322–336. https://doi.org/10.1080/14685248.2019.1641605

[186] Basara, B., Pavlovic, Z., & Girimaji, S. (2018). A new approach for the calculation of the cut-off resolution parameter in bridging methods for turbulent flow simulation. *International Journal of Heat and Fluid Flow*, *74*, 76–88. https://doi.org/10.1016/j.ijheatfluidflow.2018.09.011

[187] Davidson, L. (2014). The PANS k-ε model in a zonal hybrid RANS-LES formulation. *International Journal of Heat and Fluid Flow*, *46*, 112–126. https://doi.org/10.1016/j.ijheatfluidflow.2014.01.002

[188] Parnaudeau, P., Carlier, J., Heitz, D., & Lamballais, E. (2008). Experimental and numerical studies of the flow over a circular cylinder at Reynolds number 3900. *Physics of Fluids*, *20*(8), Article 085101. https://doi.org/10.1063/1.2957018

[189] Menter, F., & Egorov, Y. (2004, August 12). Revisiting the turbulent scale equation, In *IUTAM symposium on one hundred years of boundary layer research*. Springer. Göttingen, Germany.

[190] Liebrand, R., Klapwijk, M., Lloyd, T., & Vaz, G. (2020). Transition and turbulence modeling for the prediction of cavitating tip vortices. *Journal of Fluids Engineering*, *143*(1), Article 011202. https://doi.org/10.1115/1.4048133

[191] Menter, F. R. (1994). Two-equation eddy-viscosity turbulence models for engineering applications. *AIAA Journal*, *32*(8), 1598–1605. https://doi.org/10.2514/3.12149

[192] Hoekstra, M., & Vaz, G. (2009, August 16). The partial cavity on a 2D foil revisited, In *Proc. of 7th international symposium on cavitation*. Ann Arbor, Michigan, United States.

[193] Klapwijk, M., Lloyd, T., Vaz, G., & Van Terwisga, T. (2020). Evaluation of scale-resolving simulations for a turbulent channel flow. *Computers & Fluids*, *209*, Article 104636. https://doi.org/10.1016/j.compfluid.2020.104636

[194] Lopes, R., Fernandes, E., Eça, L., Vaz, G., & Kerkvliet, M. (2020). Coupling two correlation-based transition models to the $k-\sqrt{k}L$ eddy viscosity turbulence model. *AIAA Journal*, *59*(5), 1735–1748. https://doi.org/10.2514/1.J059523

[195] Spalart, P., & Rumsey, C. (2007). Effective inflow conditions for turbulence models in aerodynamic calculations. *AIAA Journal*, *45*(10), 2544–2553. https://doi.org/10.2514/1.29373

[196] Lopes, R., Eça, L., Vaz, G., & Kerkvliet, M. (2021). Assessing numerical aspects of transitional flow simulations using the RANS equations. *International Journal of Computational Fluid Dynamics*, 1–22. https://doi.org/10.1080/10618562.2020.1870962

[197] Lopes, R. (2021). *Simulation of transition from laminar to turbulent regime in practical applications of incompressible flow* (Doctoral dissertation). Universidade de Lisboa, Instituto Superior Técnico, Portugal.

[198] Xu, C.-Y., Zhang, T., Yu, Y.-Y., & Sun, J.-H. (2019). Effect of von Karman length scale in scale adaptive simulation approach on the prediction of supersonic turbulent flow. *Aerospace Science and Technology*, *86*, 630–639. https://doi.org/10.1016/j.ast.2019.01.030

[199] Zhang, Y. (2017). Critical transition Reynolds number for plane channel flow. *Applied Mathematics and Mechanics*, *38*(10), 1415–1424. https://doi.org/10.1007/s10483-017-2245-6

[200] Reverberi, A. (2016, October 1). *Cavitation modelling of E779A propeller accounting for transition effects: Verification studies using ReFRESCO with and without transition modelling* (Tech. report). MARIN. Wageningen, the Netherlands.

[201] Klapwijk, M., Lloyd, T., Vaz, G., & Van Terwisga, T. (2021). On the use of synthetic inflow turbulence for scale-resolving simulations of wetted and cavitating flows. *Ocean Engineering, 228*, Article 108860. https://doi.org/10.1016/j.oceaneng.2021.108860

[202] Asnaghi, A., Svennberg, U., & Bensow, R. (2020). Large eddy simulations of cavitating tip vortex flows. *Ocean Engineering, 195*, Article 106703. https://doi.org/10.1016/j.oceaneng.2019.106703

[203] Shur, M., Spalart, P., Strelets, M., & Travin, A. (2008). A hybrid RANS-LES approach with delayed-DES and wall-modelled LES capabilities. *International Journal of Heat and Fluid Flow, 29*(6), 1638–1649. https://doi.org/10.1016/j.ijheatfluidflow.2008.07.001

[204] Schumann, U. (1975). Subgrid scale model for finite difference simulations of turbulent flows in plane channels and annuli. *Journal of Computational Physics, 18*(4), 376–404. https://doi.org/10.1016/0021-9991(75)90093-5

[205] Moin, P., & Kim, J. (1982). Numerical investigation of turbulent channel flow. *Journal of Fluid Mechanics, 118*, 341–377. https://doi.org/10.1017/S0022112082001116

[206] Mason, P., & Callen, N. (1986). On the magnitude of the subgrid-scale eddy coefficient in large-eddy simulations of turbulent channel flow. *Journal of Fluid Mechanics, 162*, 439–462. https://doi.org/10.1017/S0022112086002112

[207] Kim, J., Moin, P., & Moser, R. (1987). Turbulence statistics in fully developed channel flow at low Reynolds number. *Journal of Fluid Mechanics, 177*, 133–166. https://doi.org/10.1017/S0022112087000892

[208] Piomelli, U., Moin, P., & Ferziger, J. (1988). Model consistency in large eddy simulation of turbulent channel flows. *Physics of Fluids, 31*(7), 1884–1891. https://doi.org/10.1063/1.866635

[209] Wang, Q., & Squires, K. (1996a). Large eddy simulation of particle-laden turbulent channel flow. *Physics of Fluids, 8*(5), 1207–1223. https://doi.org/10.1063/1.868911

[210] Wang, Q., & Squires, K. (1996b). Large eddy simulation of particle deposition in a vertical turbulent channel flow. *International Journal of Multiphase Flow, 22*(4), 667–683. https://doi.org/10.1016/0301-9322(96)00007-9

[211] Hughes, T., Oberai, A., & Mazzei, L. (2001). Large eddy simulation of turbulent channel flows by the variational multiscale method. *Physics of Fluids, 13*(6), 1784–1799. https://doi.org/10.1063/1.1367868

[212] Scotti, A., & Piomelli, U. (2001). Numerical simulation of pulsating turbulent channel flow. *Physics of Fluids, 13*(5), 1367–1384. https://doi.org/10.1063/1.1359766

[213] Nikitin, N., Nicoud, F., Wasistho, B., Squires, K., & Spalart, P. (2000). An approach to wall modeling in large-eddy simulations. *Physics of Fluids, 12*(7), 1629–1632. https://doi.org/10.1063/1.870414

[214] Cimarelli, A., & De Angelis, E. (2014). The physics of energy transfer toward improved subgrid-scale models. *Physics of Fluids, 26*(5), 055103. https://doi.org/10.1063/1.4871902

[215] Mukha, T., & Liefvendahl, M. (2015, May 1). *Large-eddy simulation of turbulent channel flow* (Tech. report). Uppsala University, Sweden.

[216] Razi, P. (2015, August 1). *Partially-averaged Navier-Stokes (PANS) method for turbulence simulations: Near-wall modeling and smooth-surface separation computations* (Doctoral dissertation). Texas A & M University, United States.

[217] Gilling, L., Sørensen, N., & Davidson, L. (2009, January 5). Detached eddy simulations of an airfoil in turbulent inflow, In *Proc. of 47th AIAA aerospace sciences meeting including the new horizons forum and aerospace exposition*. Orlando, Florida, United States.

[218] Jarrin, N., Prosser, R., Uribe, J.-C., Benhamadouche, S., & Laurence, D. (2009). Reconstruction of turbulent fluctuations for hybrid RANS/LES simulations using a Synthetic-Eddy Method. *International Journal of Heat and Fluid Flow*, *30*(3), 435–442. https://doi.org/10.1016/j.ijheatfluidflow.2009.02.016

[219] Poletto, R., Craft, T., & Revell, A. (2013). A new divergence free Synthetic Eddy Method for the reproduction of inlet flow conditions for LES. *Flow, Turbulence and Combustion*, *91*(3), 519–539. https://doi.org/10.1007/s10494-013-9488-2

[220] Bercin, K., Xie, Z.-T., & Turnock, S. (2018). Exploration of digital-filter and forward-stepwise synthetic turbulence generators and an improvement for their skewness-kurtosis. *Computers & Fluids*, *172*, 443–466. https://doi.org/10.1016/j.compfluid.2018.03.070

[221] Breuer, M. (2018). Effect of inflow turbulence on an airfoil flow with laminar separation bubble: An LES study. *Flow, Turbulence and Combustion*, *101*, 433–456. https://doi.org/10.1007/s10494-017-9890-2

[222] Patruno, L., & Ricci, M. (2018). A systematic approach to the generation of synthetic turbulence using spectral methods. *Computer Methods in Applied Mechanics and Engineering*, *340*, 881–904. https://doi.org/10.1016/j.cma.2018.06.028

[223] Xie, B., Gao, F., Boudet, J., Shao, L., & Lu, L. (2018). Improved vortex method for large-eddy simulation inflow generation. *Computers & Fluids*, *168*, 87–100. https://doi.org/10.1016/j.compfluid.2018.03.069

[224] Ries, F., Nishad, K., Dressler, L., Janicka, J., & Sadiki, A. (2018). Evaluating large eddy simulation results based on error analysis. *Theoretical and Computational Fluid Dynamics*, *32*, 733–752. https://doi.org/10.1007/s00162-018-0474-0

[225] Piomelli, U., & Balaras, E. (2002). Wall-layer models for large-eddy simulations. *Annual Review of Fluid Mechanics*, *34*(1), 349–374. https://doi.org/10.1146/annurev.fluid.34.082901.144919

[226] Basara, B., Pavlovic, Z., & Krajnovic, S. (2016, September 26). Effects of convection schemes on hybrid RANS-LES calculations, In *Proc. of symposium on hybrid RANS-LES methods*. Springer. Strasbourg, France.

[227] Leonard, B. (1979). A stable and accurate convective modelling procedure based on quadratic upstream interpolation. *Computer Methods in Applied Mechanics and Engineering*, *19*(1), 59–98. https://doi.org/10.1016/0045-7825(79)90034-3

[228] Basara, B., Krajnovic, S., & Girimaji, S. (2008, June 4). PANS vs. LES for computations of the flow around a 3D bluff body, In *Proc. of 7th international symposium on engineering, turbulence, modelling and measurements*. Lymassol, Cyprus.

[229] Meyers, J., & Sagaut, P. (2007). Is plane-channel flow a friendly case for the testing of large-eddy simulation subgrid-scale models? *Physics of Fluids*, *19*(4), 048105. https://doi.org/10.1063/1.2722422

[230] Rozema, W., Verstappen, R., Veldman, A., & Kok, J. (2018). Low-dissipation simulation methods and models for turbulent subsonic flow. *Archives of Computational Methods in Engineering*, *27*, 299–330. https://doi.org/10.1007/s11831-018-09307-7

[231] Kamkar, S., Jameson, A., Wissink, A., & Sankaran, V. (2010, January 4). Feature-driven cartesian adaptive mesh refinement in the Helios code, In *Proc. of 48th AIAA aerospace sciences meeting including the new horizons forum and aerospace exposition*. Orlando, Florida, United States.

[232] Foeth, E., Van Doorne, C., Van Terwisga, T., & Wieneke, B. (2006). Time resolved PIV and flow visualization of 3D sheet cavitation. *Experiments in Fluids*, *40*(4), 503–513. https://doi.org/10.1007/s00348-005-0082-9

[233] Hoekstra, M., Van Terwisga, T., & Foeth, E. (2011, June 15). SMP11 Workshop-Case 1: DelftFoil, In *Proc. of the 2nd international symposium marine propulsors*. Hamburg, Germany.

[234] Diskin, B., Thomas, J., Rumsey, C., & Schwöppe, A. (2015, January 5). Grid convergence for turbulent flows (invited), In *Proc. of 53rd AIAA aerospace sciences meeting*. Kissimmee, Florida, United States. https://doi.org/10.2514/6.2015-1746

[235] Foeth, E. (2008). *The structure of three-dimensional sheet cavitation* (Doctoral dissertation). Delft University of Technology, the Netherlands.

[236] Varadharajan, P. (2019, September 13). *The effect of upstream turbulence on a tip-vortex* (Master thesis). Delft University of Technology, the Netherlands.

[237] Koop, A. (2008). *Numerical simulation of unsteady three-dimensional sheet cavitation* (Doctoral dissertation). University of Twente, the Netherlands.

[238] Schnerr, G., Sezal, I., & Schmidt, S. (2008). Numerical investigation of three-dimensional cloud cavitation with special emphasis on collapse induced shock dynamics. *Physics of Fluids*, *20*(4), Article 040703. https://doi.org/10.1063/1.2911039

[239] Oprea, A. (2013). *Prediction of tip vortex cavitation for ship propellers* (Doctoral dissertation). University of Twente, the Netherlands.

[240] Bensow, R. (2011, June 15). Simulation of the unsteady cavitation on the Delft Twist 11 foil using RANS, DES and LES, In *Proc. of the 2nd international symposium on marine propulsors*. Hamburg, Germany.

[241] Ji, B., Luo, X., Arndt, R., & Wu, Y. (2014). Numerical simulation of three dimensional cavitation shedding dynamics with special emphasis on cavitation–vortex interaction. *Ocean Engineering*, *87*, 64–77. https://doi.org/10.1016/j.oceaneng.2014.05.005

[242] Whitworth, S. (2011, June 15). Cavitation prediction of flow over the Delft Twist 11 foil, In *Proc. of the 2nd international symposium on marine propulsors*. Hamburg, Germany.

[243] Hwang, H., Paik, K., Lee, S., & Song, G. (2021). Numerical study on the vibration and noise characteristics of a Delft Twist 11 hydrofoil. *Journal of Marine Science and Engineering*, *9*(2), Article 144. https://doi.org/10.3390/jmse9020144

[244] Reboud, J., Stutz, B., & Coutier, O. (1998, April 10). Two phase flow structure of cavitation: Experiment and modeling of unsteady effects, In *Proc. of 3rd international symposium on cavitation*. Grenoble, France.

[245] Li, D., Grekula, M., & Lindell, P. (2010). Towards numerical prediction of unsteady sheet cavitation on hydrofoils. *Journal of hydrodynamics*, *22*(5), 699–704. https://doi.org/10.1016/S1001-6058(10)60024-8

[246] Hong, F., & Zhang, F. (2020). Computational investigation of the cavitation vortex dynamics in flow over a three-dimensional hydrofoil by a new transport-based model. *Proceedings of the Institution of Mechanical Engineers, Part A: Journal of Power and Energy*, *235*(3), 506–523. https://doi.org/10.1177/0957650920939344

[247] Asnaghi, A., Feymark, A., & Bensow, R. (2017). Improvement of cavitation mass transfer modeling based on local flow properties. *International Journal of Multiphase Flow*, *93*, 142–157. https://doi.org/10.1016/j.ijmultiphaseflow.2017.04.005

[248] Chen, Y., Chen, X., Li, J., Gong, Z., & Lu, C. (2017). Large eddy simulation and investigation on the flow structure of the cascading cavitation shedding regime around 3D twisted hydrofoil. *Ocean Engineering*, *129*, 1–19. https://doi.org/10.1016/j.oceaneng.2016.11.012

[249] Ji, B., Luo, X., Peng, X., & Wu, Y. (2013). Three-dimensional large eddy simulation and vorticity analysis of unsteady cavitating flow around a twisted hydrofoil. *Journal of Hydrodynamics*, *25*(4), 510–519. https://doi.org/10.1016/S1001-6058(11)60390-X

[250] Long, X., Cheng, H., Ji, B., Arndt, R., & Peng, X. (2018). Large eddy simulation and Euler-Lagrangian coupling investigation of the transient cavitating turbulent flow around a twisted hydrofoil. *International Journal of Multiphase Flow*, *100*, 41–56. https://doi.org/10.1016/j.ijmultiphaseflow.2017.12.002

[251] Lu, N., Bensow, R., & Bark, G. (2010). LES of unsteady cavitation on the Delft twisted foil. *Journal of Hydrodynamics*, *22*(5), 742–749. https://doi.org/10.1016/S1001-6058(10)60031-5

[252] Ji, B., Luo, X., Wu, Y., & Miyagawa, K. (2014). Numerical investigation of three-dimensional cavitation evolution and excited pressure fluctuations around a twisted hydrofoil. *Journal of Mechanical Science and Technology*, *28*(7), 2659–2668. https://doi.org/10.1007/s12206-014-0622-4

[253] Lidtke, A., Turnock, S., & Humphrey, V. (2016, September 11). Multi-scale modelling of cavitation-induced pressure around the Delft Twist 11 hydrofoil, In *Proc. of 31st symposium on naval hydrodynamics*. Monterey, California, United States.

[254] Asnaghi, A., Feymark, A., & Bensow, R. (2018). Numerical investigation of the impact of computational resolution on shedding cavity structures. *International Journal of Multiphase Flow*, *107*, 33–50. https://doi.org/10.1016/j.ijmultiphaseflow.2018.05.021

[255] Eça, L., & Hoekstra, M. (2006, September 17). On the influence of the iterative error in the numerical uncertainty of ship viscous flow calculations, In *Proc. of 26th symposium on naval hydrodynamics*. Rome, Italy.

[256] Aït Bouziad, Y. (2005). *Physical modelling of leading edge cavitation: Computational methodologies and application to hydraulic machinery* (Doctoral dissertation). École polytechnique fédérale de Lausanne, Switzerland.

[257] Drela, M. (1989, June 5). XFOIL: An analysis and design system for low Reynolds number airfoils. In *Low reynolds number aerodynamics* (pp. 1–12). Springer.

[258] Rist, U., & Augustin, K. (2006). Control of laminar separation bubbles using instability waves. *AIAA journal*, *44*(10), 2217–2223. https://doi.org/10.2514/1.17518

[259] Comte-Bellot, G., & Corrsin, S. (1966). The use of a contraction to improve the isotropy of grid-generated turbulence. *Journal of Fluid Mechanics*, *25*(4), 657–682. https://doi.org/10.1017/S0022112066000338

[260] Lopes, R., Eça, L., & Vaz, G. (2020). On the numerical behavior of RANS-based transition models. *Journal of Fluids Engineering*, *142*(5). https://doi.org/10.1115/1.4045576

[261] Welch, P. (1967). The use of fast Fourier transform for the estimation of power spectra: A method based on time averaging over short, modified periodograms. *IEEE Transactions on audio and electroacoustics*, *15*(2), 70–73. https://doi.org/10.1109/TAU.1967.1161901

[262] Clancy, J. (2006). *Aerodynamics*. Sterling Book House.

[263] Sreejith, B., & Sathyabhama, A. (2018). Numerical study on effect of boundary layer trips on aerodynamic performance of E216 airfoil. *Engineering Science and Technology, an International Journal*, *21*(1), 77–88. https://doi.org/10.1016/j.jestch.2018.02.005

[264] Liebrand, R., Klapwijk, M., Lloyd, T., Vaz, G., & Lopes, R. (2019, May 13). A sensitivity analysis of CFD transition modelling in the context of vortex roll-up prediction, In *Proc. of VIII international conference on computational methods in marine engineering*. Gothenborg, Sweden.

[265] Asnaghi, A., & Bensow, R. (2020). Impact of leading edge roughness in cavitation simulations around a twisted foil. *Fluids*, *5*(4), Article 243. https://doi.org/10.3390/fluids5040243

[266] Winkler, J., Wu, H., Moreau, S., Carolus, T., & Sandberg, R. (2020). Trailing-edge broadband noise prediction of an airfoil with boundary-layer tripping. *Journal of Sound and Vibration*, *482*, Article 115450. https://doi.org/10.1016/j.jsv.2020.115450

[267] Schlatter, P., & Örlü, R. (2012). Turbulent boundary layers at moderate Reynolds numbers: Inflow length and tripping effects. *Journal of Fluid Mechanics*, *710*, 5–34. https://doi.org/10.1017/jfm.2012.324

[268] Wolf, W., Azevedo, J., & Lele, S. (2012). Convective effects and the role of quadrupole sources for aerofoil aeroacoustics. *Journal of Fluid Mechanics*, *708*, 502–538. https://doi.org/10.1017/jfm.2012.327

[269] Lloyd, T., Turnock, S., & Humphrey, V. (2014). Assessing the influence of inflow turbulence on noise and performance of a tidal turbine using large eddy simulations. *Renewable Energy*, *71*, 742–754. https://doi.org/10.1016/j.renene.2014.06.011

[270] Tangermann, E., & Klein, M. (2020, January 6). Numerical simulation of laminar separation on a NACA0018 airfoil in freestream turbulence, In *AIAA scitech 2020 forum*. Orlando, Florida, United States. https://doi.org/10.2514/6.2020-2064

[271] Klapwijk, M., Lloyd, T., Vaz, G., Van Terwisga, T., & van den Boogaard, M. (2021). *Exciting a cavitating tip vortex with synthetic inflow turbulence: A CFD analysis of vortex kinematics, dynamics and sound generation* [Submitted for publication].

[272] Arndt, R., & Keller, A. (1992). Water quality effects on cavitation inception in a trailing vortex. *Journal of Fluids Engineering, 114*(3), 430–438. https://doi.org/10.1115/1.2910049

[273] Pennings, P., Bosschers, J., Westerweel, J., & Van Terwisga, T. (2015). Dynamics of isolated vortex cavitation. *Journal of Fluid Mechanics, 778,* 288–313. https://doi.org/10.1017/jfm.2015.379

[274] Asnaghi, A., Svennberg, U., Gustafsson, R., & Bensow, R. (2020). Investigations of tip vortex mitigation by using roughness. *Physics of Fluids, 32,* Article 065111. https://doi.org/10.1063/5.0009622

[275] Lloyd, T., Vaz, G., Rijpkema, D., & Reverberi, A. (2017, June 15). Computational fluid dynamics prediction of marine propeller cavitation including solution verification, In *Proc. of 5th symposium on marine propulsion.* Espoo, Finland.

[276] Saddoughi, S., & Veeravalli, S. (1994). Local isotropy in turbulent boundary layers at high Reynolds number. *Journal of Fluid Mechanics, 268,* 333–372. https://doi.org/10.1017/S0022112094001370

[277] Pemberton, R., Turnock, S., Dodd, T., & Rogers, E. (2002). A novel method for identifying vortical structures. *Journal of Fluids and Structures, 16*(8), 1051–1057. https://doi.org/10.1006/jfls.2002.0462

[278] Phillips, A., & Turnock, S. (2013). Application of the VORTFIND algorithm for the identification of vortical flow features around complex 3D geometries. *International Journal for Numerical Methods in Fluids, 71*(11), 1461–1474. https://doi.org/10.1002/fld.3720

[279] van den Boogaard, M. (2019, September 27). *Numerical simulation of a cavitating line vortex in a converging-diverging nozzle: Using RANS and SRS methods* (Master thesis). Delft University of Technology, the Netherlands.

[280] Howe, M., & Ablowitz, M. (1998). *Acoustics of fluid-structure interactions.* Cambridge University Press.

[281] Ahrens, J., Geveci, B., & Law, C. (2005). ParaView: An end-user tool for large data visualization. In C. D. Hansen & C. R. Johnson (Eds.), *The visualization handbook.* Elsevier München. https://doi.org/10.1016/B978-012387582-2/50038-1

[282] Fitzgibbon, A., Pilu, M., & Fisher, R. (1999). Direct least square fitting of ellipses. *IEEE Transactions on Pattern Analysis and Machine Intelligence, 21*(5), 476–480. https://doi.org/10.1109/34.765658

[283] Rahier, G., Prieur, J., Vuillot, F., Lupoglazoff, N., & Biancherin, A. (2004). Investigation of integral surface formulations for acoustic post-processing of unsteady aerodynamic jet simulations. *Aerospace Science and Technology, 8*(6), 453–467. https://doi.org/10.1016/j.ast.2004.04.005

[284] Higuchi, H., Quadrell, J., & Farell, C. (1986, January 6). Vortex roll-up for an elliptically-loaded wing at moderately low Reynolds numbers, In *Proc. of 24th aerospace sciences meeting.* Reno, Nevada, United States. https://doi.org/10.2514/6.1986-562

[285] Lloyd, T., Lafeber, F., & Bosschers, J. (2018, August 5). Investigation and validation of procedures for cavitation noise prediction from model-scale measurements, In *Proc. of the 32nd symposium on naval hydrodynamics*. Hamburg, Germany.

[286] Youngs, D. (1982). Time-dependent multi-material flow with large fluid distortion. *Numerical methods for fluid dynamics*.

[287] Osher, S., & Sethian, J. (1988). Fronts propagating with curvature-dependent speed: Algorithms based on Hamilton-Jacobi formulations. *Journal of Computational Physics*, *79*(1), 12–49. https://doi.org/10.1016/0021-9991(88)90002-2

[288] Sussman, M., & Puckett, E. (2000). A coupled level set and Volume-of-Fluid method for computing 3D and axisymmetric incompressible two-phase flows. *Journal of Computational Physics*, *162*(2), 301–337. https://doi.org/10.1006/jcph.2000.6537

[289] Jacqmin, D. (1999). Calculation of two-phase Navier-Stokes flows using phase-field modeling. *Journal of Computational Physics*, *155*(1), 96–127. https://doi.org/10.1006/jcph.1999.6332

[290] Anderson, D., McFadden, G., & Wheeler, A. (1998). Diffuse-interface methods in fluid mechanics. *Annual Review of Fluid Mechanics*, *30*(1), 139–165. https://doi.org/10.1146/annurev.fluid.30.1.139

[291] Liu, J., Landi, C., Gomez, H., & Hughes, T. (2015). Liquid–vapor phase transition: Thermomechanical theory, entropy stable numerical formulation, and boiling simulations. *Computer Methods in Applied Mechanics and Engineering*, *297*, 476–553. https://doi.org/10.1016/j.cma.2015.09.007

[292] Nanda, S., van Terwisga, T., Westerweel, J., & Elsinga, G. (2021). *Mechanisms for diffusion-driven growth of cavitating wing-tip vortices* [Manuscript in preparation].

[293] Friess, C., Manceau, R., & Gatski, T. (2015). Toward an equivalence criterion for hybrid RANS/LES methods. *Computers & Fluids*, *122*, 233–246. https://doi.org/10.1016/j.compfluid.2015.08.010

A

GOVERNING EQUATIONS FOR CAVITATING FLOW SIMULATIONS

Starting from the equation describing the rate of change of a quantity ϕ in a material volume V moving in a velocity field U_i, in integral form:

$$\frac{\mathrm{d}}{\mathrm{d}t}\int \phi \mathrm{d}V = \int \left(\frac{\partial \phi}{\partial t} + \frac{\partial}{\partial x_i} \cdot \phi U_i\right) \mathrm{d}V = \int \left(\frac{\mathrm{D}\phi}{\mathrm{D}t} + \phi \frac{\partial}{\partial x_i} \cdot U_i\right) \mathrm{d}V. \tag{A.1}$$

A.1. CONSERVATION OF MASS

When using $\phi = \rho$ in Eq. A.1, the general equation for mass conservation is obtained

$$\frac{\partial \rho}{\partial t} + \frac{\partial}{\partial x_i} \cdot \left(\rho U_i\right) = \frac{\partial \rho}{\partial t} + U_i \cdot \frac{\partial \rho}{\partial x_i} + \rho \frac{\partial U_i}{\partial x_i} = \frac{\mathrm{D}\rho}{\mathrm{D}t} + \rho \frac{\partial U_i}{\partial x_i} = 0. \tag{A.2}$$

This relation holds for any material volume, hence the integral signs are omitted.

For an incompressible fluid without phase change, ρ is uniform and independent of time. In that case, Eq. A.2 reduces to

$$\frac{\partial U_i}{\partial x_i} = 0 \tag{A.3}$$

For a mixture fluid of liquid and vapour, when ignoring non-condensible gas, the mixture density can be expressed as

$$\rho = \alpha_l \rho_l + \alpha_v \rho_v \tag{A.4}$$

with α designating the vapour volume fraction, and ρ_l and ρ_v the temperature dependent, uniform in time and space, density of liquid and water respectively. Substituting this into the first formulation of Eq. A.2, leads to

$$\frac{\partial \left(\alpha_l \rho_l + \alpha_v \rho_v\right)}{\partial t} + \frac{\partial}{\partial x_i} \cdot \left(\left(\alpha_l \rho_l + \alpha_v \rho_v\right) U_i\right) = 0. \tag{A.5}$$

Using $\alpha_v + \alpha_l = 1$,

$$\frac{\partial\left(\alpha_l \rho_l + (1-\alpha_l)\rho_v\right)}{\partial t} + \frac{\partial}{\partial x_i} \cdot \left(\left(\alpha_l \rho_l + (1-\alpha_l)\rho_v\right) U_i\right) = 0. \tag{A.6}$$

Expanding the derivatives, and rewriting terms, yields

$$\frac{\partial\left(\rho_v + \left(\rho_l - \rho_v\right)\alpha_l\right)}{\partial t} + \frac{\partial}{\partial x_i} \cdot \left(\left(\rho_v + \left(\rho_l - \rho_v\right)\alpha_l\right) U_i\right) = 0, \tag{A.7}$$

$$\frac{\partial \rho_v}{\partial t} + \frac{\partial\left(\rho_l - \rho_v\right)\alpha_l}{\partial t} + \frac{\partial}{\partial x_i} \cdot \left(\rho_v U_i\right) + \frac{\partial}{\partial x_i} \cdot \left(\left(\rho_l - \rho_v\right)\alpha_l U_i\right) = 0. \tag{A.8}$$

Recall that $\partial\rho_v/\partial t = \partial\rho_l/\partial t = 0$, and that $\partial\rho_v/\partial x_i = \partial\rho_l/\partial x_i = 0$

$$\left(\rho_l - \rho_v\right)\frac{\partial \alpha_l}{\partial t} + \left(\rho_l - \rho_v\right)\frac{\partial}{\partial x_i} \cdot \left(\alpha_l U_i\right) = -\rho_v \frac{\partial U_i}{\partial x_i}, \tag{A.9}$$

$$\frac{\partial \alpha_l}{\partial t} + \frac{\partial}{\partial x_i} \cdot \left(\alpha_l U_i\right) = -\frac{\rho_v}{\rho_l - \rho_v}\frac{\partial U_i}{\partial x_i}. \tag{A.10}$$

Similarly, it can be derived that

$$\frac{\partial \alpha_v}{\partial t} + \frac{\partial}{\partial x_i} \cdot \left(\alpha_v U_i\right) = \frac{\rho_l}{\rho_l - \rho_v}\frac{\partial U_i}{\partial x_i}. \tag{A.11}$$

Eq. A.5 can be divided according to the phases:

$$\rho_l \frac{\partial\left(\alpha_l\right)}{\partial t} + \rho_l \frac{\partial}{\partial x_i} \cdot \left(\alpha_l U_i\right) + \rho_v \frac{\partial\left(\alpha_v\right)}{\partial t} + \rho_v \frac{\partial}{\partial x_i} \cdot \left(\alpha_v U_i\right) = 0. \tag{A.12}$$

Substituting Eq. A.10 and A.11, yields

$$\frac{\rho_l \rho_v}{\rho_l - \rho_v}\frac{\partial U_i}{\partial x_i} + \frac{\rho_v \rho_l}{\rho_l - \rho_v}\frac{\partial U_i}{\partial x_i} = 0. \tag{A.13}$$

This equation is an expression for condensation plus evaporation, with the source terms

$$-\frac{\rho_l \rho_v}{\rho_l - \rho_v}\frac{\partial U_i}{\partial x_i} + \frac{\rho_v \rho_l}{\rho_l - \rho_v}\frac{\partial U_i}{\partial x_i} = 0. \tag{A.14}$$

Hence, the source term can be expressed as

$$\dot{m} = \frac{\rho_l \rho_v}{\rho_l - \rho_v}\frac{\partial U_i}{\partial x_i} \tag{A.15}$$

from which the conservation of mass can be derived:

$$\frac{\partial U_i}{\partial x_i} = \frac{\rho_l - \rho_v}{\rho_l \rho_v}\dot{m} \tag{A.16}$$

$$\frac{\partial U_i}{\partial x_i} = \left(\frac{1}{\rho_v} - \frac{1}{\rho_l}\right)\dot{m}. \tag{A.17}$$

Since $\rho_l >> \rho_v$, this is approximated as

$$\frac{\partial U_i}{\partial x_i} = \frac{\dot{m}}{\rho_v}. \tag{A.18}$$

A.2. CONSERVATION OF MOMENTUM

While the cavitation models as described in the previous section (using $\dot{m}$), are typically called mass transfer models, it is important to realise that the source term also affects the momentum equation, or any other conservation equation [192].

When again the conservation equation Eq. A.1 is considered, using $\phi = \rho U_i$, the equation for momentum conservation is obtained

$$\frac{\partial\left(\rho U_i\right)}{\partial t} + \frac{\partial}{\partial x_j}\cdot\left(\rho U_i U_j\right) = -\frac{\partial P}{\partial x_i} + \frac{\partial}{\partial x_i}\left[\mu\left(\frac{\partial U_i}{\partial x_j} + \frac{\partial U_j}{\partial x_i} - \frac{2}{3}\frac{\partial U_m}{\partial x_m}\delta_{ij}\right)\right] + \rho g_i. \tag{A.19}$$

This is equation is commonly referred to as the Navier-Stokes equation. Should you wish to write the equation using a material derivative, the left hand side can be rewritten to obtain

$$\frac{\partial\left(\rho U_i\right)}{\partial t} + U_j\cdot\frac{\partial\left(\rho U_i\right)}{\partial x_j} + \rho U_i\frac{\partial U_j}{\partial x_j} = -\frac{\partial P}{\partial x_i} + \frac{\partial}{\partial x_i}\left[\mu\left(\frac{\partial U_i}{\partial x_j} + \frac{\partial U_j}{\partial x_i} - \frac{2}{3}\frac{\partial U_m}{\partial x_m}\delta_{ij}\right)\right] + \rho g_i, \tag{A.20}$$

$$\frac{\mathrm{D}\left(\rho U_i\right)}{\mathrm{D}t} = -\rho U_i\frac{\partial U_j}{\partial x_j} - \frac{\partial P}{\partial x_i} + \frac{\partial}{\partial x_i}\left[\mu\left(\frac{\partial U_i}{\partial x_j} + \frac{\partial U_j}{\partial x_i} - \frac{2}{3}\frac{\partial U_m}{\partial x_m}\delta_{ij}\right)\right] + \rho g_i. \tag{A.21}$$

In case of non-cavitating flow, the term $\rho U_i\frac{\partial U_j}{\partial x_j} = 0$. However, for cavitating flow, $\rho U_i\frac{\partial U_j}{\partial x_j} = \rho U_i\frac{\dot{m}}{\rho_v}$, meaning that this term cannot be ignored. This is often overlooked, or incorrectly documented in literature. The same holds true for the expansion rate: $\frac{2}{3}\frac{\partial U_m}{\partial x_m}\delta_{ij} = \frac{2}{3}\frac{\dot{m}}{\rho_v}\delta_{ij}$.

B

TURBULENCE MODELS

B.1. RANS

B.1.1. $k-\omega$ SST2003

TRANSPORT EQUATIONS

$$\frac{\partial\left(\rho k\right)}{\partial t}+\frac{\partial}{\partial x_j}\cdot\left(\rho k\langle U_j\rangle\right)=P_k-\rho\beta^*\omega k+\frac{\partial}{\partial x_j}\left(\left(\mu+\mu_t\sigma_k\right)\frac{\partial k}{\partial x_j}\right), \tag{B.1}$$

$$\begin{aligned}\frac{\partial\left(\rho\omega\right)}{\partial t}+\frac{\partial}{\partial x_j}\cdot\left(\rho\omega\langle U_j\rangle\right)=\frac{\alpha}{\nu_t}P_k-\beta\rho\omega^2+\frac{\partial}{\partial x_j}\left[\left(\mu+\mu_t\sigma_\omega\right)\frac{\partial\omega}{\partial x_j}\right]\\ +2\rho\left(1-F_1\right)\frac{\sigma_{\omega_2}}{\omega}\frac{\partial k}{\partial x_j}\frac{\partial\omega}{\partial x_j}.\end{aligned} \tag{B.2}$$

TURBULENT VISCOSITY

$$\nu_t=\frac{a_1k}{\max\left(a_1\omega,\langle S\rangle F_2\right)}. \tag{B.3}$$

AUXILIARY FUNCTIONS

$$P_k=\min\left(\rho\nu_t\langle S\rangle,10\rho\beta^*k\omega\right), \tag{B.4}$$

$$F_1=\tanh\left(\min\left(\max\left(\frac{\sqrt{k}}{\beta^*\omega d},\frac{500\nu}{d^2\omega}\right),\frac{4\rho\sigma_{\omega_2}k}{d^2\max\left(\frac{2\rho\sigma_{\omega_2}}{\omega}\frac{\partial k}{\partial x_j}\frac{\partial\omega}{\partial x_j},10^{-10}\right)}\right)^4\right), \tag{B.5}$$

$$F_2=\tanh\left(\max\left(\frac{2\sqrt{k}}{\beta^*\omega d},\frac{500\nu}{d^2\omega}\right)^2\right), \tag{B.6}$$

$$\Phi=\Phi_1F_1+\Phi_2\left(1.0-F_1\right). \tag{B.7}$$

Table B.1: Coefficients of the $k-\omega$ SST2003 turbulence model.

α_1	α_2	a_1	β_1	β_2	β^*	σ_{k_1}	σ_{k_2}	σ_{ω_1}	σ_{ω_2}
$\frac{5}{9}$	0.440	0.310	0.075	0.0828	0.090	0.850	1.000	0.500	0.856

B.1.2. KSKL

TRANSPORT EQUATIONS

$$\frac{\partial\left(\rho k\right)}{\partial t}+\frac{\partial}{\partial x_j}\cdot\left(\rho k\langle U_j\rangle\right)=P_k-D_k+\frac{\partial}{\partial x_j}\left[\left(\mu+\frac{\mu_t}{\sigma_k}\right)\frac{\partial k}{\partial x_j}\right], \tag{B.8}$$

$$\begin{aligned}\frac{\partial\left(\rho\sqrt{k}L\right)}{\partial t}+\frac{\partial}{\partial x_i}\cdot\left(\rho\sqrt{k}L\langle U_i\rangle\right)=&\frac{\sqrt{k}L}{k}\nu_t\langle S\rangle^2\left(\zeta_1-\zeta_2\left(\frac{L}{L_{\upsilon k}}\right)^2\right)\\&-\zeta_3\rho k+\frac{\partial}{\partial x_j}\left[\left(\mu+\frac{\mu_t}{\sigma_{\sqrt{k}L}}\right)\frac{\partial(\sqrt{k}L)}{\partial x_j}\right]-6\nu\frac{\sqrt{k}L}{d^2}f_{\sqrt{k}L}.\end{aligned} \tag{B.9}$$

TURBULENT VISCOSITY

$$\nu_t=\min\left(C_\mu^{1/4}\frac{kL}{\sqrt{k}},\frac{a_1 k}{\langle S\rangle}\right). \tag{B.10}$$

AUXILIARY FUNCTIONS

$$P_k=\rho\nu_t\langle S\rangle^2 \tag{B.11}$$

$$D_k=C_\mu^{3/4}\rho\frac{k^{3/2}}{l} \tag{B.12}$$

$$a_1=a_1^S f_b+\left(1-f_b\right)a_1^R, \tag{B.13}$$

$$f_b=\tanh\left[\left(\frac{20\left(C_\mu^{1/4}\sqrt{k}L+\nu\right)}{\kappa^2\langle S\rangle^2 d^2+0.01\nu}\right)^2\right], \tag{B.14}$$

$$L_{\upsilon K}=\max\left(\min\left(\kappa\left|\frac{\langle S\rangle^2}{\sqrt{\frac{\partial^2\langle U_i\rangle}{\partial {x_j}^2}\frac{\partial^2\langle U_i\rangle}{\partial {x_k}^2}}}\right|,c_{l_2}\kappa d\right),\frac{L}{c_{\,l_1}}\right), \tag{B.15}$$

$$f_{\sqrt{k}L}=\frac{1+c_{d_1}\xi}{1+\xi^4}, \tag{B.16}$$

$$\xi=\frac{\sqrt{0.3k}d}{20\nu}. \tag{B.17}$$

Table B.2: Coefficients of the KSKL turbulence model.

a_1^R	a_1^S	c_{d_1}	c_{l_1}	c_{l_2}	C_μ	κ	σ_k	$\sigma_{\sqrt{k}L}$	ζ_1	ζ_2	ζ_3
0.577	0.320	4.700	10.000	1.300	0.090	0.410	2/3	2/3	0.800	1.470	0.0288

B.2. HYBRID MODELS

B.2.1. DDES

AUXILIARY FUNCTIONS

$$\Delta = \max\left(\Delta_x, \Delta_y, \Delta_z\right), \tag{B.18}$$

$$C_{DDES} = F_1 C_{DDES_1} + (1 - F_1)\, C_{DDES_2}, \tag{B.19}$$

$$f_d = 1 - \tanh\left[\left(C_{d_1} \frac{\nu_t + \nu}{\kappa^2 d^2 \sqrt{0.5\left(\langle S\rangle^2 + \langle\Omega\rangle^2\right)}}\right)^{C_{d_2}}\right]. \tag{B.20}$$

Table B.3: Coefficients of the $k-\omega$ DDES turbulence model.

β^*	C_{d_1}	C_{d_2}	C_{DDES_1}	C_{DDES_2}	κ
0.09	20	3	0.78	0.61	0.41

B.2.2. IDDES

AUXILIARY FUNCTIONS

$$l_t = \tilde{f}_d\, l_t^{RANS} + \left(1 - \tilde{f}_d\right) l_t^{SRS}, \tag{B.21}$$

$$l_t^{SRS} = C_{IDDES} \min\left(C_w \max\left(d, \Delta\right), \Delta\right), \tag{B.22}$$

$$C_{IDDES} = F_1 C_{IDDES} + (1 - F_1)\, C_{IDDES}, \tag{B.23}$$

$$\tilde{f}_d = \max\left(1 - f_{dt}, f_b\right), \tag{B.24}$$

$$f_{dt} = 1 - \tanh\left[\left(C_{dt_1} \frac{\nu_t}{\kappa^2 d^2 \sqrt{0.5\left(\langle S\rangle^2 + \langle\Omega\rangle^2\right)}}\right)^{C_{dt_2}}\right], \tag{B.25}$$

$$f_b = \min\left(2.0 \exp\left(-9.0\left(0.25 - \frac{d}{\Delta}\right)^2\right), 1.0\right). \tag{B.26}$$

Table B.4: Coefficients of the $k-\omega$ IDDES turbulence model.

β^*	C_{d_1}	C_{d_2}	C_w	C_{IDDES_1}	C_{IDDES_2}	κ
0.09	20	3	0.15	0.78	0.61	0.41

B.2.3. XLES

TRANSPORT FUNCTION

$$\frac{\partial(\rho\omega)}{\partial t} + \frac{\partial}{\partial x_j}\cdot\left(\rho\omega\langle U_j\rangle\right) = P_\omega - \beta_\omega\rho\omega^2 + \frac{\sigma_d}{\omega}\rho\max\left(\frac{\partial k}{\partial x_i}\frac{\partial \omega}{\partial x_i},0\right) + \frac{\partial}{\partial x_j}\left(\left(\mu+\sigma_\omega\mu_t\right)\frac{\partial \omega}{\partial x_j}\right). \tag{B.27}$$

AUXILIARY FUNCTIONS

$$P_\omega = \rho\alpha_\omega\langle S\rangle^2. \tag{B.28}$$

$$\tilde{l} = \min\left(l, C_1\Delta\right), \tag{B.29}$$

$$\nu_t = \tilde{l}\sqrt{k}, \tag{B.30}$$

$$\varepsilon = \beta_k\frac{k^{\frac{3}{2}}}{\tilde{l}}, \tag{B.31}$$

$$\Delta = \max\left(\Delta_x, \Delta_y, \Delta_z\right), \tag{B.32}$$

$$C_2 = \frac{\beta_k}{C_1}, \tag{B.33}$$

$$\alpha_\omega = \frac{\beta_\omega}{\beta_k} - \frac{\sigma_\omega\kappa^2}{\sqrt{\beta_k}}. \tag{B.34}$$

Table B.5: Coefficients of the XLES turbulence model.

C_1	β_k	β_ω	σ_k	σ_ω	σ_d	α_ω
0.05	0.09	0.075	2/3	0.5	0.5	0.55

B.3. BRIDGING METHODS

B.3.1. PANS SST

TRANSPORT EQUATIONS

$$\frac{\partial(\rho k)}{\partial t} + \frac{\partial}{\partial x_j}\cdot\left(\rho k\langle U_j\rangle\right) = P_k - \beta^*\rho\omega k + \frac{\partial}{\partial x_j}\left[\rho\left(\nu+\nu_t\sigma_k\frac{f_\omega}{f_k}\right)\frac{\partial k}{\partial x_j}\right], \tag{B.35}$$

$$\begin{split}\frac{\partial(\rho\omega)}{\partial t} + \frac{\partial}{\partial x_j}\cdot\left(\rho\omega\langle U_j\rangle\right) = \frac{\alpha}{\nu_t}P_k - \left(P' - \frac{P'}{f_\omega} + \frac{\beta\rho\omega}{f_\omega}\right)\omega + \frac{\partial}{\partial x_j}\left[\left(\mu+\mu_t\sigma_\omega\frac{f_\omega}{f_k}\right)\frac{\partial \omega}{\partial x_j}\right]\\ + 2\rho\frac{\sigma_{\omega 2}}{\omega}\frac{f_\omega}{f_k}(1-F_1)\frac{\partial k}{\partial x_j}\frac{\partial \omega}{\partial x_j}.\end{split} \tag{B.36}$$

TURBULENT VISCOSITY

$$\nu_t = \frac{a_1 k}{\max\left(a_1\omega, \langle S\rangle F_2\right)}. \tag{B.37}$$

AUXILIARY FUNCTIONS

$$F_1 = \tanh\left(\min\left(\max\left(\frac{\sqrt{k}}{\beta^*\omega d},\frac{500\nu}{d^2\omega}\right),\frac{4\rho\sigma_{\omega_2}k}{d^2\max\left(\frac{2\rho\sigma_{\omega_2}}{\omega}\frac{\partial k}{\partial x_j}\frac{\partial \omega}{\partial x_j},10^{-10}\right)}\right)^4\right), \tag{B.38}$$

$$F_2 = \tanh\left(\max\left(\frac{2\sqrt{k}}{\beta^*\omega d},\frac{500\nu}{d^2\omega}\right)^2\right), \tag{B.39}$$

$$\Phi = \Phi_1 F_1 + \Phi_2\left(1.0 - F_1\right), \tag{B.40}$$

$$P_k = \min\left(\nu_t\langle S\rangle, 10\beta^* k\omega\right), \tag{B.41}$$

$$P' = \frac{\alpha\beta^*\rho k}{\nu_t}. \tag{B.42}$$

Table B.6: Coefficients of the PANS $k-\omega$ SST2003 turbulence model.

α_1	α_2	a_1	β_1	β_2	β^*	σ_{k_1}	σ_{k_2}	σ_{ω_1}	σ_{ω_2}
$\frac{5}{9}$	0.440	0.310	0.075	0.0828	0.090	0.850	1.000	0.500	0.856

B.3.2. PANS KSKL

TRANSPORT EQUATIONS

$$\frac{\partial\left(\rho k\right)}{\partial t} + \frac{\partial}{\partial x_j}\cdot\left(\rho k\langle U_j\rangle\right) = P_k - D_k + \frac{\partial}{\partial x_j}\left[\left(\mu + \frac{\mu_t}{\sigma_k\sqrt{f_k}f_l}\right)\frac{\partial k}{\partial x_j}\right] \tag{B.43}$$

$$\begin{aligned}\frac{\partial\left(\rho\sqrt{k}l\right)}{\partial t} + \frac{\partial}{\partial x_j}\cdot\left(\rho\sqrt{k}l\langle U_j\rangle\right) =& \rho\frac{\sqrt{k}l}{\sqrt{f_k}f_l k}\nu_t\langle S\rangle^2\left(\zeta_1 - \zeta_2\left(\frac{l}{f_l L_{\nu k}}\right)^2\right) - \zeta_3\rho k\frac{f_l}{\sqrt{f_k}}\\ &+ \frac{\partial}{\partial x_j}\left[\left(\mu + \frac{\mu_t}{\sigma_{\sqrt{k}l}\sqrt{f_k}f_l}\right)\frac{\partial\sqrt{k}l}{\partial x_j}\right].\end{aligned} \tag{B.44}$$

TURBULENT VISCOSITY

$$\nu_t = \min\left(C_\mu^{1/4}\frac{kL}{\sqrt{k}},\frac{a_1 k}{\langle S\rangle}\right). \tag{B.45}$$

AUXILIARY FUNCTIONS

$$P_k = \rho\nu_t\langle S\rangle^2 \tag{B.46}$$

$$D_k = C_\mu^{3/4}\rho\frac{k^{3/2}}{l} \tag{B.47}$$

$$a_1 = a_1^S f_b + \left(1 - f_b\right)a_1^R, \tag{B.48}$$

$$f_b = \tanh\left[\left(\frac{20\left(C_\mu^{1/4}\sqrt{k}L + \nu\right)}{\kappa^2\langle S\rangle^2 d^2 + 0.01\nu}\right)^2\right], \tag{B.49}$$

$$L_{vK} = \max\left(\min\left(\kappa\left|\frac{\langle S\rangle^2}{\sqrt{\frac{\partial^2\langle U_i\rangle}{\partial {x_j}^2}\frac{\partial^2\langle U_i\rangle}{\partial {x_k}^2}}}\right|, c_{l_2}\kappa d\right), \frac{L}{c\,l_1}\right), \tag{B.50}$$

$$f_{\sqrt{k}L} = \frac{1 + c_{d_1}\xi}{1+\xi^4}, \tag{B.51}$$

$$\xi = \frac{\sqrt{0.3k}d}{20\nu}. \tag{B.52}$$

Table B.7: Coefficients of the PANS KSKL turbulence model.

a_1^R	a_1^S	c_{d_1}	c_{l_1}	c_{l_2}	C_μ	κ	σ_k	$\sigma_{\sqrt{k}L}$	ζ_1	ζ_2	ζ_3
0.577	0.320	4.700	10.000	1.300	0.090	0.410	2/3	2/3	0.800	1.470	0.0288

C

PANS KSKL DERIVATION

Throughout this derivation, uppercase letters indicate the total, i.e. RANS quantity, while lowercase letters indicate the modelled, i.e. PANS quantity.

Following literature, the ratio of modelled-to-total turbulence kinetic energy, $f_k = k/K$, is applied for the first equation. For the second equation, which solves for $\sqrt{k}L$, a secondary ratio is defined, based on the modelled turbulent integral length scale L, as

$$f_l = \frac{l}{L}. \tag{C.1}$$

C.1. k EQUATION

The k equation is given by

$$\frac{\partial (K)}{\partial t} + \frac{\partial}{\partial x_j} \cdot \left(K\langle U_j\rangle\right) = P_K - D_K + \frac{\partial}{\partial x_j}\left[\left(\nu + \nu_{tT} c_{\sigma_k}\right)\frac{\partial k}{\partial x_j}\right], \tag{C.2}$$

with the production and destruction terms for the KSKL model defined as

$$P_K = \nu_{tT}\langle S\rangle^2 \qquad \text{and} \qquad D_K = C_\mu^{3/4}\frac{K^{3/2}}{L}. \tag{C.3}$$

Here $c_{\sigma_k} = 1/\sigma_k$ and $\langle S\rangle$ is the magnitude of the strain rate tensor $\langle S\rangle = 2\langle S_{ij}\rangle\langle S_{ij}\rangle$.

The derivation is based on the relation between RANS and PANS turbulence kinetic energy, which is given by

$$\frac{\partial (k)}{\partial t} + \frac{\partial}{\partial x_j} \cdot \left(k\langle\overline{U_j}\rangle\right) = f_k\left[\frac{\partial (K)}{\partial t} + \frac{\partial}{\partial x_j} \cdot \left(K\langle\overline{U_j}\rangle\right)\right] \tag{C.4}$$

and can be rewritten as

$$\frac{\partial (k)}{\partial t} + \frac{\partial}{\partial x_j} \cdot \left(k\langle U_j\rangle\right) = f_k\left[\frac{\partial (K)}{\partial t} + \frac{\partial}{\partial x_j} \cdot \left(K\langle\overline{U_j}\rangle\right)\right] + \frac{\partial (k)}{\partial t} + \frac{\partial}{\partial x_j} \cdot \left[k\left(\langle U_j\rangle - \langle\overline{U_j}\rangle\right)\right]. \tag{C.5}$$

When the conservation expressions on the left and right are replaced by the closure equation, the following relationship is obtained:

$$P_k - D_k + \frac{\partial}{\partial x_j}\left[\left(\nu + \nu_t c_{\sigma_k}\right)\frac{\partial k}{\partial x_j}\right] = f_k\left[P_K - D_K + \frac{\partial}{\partial x_j}\left[\left(\nu + \nu_{tT} c_{\sigma_k}\right)\frac{\partial K}{\partial x_j}\right]\right] + \frac{\partial}{\partial x_j}\cdot\left[(k\left(\langle U_j\rangle - \langle\overline{U_j}\rangle\right)\right]. \tag{C.6}$$

For the local terms, the following relationship holds:

$$P_k - D_k = f_k\left[P_K - D_K\right], \tag{C.7}$$

implying that

$$P_K = \frac{1}{f_k}\left(P_k - D_k\right) + D_K. \tag{C.8}$$

Following the zero transport model approach, where it is assumed that the resolved fluctuating velocity field does not contribute to the turbulent transport of the modeled field, the last term ($\frac{\partial}{\partial x_j}\cdot\left[k\left(\langle U_j\rangle - \langle\overline{U_j}\rangle\right)\right]$) is assumed to be zero. When Eq. C.8 is inserted in Eq. C.6, after moving f_k to the left-hand side, the relation

$$\frac{\partial(k)}{\partial t} + \frac{\partial}{\partial x_j}\cdot\left(k\langle U_j\rangle\right) = P_k - D_k + \frac{\partial}{\partial x_j}\left[\left(\nu + \nu_{tT} c_{\sigma_k}\right)\frac{\partial k}{\partial x_j}\right] \tag{C.9}$$

is obtained. Based on the definition of the eddy-viscosity

$$\nu_t = \min\left(C_\mu^{1/4}\sqrt{k}l; \frac{a_1 k}{\langle S\rangle}\right), \tag{C.10}$$

the ratios of the RANS and PANS eddy-viscosities can be expressed in terms of f_k and f_l:

$$\nu_{tT} = \frac{1}{\sqrt{f_k f_l}}\nu_t. \tag{C.11}$$

Combining Eq. C.10 with Eq. C.9 leads to the PANS k equation:

$$\frac{\partial(k)}{\partial t} + \frac{\partial}{\partial x_j}\cdot\left(k\langle U_j\rangle\right) = P_k - D_k + \frac{\partial}{\partial x_j}\left[\left(\nu + \frac{\nu_t}{\sigma_k\sqrt{f_k f_l}}\right)\frac{\partial k}{\partial x_j}\right]. \tag{C.12}$$

C.2. $\sqrt{k}l$ EQUATION

The KSKL $\sqrt{k}l$ equation is given by

$$\frac{\partial\left(\sqrt{K}L\right)}{\partial t} + \frac{\partial}{\partial x_j}\cdot\left(\sqrt{K}L\langle U_j\rangle\right) = \frac{\sqrt{K}L}{K}\nu_{tT}\langle S\rangle^2\left(\zeta_1 - \zeta_2\left(\frac{L}{L_{vk}}\right)^2\right) - \zeta_3 K + \frac{\partial}{\partial x_j}\left[\left(\nu + \frac{\nu_{tT}}{\sigma_{\sqrt{K}L}}\right)\frac{\partial\left(\sqrt{K}L\right)}{\partial x_j}\right] - 6\nu\frac{\sqrt{K}L}{d^2}f_{\sqrt{K}L}, \tag{C.13}$$

with the von Kármán length scale defined as

$$L_{vk} = \max\left(\min\left(\frac{\kappa\langle S\rangle}{\sqrt{\frac{\partial^2\langle U_i\rangle}{\partial {x_k}^2}\frac{\partial^2\langle U_i\rangle}{\partial {x_j}^2}}}; c_{l_2}\kappa d\right); \frac{L}{c_{l_1}}\right), \tag{C.14}$$

where d indicates the near wall distance. Again relating RANS to PANS:

$$\frac{\partial\left(\sqrt{k}l\right)}{\partial t} + \frac{\partial}{\partial x_j}\cdot\left(\sqrt{k}l\langle\overline{U_j}\rangle\right) = \sqrt{f_k f_l}\left[\frac{\partial\left(\sqrt{K}L\right)}{\partial t} + \frac{\partial}{\partial x_j}\cdot\left(\sqrt{K}L\langle\overline{U_j}\rangle\right)\right], \tag{C.15}$$

which can be rewritten as

$$\begin{aligned}\frac{\partial\left(\sqrt{k}l\right)}{\partial t} + \frac{\partial}{\partial x_j}\cdot\left(\sqrt{k}l\langle U_j\rangle\right) =& \sqrt{f_k f_l}\left[\frac{\partial\left(\sqrt{K}L\right)}{\partial t} + \frac{\partial}{\partial x_j}\cdot\left(\sqrt{K}L\langle\overline{U_j}\rangle\right)\right] \\ &+ \frac{\partial}{\partial x_j}\cdot\left[\sqrt{k}l\left(\langle U_j\rangle - \langle\overline{U_j}\rangle\right)\right].\end{aligned} \tag{C.16}$$

Next, the conservation expression on the right hand side is again replaced by the KSKL closure, and again the zero transport assumption is applied. To relate all quantities to known, sub-filter, quantities, L is replaced by l/f_l. After simplification, the PANS $\sqrt{k}l$ equation is obtained:

$$\begin{aligned}\frac{\partial\left(\sqrt{k}l\right)}{\partial t} + \frac{\partial}{\partial x_j}\cdot\left(\sqrt{k}l\langle U_j\rangle\right) =& \frac{\sqrt{f_k}\sqrt{k}l}{f_l k}\nu_t\langle S\rangle^2\left(\zeta_1 - \zeta_2\left(\frac{l}{f_l L_{vk}}\right)^2\right) - \zeta_3 k\frac{f_l}{\sqrt{f_k}} \\ &+ \frac{\partial}{\partial x_j}\left[\left(\nu + \frac{\nu_t}{\sigma_{\sqrt{k}l}\sqrt{f_k f_l}}\right)\frac{\partial\left(\sqrt{k}l\right)}{\partial x_j}\right] - 6\nu\frac{\sqrt{k}l}{d^2}f_{\sqrt{k}l}.\end{aligned} \tag{C.17}$$

D

PANS f_k ESTIMATES

The f_k estimates found in literature are divided according to category (*Static*, based on an a priori RANS computation, and *Dynamic*, computed during a PANS computation). Within this thesis the original notation is modified to maintain consistency between the different estimates and to properly compare them. Some general definitions are the cell sizes

$$\Delta_{min} = \min\left(\Delta_x, \Delta_y, \Delta_z\right), \tag{D.1}$$

$$\Delta_{max} = \max\left(\Delta_x, \Delta_y, \Delta_z\right), \tag{D.2}$$

$$\Delta_{avg} = \left(\Delta_x \cdot \Delta_y \cdot \Delta_z\right)^{1/3}, \tag{D.3}$$

and the characteristic turbulent length scales L_t and l_t

$$L_t = \frac{K^{\frac{3}{2}}}{E} = \frac{K^{\frac{1}{2}}}{C_\mu \Omega} \qquad \text{and} \qquad l_t = \frac{k^{\frac{3}{2}}}{\varepsilon} = \frac{k^{\frac{1}{2}}}{C_\mu \omega} \tag{D.4}$$

with a constant $C_\mu = 0.09$.

D.1. STATIC PANS ESTIMATES

These estimates are based on an a priori RANS computation, so all turbulence kinetic energy is modelled, i.e. $K = k$, $\langle K \rangle = 0$ and $L_t = l_t$.

D.1.1. ABDOL-HAMID AND GIRIMAJI (2004)

Abdol-Hamid and Girimaji [176] estimated f_k based on the ratio between the unresolved turbulent length-scale and characteristic grid size using

$$f_k \geq C_h \left(\frac{\Delta_{max}}{l_t}\right)^{2/3}. \tag{D.5}$$

C_h is a model coefficient which must be calibrated; in the original paper a value of 1.0 is used.

D.1.2. GIRIMAJI AND ABDOL-HAMID (2005)

Girimaji and Abdol-Hamid [51] use an estimate very similar to that of Abdol-Hamid and Girimaji [176], but with a different constant, and replacing Δ_{max} with Δ_{min}. The estimate is given as

$$f_k \geq \frac{1}{\sqrt{C_\mu}} \left(\frac{\Delta_{min}}{l_t} \right)^{2/3}. \tag{D.6}$$

D.1.3. FRENDI ET AL. (2007)

Frendi et al. [166] modified the estimate of Girimaji and Abdol-Hamid [51] to take f_ε into account:

$$f_k \geq \frac{1}{\sqrt{C_\mu}} \left(\frac{\Delta_{min}}{l_t} \right)^{2/3} f_\varepsilon^{2/3}. \tag{D.7}$$

In the limit $f_\varepsilon = 1.0$, equation D.7 reduces to equation D.6, therefore this estimate is not addressed any further in the current work.

D.1.4. JEONG AND GIRIMAJI (2010)

Jeong and Girimaji [177] define the estimate as

$$f_k \geq 3 \frac{\lambda_T}{\Delta}, \tag{D.8}$$

with λ_T the Taylor scale of turbulence and Δ the grid size. The precise definition of the grid size is not given; in the current work Δ is taken as Δ_{avg}. Surprisingly this estimate uses the grid size in the denominator, while all other methods use a ratio with the grid size in the numerator. This choice is questionable, since this implies that grid refinement leads to a grid which is less capable of resolving structures, which is counterintuitive. The authors do not actually use this estimate in their work, they use a constant f_k in the domain.

D.1.5. HAN ET AL. (2013)

Han et al. [178] use the same definition as Girimaji and Abdol-Hamid [51], but choose the average cell size, Δ_{avg}:

$$f_k \geq \frac{1}{\sqrt{C_\mu}} \left(\frac{\Delta_{avg}}{l_t} \right)^{2/3}. \tag{D.9}$$

D.1.6. FOROUTAN AND YAVUSKURT (2014)

Foroutan and Yavuzkurt [179] define a different estimate, derived from an energy spectrum equation, to circumvent the issue of too high f_k values as observed by Davidson [187]:

$$f_k = 1 - \left(\frac{\left(\frac{l_t}{\Delta_{avg}} \right)^{\frac{2}{3}}}{0.23 + \left(\frac{l_t}{\Delta_{avg}} \right)^{\frac{2}{3}}} \right)^{4.5}. \tag{D.10}$$

For a coarse grid $l_t \ll \Delta$, so f_k goes to 1. Equation D.10 does satisfy the definition that f_k should be bounded between 0.0 and 1.0, which is not a common property of the estimates addressed.

D.2. DYNAMIC PANS ESTIMATES

These estimates are evaluated during a PANS computation. At every time step the used f_k is computed based on the instantaneous flow field, i.e. f_k is updated per time step and is therefore spatially and temporally varying. Since the estimates are evaluated during a PANS computation part of the turbulence spectrum is being resolved, so $k \leq K$, $\langle K \rangle > 0$ and $L_t > l_t$.

D.2.1. ELMILIGUI ET AL. (2004)

Elmiligui et al. [180] use a variable f_k defined as

$$f_k \geq \frac{1+\tanh\left(2\pi\left(\Lambda-0.5\right)\right)}{2}, \tag{D.11}$$

following the damping function from a Hybrid model. The turbulent length scale is defined here as

$$\Lambda = \frac{1}{1+\left(\frac{l_t}{\Delta_{max}}\right)^{4/3}}. \tag{D.12}$$

f_k is defined in such a way that it equals 1.0 in the viscous sub layer, where the unresolved characteristic length scale tends to be small. f_k is also bounded to 1.0.

D.2.2. BASU ET AL. (2007)

Basu et al. [181] use

$$f_k \geq \frac{1}{1+\beta\left(\frac{l_t}{C_{PANS}\cdot\tilde{\Delta}_{\mathrm{max}}}\right)^{2/3}}. \tag{D.13}$$

Interestingly the definition of the grid size is slightly different by taking the time step and velocity into account:

$$\tilde{\Delta}_{\mathrm{max}} = \max\left(\Delta_{max}, \Delta t \cdot ||\langle \boldsymbol{U} \rangle||_2\right). \tag{D.14}$$

Theoretically, not only grid resolution but also temporal resolution determines to which extent the turbulence kinetic energy spectrum can be resolved. Most estimates implicitly rely on the user to ensure a sufficient temporal resolution based on Courant number and/or t^+. In contrast equation D.13 incorporates this explicitly, which increases the robustness. Nevertheless, for the grids and time steps considered in this work $\tilde{\Delta}_{\mathrm{max}} = \Delta_{\mathrm{max}}$. The additional constants are $C_{PANS} = 0.8$ and $\beta = 0.3$.

D.2.3. SONG AND PARK (2009)

Song and S.-O. Park [182] give an estimate (I) and its approximation (II), defined as

$$f_k \geq \underbrace{\left(\frac{\Delta}{L_t}\right)^{2/3}\left(\frac{1-\left(\frac{\eta}{\Delta}\right)^{2/3}}{1-\left(\frac{\eta}{L_t}\right)^{2/3}}\right)}_{I} \approx \underbrace{\left(\frac{\Delta}{\eta}\right)^{2/3}\left(1-\left(\frac{\eta}{\Delta}\right)^{2/3}\right),\left(\frac{\eta}{L_t}\right)^{2/3}}_{II} \tag{D.15}$$

in which η indicates the Kolmogorov length scale, defined as

$$\eta = \left(\frac{\nu^3}{\varepsilon}\right)^{1/4}. \tag{D.16}$$

An advantage of the approximation, II, is the absence of the singularity, which is present in formulation I. In the current work, the difference between the formulation (I) and the approximation (II) was investigated. For an external flow the difference was found to be negligible, but the singularity in formulation I leads to additional peaks inside a boundary layer. Consequently in the current work the approximation is applied. It is mentioned that for Δ either the maximum or volumetric average can be used, although the authors do not specify which one is used in their work. The differences were found to be marginal, and therefore in the current work Δ_{avg} is employed for this estimate.

D.2.4. BASARA ET AL. (2011)

Basara et al. [183] uses an estimation similar to Han et al. [178] (equation D.9), but based on total quantities

$$f_k \geq \frac{1}{\sqrt{C_\mu}}\left(\frac{\Delta_{avg}}{L_t}\right)^{2/3}. \tag{D.17}$$

This estimate is also used by Davidson [187], who recognised that on a coarse grid the f_k obtained is too high, leading to dissipation of the turbulent fluctuations.

D.2.5. LUO ET AL. (2014)

D. Luo et al. [62] use the same estimate as Abdol-Hamid and Girimaji [176], but with the inclusion of a different constant, C_{PANS}, which is taken as 0.1. The authors state that the constant should be further calibrated. The estimate is given by

$$f_k \geq C_{PANS}\left(\frac{\Delta_{max}}{l_t}\right)^{2/3}. \tag{D.18}$$

Note that this implies that an estimate formulated for *Static* PANS is employed in a *Dynamic* approach, resulting in a different estimate for the unresolved length scale, l_t, due to the reduction in k. This explains the need for the inclusion of the constant C_{PANS}.

D.2.6. LUO (2019)

D. Luo [184] uses the same estimate as D. Luo et al. [62]. It is remarked that the estimate is not rigorous in theory and needs additional validation. To this end, for the constant

C_{PANS} three values are employed (0.1, 0.3 and 0.5). The value determines the extent of the near wall RANS region, and it is concluded that 0.3 yields the best results. Since this estimate with $C_{PANS} = 0.1$ is identical to that of D. Luo et al. [62], and otherwise just 3 or 5 times higher, it is not addressed further in the current work.

D.2.7. DAVIDSON AND FRIESS (2019)

Davidson and Friess [185] derive an estimate based on the equivalence criterion between DES and PANS [293]. The estimate is formulated as

$$f_k = 1 - \frac{\psi - 1}{C_{\varepsilon 2} - C_{\varepsilon 1}}, \tag{D.19}$$

with

$$\psi = \max\left(1, \frac{l_t}{C_{DES}\Delta_{\max}}\right), \tag{D.20}$$

including the constants $C_{\varepsilon 1} = 1.5$, $C_{\varepsilon 2} = 1.9$ and $C_{DES} = 0.78 \cdot F1 + 0.61 \cdot (1 - F1)$. The estimate is designed to make the PANS model behave as a DES model. According to the authors, the estimate self-adapts, by forcing $\tilde{f}_k$ towards f_k, without the need for computing $\tilde{f}_k$. This feature is designated ‘passive control’ by the authors.

D.2.8. BASARA ET AL. (2018)

[186] Finally Basara et al. [186] employ the estimate of Basara et al. [183], but with L_t defined differently, here designated $\tilde{L_t}$. $\tilde{L_t}$ is defined based on k_t instead of K, where k_t is defined as

$$k_t = k + k_{ssv}, \tag{D.21}$$

with k_{ssv} the ‘scale-supplying’ resolved kinetic energy, which requires that an additional transport equation is solved. k_t is the total kinetic energy (modelled plus resolved), but obtained solely from the additional transport equation and the k equation in the PANS model. This implies that $k_t \approx K$. An advantage of this is that no (expensive) averaging operations are needed to obtain the resolved, and thereby total, kinetic energy. However, it must be noted that this only works if this extra equation is solved. In Basara et al. [186] this equation is formulated in the context of the four equation PANS $k - \varepsilon - \zeta - f$ model.

E

PANS EDDY-VISCOSITY DECAY DERIVATIONS

E.1. PANS-SST

The PANS-SST equations are

$$\frac{\partial k}{\partial t}+\frac{\partial}{\partial x_j}\cdot\left(k\langle U_j\rangle\right)=P_k-\beta^*\omega k+\frac{\partial}{\partial x_j}\left[\left(\nu+\nu_t\sigma_k\frac{f_\omega}{f_k}\right)\frac{\partial k}{\partial x_j}\right], \tag{E.1}$$

and

$$\begin{aligned}\frac{\partial \omega}{\partial t}+\frac{\partial}{\partial x_j}\cdot\left(\omega\langle U_j\rangle\right)=&\frac{\alpha}{\nu_t}P_k-\left(P'-\frac{P'}{f_\omega}+\frac{\beta\omega}{f_\omega}\right)\omega+\frac{\partial}{\partial x_j}\left[\left(\nu+\nu_t\sigma_\omega\frac{f_\omega}{f_k}\right)\frac{\partial \omega}{\partial x_j}\right]\\&+2\frac{\sigma_{\omega 2}}{\omega}\frac{f_\omega}{f_k}(1-F_1)\frac{\partial k}{\partial x_j}\frac{\partial \omega}{\partial x_j},\end{aligned} \tag{E.2}$$

with

$$P'=\frac{\alpha\beta^* k}{\nu_t}. \tag{E.3}$$

When assuming a steady, uniform flow aligned with the x axis, sufficiently far away from walls and neglecting the diffusion terms, with $\nu_t=k/\omega$, the equations simplify to:

$$\langle U\rangle\frac{\mathrm{d}k}{\mathrm{d}x}=-\beta^* k\omega, \tag{E.4}$$

which can also be written as,

$$\langle U\rangle\frac{\mathrm{d}k}{\mathrm{d}x}=-\beta^*\frac{k^2}{\nu_t}, \tag{E.5}$$

and

$$\langle U\rangle\frac{\mathrm{d}\omega}{\mathrm{d}x}=-\left(P'-\frac{P'}{f_\omega}+\frac{\beta\omega}{f_\omega}\right)\omega. \tag{E.6}$$

Inserting Eq. E.3, yields

$$\begin{aligned}\langle U\rangle \frac{\mathrm{d}\omega}{\mathrm{d}x} &= -\left(\frac{\alpha\beta^* k}{\nu_t} - \frac{\alpha\beta^* k}{f_\omega \nu_t} + \frac{\beta\omega}{f_\omega}\right)\omega \\ &= -\left(\alpha\beta^*\omega - \frac{\alpha\beta^*\omega}{f_\omega} + \frac{\beta\omega}{f_\omega}\right)\omega \\ &= -\left(\alpha\beta^* - \frac{\alpha\beta^* f_k}{f_\varepsilon} + \frac{\beta f_k}{f_\varepsilon}\right)\omega^2.\end{aligned} \tag{E.7}$$

Using the common assumption of $f_\varepsilon = 1.0$, this reduces to

$$\langle U\rangle \frac{\mathrm{d}\omega}{\mathrm{d}x} = -\left(\alpha\beta^* - \alpha\beta^* f_k + \beta f_k\right)\omega^2. \tag{E.8}$$

This equation can be solved after rewriting it to

$$\frac{1}{\omega^2}\mathrm{d}\omega = -\frac{1}{\langle U\rangle}\left(\alpha\beta^* - \alpha\beta^* f_k + \beta f_k\right)\mathrm{d}x. \tag{E.9}$$

Integrating yields

$$\int_{\omega_{in}}^{\omega} \frac{1}{\omega^2}\mathrm{d}\omega = \int_{x_{in}}^{x} -\frac{1}{\langle U\rangle}\left(\alpha\beta^* - \alpha\beta^* f_k + \beta f_k\right)\mathrm{d}x \tag{E.10}$$

$$\left[-\frac{1}{\omega}\right]_{\omega_{in}}^{\omega} = -\frac{1}{\langle U\rangle}\left(\alpha\beta^* - \alpha\beta^* f_k + \beta f_k\right)(x - x_{in}) \tag{E.11}$$

$$\frac{1}{\omega} - \frac{1}{\omega_{in}} = \frac{1}{\langle U\rangle}\left(\alpha\beta^* - \alpha\beta^* f_k + \beta f_k\right)(x - x_{in}) \tag{E.12}$$

$$\frac{1}{\omega} - \frac{1}{\omega_{in}} = \frac{1}{\langle U\rangle}\left(\alpha\beta^* - \alpha\beta^* f_k + \beta f_k\right)(x - x_{in}) \tag{E.13}$$

$$\frac{1}{\omega} = \frac{\langle U\rangle + \left(\alpha\beta^* - \alpha\beta^* f_k + \beta f_k\right)(x - x_{in})\,\omega_{in}}{\langle U\rangle\omega_{in}} \tag{E.14}$$

$$\omega = \frac{\langle U\rangle\omega_{in}}{\langle U\rangle + \left(\alpha\beta^* - \alpha\beta^* f_k + \beta f_k\right)(x - x_{in})\,\omega_{in}}. \tag{E.15}$$

Here the subscript in indicates values at the inlet of the domain.

Using this solution, Eq. E.5 can be solved by integrating

$$\langle U\rangle \frac{\mathrm{d}k}{\mathrm{d}x} = -\beta^* k \frac{\langle U\rangle\omega_{in}}{\langle U\rangle + \left(\alpha\beta^* - \alpha\beta^* f_k + \beta f_k\right)(x - x_{in})\,\omega_{in}} \tag{E.16}$$

$$\frac{1}{k}\mathrm{d}k = \frac{-\beta^*\omega_{in}}{\langle U\rangle + \left(\alpha\beta^* - \alpha\beta^* f_k + \beta f_k\right)(x - x_{in})\,\omega_{in}}\mathrm{d}x \tag{E.17}$$

$$\int_{k_{in}}^{k} \frac{1}{k}\mathrm{d}k = \int_{x_{in}}^{x} \frac{-\beta^*\omega_{in}}{\langle U\rangle + \left(\alpha\beta^* - \alpha\beta^* f_k + \beta f_k\right)(x - x_{in})\,\omega_{in}}\mathrm{d}x \tag{E.18}$$

$$[\ln k]_{k_{in}}^{k} = \left[\frac{-\beta^* \omega_{in}}{\left(\alpha\beta^* - \alpha\beta^* f_k + \beta f_k\right)\omega_{in}} \ln\left(\langle U\rangle + \left(\alpha\beta^* - \alpha\beta^* f_k + \beta f_k\right)(x - x_{in})\,\omega_{in}\right)\right]_{x_{in}}^{x} \tag{E.19}$$

$$\ln k - \ln k_{in} = \frac{-\beta^*}{\alpha\beta^* - \alpha\beta^* f_k + \beta f_k} \left[\ln\left(\langle U\rangle + \left(\alpha\beta^* - \alpha\beta^* f_k + \beta f_k\right)(x - x_{in})\,\omega_{in}\right) - \ln\left(\langle U\rangle\right)\right] \tag{E.20}$$

$$\ln\left(\frac{k}{k_{in}}\right) = \frac{-\beta^*}{\alpha\beta^* - \alpha\beta^* f_k + \beta f_k} \ln\left(\frac{\langle U\rangle + \left(\alpha\beta^* - \alpha\beta^* f_k + \beta f_k\right)(x - x_{in})\,\omega_{in}}{\langle U\rangle}\right) \tag{E.21}$$

$$\frac{k}{k_{in}} = \left(\frac{\langle U\rangle + \left(\alpha\beta^* - \alpha\beta^* f_k + \beta f_k\right)(x - x_{in})\,\omega_{in}}{\langle U\rangle}\right)^{\frac{-\beta^*}{\alpha\beta^* - \alpha\beta^* f_k + \beta f_k}} \tag{E.22}$$

$$k = \frac{k_{in}}{\left[\frac{1}{\langle U\rangle}\left(\langle U\rangle + \left(\alpha\beta^* - \alpha\beta^* f_k + \beta f_k\right)(x - x_{in})\,\omega_{in}\right)\right]^{\frac{\beta^*}{\alpha\beta^* - \alpha\beta^* f_k + \beta f_k}}}. \tag{E.23}$$

$$k = \frac{k_{in}}{\left[\frac{1}{\langle U\rangle}\left(\langle U\rangle + \left(\alpha\beta^* - \alpha\beta^* f_k + \beta f_k\right)(x - x_{in})\,\frac{k_{in}}{\nu_{t,in}}\right)\right]^{\frac{\beta^*}{\alpha\beta^* - \alpha\beta^* f_k + \beta f_k}}}. \tag{E.24}$$

To derive a transport equation for the eddy-viscosity, the definition

$$\begin{aligned}
\langle U\rangle \frac{\mathrm{d}\nu_t}{\mathrm{d}x} &= \langle U\rangle \frac{\mathrm{d}\left(k\omega^{-1}\right)}{\mathrm{d}x_j} \\
&= \langle U\rangle \left(\frac{1}{\omega}\frac{\mathrm{d}k}{\mathrm{d}x} + k\frac{\mathrm{d}\left(\omega^{-1}\right)}{\mathrm{d}x}\right) \\
&= \langle U\rangle \left(\frac{1}{\omega}\frac{\mathrm{d}k}{\mathrm{d}x} - \frac{k}{\omega^2}\frac{\mathrm{d}\omega}{\mathrm{d}x}\right) \\
&= \frac{1}{\omega^2}\left(\omega\langle U\rangle\frac{\mathrm{d}k}{\mathrm{d}x} - k\langle U\rangle\frac{\mathrm{d}\omega}{\mathrm{d}x}\right)
\end{aligned} \tag{E.25}$$

can be used. Inserting Eq. E.5 and E.6, yields

$$\langle U\rangle \frac{\mathrm{d}\nu_t}{\mathrm{d}x} = \frac{1}{\omega^2}\left(-\beta^* k\omega^2 + \left(\alpha\beta^* - \alpha\beta^* f_k + \beta f_k\right) k\omega^2\right), \tag{E.26}$$

which reduces to

$$\langle U\rangle \frac{\mathrm{d}\nu_t}{\mathrm{d}x} = -\left(\beta^* - \alpha\beta^* + \alpha\beta^* f_k - \beta f_k\right) k. \tag{E.27}$$

A solution for this equation can be obtained, again using the definition of $\nu_t = k/\omega$, and the solutions for the decay functions of k and ω, Eq. E.15 and E.24,

$$\nu_t = \frac{\dfrac{k_{in}}{\left[\frac{1}{\langle U\rangle}\left(\langle U\rangle + \left(\alpha\beta^* - \alpha\beta^* f_k + \beta f_k\right)(x - x_{in})\omega_{in}\right)\right]^{\frac{\beta^*}{\alpha\beta^* - \alpha\beta^* f_k + \beta f_k}}}}{\dfrac{\langle U\rangle\omega_{in}}{\langle U\rangle + \left(\alpha\beta^* - \alpha\beta^* f_k + \beta f_k\right)(x - x_{in})\omega_{in}}} \tag{E.28}$$

$$\nu_t = \nu_{t,in} \frac{\frac{1}{\langle U\rangle}\left(\langle U\rangle + \left(\alpha\beta^* - \alpha\beta^* f_k + \beta f_k\right)(x - x_{in})\,\omega_{in}\right)}{\left[\frac{1}{\langle U\rangle}\left(\langle U\rangle + \left(\alpha\beta^* - \alpha\beta^* f_k + \beta f_k\right)(x - x_{in})\,\omega_{in}\right)\right]^{\frac{\beta^*}{\alpha\beta^* - \alpha\beta^* f_k + \beta f_k}}} \tag{E.29}$$

$$\nu_t = \frac{\nu_{t,in}}{\left[\frac{1}{\langle U\rangle}\left(\langle U\rangle + \left(\alpha\beta^* - \alpha\beta^* f_k + \beta f_k\right)(x - x_{in})\,\frac{k_{in}}{\nu_{t,in}}\right)\right]^{\frac{\beta^*}{\alpha\beta^* - \alpha\beta^* f_k + \beta f_k} - 1}}. \tag{E.30}$$

E.2. PANS-KSKL

The PANS-KSKL equations are

$$\frac{\partial k}{\partial t} + \frac{\partial}{\partial x_j} \cdot \left(k\langle U_j\rangle\right) = P_k - D_k + \frac{\partial}{\partial x_j}\left[\left(\nu + \frac{\nu_t}{\sigma_k \sqrt{f_k} f_l}\right)\frac{\partial k}{\partial x_j}\right] \tag{E.31}$$

and

$$\begin{aligned} \frac{\partial\left(\sqrt{k}l\right)}{\partial t} + \frac{\partial}{\partial x_j} \cdot \left(\sqrt{k}l\langle U_j\rangle\right) = {} & \frac{\sqrt{k}l}{\sqrt{f_k} f_l k}\nu_t \langle S\rangle^2 \left(\zeta_1 - \zeta_2\left(\frac{l}{f_l L_{vk}}\right)^2\right) - \zeta_3 k \frac{f_l}{\sqrt{f_k}} \\ & + \frac{\partial}{\partial x_j}\left[\left(\nu + \frac{\nu_t}{\sigma_{\sqrt{k}l}\sqrt{f_k} f_l}\right)\frac{\partial\left(\sqrt{k}l\right)}{\partial x_j}\right] - 6\nu \frac{\sqrt{k}l}{\sqrt{f_k} f_l d^2} f_{\sqrt{k}l}. \end{aligned} \tag{E.32}$$

Again, under the assumption of a steady, uniform flow aligned with the x axis, sufficiently far away from walls, with neglecting the diffusion terms, the equations simplify to:

$$\langle U\rangle \frac{\mathrm{d}k}{\mathrm{d}x} = -C_\mu^{3/4}\frac{k^{3/2}}{l} \tag{E.33}$$

and

$$\langle U\rangle \frac{\mathrm{d}\left(\sqrt{k}l\right)}{\mathrm{d}x} = -\zeta_3 k \frac{f_l}{\sqrt{f_k}}. \tag{E.34}$$

These equations have no simple solution, hence a transport equation for the eddy-viscosity is considered. When assuming uniform flow, the eddy-viscosity is given by

$$\nu_t = C_\mu^{1/4}\sqrt{k}l. \tag{E.35}$$

Using this, Eq. E.33 and E.34 can be rewritten to

$$\langle U\rangle \frac{\mathrm{d}k}{\mathrm{d}x} = -C_\mu \frac{k^2}{\nu_t} \tag{E.36}$$

and

$$\begin{aligned} \langle U\rangle \frac{\mathrm{d}\left(\nu_t\right)}{\mathrm{d}x} &= -\zeta_3 C_\mu^{1/4} k \frac{f_l}{\sqrt{f_k}} \\ &= -\zeta_3 C_\mu^{1/4} k \frac{f_k}{f_\varepsilon}, \end{aligned} \tag{E.37}$$

which, under the assumption of $f_\varepsilon = 1.0$ becomes

$$\langle U \rangle \frac{\mathrm{d}\left(\nu_t\right)}{\mathrm{d}x} = -\zeta_3 C_\mu^{1/4} f_k k. \tag{E.38}$$

An additional constant β_{KSKL} is defined, such that

$$\zeta_3 C_\mu^{1/4} f_k = \beta^* - \beta_{KSKL}, \tag{E.39}$$

leading to

$$\langle U \rangle \frac{\mathrm{d}\left(\nu_t\right)}{\mathrm{d}x} = -\left(\beta^* - \beta_{KSKL}\right) k. \tag{E.40}$$

While the functions Eq. E.36 and E.40 are not easily solved, it is important to realise the similarity with the decay functions of the PANS-SST model (Eq. E.5 and E.27, respectively). The functions are identical, except for the constants, implying solutions of a similar form. Consequently, based on Eq. E.24, the decay of k is given by

$$k = \frac{k_{in}}{\left[\frac{1}{\langle U \rangle}\left(\langle U \rangle + \beta_{KSKL}\left(x - x_{in}\right)\frac{k_{in}}{\nu_{t,in}}\right)\right]^{\frac{\beta^*}{\beta_{KSKL}}}} \tag{E.41}$$

and, based on Eq. E.30, the decay of ν_t is given by

$$\nu_t = \frac{\nu_{t,in}}{\left[\frac{1}{\langle U \rangle}\left(\langle U \rangle + \beta_{KSKL}\left(x - x_{in}\right)\frac{k_{in}}{\nu_{t,in}}\right)\right]^{\frac{\beta^*}{\beta_{KSKL}} - 1}}. \tag{E.42}$$

CURRICULUM VITÆ

Maarten Derk KLAPWIJK

15-12-1994	Born in Capelle aan den IJssel, the Netherlands.

EDUCATION

2007–2012	Erasmiaans Gymnasium, Rotterdam
2012–2015	BSc. in Marine Technology Delft University of Technology
2015–2017	MSc. in Marine Technology Delft University of Technology
2017–2021	PhD. at Delft University of Technology in collaboration with MARIN, Wageningen, the Netherlands *Thesis:* Towards predicting cavitation noise using scale-resolving simulations: The importance of inflow turbulence *Promoters:* T. van Terwisga & J. Westerweel *Supervisors:* T. Lloyd & G. Vaz

AWARDS

2013	Jong Talent Aanmoedigingsprijs by: Koninklijk Hollandsche Maatschappij der Wetenschappen
2017	KNVTS Maritime Student Award by: Koninklijke Nederlandse Vereniging van Technici op Scheepvaartgebied
2018	Prof. ir. dr. Kooy afstudeerprijs by: Koninklijk Instituut van Ingenieurs
2019	Nominated for RNLN Hengel-Spengler award by: Maritime Awards Gala

LIST OF PUBLICATIONS

Journal papers:

8. **M. Klapwijk**, T. Lloyd, G. Vaz. *On the accuracy of partially averaged Navier-Stokes resolution estimates*, International Journal of Heat and Fluid Flow **80**, Article 108484 (2019).
7. **M. Klapwijk**, T. Lloyd, G. Vaz, T. van Terwisga. *Evaluation of scale-resolving simulations for a turbulent channel flow*, Computers & Fluids **209**, Article 104636 (2020).
6. R. Liebrand, **M. Klapwijk**, T. Lloyd, G. Vaz. *Transition and turbulence modeling for the prediction of cavitating tip vortices*, Journal of Fluids Engineering **143(1)**, Article 011202 (2020).
5. **M. Klapwijk**, T. Lloyd, G. Vaz, T. van Terwisga. *On the use of synthetic inflow turbulence for scale-resolving simulations of wetted and cavitating flows*, Ocean Engineering **228**, Article 108860 (2021).
4. **M. Klapwijk**, T. Lloyd, G. Vaz. *The development of a partially averaged Navier-Stokes KSKL model*, Journal of Fluids Engineering (2021).
3. **M. Klapwijk**, S. Lemaire. *And... Action! Setting the scene for accurate visual comparisons in CFD using ray tracing*, Journal of Marine Science and Engineering **9**, Article 1066 (2021).
2. **M. Klapwijk**, T. Lloyd, G. Vaz, M. van den Boogaard, T. van Terwisga. *Exciting a cavitating tip vortex with synthetic inflow turbulence: a CFD analysis of vortex kinematics, dynamics and sound generation*, (Submitted for publication).
1. A.P. Lidtke, **M. Klapwijk**, T. Lloyd. *Effect of inflow turbulence on sound radiated by a circular cylinder in a low Mach number flow*, (Submitted for publication).

Conference papers:

3. **M. Klapwijk**, T. Lloyd, G. Vaz, T. van Terwisga. *Channel flow at* $Re_\tau = 395$*: LES is more (turbulent than PANS)*, 21th Numerical Towing Tank Symposium, October 2018, Cortona, Italy.
2. **M. Klapwijk**, T. Lloyd, G. Vaz, T. van Terwisga. *PANS simulations: low versus high Reynolds number approach*, MARINE Conference, May 2019, Gothenborg, Sweden.
1. R. Liebrand, **M. Klapwijk**, T. Lloyd, G. Vaz, R. Lopes. *A sensitivity analysis of CFD transition modelling in the context of vortex roll-up prediction*, MARINE Conference, May 2019, Gothenborg, Sweden.